Gamma spectrometry for chronology of recent sediments

⁂

Daniela Pittauerová

Universität Bremen
2013

Universität Bremen

Fachbereich 1
(Physik und Elektrotechnik)

Gamma spectrometry for chronology of recent sediments

Dissertation zur Erlangung des akademischen Grades
Doktor der Naturwissenschaften (Dr. rer. nat.)

vorgelegt von
RNDr. Mgr. Daniela Pittauerová

1. Gutachter: Dr. Helmut W. Fischer
2. Gutachter: Prof. Dr. Bernd Zolitschka

Eingereicht am: 15.10.2013
Tag des Promotionskolloquiums: 17.12.2013

To 'nic and Timmy.

Acknowledgments

Completing this manuscript would not be possible without contributions from many people.

My supervisor Dr. Helmut Fischer, trusting my skills and abilities, gave me the opportunity to find my place in a completely new world shortly after my arrival to Germany and made me part of his team. Later on, after my son was born, he enabled me to combine family and professional life according to my needs and preferences. I really admire his empathic attitude and careful and detailed involvement in all projects we have worked on together.

My lab colleague Bernd Hettwig patiently and scholarly answered the endless stream of my questions and helped me become an experienced spectrometrist. He also created a calm and friendly atmosphere in our lab and contributed to my coffee addiction.

Dr. Volker Hormann helped me out on many occasions with his valuable advice and proofreading. I spent great time talking to him about Life, the Universe and Everything. He himself and Felix Rogge formed the healthy heart of our lab team, together with the girls: Susanne Ulbrich, Marievi Souti, Edda Toma and Regine Braatz that we have done lots of work and had lots of fun together. There’s been a stream of dear co-workers and students that were always eager to help out when I needed it: Dr. Ahmed Qwasmeh, Andrei Burak, Homa Ghasemifard, Dorothea Gradic, Dominic Höweling, Dr. Maarten Veevaete, Dr. Mohammed Khalil Saeed Salih, Oliver Bislich, Dr. Rolf Goedecke, Tom Bielefeld and Wissam Chehade.

The PIP (Postgraduate International Programme in Physics and Electrical Engineering) supported me financially by contributing to my international trips for sharing my results at conferences or learning new skills at workshops.

My greatest THANKS go to my family. ’nic patiently made this thesis materialize and supported me by all possible and impossible means, while dragging me all around the globe or at least burning diesel with me while “conquering large parts of Europe”. Timmy was very brave when his Mom was busy. And my parents, my brother and my grandmother kept their fingers crossed far far away.

Abstract

This thesis deals with several aspects of gamma spectrometric analysis of natural and artificial isotopes in sediments and their use as tracers for qualification and quantification of accumulation and mixing processes in different aquatic environments. Sediment cores from three distinct areas including terrigenous sediments deposited on the continental slope off NW Africa, deep sea sediments off Sumba Island and five stations from the Gulf of Eilat in the Red Sea area were measured and interpreted within this dissertation.

The main concern in gamma spectrometry of voluminous environmental samples is a reliable efficiency calibration. This is specially relevant for the analysis of low energy gamma emitters ($<$100 keV). ^{210}Pb, an important isotopic tracer to cover the period of the last century, is one of them. Within this work mathematical efficiency calibration was applied using a commercial software package. A series of validation tests was performed and evaluated for point and voluminous samples.

When using ^{210}Pb as a tracer it is necessary to determine its excess portion, which is not supported by ingrowth from the parent nuclide ^{226}Ra. Its analysis is mostly performed via short lived daughter isotopes that follow after the intermediate gaseous member ^{222}Rn. Preventing the escape of radon from the sample is a critical step before analysis due to a negative effect of supported ^{210}Pb underestimation on the chronology, which was also documented in this thesis. Time series registering ingrowth of ^{214}Pb and ^{214}Bi towards radioactive equilibrium with ^{226}Ra in different containers were evaluated for analyses of ^{226}Ra. Direct analyses of ^{226}Ra was compared to its detection via daughter products.

A method for aligning parallel radionuclide depth profiles was described and applied successfully in two case studies from the continental slope off NW Africa and off Sumba Island, Indonesia. This is primarily important when combined profiles obtained from short multicorer cores and long gravity cores (with topmost parts not being preserved) need to be studied.

Another useful strategy involving summing up spectra was suggested for the Indonesian sediments, which lead to reducing detection limits and allowed quantifying artificial radionuclides activity concentrations, ratios and inventories.

Finally, an approach of using ^{232}Th series additionally to ^{210}Pb and ^{137}Cs gamma emitters for interpretation of depth profiles in order to quantify accumulation and mixing rates was applied within a study of phosphorous contribution to eutrophication in the Gulf of Eilat.

The three upper mentioned approaches lead to easier and more complete interpretation of radionuclide data and their practical use within interdisciplinary studies of climate of the past and environmental pollution.

Sediment chronology, Gamma spectrometry, Excess ^{210}Pb, Excess ^{228}Th, ^{137}Cs, ^{241}Am

Contents

List of Figures

List of Tables

List of Abbreviations

$^{210}\mathrm{Pb}_{\mathrm{sup}}$	Supported $^{210}\mathrm{Pb}$
$^{210}\mathrm{Pb}_{\mathrm{xs}}$	Excess (unsupported) $^{210}\mathrm{Pb}$
AD	Anno Domini, years after the start of the Julian calendar
ADC	Analogue to digital converter
AMS	Accelerator mass spectroscopy
BfS	Bundesamt für Strahlenschutz, German Federal office for Radiation Protection
BP	(alternatively, cal BP) before present, age before AD 1950 used in expressing calibrated ages in radiocarbon chronology
CAVS	Constant specific activity - variable sedimentation rate (model), also called CIC model
CF	Constant flux (model), also called CRS model
CF-CS	Constant flux - constant sedimentation (model)
CIC	Constant initial concentration (model)
CRS	Constant rate of supply (model), also called CF model
CSA	Constant specific activity (model), also called CIC model
CSC	Cascades summing correction
D-S	Detector to source (distance)
DDEP	Decay Data Evaluation Project
EC	Electron capture
EML	Environmental Measurements Laboratory, USA
ESR	Electron spin resonance

FEP	Full energy peak
FWHM	Full width at half maximum
GC	Gravity core
GOE	Gulf of Eilat / Aqaba
HPGe	High-purity germanium (detector)
IC	Internal conversion
ICP-MS	Inductively coupled plasma mass spectrometry
ISOCS	In-Situ Object Calibration Software
ITF	Indonesian throughflow
KC	Kuroshio Current
Laboratory	Radioactivity measurements laboratory of the Institute of Environmental Physics (Institut für Umwelphysik, IUP) at the University of Bremen
LabSOCS	Laboratory Sourceless Object Calibration Software
LS	Luminescence
LSC	Liquid scintillation counting
MC	Mindanao Current
MC	Monte Carlo (method)
MCA	Multichannel analyzer
MCNP	Los Alamos National Laboratory Monte Carlo N-Particle modelling code
MUC	Multicorer core
NEA	The Nuclear Energy Agency of the Organisation for Economic Co-operation and Development
NEC	North Equatorial Current
NECC	North Equatorial Countercurrent
NNDC	National Nuclear Data Center - Brookhaven National Laboratory
NPP	Nuclear power plant

OSL	Optically-stimulated luminescence or photoluminescence
PTB	Physikalisch-Technische Bundesanstalt, the National metrology institute
QA	Quality assurance
RIMS	Resonance ionization mass spectrometry
ROI	Region of interest
SEC	South Equatorial Current
SIT	Sediment isotope tomography (model)
TCN	Terrestrial (in-situ) cosmogenic nuclides
TCS	True coincidence summing
TFY	Fission product yield for thermal neutron fission
TIMS	Thermal ionization mass spectrometry
TL	Thermoluminescence
UNSCEAR	United Nations Scientific Committee on the Effects of Atomic Radiation
WMO	World Meteorological Organization

List of symbols

Symbol	**Units**	**Description**
$\Delta^{14}C$	‰	per mil depletion/enrichment with regard to standard normalized for isotope fractionation
ΔR	yr	reservoir age correction
ϵ	–	efficiency
θ	rad	scattering angle
λ	yr^{-1}	decay constant
μ	–	arithmetical mean
ρ	$g \cdot cm^{-3}$	density
ϕ	–	porosity
σ	–	standard deviation
τ	yr	radionuclide mean life
χ	–	sum of squared deviations
a	cm^{-1}	linear attenuation coefficient
A	Bq	activity
BR	–	branching ratio
c_v	–	coefficient of variation
C	$Bq \cdot kg^{-1}$ $(Bq \cdot cm^{-3})$	activity concentration
D	$cm^2 yr^{-1}$	diffusive mixing coefficient
DoF	–	degrees of freedom
E	keV	energy, E_γ stands for gamma energy
fMC	–	fraction of modern carbon
F	–	F-value for F-test
$\mathcal{F}$	$Bq \cdot cm^{-2} yr{-1}$	radionuclide flux to sediment surface
I_γ	%	emission probability (γ-line intensity)
$\mathcal{I}$	$Bq \cdot cm^{-2}$	radionuclide inventory in sediment profile
$\mathcal{J}$	$Bq \cdot cm^{-2}$	total activity deposited per unit area
K	–	scaling factor

L_C	imp	decision threshold
L_D	imp	detection limit
m	$g \cdot cm^{-2}$	mass depth
M	kg	mass
N	–	number (of atoms), counts, ...
n	cps	count rate (counts per second)
N_{net}	–	net peak area
P	–	probability
r	$g \cdot cm^{-2}yr-1$	mass accumulation rate
r_S	–	Spearman rank correlation coefficient
RSS	–	residual sum of squares
S	$cm \cdot yr^{-1}$	sedimentation rate
$T_{1/2}$	s (yr)	half-life
T_L	s	life-time (counting time)
t	s (yr)	time, age
w	–	weighting factor
x	cm	thickness (sample height)
z	cm	depth (below sediment surface)

Factors and other symbols used in individual equations only might not be included in this list.

Chapter 1

Introduction and overview

> Human beings would split the atom and invent television, nylon, and instant coffee before they could figure out the age of their own planet.
>
> Bill Bryson, *A Short History of Nearly Everything*

Accurate age estimation of upper parts of marine and lacustrine sediment cores is a powerful tool for enabling correct interpretations of geoscientific data, e.g. environmental pollution or recent climate change. Chronology based on excess ^{210}Pb analysis allows dating up to 150 years (e.g., Appleby, 2001, 2008) in favorable conditions. This timescale is ideal to cover the most significant anthropogenic effects to the environment.

^{210}Pb can be estimated by two different laboratory techniques: alpha or gamma spectrometry. The advantage of the latter is that it is a non-destructive method and multiple gamma emitters are detected within a single spectrum. Therefore, this work deals mainly with gamma spectrometry. It was attempted to present (probably for the first time) a comprehensive overview on sediment chronology using gamma spectrometry, including understanding the physical effects and difficulties, together with showing several geoscientific applications. This is atruly interdisciplinary approach, requiring skills and collaborations in both fields.

Main objectives

The leading obstacle within gamma spectrometry of voluminous environmental samples seems to be the attenuation of low-energy gamma rays in the bulk material. An important aim of this work is to establish a reliable efficiency calibration method for the whole range of gamma emitters in the spectra with special attention to the low energy ^{210}Pb, independent on physical sample properties like geometry, composition or density. Such a method is available in the form of mathematical calibration using Monte Carlo based commercial software like Canberra LabSOCS (Laboratory Sourceless Object Calibration Software) for factory characterized detectors. One of the goals of this thesis is validation of such use of LabSOCS.

Although the most extensive part of this thesis is devoted to successful quantification of ^{210}Pb, the signals of other natural and artificial isotopes in spectra offer the opportunity of additionally exploiting their potential. More common examples are verification of ^{210}Pb based chronologies by man-made radiotracer ^{137}Cs or ^{241}Am or using the ^{226}Ra signal as a proxy for supported lead in ^{210}Pb chronology. Less frequently used options are studying profiles of Th-series isotopes, ^{40}K or short-lived isotopes like ^{7}Be. An additional aim of this study is to find ways to maximize the use of the information provided by the gamma spectra.

In existing literature much attention is paid to the importance of accurate detection of ^{210}Pb. As excess ^{210}Pb is calculated as a difference of total ^{210}Pb and its supported portion represented by ^{226}Ra activity, a closer look is devoted to the gamma analyses of the latter isotope.

Problematic issues regarding Pb-chronology are not only the radionuclide analysis, but also the processes in the sediment itself, which might have undergone different post-sedimentation changes: mixing, compaction, perhaps diffusion. Interpretation of this type of profile is only possible by choosing appropriate models. Explaining and comparing models in order to be able to choose the right one and their application within site related studies is another aim of this study.

Overview of the thesis

The thesis is divided into following parts (Fig. 1.1):

- **Chapter 2** presents radionuclide and non-radionuclide methods of chronology for material from the most recent periods, which are partially complementary to ^{210}Pb and ^{137}Cs methods.
- **Chapter 3** describes the principles and most frequently used models for ^{210}Pb chronology.
- An introduction to radioactivity and a description of gamma spectrometric method is given in **chapter 4**.
- The following **chapter 5** contains an experimental part devoted to long-term background in the gamma detectors used in the study.
- **Chapter 6** compiles a list of gamma emitting natural and most common artificial radionuclides which are present in sediment spectra. The advantages and disadvantages of detecting ^{210}Pb using either alpha or gamma spectrometry are addressed. Also suitable gamma lines for individual radionuclides are discussed, mentioning possible interferences or other obstacles to their successful application.
- In **chapter 7** efficiency calibration of gamma spectrometry, as well as advantages and disadvantages of both classical experimental calibration and more recent methods of mathematical calibration are covered. An experimental part deals with validation of the LabSOCS mathematical efficiency calibration method in the Laboratory.
- **Chapter 8** describes difficulties connected to supported lead estimation for ^{210}Pb chronology. It explores the effect of possible underestimation of ^{226}Ra on resulting chronology. The question of establishing radioactive equilibrium between ^{226}Ra and its progeny in samples is treated.

The first more general part of the thesis is followed by three site-related studies, where ^{210}Pb chronologies and sedimentation rates were determined within this thesis. Furthermore, each of the chapters deals with different specific aspects connected to detected radionuclides.

- Within **chapter 9** a new procedure of depth alignment of the sediment master cores with associated short (multicorer) cores based on gamma emitting radionuclides from atmospheric fallout, namely excess ^{210}Pb and ^{137}Cs, is introduced. Its main purpose is to estimate the amount of material missing at the top of the gravity cores, to perform

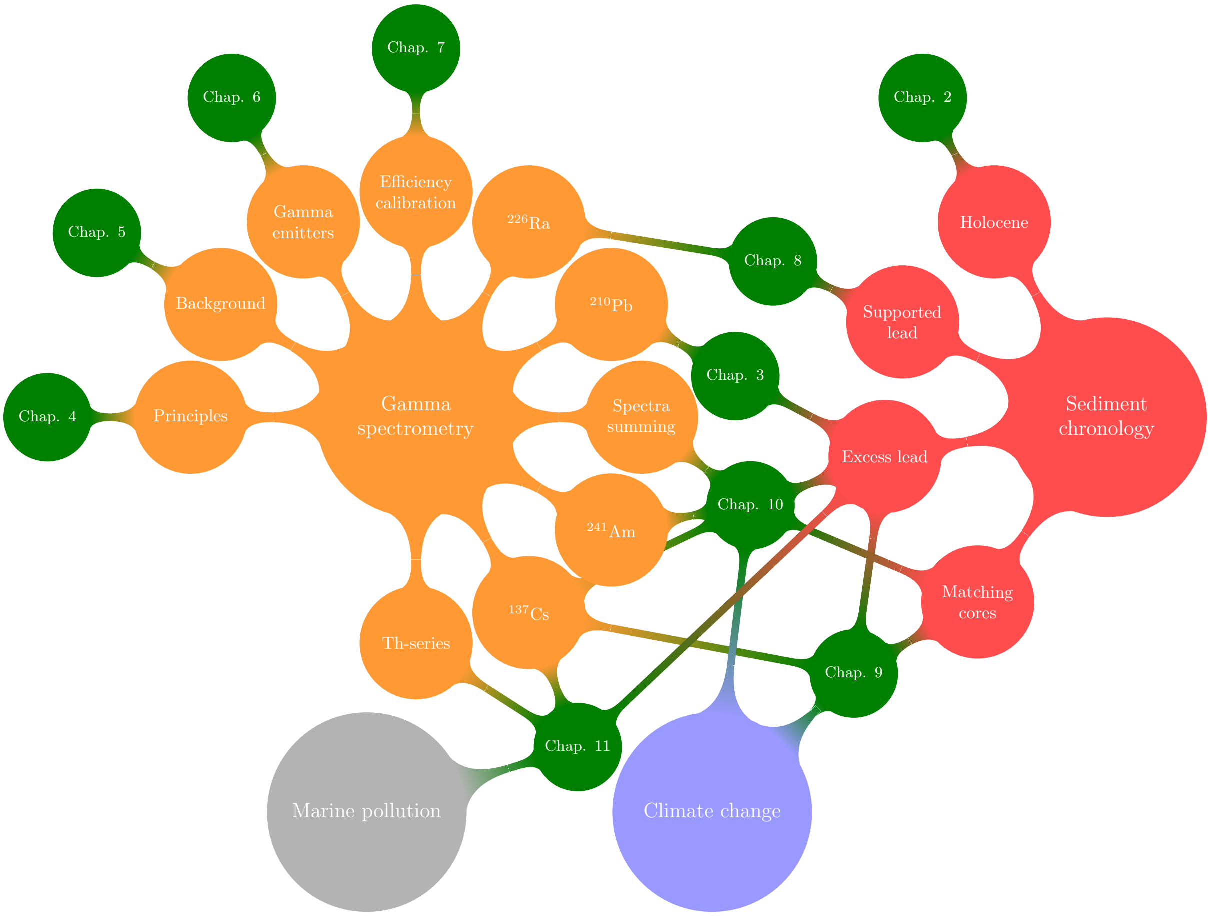

Figure 1.1: *Schematic overview of topics dealt with in this thesis and the corresponding chapters.*

associated cores depth matching and to provide combined chronologies. The method was tested on modelled ^{210}Pb and ^{137}Cs profiles and successfully applied in two case studies of marine sediments from the NW Africa continental slope.

- **Chapter 10** presents a chronology of a deep-sea core from Lombok basin, Indonesia, with unusual artificial radionuclide ratios. In order to improve detection limits of radionuclides and to calculate their ratios and inventories a new method using spectra summing was applied.

- In **chapter 11** for five cores recovered from the Gulf of Eilat, near the Israeli coast, radionuclide profiles were studied in order to calculate sedimentation rates and to look for the effect of environmental pollution connected to the phosphate industry. In these cores a Th-series radioactive disequilibrium was observed and studied.

- Finally, the last **chapter 12** combines and summarizes the results from the previous chapters.

The measured data not presented in main text, as well as codes and procedures are attached in two appendices.

General comments

All gamma spectra (unless specifically mentioned otherwise) within this thesis were obtained in the Radioactivity measurements laboratory of the Institute of Environmental Physics (Institut für Umwelphysik, IUP) at the University of Bremen (in further text only Laboratory).

Throughout this thesis the decay data are taken from the Decay Data Evaluation Project (DDEP) without further reference. DDEP is recommended as the most up-to-date gamma spectrometry data source of first choice for example by Gilmore (2008) or Pearce (2008). If DDEP data are not available for some isotope at the time of writing this thesis, a reference for another source of data is given.

DDEP is an international collaboration led by the Laboratoire national de métrologie et d'essais - Laboratoire national Henri Becquerel (LNE-LNHB) in order to provide nuclear data for the purposes of applied research and detector calibration. Within this project earlier IAEA-TECDOC-619 data were re-evaluated. An on-line database synchronous with the DDEP project used to be available at `http://www.nucleide.org/DDEP.htm`, but was out of operation at the time of finalizing this thesis. However, the data can be downloaded in the form of a monograph (Bé et al., 2011) from the Bureau International des Poids et Mesures (International weights and measures bureau) `http://www.bipm.org/en/publications/monographie-ri-5.html` in pdf format.

Chapter 2

Chronology in the Holocene

Sediments at the bottom of lakes, seas and oceans can serve as an unique archive of climate and environmental data. They are collected and studied by a variety of geophysical and geochemical methods in order to obtain proxies of different parameters for water bodies and the climate in the past times. Past conditions can be reconstructed using these indicators and compared to the present situation. Estimation of the age profile of sediment cores is an important part of climate and environmental research, because often the obtained data would be worthless without information about the age of a specific sample. A list and short description of the most important chronological methods used in environmental research in the Holocene, the youngest geological epoch, which began approximately 11.7 thousand years ago, is given below.

2.1 Radionuclide dating methods

Radionuclide dating methods include methods of age determination of rocks and minerals based on nuclear decay of radioactive isotopes (Lanphere, 2001). The 90 elements found in Nature are represented by approximately 254 stable isotopes and 85 radioactive isotopes (these numbers change occasionally with new observations of decay of the isotopes with a very long half-life, originally believed to be stable). About 35 of the radioactive isotopes have half-lives comparable or greater than the Earth age and have not decayed completely since the elements of the solar system were created. These long-lived isotopes are called primordial. The remaining shorter lived isotopes are being continuously produced by decay of long-lived radioactive isotopes (often as members of radioactive decay chains) or by nuclear reactions by particles from extraterrestrial origin (these are called cosmogenic). Another group of radionuclides are those of artificial origin which have been introduced to the environment only since the beginning of the atomic age (after 1945). In Fig. 2.1 radionuclides suitable for the Holocene chronology are shown together with their approximate dating ranges.

2.1.1 Primordial radionuclides and natural decay chains

U-238 and U-235 series

^{238}U and ^{235}U series methods (Thompson, 2007; Dickin, 2005) are based on disequilibrium within decay series caused by different physical and chemical properties of the individual decay series members. For example, the elements radium and uranium in water environment do not attach to particles easily, but remain in the dissolved phase, while thorium, protactinium and lead are strongly particle reactive. Separation of radionuclides leads to radioactive disequilibrium between parent-daughter pairs. The resulting excesses or deficiencies in these isotope pairs are the

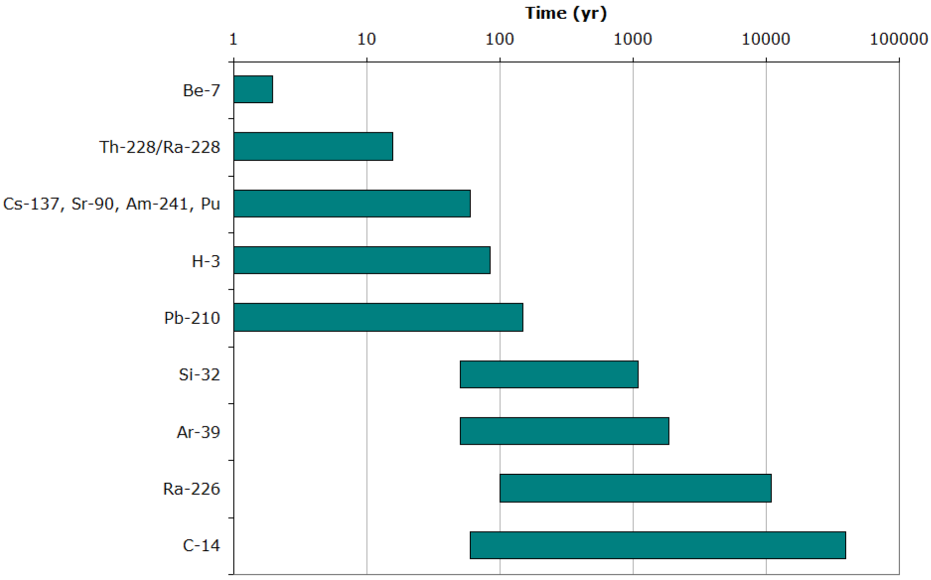

Figure 2.1: *Timescale of radiometric dating methods suitable for the Holocene chronology with approximate age ranges. ”Primordial / series” stands for isotopes that are part of natural decay chains with a primordial isotope as a parent nuclide.*

fundamentals for chronologies. As the isotope is incorporated into sedimentary accumulations, it decays at a known rate, "unsupported" by further decay of the parent isotope from which it has been separated. In carbonate sediments younger than 10^4 years, a system ^{234}U(-^{230}Th)-^{226}Ra$_{xs}$ is used assuming that only U and Ra are co-precipitated during mineralization (Schmidt & Cochran, 2010). This so called ^{226}Ra$_{xs}$ chronology was previously used for sediments (Grayson & Plater, 2007; Fairclough et al., 2006; Koide et al., 1976). Also ^{210}Pb$_{xs}$ chronology belongs to this group of methods, but will be discussed in detail in Chapter 3.

Another approach relies on the build up of an isotope that is initially absent or present in negligible amounts towards equilibrium with its parent isotope. This is known as "daughter deficiency" dating and is most commonly applied to carbonate materials (Ku, 1976; Schmidt & Cochran, 2010). The assumption is that uranium (^{234}U and ^{235}U) is co-precipitated with calcite or aragonite from natural waters that do not contain thorium (^{234}Th) and protactinium (^{231}Pa). The ingrowths of ^{230}Th and ^{231}Pa to equilibrium with the uranium isotopes can then be used as chronometers, but this is hardly ever used in the Holocene time scale due to their long half-lives (75,380 years and 32,760 years, respectively).

Th-232 series

Th series disequilibrium methods are occasionally used for dating recent biological and geological materials. The half-life of ^{228}Ra is 5.75(4) years and of ^{228}Th 1.9140(6) years.

The ^{228}Th/^{228}Ra ratio can serve as an indicator for the growth rate of marine bivalves shells in a hydrothermal spring region (Turekian et al., 1979), life span or tissue age of certain plants (Chao et al., 2007) and has been proposed for estimation of post-mortal interval in bone tissue (Kandlbinder et al., 2009). The ^{228}Th /^{232}Th ratio has previously been used for dating young marine sediments (Koide et al., 1973) and hydrothermal minerals in mid-ocean ridge chimneys (Grasty et al., 1988; Reyes et al., 1995) or minerals precipitated from a geothermal well in Rome (Voltaggio et al., 1987). Another possibility is estimating age based on the ^{228}Ra/^{226}Ra ratio.

These two radium isotopes from U and Th decay series with the same chemical properties, but different half-lives, were used for dating mineral growth rates of hokutolite (Saito, 2007) and radiobarite (Zielinski et al., 2001) and for estimation of sedimentation rates at the Amazon continental shelf (Dukat & Kuehl, 1995).

Excess ^{228}Th in surface sediment layers was observed in the China Sea (Chen & Huh, 1999) and and used for estimation of particle mixing rates at eutrophic, mesotrophic and oligotrophic sites in the NE tropical Atlantic (Legeleux et al., 1994). In combination with ^{210}Pb dating, excess ^{228}Th can be used for the estimation of mixing rates (Hancock & Hunter, 1999; Chih-An et al., 1987).

2.1.2 Cosmogenic radionuclides

Radiocarbon

^{14}C dating is a widely used method in hydrology, atmospheric science, oceanography, geology, palaeoclimatology and archeology for age estimation of materials of organic origin up to $6{\cdot}10^4$ years (e.g., Björck & Wohlfarth, 2002; Hua, 2009). Collisions of cosmic-rays produced thermal neutrons with N_2 and O_2 in the upper atmosphere generate radiocarbon by two major reactions:

$^{14}_{7}N(n,p)^{14}_{6}C$ and $^{17}_{8}O(n,\alpha)^{14}_{6}C$,

from which the former one is more frequent due to high neutron capture cross section and high isotopic ratio of ^{14}N of 99.6% (Lehto & Hou, 2010). Carbon is oxidized rapidly and radioactive CO_2 joins the carbon cycle. It may photosynthetically enter plants or may be exchanged with CO_2 in water and subsequently be incorporated by biota or deposited in the form of carbonate. Since the death of the organism (or crystallization of the mineral) a closed system is assumed (there is no more isotopic exchange between the organisms' remains or the minerals, respectively, and the surrounding media) which enables to construct a chronology based on decay of ^{14}C with a half-life of approximately 5500 years. The team of Prof. Willard F. Libby was the first to start using radiocarbon for dating purposes (Libby et al., 1949) and his team measured the rate of ^{14}C decay. Its half-life was estimated to 5568(30) years (so called Libby half-life). Later the half-life was corrected to be 5730(40) years (NNDC, 2011). Despite the new half-life's greater precision, the Libby half-life is still widely used to avoid discrepancies among different studies and sets of data. This does not cause a great difficulty, as the Libby ages can be simply converted to the precise ages by multiplying by a constant of 1.03.

In the past, ^{14}C concentrations were measured by means of radiometric counting techniques (gas counting and LSC, liquid scintillation counting), presently the predominant method is accelerator mass spectroscopy (AMS) due to its higher sensitivity.

Correction for temporal variations in the natural atmospheric ^{14}C content is applied using calibration curves, obtained by dating samples by ^{14}C and other independent methods (dendrochronology, other radiometric techniques on deep ocean sediment cores, lake sediment varves, coral samples, speleotherms and even absolute ages of archaeological artifacts). This varying natural ^{14}C content (expressed in Δ^{14}C) is a proxy for changes in the geomagnetic field strength, solar fluctuations, carbon reservoir reorganizations, and climatic changes in the past.

Another correction has to be applied when samples obtained their carbon from a different source (reservoir) than atmospheric carbon. Ocean water is not in equilibrium with the atmospheric carbon composition due to delay in exchange between atmospheric CO_2 and ocean bicarbonate and the dilution effect caused by mixing of young surface waters with old upwelled deep waters. This may result in marine organisms appearing older than contemporaneous terrestrial materials. The offset between surface ocean and terrestrial samples is known as the reservoir age. The surface ocean has a reservoir age of about 400 years, but this number varies significantly depending on geographical position and source of water; the deep ocean appears older.

Decrease in the atmospheric ^{14}C due to fossil fuel combustion since the industrial revolution (about 1890), the so called Suess effect (Tans et al., 1979), later a ^{14}C peak from nuclear bomb tests (e.g., Broecker, 2011), which doubled the pre-bomb ^{14}C and continuous nuclear energy industry ^{14}C releases make precise dating of the youngest sediments impossible. Due to these difficulties in modern radiocarbon dating, and due to the suitable half-life of ^{210}Pb to cover exactly this period, both techniques are used frequently as complementary methods for sediment chronology.

Beryllium-7

^{7}Be is a short lived cosmogenic radionuclide with the half-life of 53.22(6) days. It is formed mainly in the stratosphere by cosmic ray spallation of nitrogen and oxygen (Yoshimori et al., 2003). It attaches to airborne particals and is removed from the atmosphere primarily during precipitation. ^{7}Be in precipitation shows high spatial and temporal variations. The amount of ^{7}Be that reaches the Earth's surface depends on its production rate in the atmosphere, which is a function of solar activity (Papastefanou & Ioannidou, 2004), the extent of stratosphere-troposphere air exchange, tropospheric circulation patterns, and the efficiency of the removal via wet and dry deposition (Zhu & Olsen, 2009). ^{7}Be can be measured easily by gamma spectrometry. In geochronology it is used for estimating soil erosion rates (Jha, 2012)and sedimentation processes associated with individual periods of heavy rain on small scale (Wilson et al., 2003). In oceanography ^{7}Be can be used as a tracer of water masses and mixing in the surface layers of the open ocean. Also, ^{7}Be can be detected in very young sediments (Fischer et al., 2009), where it may serve as a tracer for mixing processes (Dibb & Rice, 1989), sediment dynamics and accumulation patterns (Zhu & Olsen, 2009).

Tritium

^{3}H is a radioactive hydrogen isotope of cosmogenic origin with a half-life of 12.32(2) years (NNDC, 2011). It decays by β^- decay to ^{3}He. In the atmosphere tritium is produced mainly by the reaction of fast neutrons (>4 MeV) with nitrogen (CNSC, 2009):

$$^{14}_{7}N + n \rightarrow ^{12}_{6} C + ^{3}_{1} H.$$

^{3}H atoms combine with oxygen to form water molecules and reach the ground in form of precipitation.

Tritium also has an artificial origin. It was produced in amounts that greatly exceeded the natural levels during atmospheric nuclear testing as a fusion product in thermonuclear weapons and U and Pu fission product (CNSC, 2009). In smaller amounts (fraction of natural level) it has been introduced to the environment as liquid and gaseous discharges of nuclear power plants and fuel reprocessing plants (Luykx & Fraser, 1986). Since the early 1960's artificial tritium entered the groundwater reservoirs. From ^{3}H/^{3}He ratio the period since the last contact with the atmosphere can be calculated. Tritium is also used as a tracer in ocean circulation studies (e.g., Povinec et al., 2003).

Tritium can be analyzed using low level LSC (Morgenstern & Taylor, 2009). Even lower detection limits can be achieved by mass spectrometric measurement of ^{3}He ingrowth (Sültenfuß et al., 2009).

Terrestrial (in-situ) cosmogenic nuclides (TCN)

Terrestrial cosmogenic nuclides (Manz, 2002) are formed within the upper few meters of the Earth's surface by interaction of nuclei in minerals with cosmic radiation in-situ. Concentrations of cosmogenic nuclides present in geological material are proportional to its exposure time at the Earth's surface. Several TCNs (^{14}C, ^{3}He, ^{10}Be, ^{21}Ne, ^{26}Al and ^{36}Cl) are measured in minerals or whole rock samples to determine the exposure age of a wide range of landforms, but of these nuclides, only radiocarbon is suitable for dating the Holocene surface processes due to its relatively short half-life.

Silicon-32

^{32}Si is produced in the atmosphere via spallation reactions of ^{40}Ar nuclei with cosmic rays. Its activity estimation is rather difficult due to the low production rate and can be done by radiometric counting (LSC) of its daughter nuclide ^{32}P or by AMS. Despite this, it has the potential to fill up the dating gap between chronologies based on the shorter-lived isotopes of ^{3}H and ^{210}Pb and longer lived ^{14}C in sediments containing biogenic silica (radiolarites, diatomites) (Fifield & Morgenstern, 2009; DeMaster & Cochran, 1982; Lal et al., 1960) due to its suitable half-life. Its exact value is still a question of scientific debate, since the reported half-lives vary significantly from 101 to 330 years. However, two recent works gave similar values of 178 ±10 years measured by activity decrease with depth in an accurately dated varved sediment core (Nijampurkar et al., 1998), and 162 ±12 years determined by means of AMS (Thomsen et al., 1991).

Argon-39

^{39}Ar (Loosli, 1983) with a half-life of 269(3) years (NNDC, 2011) is another isotope which can cover the gap between short-term and longer-term chronologies of glaciers, oceans and groundwater. ^{39}Ar is produced mainly by cosmic rays in the stratosphere by

$$^{40}_{18}Ar(n,2n)^{39}_{18}Ar$$

reaction. Dating is based on the ^{39}Ar/Ar ratio. Detection is possible using proportional gas counters in low level underground laboratories.

2.1.3 Artificial radionuclides

Caesium-137 (radiocaesium) and Caesium-134

With a half-life of 30.05(8) years, ^{137}Cs is widely used as an independent chronometer in recent sediment studies. It belongs to the most abundant fission products. The fission yield for thermal neutron fission of ^{235}U (TFY) is 6.3% (Lehto & Hou, 2010).

^{137}Cs was introduced to the atmosphere on a global scale as a consequence of nuclear bomb tests; the onset (first appearance) horizon in sediments not being affected by later reworking should correspond to 1954–1955 (Leslie & Hancock, 2008), maximal deposition occurred in 1963, when the atmospheric ^{137}Cs linked to nuclear bomb test fallout culminated. These chronomarkers are easier to identify in the northern hemisphere; in the southern hemisphere nuclear weapons fallout is about three times lower than in the north due to atmospheric circulation patterns, as well as geographical distribution of atmospheric tests. Therefore, recognition of the radiocaesium signal can be challenging in the southern hemisphere. Details of deposition of this isotope are described in the UNSCEAR 2000 Report (UNSCEAR, 2000) (Fig. 2.2, 2.3).

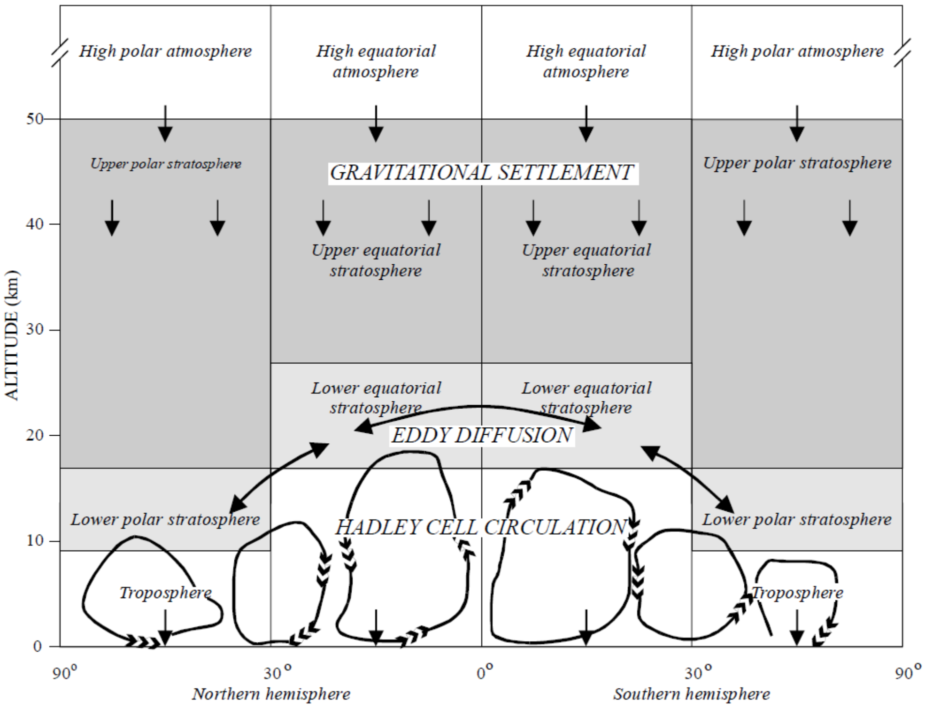

Figure 2.2: *A compartment diagram representing atmospheric regions and the predominant atmospheric transport processes, used to describe atmospheric dispersion and deposition of radioactive debris produced in atmospheric nuclear testing. Source: UNSCEAR (2000).*

Further significant large scale inputs of the isotope to the environment occurred after the Chernobyl nuclear power plant (NPP) accident in May 1986 and the Fukushima Daiichi NPP accident in March 2011. While the fallout from the former accidental release affected mainly the European continent, traces of the later one could hardly be distinguished from the older contamination in Europe (e.g., Pittauerová et al., 2011) and could mainly be identified based on other short-lived isotopes, like ^{134}Cs and ^{131}I. Beside some 13 PBq of atmospheric ^{137}Cs emission (Chino et al., 2011), an estimated amount of 27 PBq ^{137}Cs was released to the Pacific ocean from Fukushima NPP as liquid effluent, making Fukushima accident one of most important sources of ^{137}Cs to the marine environment (Bailly du Bois et al., 2012).

Other than the aforementioned sources of ^{137}Cs in the environment include routine and accidental releases from nuclear materials production plants (Mayak, Krasnoyarsk, Oak Ridge, Windscale, ...), liquid effluents from spent fuel reprocessing plants (Sellafield, La Hague) and to a much lower extent from operating nuclear reactors.

^{137}Cs can be easily detected by gamma spectrometry using a predominant gamma line of its daughter nuclide, a metastable nuclear isomer of $^{137\mathrm{m}}$Ba with a half-life of 2.55 min.

The shorter lived caesium isotope ^{134}Cs with a half-life of 2.0652(4) yr (NNDC, 2011) can occasionally be detected in sediments following a fresh radionuclide release, like after the Chernobyl accident (Kempe & Nies, 1987; Rostan et al., 1997). It is mainly produced by neutron capture of stable ^{133}Cs, a fission product in a nuclear reactor and it is an indicator for fuel burn-up (Kirchner et al., 2012). It is not produced during nuclear explosions due to a lack of time available for the activation. The initial ratio of ^{134}Cs/^{137}Cs after the Chernobyl accident was reported to be close to 0.58 compared to close to 1 (Masson et al., 2011) or more precisely 0.874(17) (Kirchner et al., 2012) in fallout from the Fukushima Daiichi NPP accident. From

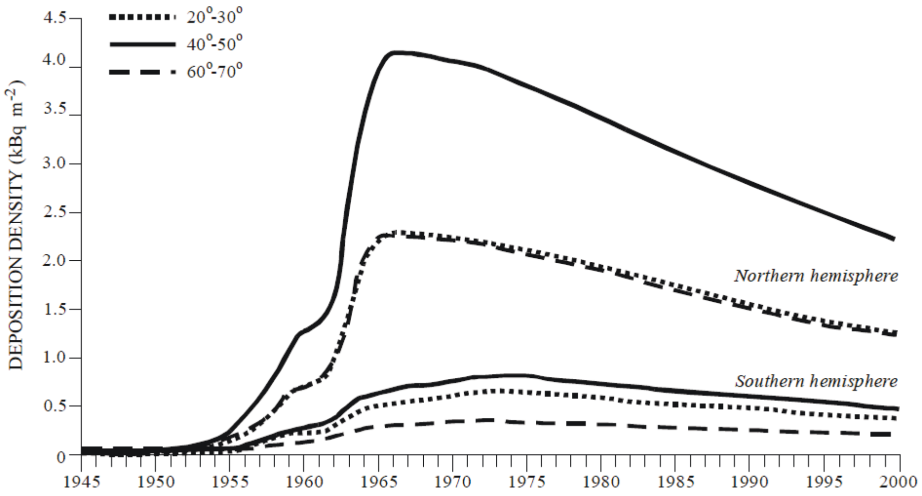

Figure 2.3: *^{137}Cs deposition density in the northern and southern hemispheres calculated from fission production amounts with the atmospheric model. This figure does not include contribution of the Chernobyl accident fallout, which can be relatively significant mainly in Europe. Source: UNSCEAR (2000).*

data published by MEXT (2013) on ocean sediment activity concentrations in the vicinity of the NPP it is clear that the accident is the main source of Cs in the area given the ^{134}Cs/^{137}Cs being close to 0.59, a value expected given by decay of ^{134}Cs from a ratio close to 1 after 19 months. In the near future part of the freshly deposited Cs settled in the sediment is expected to be remobilised to the water column (Laguionie et al., 2012).

Strontium-90

^{90}Sr is another abundant fission product with TFY of 5.8% (Lehto & Hou, 2010). It is a pure β^- emitter with a half-life of 28.90(3) years (NNDC, 2011). It can be determined by beta counting after chemical separation. Despite being relatively more difficult to detect compared to ^{137}Cs, ^{90}Sr is sometimes used as an independent chronometer in sediment dating, for example in Greifensee, Switzerland (Wan et al., 1987). According to UNSCEAR (2000), in nuclear bomb fallout it is usually present in a stable ^{137}Cs/^{90}Sr ratio of 1.5. This ratio does not reflect the TFY ratio of both isotopes, because in nuclear explosions both isotopes are produced often by fast fission of ^{239}Pu and other fissile isotopes, for which the yield of ^{137}Cs has higher values than ^{90}Sr.

Plutonium isotopes

The most widely studied Pu isotopes in the environment are listed in Tab. 2.1. They are mainly produced by neutron activation of uranium (and following beta decays) and the isotopic composition depends on duration of irradiation and neutron flux. The isotopic ratios of plutonium in the environment are therefore very characteristic for different sources, including most importantly atmospheric nuclear weapons fallout and discharges from reprocessing plants.

Other sources are releases connected to accidental events. In 1986 the Chernobyl reactor accident polluted large parts of Europe with radioactive fallout, including plutonium isotopes. In 1964 the U.S. navigation satellite SNAP-9A carrying a ^{238}Pu radioisotope thermoelectric

Table 2.1: *List of plutonium isotopes in sediments, their half-lives and decay modes (NNDC, 2011)*

Isotope	Half-life years	Decay mode	Energy (Intensity) keV (%)
^{238}Pu	87.7(1)	alpha	5499 (70.91), 5456 (28.98)
^{239}Pu	24110(30)	alpha	5157 (70.77), 5144 (17.11), 5106 (11.94)
^{240}Pu	6561(7)	alpha	5168 (72.80), 5124 (27.10)
^{241}Pu	14.290(6)	beta$^-$	5.23 (mean), 20.78 (max)

generator burnt up in the atmosphere over the Indian Ocean, an event influencing global Pu ratios. Two U.S. B-52 bombers crashes in Palomares, Spain, in 1966 and Thule, Greenland, in 1968 led to destruction of hydrogen weapons on board and dispersion of plutonium to the local environment.

^{238}Pu was deposited globally in much lower activities than ^{239,240}Pu. Although the total activity of fallout plutonium is 1–2 orders of magnitude lower than ^{137}Cs, its historical pattern is similar. Plutonium provides additional chronomarkers associated with changes in its isotopic composition of fallout during the 1950s and 1960s. Because plutonium from atmospheric weapons tests consists mainly of ^{239}Pu and ^{240}Pu with an activity ratio ^{238}Pu/^{239,240}Pu of 0.019(6) (Lindahl et al., 2010), the SNAP-9A accident was the main source of ^{238}Pu in the stratosphere. A sharp increase of the ^{238}Pu/^{239,240}Pu activity ratio associated to the SNAP-9A event, can be observed globally (Koide et al., 1979; Wan et al., 1987; Hancock et al., 2011). Also the Chernobyl accident increased the ^{238}Pu/^{239,240}Pu activity ratio on a local and regional scale with a value 0.42 being measured in hot particles from the Chernobyl exclusion zone (Warneke, 2002).

The ^{240}Pu/^{239}Pu atomic ratio provides additional information about the source of plutonium (Koide et al., 1985; Lindahl et al., 2010). The typical values are 0.178 ± 0.023 for plutonium originating from integrated global fallout, whereas thermonuclear tests at the Pacific Proving Grounds (PPG), namely Enewetak and Bikini Atolls, resulted in an isotopic signature of 0.34–0.36 (Lindahl et al., 2010). The weapon tests at Monte Bello Islands off Australia have yet another typical ^{240}Pu/^{239}Pu signature of 0.05 (Child & Hotchkis, 2013).

Ratios of ^{241}Pu to ^{239}Pu and ^{240}Pu serve as indicators of the reactor origin of plutonium and increase with the fuel burn-up time in the reactor. While Fukushima Daiichi NPP accident caused a massive release of radioactivity to the environment, the major radionuclides of concern were volatile iodine, caesium and tellurium isotopes. Greater release of actinides was not reported and the ^{239,240}Pu activity concentrations measured in soils in Fukushima Prefecture are in the range of global fallout values (Zheng et al., 2012b). However, increased ^{241}Pu/^{239,240}Pu isotope ratios in soils in the 30 km zone of the NPP indicate reactor origin. Plutonium release from Fukushima Daiichi NPP is likely to be associated with fuel fragments distributed by hydrogen explosions (Zheng et al., 2012b). In nearby ocean sediments from outside the 30 km zone from the NPP no isotopic signature was found for Fukushima related Pu based on ^{240}Pu/^{239}Pu or ^{241}Pu/^{239}Pu atomic ratios (Zheng et al., 2012a). The ratios and absolute values were in the range of those reported for the NW Pacific and its marginal seas and Japanese estuaries before the accident.

Several plutonium isotopes can be measured by alpha spectrometry. Alpha energies of ^{239}Pu and ^{240}Pu lie very close to each other (Tab. 2.1), therefore only ^{239,240}Pu combined activity can be determined, along with activity of ^{238}Pu. The ratios of ^{239}Pu and ^{240}Pu can be analyzed by mass spectrometry methods, which include inductively coupled plasma mass spectrometry (ICP-MS), accelerator mass spectrometry (AMS), thermal ionization mass spectrometry (TIMS) and resonance ionization mass spectrometry (RIMS). Additionally, the low energy beta emitter

^{241}Pu can be detected by LSC after chemical separation. Better detection limits can be achieved by alpha counting of the daughter nuclide ^{241}Am, but this requires long ingrowth times (Lehto & Hou, 2010). Another possibility is mass spectrometry.

Americium-241

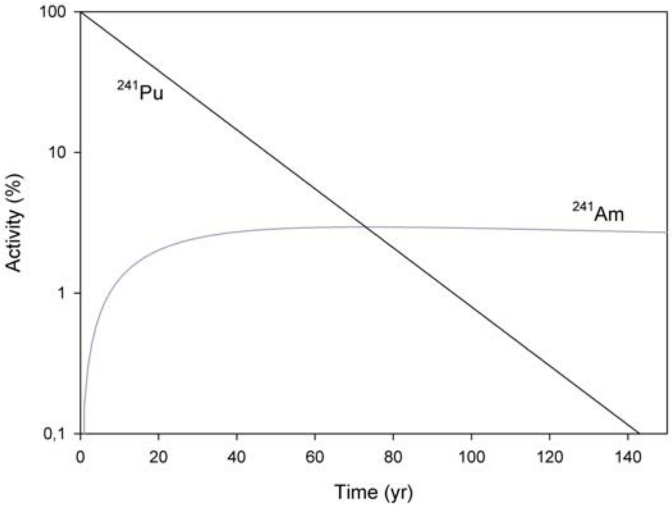

Figure 2.4: *Ingrowth of ^{241}Am from ^{241}Pu*

^{241}Am with a half-life of 432.6(6) years, is derived mostly from decay of the nuclear fallout isotope ^{241}Pu. In fresh nuclear fallout it is virtually absent, but ingrows from its parent isotope, as shown in the Fig. 2.4. Its activity in the environment is therefore increasing and will do so for several decades. An estimated activity of 142 PBq ^{241}Pu was released to the atmosphere by nuclear testing (UNSCEAR, 2000). Another great portion, about 22 PBq ^{241}Pu and additional 0.5 PBq ^{241}Am directly, originates from liquid discharges from the Sellafield reprocessing facility up to 1992 (Gray et al., 1995). For comparison, the Chernobyl accident release of ^{241}Pu is estimated to 6 PBq (NEA, 2002).

^{241}Am can be analyzed by either low level gamma or alpha spectrometry. In gamma spectrometry, self absorption effects of low level gamma energy must be carefully considered, similarly to ^{210}Pb. Appleby et al. (1991) suggest that ^{241}Am is considerably less mobile in lake sediments than ^{137}Cs and can provide a useful chronometer from the early 1960's in cases where the ^{137}Cs record has become degraded. According to Aston & Stanners (1981), americium is rapidly and effectively removed from sea water to sediments. It has successfully been used as complementary chronometer for validation of ^{210}Pb derived chronologies (Appleby et al., 1991; Appleby, 2008; O'Reilly et al., 2011).

2.2 Non-radionuclide dating methods

2.2.1 Radiation exposure methods

The emission of particles and radiation causes changes in structure of solid material. This enables the usage of a variety of methods for quantification of the age of minerals or archaeological artifacts.

Luminescence (LS) dating

Luminescence dating is based on the fact, that minerals being dated (usually quartz or feldspar, or ceramics in archeology) contain defects and impurities in their structure. These defects act as traps for free electrons, which are produced by excitation during decay of radioactive elements in the surrounding material or by cosmic radiation, and the traps are therefore gradually filled at a rate proportional to the radiation dose rate. The traps can be emptied by receiving enough heat or light energy after being exposed to high temperature (e.g. in case of volcanic minerals) or sunlight before being buried (in case of sedimentation). This is the event in history being dated, during which the traps are presumably emptied.

In the laboratory, the sample is subjected to heat in order to record light signal as a result to previously obtained dose (thermoluminescence, TL). The information is collected in the form of a "glow curve" of TL intensity versus stimulation temperature. Similarly after subjecting the sample to photons of a specific energy or energy range, photons are emitted as a result of previously trapped electrons (optically-stimulated luminescence, OSL, or photoluminescence) and a decay curve of OSL intensity versus stimulation time is recorded.

The natural signal is compared to one obtained after irradiation of the sample with a calibrated source. These examinations provide information about the total palaeodose a sample received since the "zeroing event" in the past. The natural dose rate can be estimated based on content of natural radionuclides in and around the sample including contributions of cosmic radiation or can be measured directly in situ using TL detectors buried at the sampling location for several months. Knowing the dose rate together with the palaeodose enables age estimation of the sample. Luminescence methods can be used for materials as young as a few years to an age of 10^6 years (Prescott & Robertson, 1997; Lian & Roberts, 2006; Pietsch, 2009).

Electron spin resonance (ESR) dating

ESR dating is based similarly as LS dating on presence of trapped excited electrons, which can be measured by ESR spectrometry. They detect absorption of microwave radiation by electrons after application of a strong magnetic field, which causes them to split depending on their magnetic moments relative to the applied magnetic field and makes them absorb microwave radiation in specific frequencies. The total dose is estimated by the addition method from a plot of ESR intensities after irradiation of the sample. Additionally, information about the radiation dose rate from the sample and its vicinity must be determined (Faure & Mensing, 2004) in order to calculate ages. The method is suitable for a relatively wide age range in the Quaternary period and most widely used for carbonates of terrestrial (speleotherms, travertines), marine (corals, mollusks, foraminifera) or fresh water (mollusks) origin, as well as bones and teeth. Samples from 200 years to about $2 \cdot 10^6$ years can be dated (Hennig & Grün, 1983; Rink, 1997).

Fission tracks and alpha decay tracks

Dating using fission tracks method relies on spontaneous fission of ^{238}U contained within the mineral or glass dated. The fission fragments cause structural damage in the form of tracks along their trajectories in the dated material. The tracks can be etched to be visible in an optical microscope and counted. In principle, age is proportional to the density of the tracks and ^{238}U concentration (Enkelmann et al., 2005). The method is suitable for age determination of formation or secondary heating events of the uranium rich minerals titanite, zircon or apatite contained in basalts, tuffs, tephra and volcanites. Another suitable material is glass, including volcanic glasses, impact glasses, archaeological artifacts, as well as recent glasses, mainly those coloured by uranium. The method finds application for a very wide range of ages, but for younger dated materials (100 years and younger) high content of uranium is a prerequisite for a successful chronology (Wagner, 1998).

Alpha decay tracks are material damage in minerals, including pleochroic halos and alpha recoil tracks. Pleochroic halos are spheroidal zones of discoloration around miniature U or Th rich inclusions in minerals, usually micas. Their diameter is a function of alpha particles' energy, the biggest being assigned to ^{212}Po decay. Due to high uncertainties connected to a non-linear relationship of the degree of discoloration and alpha dose, this method is nowadays rarely used (Faure & Mensing, 2004). Similarly, the method of alpha recoil tracks is based on emissions of alpha particles from U and Th (and the daughter nuclides), which cause structural damage in silicate material. The density of the tracks, which can be etched by acids and counted using a phase-contrast microscope is proportional to age and radionuclide concentration (Faure & Mensing, 2004). Gögen & Wagner (2000) showed, that the method can be used for dating micas (for example in tephra) in the age range 10^2 to 10^6 years.

2.2.2 Incremental dating techniques

Incremental dating techniques are characteristic for year-by-year annual chronologies, which can be either fixed to a certain date or floating.

Dendrochronology

Tree-ring dating, dendrochronology, uses seasonal changes in mechanical properties of the tissue growing on the outer perimeter of tree trunks, forming yearly rings which can be counted at the trunk cross sections. Usual species employed in dendrochronology include oak, pine, sequoia or Douglas fir (Walker, 2005). Continuous chronologies for different species and regions can be constructed using distinctive rings or groups of rings (signatures), corresponding to exceptionally good or bad growth years, and crossdating sections of overlapping ages from present back to the past. Such a scale is then called a master chronology. It can be used for precise dating of individual samples. Additionally, dendrochronological records serve as an archive of past temperature or precipitation and can be used for dating volcanic events. Dendrochronology together with varve chronology and U-series chronology of corals or speleotherms are important methods to verify radiocarbon calibration (Wagner, 1998; Walker, 2005; Broecker, 2011).

Varve chronology

This method based on sediment annual layers counting is very important in studies of high-resolution sediment records mainly in lacustrine (Lamoureux, 2002), but also marine environments (Thunell et al., 1995). Formation of laminae is connected to seasonal variation of biological and sedimentation processes. These are usually very prominent in glacial lakes with winter ice cover, where coarse spring-to-autumn layers alternate with fine winter clay layers (Walker, 2005). In another example from marine environments, Thunell et al. (1995) showed that the varves in sediments of the Santa Barbara Basin, offshore California, are composed of diatom opal rich light laminae formed during highly productive spring-summer periods and dark laminae rich in lithogenic fractions being deposited in the autumn-winter period. Individual varves are usually counted and the thicknesses measured using image analysis techniques (Saarinen & Petterson, 2002).

Varve counting is often used as a complementary technique together with ^{137}Cs and ^{210}Pb chronology (e.g., Enters et al., 2006) or radiocarbon dating. For example, laminated sediments of the Cariaco basin (Hughen et al., 1998) were used to calibrate radiocarbon calendar ages (Stuiver et al., 1998).

Ice-core chronology

Ice-core chronology relies on counting annual layers in glacial ice based on visible stratigraphy (Walker, 2005) and other parameters varying annually, including chemical and isotopic changes, acidity or dust content (Wagner, 1998) in a similar way like dendrochronology or varve chronology.

Other incremental dating methods

These include counting annual layers of speleotherms, corals or mollusks or gradual growth of lichens.

2.2.3 Other chronological methods

A number of other techniques can be helpful for relative dating, often in combination or for supporting other aforementioned dating methods.

Event chronology is a wide field using markers of events in dated sediment sequences. These might include for example tephra layers, lavas, charcoal, impact deposits, tectonostratigraphic markers, tsunamiites, tempestites, debrites, palaeomagnetic markers, weathering/pedogenic horizons, markers of short-term environmental changes, extinction events or appearance of new taxa. Besides natural markers, in young sediments markers caused by human activities can be distinguished and are widely used: datable artifacts, charcoal or pollution events (Gale, 2009). Biostratigraphic markers (pollen, diatoms, foraminifera, . . .) are sometimes helpful.

An example of natural events is studying tephra - ash and other pyroclastic material - originating from volcanic eruptions. In areas close to the volcanic eruption, tephra layers can be optically visible in the sediment sequence. Also a sharp increase of magnetic susceptibility can be used as an indicator for tephra presence, along with chemical composition, grain size, glass shards or mineralogy (Lowe, 2011). Boer et al. (2006), for example, used the 1883 Krakatau event tephra layer as an independent time-marker in order to check the validity of some common ^{210}Pb chronology models.

Chapter 3

Chronology using excess Pb-210

Sediment chronology using ^{210}Pb was pioneered in the 1960-70's (e.g., Goldberg, 1963; Krishnaswamy et al., 1971; Koide et al., 1972). The early works were reviewed by Robbins (1978) and the basic conceptual models were introduced (Robbins, 1978; Appleby & Oldfield, 1978), which are valid and widely used until nowadays. Robbins (1978) expressed three basic requirements which are important for a successful chronology:

1. The accumulation of sediment must be ordered in time, although not necessarily constant.
2. The time marker must be incorporated into the sediment so that it is preserved in time, ideally it should be completely immobilized.
3. The rate of supply of the time marker must be known in time, preferably constant.

These criteria are assumed to be fulfilled in the applications of the dating models in later chapters.

3.1 Principle

^{210}Pb is one of the natural lead isotopes, a member of the ^{238}U decay series, with a half-life of 22.23(12) years. ^{210}Pb is the first longer living member of the chain following ^{226}Ra with a half-life of 1600(7) years, however there is the only gaseous member ^{222}Rn separating ^{226}Ra and ^{210}Pb, which, having substantially different physical and chemical properties from its parent Ra, causes important radioactive equilibrium changes within the chain members contained in the environmental media.

Comprehensive overviews of the ^{210}Pb cycle in the environment can be found in works of Robbins (1978) and El-Daoushy (1988).

3.1.1 Lead-210 in the atmosphere

The source of ^{210}Pb in the atmosphere is ^{222}Rn, a radioactive noble gas with half-life of 3.8232(8) days, which emanates from soil due to the presence of its parent radionuclide ^{226}Ra as shown schematically in Fig. 3.1. The residence time of ^{222}Rn in the atmosphere, up to several weeks, is given by its physical half-life.

For a dataset from Great Britain and Central Europe Appleby (2001) showed that ^{210}Pb fallout is correlated with mean annual rainfall on a regional scale. There was, however, a difference between the British Islands and continental Europe in absolute flux values. They were about 50% higher in continental Europe that in Great Britain at sites with comparable rainfall

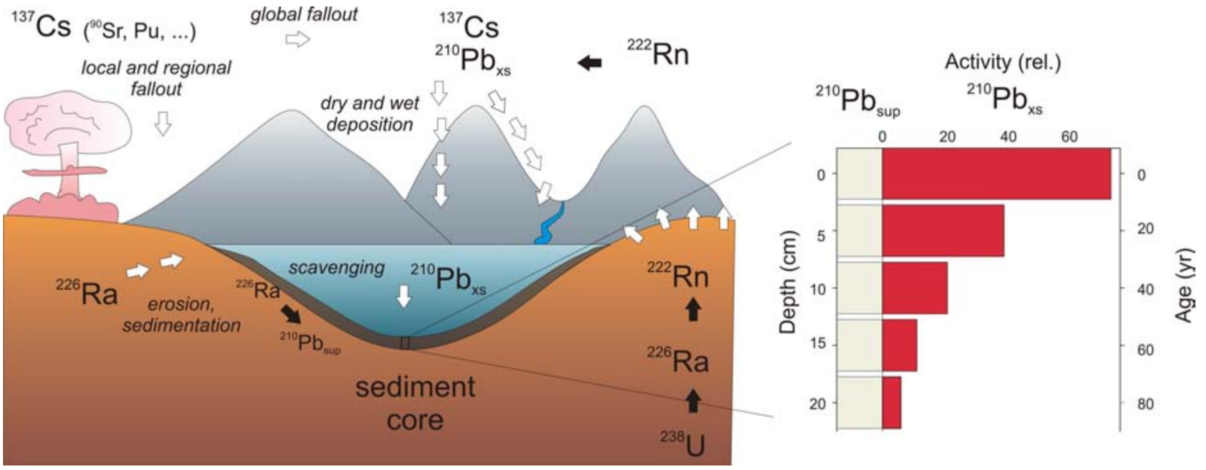

Figure 3.1: *Sources of ^{210}Pb in sediments. (As supporting tracers in sediments artificial isotopes (^{137}Cs, ^{90}Sr, Pu isotopes) are often used. One of their main sources globally is fallout from nuclear bomb testing.)*

presumably due to the fact that in continental Europe a higher portion of air masses is carried over the land and allows to build up higher Rn concentrations. This feature was modelled and compared to empirical data on ^{210}Pb global distribution at northern hemisphere mid-latitudes (Appleby, 1998; Piliposian & Appleby, 2003; Appleby, 2008) showing that ^{210}Pb concentrations gradually rise from west shores to east shores of American and Eurasian continents and fall over the oceans. This demonstrates the long-range transport importance.

^{210}Pb concentration also varies with latitude, as Paatero et al. (2009) showed on a dataset of ^{210}Pb air activity from ocean and continental measurements (Fig. 3.2). Included were data from transatlantic polar expeditions (Akademik Fedorov and Swedarp-88), Arctic expeditions (Arctic-91 and ASCOS) and land stations (Ny-Ålesund, Spitzbergen; Marambio and Aboa, Antarctica; Sodankylä and Nurmijärvi, Finland and Sofia, Bulgaria). Measured activities reflect the amount of land in different latitudinal bands. This finding agrees well with a compilation of the data from an international database provided by Preiss et al. (1996). The authors summarize data of ^{210}Pb deposition flux in different geographical areas. Baskaran (2011) reviews the existing global atmospheric inventory data of ^{210}Pb and a distribution of the depositional fluxes of ^{210}Pb.

3.1.2 Lead-210 in aquatic environment

The principal sources of ^{210}Pb in the water column are direct deposition from the atmosphere, input from tributaries (and the catchment area) and direct production from decay of ^{222}Rn in the water column. The riverine input portion is important for lakes with a relatively large catchment area and majority of ^{210}Pb is associated with particulate phase (Stiller & Imboden, 1986). ^{222}Rn responsible for the in-situ portion of ^{210}Pb is either in equilibrium with dissolved ^{226}Ra in the water column, or it can be in excess due to ^{222}Rn input through rivers and escape from the bottom sediments. Therefore the portions of the ^{210}Pb sources vary for different environments (Stiller & Imboden, 1986).

The average removal residence times in water columns of lakes are most often between 1–2 months (e.g., Stiller & Imboden, 1986; Wieland et al., 1991; Chai & Urban, 2004, and citations therein). In the estuarine environment the residence times are similarly short, less than 2 months in Tampa Bay, Florida (Baskaran & Swarzenski, 2007). The residence times at continental shelf (East China and Yellow Seas) are about 2 months, as opposed to 7 months in deeper parts below the shelf edge (Nozaki et al., 1991). The residence times were found to be well correlated to

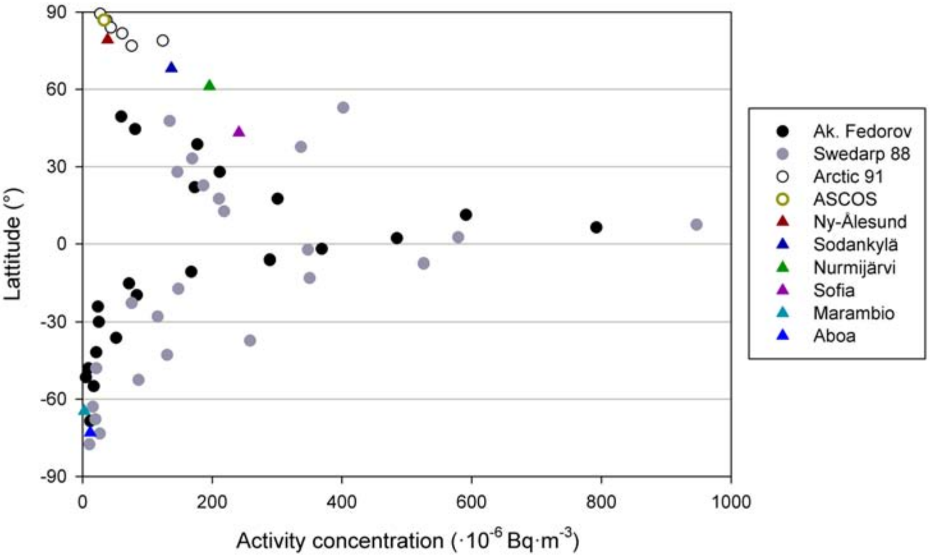

Figure 3.2: *Latitudal distribution of ^{210}Pb in the air (Source: Paatero et al., 2009). Data obtained from transatlantic polar and Arctic expeditions are marked with circles, triangles stand for data from land stations.*

water depth in continental shelf and slope regions of the Gulf of Mexico (Baskaran & Santschi, 2002) showing faster scavenging in shallow waters. The absolute values ranged from 0.1 years in the depth of 40 m to 4 years in 1500 m water depth.

3.1.3 Lead-210 in sediments

^{210}Pb in sediments consists of two components (Fig. 3.1): supported ^{210}Pb (^{210}Pb$_{\text{sup}}$), which is present due to autigenic material of the sediment and unsupported (or excess) ^{210}Pb (^{210}Pb$_{\text{xs}}$), which originates from atmospheric deposition. Excess ^{210}Pb is then determined by subtracting supported activity from the total activity and used for estimation of accumulation rates and age models.

Supported lead is assumed to be in equilibrium with ^{226}Ra, although there were some cases of disequilibrium documented (e.g., Brenner et al., 2004), where ^{226}Ra activity exceeded total ^{210}Pb activity for example due to seepage of ^{226}Ra-rich groundwater to lakes.

3.2 Radionuclide profiles modelling

The variation of the excess lead activity concentration with depth can be used for quantification of processes in sediment (accumulation rates, mixing). In an ideal case (Fig. 3.1) if the sedimentation rate and flux of excess lead are both constant and no mixing is present, the activity decreases exponentially with increasing depth due to radioactive decay of ^{210}Pb.

The leading processes affecting activity concentration C of ^{210}Pb, as well as other short lived radionuclides, in sediment profiles are sediment accumulation, radioactive decay of unsupported activity and mixing. Mixing is often caused by biological activities (bioturbation) and is frequently approximated as a diffusive process. Radionuclide transport in sediments can be described by the advection-diffusion equation, treating bioturbation as diffusive and sedimentation as advective process:

$$\frac{\mathrm{d}C}{\mathrm{d}t} = D\frac{\mathrm{d}^2C}{\mathrm{d}z^2} - S\frac{\mathrm{d}C}{\mathrm{d}z} - \lambda C, \tag{3.1}$$

where S is the sedimentation rate ($cm \cdot yr^{-1}$), λ the decay constant (yr^{-1}), t stands for time (yr), z for depth (cm). D is the diffusive mixing coefficient (cm^2yr^{-1}).

Unlike radiocarbon dating which can provide an absolute age of an individual sample, ^{210}Pb based methods can not assign a unique age to a single sediment sample. In case of ^{210}Pb the information on age and sedimentation rate is derived from activity profiles, where usually between 10 and 50 individual samples are analyzed.

Quantitative process models are based on extensive supporting data as well as long observation and description of local systems, therefore are rarely used. Instead, some simplified approaches were developed including fitting (CF-CS) and mapping algorithms (CRS, CIC), which are widely used for interpreting ^{210}Pb profiles (Hancock et al., 2002). Sometimes these are called conceptual models. They are described in the following section. The recent publication of Sanchez-Cabeza & Ruiz-Fernández (2012) provides an overview of the most frequently used models and their use. The book by Carroll & Lerche (2003) goes beyond the conceptual models and deals with inductive modeling approaches (SIT method) and effects of mixing in sediment profiles.

3.2.1 CF-CS

The simple Constant Flux - Constant Sedimentation (CF-CS) model (Robbins et al., 1978; Appleby & Oldfield, 1992) assumes constant atmospheric deposition of $^{210}\mathrm{Pb}_{\mathrm{xs}}$ and constant accumulation rates, therefore it is suitable for sites, where the environmental factors are stable enough to allow constant mass flux. Each newly deposited layer is assumed to have the same initial activity concentration of unsupported ^{210}Pb:

$$C_0 = C(0), \tag{3.2}$$

where $C(0)$ is the activity of the current surface layer. The activity of layer of age t is then:

$$C_i = C(0) \cdot e^{-\lambda m_i/r}, \tag{3.3}$$

where λ is ^{210}Pb decay constant (0.03122 ± 0.00028 yr^{-1}) and m the cumulative dry mass accumulated per unit area above the layer and r is the mass accumulation rate ($g \cdot cm^{-2}yr^{-1}$).

The model is often applied for $^{210}\mathrm{Pb}_{\mathrm{xs}}$ profiles, in which concentrations plotted against cumulative dry mass decrease exponentially. Applying least square fit through the data (Fig. 3.3), the mass accumulation rate can be determined[1]. The age of i^{th} layer can be determined as

$$t_i = \frac{m_i}{r}. \tag{3.4}$$

Even though mass accumulation rate r is constant, sedimentation rate S ($cm \cdot yr^{-1}$) can vary due to compaction. The relationship between the mass accumulation rate r and sedimentation rate S is related to cumulative dry mas m (Robbins, 1978):

$$r = \frac{\mathrm{d}m}{\mathrm{d}t} = \frac{\mathrm{d}m}{\mathrm{d}z} \cdot \frac{\mathrm{d}z}{\mathrm{d}t} = \frac{\mathrm{d}m}{\mathrm{d}z} \cdot S. \tag{3.5}$$

---

[1] Within this thesis the exponential model was fitted using SigmaPlot (Systat Software).

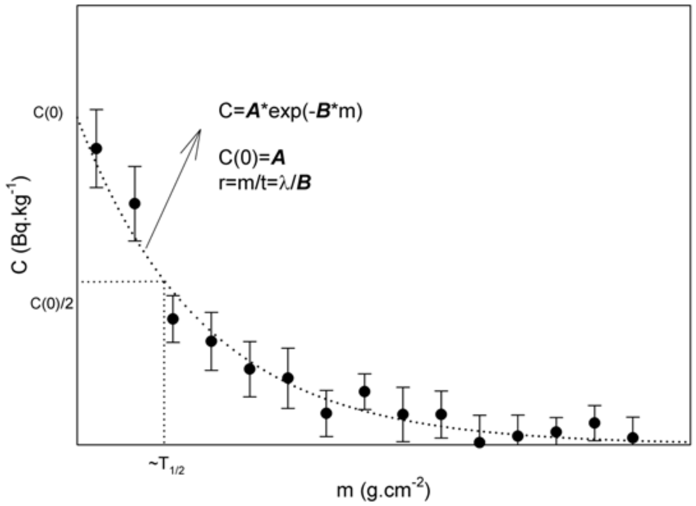

Figure 3.3: *Example of an application of the CF-CS model. Accumulation rate r can be calculated directly from the exponential parameter of the fitted function.*

In case exact values of cumulative mass are not known or uncertain, the $\frac{\mathrm{d}m}{\mathrm{d}z}$ term can be substituted by the porosity term, as

$$\frac{\mathrm{d}m}{\mathrm{d}z} = \rho_s(z)\left[1 - \phi(z)\right] \approx \bar{\rho_s}\left[1 - \phi(z)\right], \tag{3.6}$$

where ρ_s is density of solids in the sediment and ϕ porosity. ρ_s can be approximated by a mean density $\bar{\rho_s}$, because its variation is often lower than variation in porosity. For $r = const.$, the relation between sedimentation rate $S(0)$ at the sediment surface and at any depth is:

$$S(z) = S(0) \cdot \frac{1 - \phi(0)}{1 - \phi(z)}. \tag{3.7}$$

3.2.2 CRS

The constant rate of supply (CRS) model (Appleby & Oldfield, 1978), sometimes called constant flux (CF) model (Robbins, 1978), is applicable when the flux of ^{210}Pb to the sediment remains constant, while sedimentation rate can vary. The $^{210}\mathrm{Pb}_{\mathrm{xs}}$ vertically integrated to the mass depth m equals the constant flux integrated over the corresponding time t. The cumulative residual $^{210}\mathrm{Pb}_{\mathrm{xs}}$ activity for layer i beneath the mass depth m_i calculated as

$$A(i) = \int_{m_i}^{\infty} C \,\mathrm{d}m \tag{3.8}$$

is then

$$A(i) = A(0) \cdot e^{-\lambda t}, \tag{3.9}$$

where $A(0)$ is total $^{210}\mathrm{Pb}_{\mathrm{xs}}$ inventory (Fig. 3.4) in the sediment profile

$$A(0) = \int_{0}^{\infty} C \,\mathrm{d}m. \tag{3.10}$$

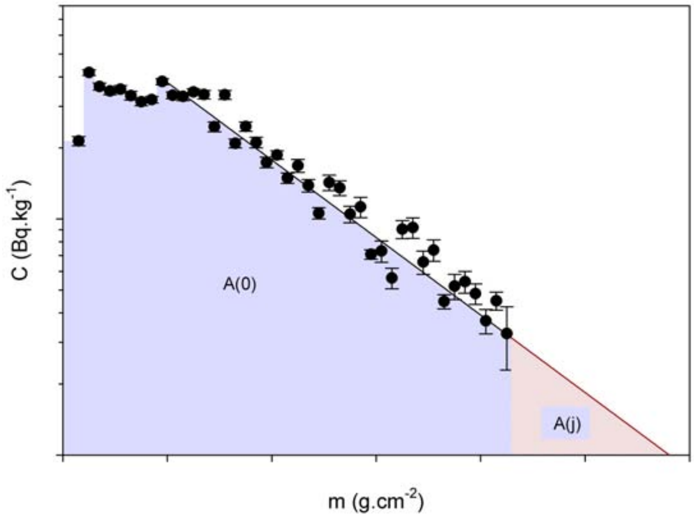

Figure 3.4: *Example of an application of the CRS model (semi-log scale). The total* $^{210}Pb_{xs}$ *inventory is marked as* $A(0)$*. In some cases, when the dating horizon is not reached, it can also include the "residual" inventory* $A(j)$ *below the lowest layer* j *(see text).*

The age of the sediment in depth m can be expressed as

$$t = \frac{1}{\lambda} \cdot ln\left(\frac{A(0)}{A(i)}\right). \tag{3.11}$$

The mass accumulation rate of the layer is calculated as (Appleby & Oldfield, 1978)

$$r(i) = \lambda \cdot \frac{A(i)}{C(i)}, \tag{3.12}$$

where $C(i)$ is $^{210}\mathrm{Pb}_{\mathrm{xs}}$ activity concentration of the layer and the sedimentation rate is

$$S(i) = \frac{r(i)}{\rho}. \tag{3.13}$$

The CRS model relies on the correct estimates of the $^{210}\mathrm{Pb}_{\mathrm{xs}}$ inventory. A frequent case in $^{210}\mathrm{Pb}$ chronologies is that the dating horizon has not been reached, that means $^{210}\mathrm{Pb}_{\mathrm{xs}}$ activities in the profiles do not reach zero values at the bottom of the sediment core. Underestimation of inventories can lead to calculated ages to be too old (Appleby, 1998; MacKenzie et al., 2011). Appleby (1998) offers two strategies to deal with this situation. If the $^{210}\mathrm{Pb}_{\mathrm{xs}}$ in older sequences decrease more or less exponentially with the depth and a constant accumulation rate can be expected, reference accumulation rates may be derived at a part of the profile near the base of a core by using CF-CS model. The residual inventory $A(j)$ below the lowest layer j can then be calculated as

$$A(j) = \frac{r \cdot C(j)}{\lambda}. \tag{3.14}$$

Value of $A(j)$ is then added to the inventory above the layer j in order to make the inventory complete.

In case of variable accumulation in lower parts using independently dated reference level at or above the ^{210}Pb dating horizon is recommended (Appleby, 1998).

The age uncertainty can be calculated using a first-order-analysis method described in Binford (1990).

3.2.3 CIC

Constant initial concentration (CIC) (Appleby & Oldfield, 1978, 1992), also named constant specific activity (CSA) (Robbins, 1978) or constant specific activity - variable sedimentation rate (CAVS) model (Chanton et al., 1983), assumes constant initial activity of $^{210}\mathrm{Pb}_{\mathrm{xs}}$ regardless of changes in mass accumulation rates. The activity of layer of mass depth m is:

$$C(m) = C(0) \cdot e^{-\lambda t}, \tag{3.15}$$

and age of the layer:

$$t = \frac{1}{\lambda} \cdot ln \frac{C(0)}{C(m)}. \tag{3.16}$$

3.2.4 Variations on conceptual models

There are numerous variations on the listed models developed in order to suit local conditions of each individual site. A correction for grain size in environments with rapidly changing sedimentological conditions in a coastal basin (Chanton et al., 1983) made it possible to construct a chronology consistent with changes in basin morphology and major storm events. Corrections for variations in the grain size can also be performed using the Al content, fine fractions (<63 μm and <32 μm) and clay (<2 μm) (Álvarez-Iglesias et al., 2007; Kirchner & Ehlers, 1998). When sediment profiles reveal several independent periods of deposition, it is possible to apply the models in a piecewise way to different sections of the core (e.g., Gale et al., 1995; Appleby, 2001).

3.2.5 SIT

For interpretation of complex depth profiles, a model allowing the interpretation of ^{210}Pb profiles when both sediment accumulation rates and ^{210}Pb fluxes vary with time, the Sediment Isotope Tomography (SIT) method was developed (Carroll et al., 1995). Here inverse numerical techniques were combined with predictive models to simulate sedimentation. Non-exponential changes in ^{210}Pb activity caused by sedimentation are modeled by a Fourier sine series; changes caused by other processes are modeled by a Fourier cosine series. The values of the Fourier coefficients are determined for the measured data by inverse numerical analysis, yielding a mathematical expression describing changes in ^{210}Pb activity with sediment depth (Carroll et al., 1999).

The advantage of the inverse modelling is that for interpreting the ^{210}Pb profile no prior information on the system is needed; it is extracted entirely from the response function. But similarly to other models, the results must be verified with other independent time markers, since results of the numerical algorithms used do not necessarily represent physical reality (Kirchner, 2011). The SIT model, like all other aforementioned models, does not take into account sediment mixing.

3.2.6 Validation of Pb-210 chronologies

No matter which model is applied for interpretation of ^{210}Pb profiles, an independent tracer must validate the correctness of the chronology, as ^{210}Pb ages can only provide relative ages. This has been stressed for example by Smith (2001) in his paper "*Why should we believe ^{210}Pb sediment geochronologies?*". Most often positions of the ^{137}Cs global nuclear test fallout maximum in 1963 is used. In areas affected by Chernobyl regional fallout the 1986 maximum is frequently observed.

The age of the ^{137}Cs peak alone can falsely agree with ^{210}Pb dates in case that near surface steady state mixing is present, because ^{137}Cs would be displaced by mixing as well as ^{210}Pb. While wrong interpretation of a ^{210}Pb profile affected by mixing would lead to higher accumulation rates, the peak location would also be shifted downward by mixing. J.A. Robbins recommends in Hancock et al. (2002) to additionally compare the ^{137}Cs horizon (the deepest level where activity can be detected) against a 1952 date of atmospheric nuclear testing onset. While agreement with the ^{210}Pb age model can contribute to its validation, disagreement can initiate discussion and call for considering the reasons.

In some cases, however, the location of the ^{137}Cs peak does not provide a definitive support for ^{210}Pb chronologies and the study of the whole ^{137}Cs activity profile using more sophisticated models is recommended (Abril, 2004).

Besides ^{137}Cs other radionuclide and non-radionuclide supporting methods can be used, as described in Chapter 2. Examples are dated tephra layers (Boer et al., 2006), pollen records (Robbins et al., 1978), and others.

3.2.7 Mixing

Describing mixing as a diffusive process according to Fick's law as random displacements of sediment particles due to faunal activity has been used in sediment radionuclide studies (e.g., Goldberg & Koide, 1962; Cochran, 1985; DeMaster & Cochran, 1982). The concept of sediment mixing described by the diffusive term of Eq. 3.1 is based on several assumptions: mixing intensity is considered constant over the entire mixed layer with time invariant and radionuclide is adsorbed on solid particles.

Mixing, no sedimentation

Under certain conditions, specially when sedimentation rates are low and biological activity in the surface sediment layer relatively high, bioturbation can be the leading process controlling the short lived radionuclides' depth distributions, as opposed to sedimentation. This is often the case for deep sea sediments with very low sediment accumulation.

When mixing is the leading process and accumulation is close to zero within the tracer's time scale, the advective term from Eq. 3.1 can be omitted. The general solution for continuous flux of tracer (in sediments usually applicable for $^{210}\mathrm{Pb}_{\mathrm{xs}}$ or $^{228}\mathrm{Th}_{\mathrm{xs}}$) is (Jha, 2012):

$$C(z,t) = \frac{\mathcal{F}}{2\sqrt{\lambda D}}\left[e^{-z\sqrt{\frac{\lambda}{D}}}erfc\left(\frac{z}{2\sqrt{D\cdot t}} - \sqrt{\lambda t}\right) - e^{z\sqrt{\frac{\lambda}{D}}}erfc\left(\frac{z}{2\sqrt{D\cdot t}} + \sqrt{\lambda t}\right)\right], \quad (3.17)$$

where $\mathcal{F}$ is flux of the tracer to the sediment ($Bq\cdot cm^{-2}y^{-1}$), D is diffusive mixing coefficient (cm^2yr^{-1}) and t (yr) the time since the beginning of the tracer influx.

For the steady state conditions ($t \to \infty$) Eq. 3.17 reduces to:

$$C(z) = \frac{\mathcal{F}}{\sqrt{\lambda D}} e^{-z\sqrt{\frac{\lambda}{D}}}. \tag{3.18}$$

For ^{137}Cs a pulse-like input can be considered. Such pulse would represent for example 1963 atmospheric fallout maximum or the Chernobyl fallout. The analytical solution of Eq. 3.1 can be found (Jha, 2012):

$$C(z,t) = \frac{\mathcal{J}_0}{\sqrt{\pi D t}} e^{-z^2/(4Dt)} e^{-\lambda t}, \tag{3.19}$$

where $\mathcal{J}_0$ is total activity deposited during the pulse and t (yr) the time between the pulse input and the reference date (usually date of sampling).

Mixing and sedimentation

A more general solution of Eq. 3.1 can be applied for cases when both mixing and sedimentation are present and contribute significantly to radionuclides' depth distributions. For a pulse-like input analytical solution is available (Bossew & Kirchner, 2004):

$$C(z) = \mathcal{J}_0 \cdot e^{-\lambda t} \left[\frac{1}{\sqrt{\pi D t}} e^{-(z-St)^2/(4Dt)} - \frac{S}{2D} e^{Sz/D} erfc\left(\frac{S}{2}\sqrt{\frac{t}{D}} + \frac{z}{2\sqrt{Dt}} \right) \right]. \tag{3.20}$$

The upper listed solutions can be applied in an inverse manner to estimate the values of the mixing coefficient and flux or deposited activity, respectively, by fitting the functions to radionuclide depth profiles[2].

F-test

When comparing results from two models that are nested, that means that model 2 is an extension of model 1 with an additional free parameter (or more parameters), the F-test can be applied to decide if the improvement in the fit result was statistically significant or merely result of adding additional free parameters.

The F value is calculated as

$$F = \frac{(RSS_1 - RSS_2)/(DoF_1 - DoF_2)}{RSS_2/DoF_2}, \tag{3.21}$$

where RSS is residual sum of squares and DoF degrees of freedom expressed as number of data points lowered by number of free model parameters. The F value calculated from Eq. 3.21 is then compared to a critical value or F-distribution $F_{crit}(DoF_1 - DoF_2; DoF_2)$. If $F > F_{crit}$, the null hypothesis (*model 2 is not a significant improvement to model 1*) can be rejected under a defined probability of false rejection (here 0.05).

3.3 Radionuclide inventories and fluxes

Total inventories in sediment profiles are important parameters for evaluating the accumulation of natural and anthropogenic radionuclides in the marine environment, mainly erosion input from terrestrial sources or sediment focusing. For an individual radionuclide (e.g., $^{210}\mathrm{Pb}_{\mathrm{xs}}$,

---

[2] Within this thesis the parameters of mixing functions were determined using OriginPro (OriginLab).

^{137}Cs, ^{228}Th$_{\mathrm{xs}}$ or ^{241}Am) inventory ($Bq \cdot m^{-2}$) can be estimated as a sum of all respective values in the sediment core:

$$\mathcal{I} = \sum C_i \cdot \Delta z_i \cdot \rho_i, \tag{3.22}$$

where C_i is activity concentration, Δz_i thickness and ρ_i the dry bulk density of the i$^{\mathrm{th}}$ slice.

For radionuclides with a continuous influx to the sediment (^{210}Pb$_{\mathrm{xs}}$), assuming time invariant nuclide deposition rates, the mean yearly flux can be calculated as

$$\mathcal{F} = I \cdot \lambda, \tag{3.23}$$

with λ being radionuclide's decay constant.

Chapter 4

Gamma spectrometry

4.1 Radioactivity

4.1.1 Radioactive decay

Atomic nuclei consist of two kinds of particles: positively charged protons (atomic number Z = number of protons) and non-charged neutrons. These both together are called nucleons. A nuclide is characterized by the atomic number Z, which is characteristic for each element, and a mass number A (A = Z + number of neutrons). A nuclide consisting of Z protons and N neutrons is thus denoted as ${}^{A}_{Z}X$, where X is a chemical symbol of the element (for example ${}^{137}_{52}Cs$) or most often simply ${}^{A}X$ (for example ${}^{137}Cs$). Nuclides of the same chemical element with a different number of neutrons are referred to as isotopes. All chemical elements have radioactive isotopes and most of them have one or several stable isotopes. Radioactive isotopes (also called radionuclides) undergo a process called radioactive decay, a spontaneous transformation of an unstable atomic nucleus (of a parent radionuclide) into another nucleus (daughter nuclide), accompanied by loss of energy and emission of one or more particles.

Given a sample of a particular radioisotope, the number of decay events $\mathrm{d}N$ expected to occur in an infinitely small interval of time $\mathrm{d}t$ is proportional to the number of atoms present. If N is the number of atoms, then the probability of decay $(-\mathrm{d}N/N)$ is proportional to $\mathrm{d}t$:

$$\left(-\frac{\mathrm{d}N}{N}\right) = \lambda \cdot \mathrm{d}t. \tag{4.1}$$

Particular radionuclides decay at different rates, each characterized by its own decay constant λ (s^{-1}). The solution to the differential equation 4.1 is:

$$N(t) = N_0 e^{-\lambda t}, \tag{4.2}$$

where N(t) is the quantity at time t, and $N_0 = N(0)$ is the initial quantity at time $t = 0$. Decay constant λ is inversely proportional to the half-life $T_{1/2}$:

$$T_{1/2} = \frac{\ln(2)}{\lambda}. \tag{4.3}$$

Activity (A) is the number of disintegrations per unit time

$$A = \lambda N, \tag{4.4}$$

measured in Bq (Becquerel) $= s^{-1}$. Other (non-SI) units are Ci (Curie), 1 $Ci = 3.7 \cdot 10^{10} Bq$ (defined historically as activity of 1 g of ^{226}Ra) or dpm (disintegrations per minute, 1 $dpm = 1/60\ Bq$). For practical reasons, activity of a unit mass (or volume) is often expressed as activity concentration C (C_m, C_V) in units $Bq \cdot kg^{-1}$ and $Bq \cdot cm^{-3}$, respectively.

Analogue to Eq. 4.2, activity reduction in time follows exponential decay:

$$A(t) = A_0 e^{-\lambda t}, \tag{4.5}$$

sometimes also expressed as

$$A(t) = A_0 \cdot 2^{-\frac{t}{T_{1/2}}}, \tag{4.6}$$

where A_0 is initial activity and $A(t)$ is activity at time t.

Radioactive decay is the process that enables radionuclide dating methods. By determining the decrease of the initial activity, the time elapsed from the radionuclide entering the dated system can be derived (Fig. 4.1). The portion of the activity left after n half-lives can be expressed as:

$$A(n \cdot T_{1/2}) = A_0 \cdot 2^{-n} \tag{4.7}$$

and the numerical values are given in the Tab. 4.1.

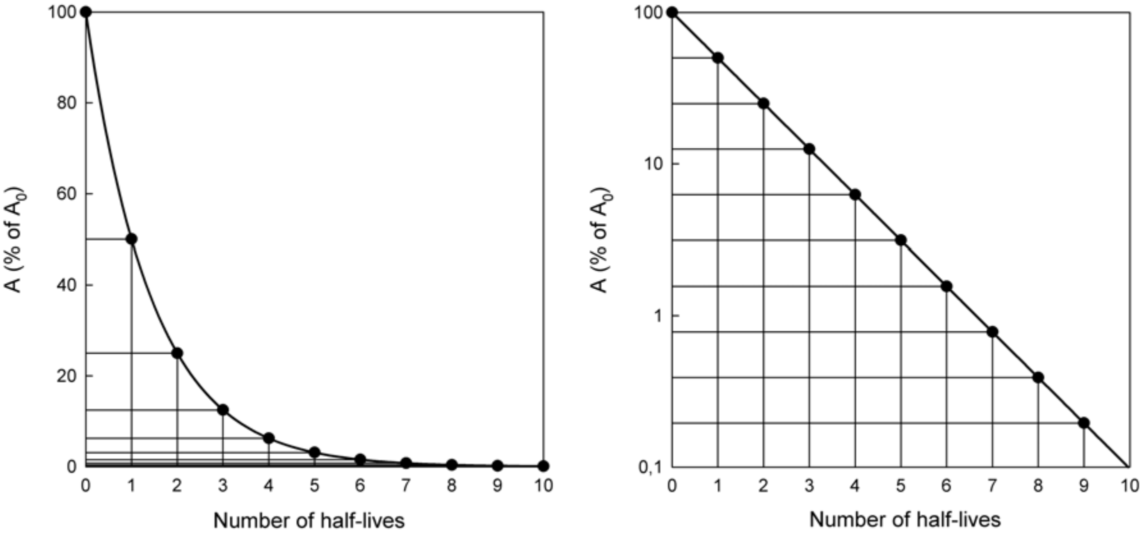

Figure 4.1: *Radioactive decay plotted in linear (left) and logarithmic (right) scale as a function of number of half-lives and fraction of initial activity.*

4.1.2 Decay chains

Many radionuclides do not decay directly to a stable state, but rather undergo a sequence of several decays until a stable isotope is reached. They form radioactive chains (also called radioactive series). Although number of chains is formed by artificial radionuclides, for this thesis those natural ones are important. In Nature three decay chains exist, starting with primordial isotopes ^{232}Th, ^{238}U and ^{235}U. Members of the first two chains are important for

Table 4.1: *Values of fraction of an isotope left after elapsing of n half-lives.*

Time $n \cdot T_{1/2}$	$A(t)/A_0(\%)$
0	100
1	50
2	25
3	12.50
4	6.25
5	3.13
6	1.56
7	0.78
8	0.39
9	0.20
10	0.10

sediment chronology and will be discussed in Chapter 6. A simple decay chain can be expressed as:

$$N_1 \overset{\lambda_1}{\rightarrow} N_2 \overset{\lambda_2}{\rightarrow} ...N_{n-1} \overset{\lambda_{n-1}}{\rightarrow} N_n(\text{stable})$$

where N_1 ... N_n are numbers of atoms of parent and daughter products and λ_1 ... λ_{n-1} their respective decay constants. The rates of disintegration for individual series members are (Krieger, 2007):

$$\frac{\mathrm{d}N_1}{\mathrm{d}t} = -\lambda_1 N_1 \tag{4.8a}$$

$$\frac{\mathrm{d}N_2}{\mathrm{d}t} = +\lambda_1 N_1 - \lambda_2 N_2 \tag{4.8b}$$

$$\frac{\mathrm{d}N_3}{\mathrm{d}t} = +\lambda_2 N_2 - \lambda_3 N_3 \tag{4.8c}$$

$$\dots$$

$$\frac{\mathrm{d}N_n}{\mathrm{d}t} = +\lambda_{n-1} N_{n-1} - \lambda_n N_n \tag{4.8d}$$

The solution of the differential equations for the first three terms (Seelmann-Eggebert et al., 1962), assuming $N_1(0) \neq 0$ and $N_2(0) = N_3(0) = 0$, can be expressed as:

$$N_1(t) = N_1(0) e^{-\lambda_1 t} \tag{4.9a}$$

$$N_2(t) = N_1(0) \frac{\lambda_1}{\lambda_2 - \lambda_1} \left(e^{-\lambda_1 t} - e^{-\lambda_1 t} \right) \tag{4.9b}$$

$$N_3(t) = N_1(0) \lambda_0 \lambda_1 \left(\frac{e^{-\lambda_0 t}}{(\lambda_1 - \lambda_0)(\lambda_2 - \lambda_0)} + \frac{e^{-\lambda_1 t}}{(\lambda_0 - \lambda_1)(\lambda_2 - \lambda_1)} + \frac{e^{-\lambda_2 t}}{(\lambda_0 - \lambda_2)(\lambda_1 - \lambda_2)} \right). \tag{4.9c}$$

A general solution for n daughter products in a simple decay chain, assuming $N_1(0) \neq 0$ and $N_2(0) = N_3(0) = ... = N_n = 0$, known as solution of the Bateman-equation (Bateman, 1910; Pressyanov, 2002):

$$N_n(t) = N_1(0)\lambda_1\lambda_2...\lambda_{n-1} \sum_{i=1}^{n} \frac{e^{-\lambda_i t}}{\prod\limits_{j=1,k\neq 1}^{n} (\lambda_j - \lambda_i)}, (n > 1) \tag{4.10}$$

Sometimes a nuclide in the decay chain can "branch"-decays to more than one daughter with certain probability. The total decay constant for the decay of the parent nuclide is then the sum of partial decay constants $\lambda_1, \lambda_2, ...\lambda_i$. Branching ratios for individual decay modes are defined as

$$BR_i = \frac{\lambda_i}{\lambda_1 + \lambda_2 + ... + \lambda_i} = \frac{\lambda_i}{\lambda}. \tag{4.11}$$

An example within natural series is ^{212}Bi, which branch-decays to ^{208}Tl (36%) by α-decay and ^{212}Po (64%) by β^--decay (Fig. 6.3).

4.1.3 Radioactive equilibrium

Several special cases of relationships between two successive parent (P) and daughter (D) nuclides with half-lives $T_{1/2}(P)$ and $T_{1/2}(D)$, respectively, are described depending on their relative half-lives ratio. In the following cases it is always assumed, that $A(P) = 100\%$ and $A(D) = 0$ at time $t = 0$.

Transient equilibrium - $T_{1/2}(P) > T_{1/2}(D)$

The case when the half-life of the parent nuclide is longer, but in the same order of magnitude as the daughter nuclide, is called transient equilibrium. As an example from the ^{238}U natural decay chain a nuclide pair ^{234}U-^{230}Th can be taken, with respective half-lives $2.455 \cdot 10^5$ and $7.54 \cdot 10^4$ years (Fig. 4.2).

After several daughter half-lives the transient equilibrium is established. The activity of the daughter nuclide is then higher than the parent activity due to its shorter half-life. The activity of the daughter isotope in equilibrium state follows the decay of the parent nuclide and can be expressed as:

$$A(D) = A(P)\frac{T_{1/2}(P)}{T_{1/2}(P) - T_{1/2}(D)}. \tag{4.12}$$

The maximum activity of daughter nuclide is reached at time t_m,

$$t_m = \frac{T_{1/2}(P) \cdot T_{1/2}(D)}{(T_{1/2}(D) - T_{1/2}(P))ln(2)} \cdot ln\frac{T_{1/2}(D)}{T_{1/2}(P)}. \tag{4.13}$$

Secular equilibrium - $T_{1/2}(P) >> T_{1/2}(D)$

There are several successive nuclide pairs in the natural decay series, where half-life of the parent nuclide is much longer than that of its daughter and in these cases we speak of a secular equilibrium. An example is the decay of ^{226}Ra (half-life 1600 years) to ^{222}Rn (half-life 3.8 days) (Fig. 4.3). Decay of the parent nuclide is negligible on the time-scale of daughter's half-life. After reaching the equilibrium, the activities of both successive nuclides are equal: $A(D) = A(P)$.

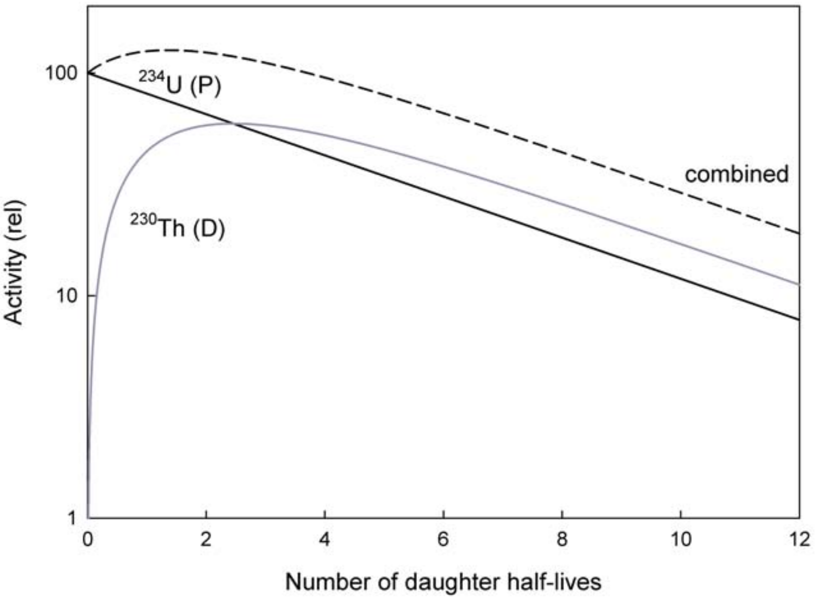

Figure 4.2: *Transient radioactive equilibrium between ^{234}U and ^{230}Th.*

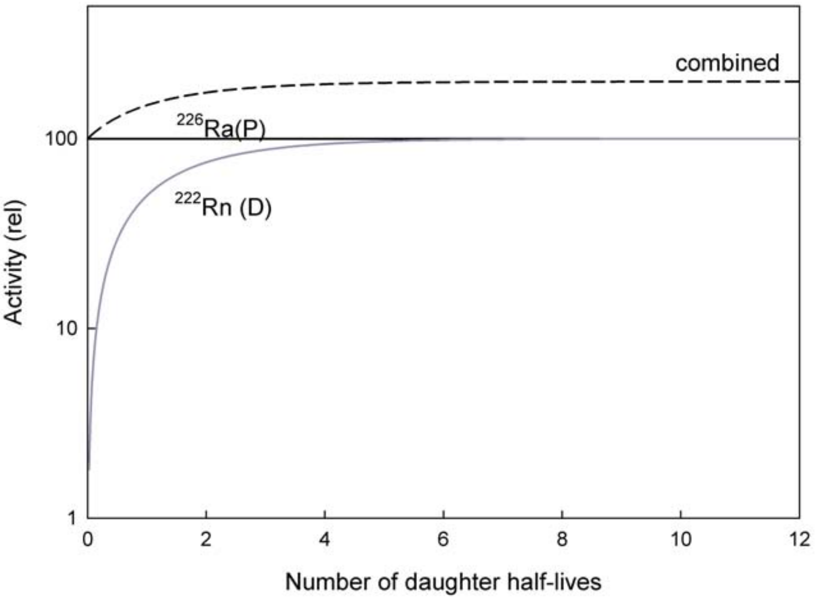

Figure 4.3: *Secular radioactive equilibrium between ^{226}Ra and ^{222}Rn.*

Non-equilibrium - $T_{1/2}(P) < T_{1/2}(D)$

When parent's half-life is shorter than that of its daughter, no equilibrium is established, the parent will decay leaving the "orphan" daughter behind. An example is shown using the fallout radionuclide ^{241}Pu (half-life 14.29 years) and its daughter ^{241}Am (half-life 432.6 years) (Fig. 4.4).

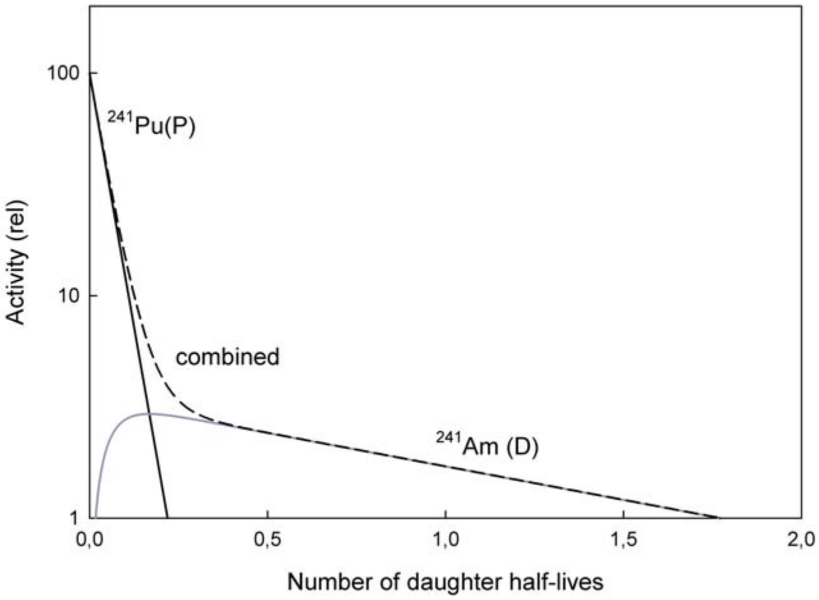

Figure 4.4: *There is no radioactive equilibrium established between separated* ^{241}*Pu and* ^{241}*Am.*

4.1.4 Modes of decay

The four principal types of radioactive decay are presented below.

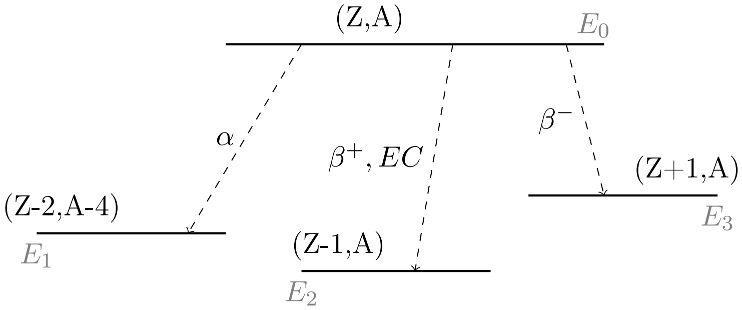

Figure 4.5: *Illustration of radioactive decay using a decay scheme.* β^- *decay is directed to the right (atomic number rises), while* α *decay,* β^+ *decay and electron capture to the left (atomic number is reduced) [After Krieger (2007)].*

α decay

In α decay, an α particle (a Helium nucleus, ${}^4_2He$) is emitted, while the parent nucleus loses two protons and two neutrons (Fig. 4.5). α decay usually occurs in heavy nuclei (roughly Z > 83). α particles have relatively sharply defined kinetic energies, which are nuclide characteristic and therefore allow the use of spectrometric methods for their identification. An example of an α decay is

$$^{226}Ra \rightarrow ^{222}Rn + ^4_2He.$$

.

β^- decay

This transformation is typical for neutron rich nuclei, often fission products. As a result of the neutron excess, a neutron (n) is transformed into a proton (p), an electron (β^- particle) and an antineutrino ($\bar{\nu}$):

$$n \rightarrow p + \beta^- + \bar{\nu}.$$

Therefore, during β^- decay the atomic number is increased by 1 and the mass number remains constant:

$$^{214}Bi \rightarrow ^{214}Pb + \beta^- + \bar{\nu}.$$

In terms of β decay, electrons (e^-) are referred to as β^- particles and positrons (e^+) are referred to as β^+ particles. Resulting from the fact that the decay energy is shared between β^- particle and antineutrino in variable proportions, the β spectrum emitted by a certain radioisotope is not discrete, but continuous and is specified by maximum and mean energies, $E_{\beta max}$ or $E_{\beta mean}$.

β^+ (positron) decay

β^+ emitters have a neutron deficiency. In this case, a proton is transformed into a neutron, a positron (e^+ - the antimatter counterpart of an electron) and a neutrino (ν).

$$p + Energy \rightarrow n + \beta^+ + \nu.$$

β^+ decay can only happen inside nuclei when the difference of the binding energy of the mother nucleus and the daughter nucleus $\Delta E > 1.022$ MeV. The difference between these energies goes into the reaction of converting a proton into a neutron, a positron and a neutrino and into the kinetic energy of these particles. Similarly to β^- decay, the energy is distributed between the β^+ particle and the neutrino. During β^+ decay the atomic number decreases by 1 and mass number remains constant:

$$^{40}K \rightarrow ^{40}Ar + \beta^+ + \nu.$$

The positron produced during a β^+ decay reacts with electron during a process called annihilation, when both electron and positron disappear and a pair of photons with energy equal to the electron mass (511 keV[1] each) is created and emitted in opposite directions.

---

[1] The electronvolt (eV) is a unit of energy equal to the kinetic energy gained by an electron accelerated through a potential difference of 1 V. 1 eV = $1.602 \cdot 10^{-19} J$. This is a small unit and the multiple units keV ($10^3 eV$) and MeV ($10^6 eV$) are useful for describing energy on atomic scales.

Electron capture (EC)

This transformation happens with neutron deficient nuclides and is a competing process to β^+ decay, as it requires less ΔE. The electron needed to convert the proton is captured in the nucleus from one of the electron shells, most frequently the closest K-shell.

$$p + e^- + Energy \rightarrow n + \nu.$$

A vacancy in the electron shell left by the missing electron is filled by another electron dropping from a higher shell, which is accompanied by release of energy in the form of x-ray photon or Auger electron. Since the proton is changed to a neutron, the number of neutrons increases by 1, the number of protons decreases by 1, and the atomic mass number remains unchanged:

$$^7Be + e^- \rightarrow ^7 Li + \nu.$$

4.2 Gamma radiation

4.2.1 Origin of gamma radiation

Gamma radiation is electromagnetic radiation of high frequency (very short wavelength). The energy of photons is proportional to their frequency ν,

$$E = h \cdot \nu, \tag{4.14}$$

where Planck's constant $h = 4.14 \cdot 10^{-21}\ MeV \cdot s^{-1}$. The usual energy of gamma rays detected in the field of environmental radioactivity ranges from 10 to 3000 keV.

Gamma rays are produced by transitions from excited states in atom nuclei as a result of radioactive decay, which rarely leads to the ground state. Therefore gamma decay frequently accompanies other previously mentioned decays. For each nuclide, the rate and energy of photons emitted during decay is unique, which is a basis for their identification and quantification by means of gamma spectrometry.

The change of the energy level from an excited to a lower level or ground state can occur directly or stepwise and is also characterized by a certain half-life, which is usually very short (most often $< 10^{-12}$ s), but when the half-life is long enough to be easily measurable, the condition of the nucleus is described as isomeric state, or metastable state (metastate). An example of isomeric transition is shown in Fig. 4.6. The 661.7 keV gamma line used in gamma spectrometry for determination of a common environmental radionuclide ^{137}Cs ($T_{1/2}$ = 30 y) is in fact due to gamma-emission of isomer $^{137\mathrm{m}}$Ba ($T_{1/2}$ = 2.55 m), which is in radioactive equilibrium with its parent.

Another type of de-excitation of a nuclear level occurs in the form of internal conversion (IC). During this process a monoenergetic electron (internal conversion electron) is expelled from the atom, carrying excess energy of the nucleus, and the vacancy in the shell is filled by another electron from a higher electron shell, leading to x-ray and Auger electron emission, similar to electron capture. In ^{137}Cs decay (decay scheme in Fig. 4.6) the probability of decay branch via $^{137\mathrm{m}}$Ba is 94.7 %. The 661.7 keV gamma emission probability listed in Bé et al. (2011) is only 85.1% though, and the remaining energy is internally converted.

4.2.2 Other sources of photon emissions

Several other sources of photon registered in gamma spectra can be considered, although being usually rather rare in comparison to gamma radiation from radioactive decay.

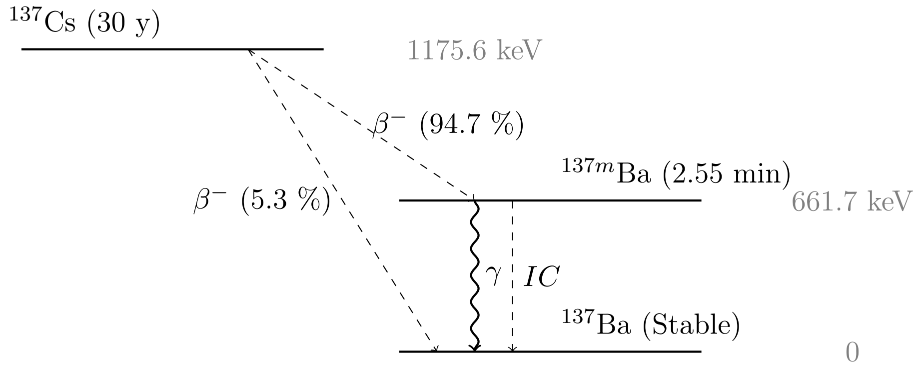

Figure 4.6: *A decay scheme of β^- decay of ^{137}Cs followed by isomeric transition to stable ^{137}Ba. Data from: NNDC (2011).*

X-rays

X-rays being emissions of photons are in principle identical to gamma rays. The energy of x-rays is approximately 1–100 keV, therefore the energy range of both is overlapping, but their origin is different. X-rays are emitted during re-arrangement of the atomic electron structure rather than changes in nuclear structure. As mentioned in Sec. 4.1.4, they commonly accompany nuclear decay processes (EC, IC), which destabilize the atomic electron shell. X-ray energies are unique to each element but the same for different isotopes of one element. All elements have the same x-ray pattern, but the absolute energies vary depending on difference of electron shell levels. A roman letter in the x-ray line description indicates the final level to which the electron moves, and a Greek letter plus a number indicates the electrons initial energy level ($K_{\alpha 1}$, for example).

There is a principle difference in x-rays produced during electron capture and internal conversion. Because there is no change in Z during IC, the x-ray produced is characteristic to the parent nuclide (element), as opposed to electron capture, during which daughter characteristic x-rays are emitted. However, as IC occurs during gamma emission after decay, daughter product's x-rays can be observed (for example Ba K_{α} lines in ^{137}Cs decay, Fig. 4.6).

Bremsstrahlung

Bremsstrahlung, meaning "breaking radiation" in German, is electromagnetic radiation produced by deceleration of fast electrons emitted by a high energy β-emitter within the nuclear Coulomb field. Its effect in the form of increased continuum can be observed in the low energy part of gamma spectra. Bremsstrahlung is most pronounced for absorbers with high Z.

Fluorescence

Fluorescence is an emission of a characteristic x-ray accompanying photoelectric effect (see below). Fluorescence x-rays formed during absorption of photons from a sample in lead shielding can result in significant Pb x-ray peaks in gamma spectra.

Annihilation radiation

Annihilation occurs when an electron interacts with its anti-particle positron (from β^+ decay or pair production). As a result, two photons are emitted with the energy of 511 keV.

Nuclear reactions

Another source of gamma radiation can be nuclear reactions, for example thermal neutron activation. In long term background gamma spectra a product of thermal neutron capture in cadmium from shielding can be observed (Chap. 5).

4.2.3 Interaction of gamma radiation with matter

Photons can interact with atomic electrons, with nucleons and with electric field surrounding nucleus. During their interactions they can be completely absorbed, or scattered elastically (coherently) or inelastically (incoherently). For practical gamma spectrometry, three processes are important: the photoelectric effect, Compton scattering and pair production.

Photoelectric effect

Photoelectric effect is an inelastic scattering by electrons. Photons collide with electrons from an inner shell and its entire energy is absorbed by this electron. If the photon energy E_γ is higher than the binding energy of the electron E_b, the electron is ejected with energy:

$$E_e = E_\gamma - E_b. \tag{4.15}$$

Following interactions can include bremsstrahlung or ionization of another atom. The missing electron causes a characteristic x-ray emission (fluorescence), as the vacancy is occupied by another electron from a higher shell, or Auger electron emission.

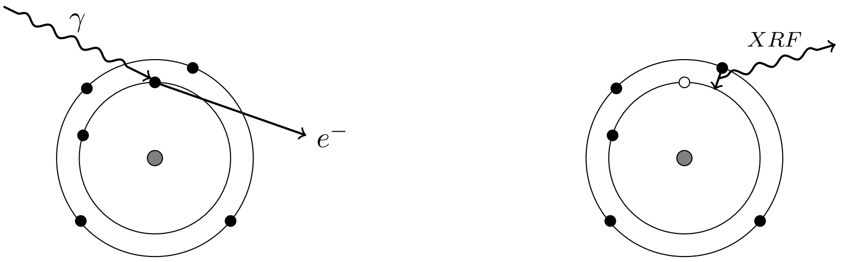

Figure 4.7: A scheme of the photoelectric effect (left) followed by emission of characteristic x-rays (right).

Compton scattering

The Compton effect is an inelastic scattering by electrons, resulting in reduction of the photon's energy. A photon collides with an electron (usually from an outer shell) and part of its energy E_γ is absorbed by this electron, which is ejected (Fig. 4.8). The photon is scattered at an angle θ with the rest energy $E_{\gamma'}$. The energy transfer is described as:

$$E_e = E_\gamma - E_{\gamma'}, \tag{4.16}$$

where

$$E_{\gamma'} = \frac{E_\gamma}{1 + \frac{E_\gamma}{M_0c^2}(1 - cos\theta)}, \tag{4.17}$$

with M_0c^2 being electron rest mass of 511 keV. The dependence of the $E_{\gamma'}$ and E_e on the angle θ is presented in the Fig. 4.9. It also illustrates, that during Compton scattering, always less than 100% of the photon energy will be absorbed. The highest energy corresponding to full backscatter is described as the Compton edge (see also Fig. 4.13).

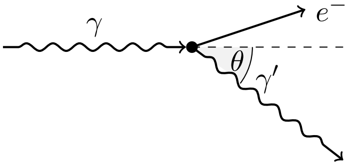

Figure 4.8: *A scheme of the Compton effect: a photon of energy E_γ collides with an electron and a new photon of reduced energy $E_{\gamma'}$ is scattered at an angle θ.*

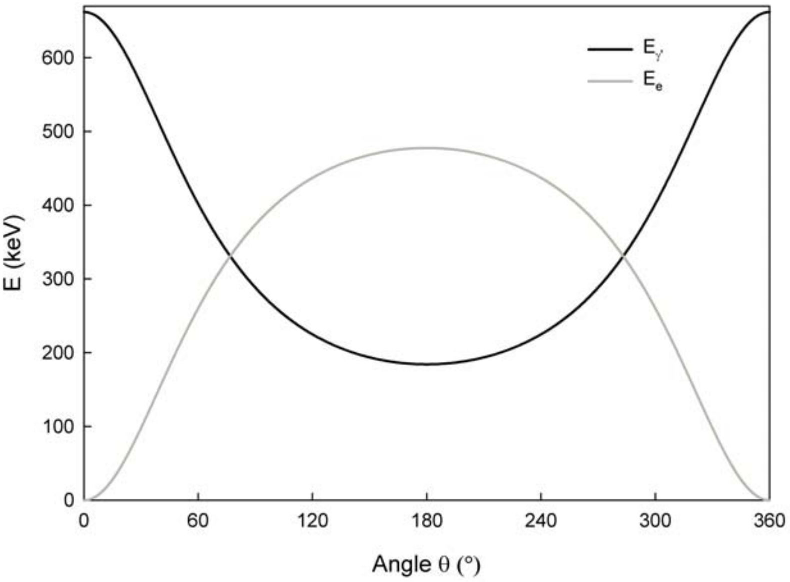

Figure 4.9: *Distribution of the energy $E_{\gamma'}$ of a 662 keV scattered photon (^{137}Cs) and E_e of a recoil electron after Compton scattering as a function of the angle θ.*

Pair production

This photon interaction requires that the incident photon has a minimum energy of two times the equivalent of the electron rest mass, i.e. an energy greater than 1022 keV. After interaction of a highly energetic photon with a Coulomb field of a nucleus, an electron / positron pair is produced (Fig. 4.10).

Interactions in Ge detector

In gamma spectrometry all three formerly described interactions occur in the detector and in its surrounding materials (housing, electronics, shielding). They lead to characteristic features

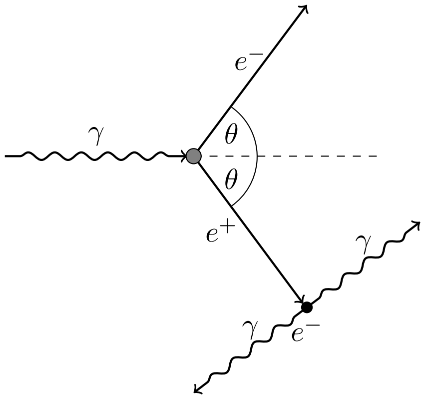

Figure 4.10: *A scheme of the electron-positron pair production after a photon interaction with a nucleus. Following interaction of the newly formed positron with an electron leads to annihilation.*

visible in gamma spectra (Sec. 4.4). Photon cross sections for the detector material germanium are shown in the Fig. 4.11 in order to demonstrate relative frequencies of individual interactions as a function of energy. In a gamma spectrometry setup directed to natural and artificial radionuclides of environmental relevance, an energy range of about 40-2000 keV is taken into account. The photoelectric effect dominates in lower energies, while its cross section falls sharply and Compton effect and pair production gain importance in higher energies.

4.3 Detection of gamma radiation

4.3.1 Gamma detectors

For detection of gamma radiation and its spectrometry two types of detectors are widely used: solid state semiconductor detectors and scintillators. Scintillation detectors produce light in response to incident charged particle and emit a light pulse (scintillation), the intensity of which is proportional to the incident particle energy. The most common scintillation detectors used for gamma spectrometry are those made of NaI(Tl) crystals.

Nowadays, high-purity germanium detectors (HPGe) are “golden standard” in gamma spectrometry. The efficiency of HPGe detectors is often expressed in relative terms to a “standard” 3” × 3” NaI(Tl) detector for historical reasons.

Fig. 4.12 shows a comparison of spectra of the same specimen of a radioactive mineral Trinitite (Pittauerová et al., 2010a) measured with both formally mentioned types of detector. The HPGe spectrum was produced by the Det. 3 in the Laboratory as described in detail in Tab. 5.1 and the scintillation spectrum by a standard 3” × 3” NaI(Tl) detector Harshaw (10 cm Pb + 0.5 mm Cu shielding) connected to a 4096 channel analyzer Canberra Series 10 in the Radiometric laboratory of the Institute of geochemistry, mineralogy and mineral resources, Faculty of Science, Charles University in Prague (Goliáš, 2010). Illustrated is a difference in the energy resolution, which is represented by the value of full width at half maximum (FWHM, Sec. 4.5.1) measured at 662 keV peak of ^{137}Cs: for NaI(Tl) spectrum it is 50.6 keV (7.6 %) compared to 1.4 keV (0.2%) for HPGe spectrum. The low resolution can present problems when analyzing complex gamma spectra obtained with scintillation detectors.

Recent development in the field of scintillation detectors improves usability of $LaBr_3$(Ce) detectors. They can achieve 2.7% relative resolution at 662 keV with efficiency about 1.3 times

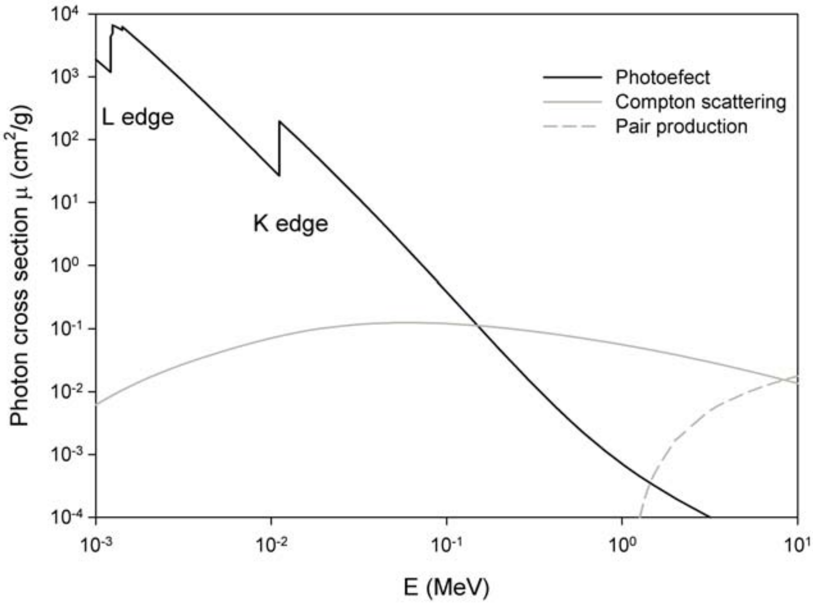

Figure 4.11: *Photon cross sections in Ge for photoelectric effect, Compton scattering and pair production based on data extracted from on-line database XCOM (Berger et al., 2009).*

that of NaI(Tl) due to higher density. The scintillation decay time (decay time of the excited state) is much shorter than for NaI(Tl), which makes $LaBr_3$ detectors more suitable for high count rates. $LaBr_3$(Ce) however contains a naturally occurring radioisotope, ^{138}La, which causes increased background and diminishes suitability of these detectors for low level spectrometry (Gilmore, 2008).

4.3.2 HPGe gamma spectrometry system

Germanium is a material suitable for detector construction, as it has a high absorption coefficient due to high Z. After interaction with incident gamma ray it produces a high number of electron–hole pairs and allows their high mobility. The technology available to grow relatively large crystals in high purity at reasonable costs makes Ge the most common gamma spectrometry detector material (Gilmore, 2008).

The incident photon produces a primary electron in Ge, which in turn can promote electrons from valence band to conduction band. The vacancy left after the electron is called a hole. The number of electrons and holes produced during an interaction is proportional to the absorbed energy. Electrons and holes carry electric charge, which is swept by a strong electric field toward the electrodes. Ge monocrystals used for detector manufacture are either n-type (containing 5-valent impurities, for example lithium) with excess of electrons, or p-type (containing 3-valent impurities, like boron), which are electron acceptors. The electric contacts are provided on the outer and on the inner surface of the detector and consist of n^+ or p^+ doped layers. n^+ layer is typically produced by Li diffusion and is about 0.5 mm thick, while p^+ layer is typically achieved by B ion implantation and therefore only some 0.3 μm thick. The contact layer acts as a “dead” layer, because photons absorbed in this layer can not be registered. Similarly, aluminium detector cap absorbs part of mainly low energy radiation incoming to the detector. Therefore for low energy spectrometry (10–40 keV) the use of detectors with beryllium

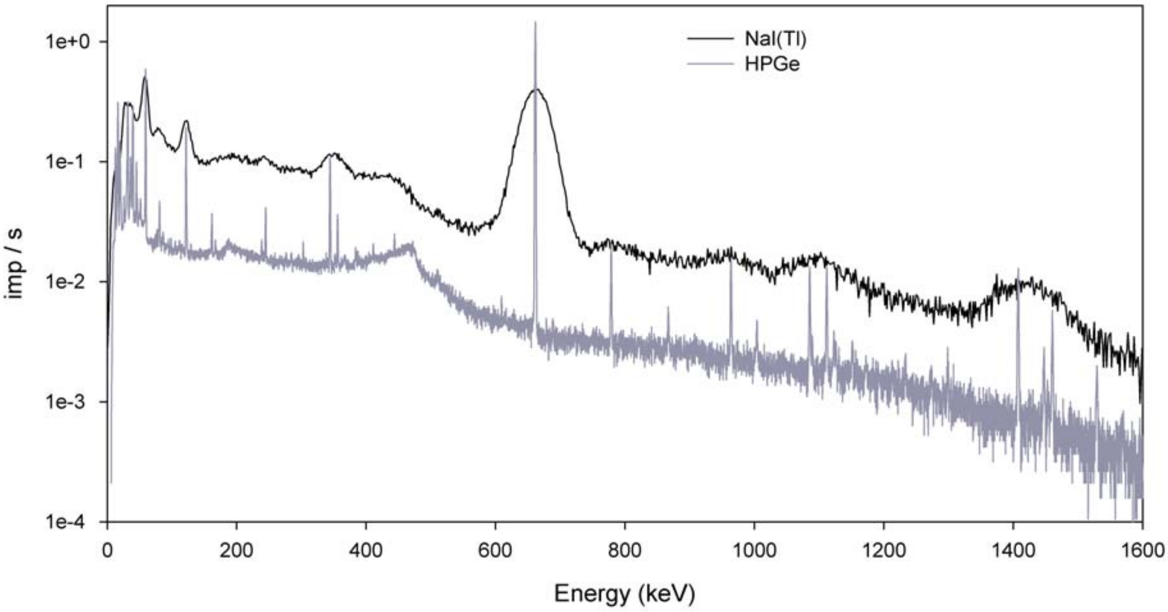

Figure 4.12: *A comparison of gamma spectra of a radioactive mineral Trinitite produced by a HPGe detector (Det3) and a 3" × 3" NaI(Tl) detector.*

or carbon composite window and outer ion implanted p^+ contact are used, which is also the case of the Laboratory's detectors used in this study (Tab. 5.1).

During operation the HPGe detector must be cooled to very low temperatures (close to 77 K), which reduces the background current caused by thermal excitation. Although nowadays electro-mechanical cooling is available, all Laboratory's detectors use traditionally liquid nitrogen cooling systems.

The charge collected at the detector electrodes is converted to voltage pulses in a charge-sensitive preamplifier located close to the detector itself. The voltage pulses are proportional to the primary electron energy. In traditional gamma spectrometry systems the signal coming from the preamplifier is further treated in the amplifier, where the pulse height information is extracted by pulse shaping and the signal is enhanced. In a multichannel analyzer (MCA) the pulses are measured by an analogue to digital converter (ADC) which generates a number proportional to the analogue signal and sorted by their size into channels assigned to certain pulse height intervals, counted and stored.

In more recent gamma spectrometry systems the pulses from the preamplifier are processed digitally in a device (called for example desktop spectrum analyzer), which takes over the functions of the mentioned electronic devices. The Laboratory uses the traditional signal processing line.

4.4 Characteristics of gamma spectra

The most important feature of a gamma spectrum used to identify and quantify radionuclide activities, the **full energy peak** (FEP), is the result of photoelectric absorption. It is shown in a simplified spectrum of a single-line emitter in Fig. 4.13.

Compton scattering will appear in the spectra as a **Compton continuum** in the low energy part extending from zero to the **Compton edge**. It is a consequence of incomplete absorption of gamma rays described in Sec. 4.2.3. The **Compton edge** is characterized by the maximum energy of scattered electrons at 180° scattering angle (Fig. 4.8 and Eq. 4.17) followed by steep decrease to multiple Compton region between the Compton edge and the FEP. In Fig. 4.13 it is described as primary photon continuum.

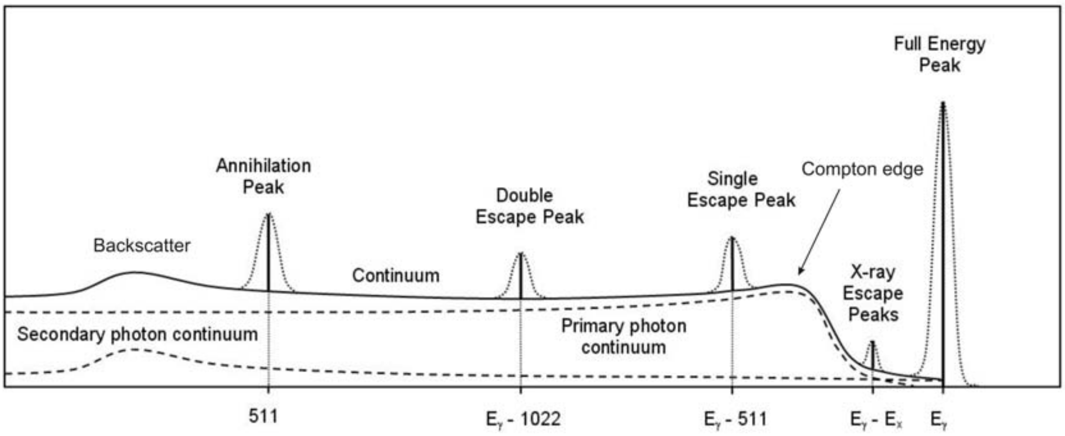

Figure 4.13: *The main features of a simple gamma spectrum, edited from Nucleonica (2011).*

An **annihilation peak** at 511 keV is present due to positron annihilation virtually in each gamma spectrum. Theoretically, no signal caused by gamma radiation is expected to be present in energies higher than that of FEP, but in practice the continuum beyond the FEP is due to **random summing**, when two or more events are detected almost simultaneously (pile-up). This is not obvious in Fig. 4.13.

A number of situations further complicate even spectra of relatively simple sources. These include for example a **double escape peak**, which can be present when both annihilation photons created from pair production escape from the detector. Then energy equal to FEP - 1022 keV is registered. **Single escape peak** results from situation when only one of the annihilation photons created from pair production events in the detector escapes from the detector and the other is fully absorbed. When this happens, the registered energy of FEP is lowered by 511 keV.

True coincidence sum peaks appear in the spectra when a radionuclide decays via several successive gamma emissions which might be recorded simultaneously (Sec. 4.5.7). **Random sum peaks** occur as a special case of random summing for very high count rates when two independent full absorption events are registered simultaneously and appear as a peak in the spectrum.

X-ray escape peaks occur in the spectra as a result of escape of the detector of a characteristic x-ray formed during photoelectric effect. The peak is then observed in the energy of FEP lowered by x-ray characteristic energy.

Other spectral features are result of interaction of gamma rays with surrounding shielding, the sample itself or other materials surrounding the detector.

Characteristic X-rays (frequently from Pb in the shield) often occur in spectra as an effect of photoelectric absorption of radiation from the sample (Gilmore, 2008), cosmic radiation or even radionuclides in the shield itself (they are sometimes also present in background spectra). Lead is used for construction of shielding in gamma spectrometry and the interacting radiation source can be the sample, cosmic radiation and even shielding itself. One possible way to practically reduce the effect is installation of a graded shielding made of layers with decreasing

Z from outside in (Pb, Cd, Cu, plastic). Each of the layers would significantly absorb x-rays emitted from the outer layer.

Characteristic x-rays of daughter products can sometimes be registered, for example Ba K_α line following ^{137}Cs decay.

Backscatter peak is produced when incident photons emitted from the source are Compton scattered from the shield back to the detector and absorbed in it. In Fig. 4.13 it is a part of the secondary photon continuum. Also pair-production derived 511 keV photons from the shielding can contribute to the annihilation peak (Debertin & Helmer, 1988).

4.5 Analysis of gamma spectra

In this section individual steps in spectra analysis are described. In the Laboratory Canberra Genie 2000 gamma spectrometry software (version 3.1) is routinely used and therefore employed also for analysis of spectra within this work.

4.5.1 Energy and peak shape calibration

The purpose of energy calibration is to derive a relationship between the position in the spectrum (channel number) and the corresponding gamma energy in order to identify FEPs of radionuclides. The modern ADCs have a high level of linearity (Gilmore, 2008) and therefore using the linear model

$$E_\gamma = O + G \cdot Ch, \tag{4.18}$$

where E_γ is energy (in keV), O intercept (offset), G gradient (gain) and Ch is the channel number, is suitable. The calibration is preset in the analyzing software for each detector and is always checked before the analyses with energies of known isotopes in the spectra. For sediment samples, these included most often ^{210}Pb, ^{214}Pb, ^{40}K and the annihilation peak. In successful calibration, the energies deduced from the calibration vary by less than 0.5 keV over the spectrum range.

For automated peak search and fitting, FWHM[2] calibration is performed as a function of the energy for nuclide identification and recognizing multiplets (overlapping peaks) in the spectra. Genie 2000 uses the Gaussian model to describe peaks with an additional parameter - tail - being introduced for asymmetric peak shapes in HPGe gamma spectrometry (Canberra, 2002a). The peak shape calibration usually does not well describe the annihilation peak (511 keV) and single escape peaks, which tend to be broader than the FWHM calibration would suggest, due to Doppler broadening (Gilmore, 2008). As a consequence the annihilation peak might not be well fitted, but that does not cause any serious problem, because it is not used for any nuclide analysis. It does not form multiple peaks with any radionuclide analyzed within this work either.

The actual model function that the Genie 2000 algorithm (Canberra, 2002a) uses for fitting the FWHM data is

$$FWHM = \frac{F_0 + F_1\sqrt{E_\gamma}}{G}, \tag{4.19}$$

where G is the gain parameter from energy calibration equation (Eq. 4.18) and F_0 and F_1 are fitted parameters (Fig. 4.14). Using this model often leads to rather unsatisfactory results

---

[2] Full width at half maximum (FWHM) is described as the width of the peak at a height that is one half of its maximum height above the background continuum. It is a measure of the energy resolution.

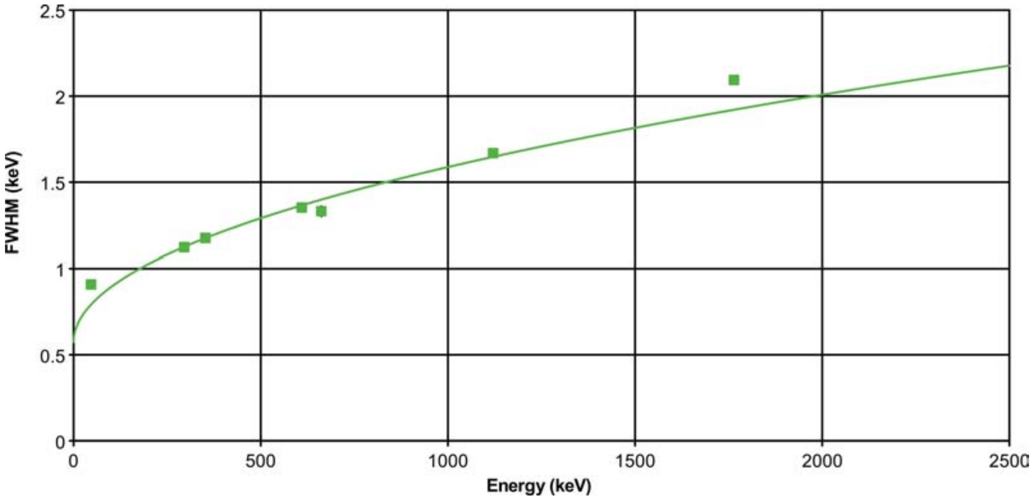

Figure 4.14: *An example of FWHM calibration in Genie 2000. Measured FWHM data points fitted by a non-suitable model using Eq. 4.19.*

and according to Gilmore (2008, 2009) has no theoretical justification, it is possibly based on mistaken use of square root function recommended by Debertin & Helmer (1988):

$$FWHM = \sqrt{F_0 + F_1 \cdot E_\gamma}, \tag{4.20}$$

whereas in practice square root quadratic functions or a simple linear function provide the best practical fits (Gilmore, 2008). This Genie 2000 "bug" might have negative consequences for the following analyses, for example multiplets recognition, but the current version does not offer any alternative. The difficulties resulting from inferior resolution calibration can be resolved by manual interventions (see "Interactive peak fit" in Sec. 4.5.3).

4.5.2 Full energy peak efficiency calibration

Efficiency ϵ of detection varies with gamma radiation energy E, geometry and physical properties of the sample. It can be measured or calculated for distinct energies. Its proper determination is one of the key steps in nuclide quantification and therefore a separate Chapter 7 is devoted to this topic.

No matter whether experimental or mathematical efficiency calibration data are used, normally the calibration curve is fitted within Genie 2000 (Canberra, 2002a) using a function:

$$\epsilon = exp\left(\sum_{i=0}^{N} b_i \cdot (ln(E_\gamma)^i)\right). \tag{4.21}$$

This option is usually separately for two regions with crossover at maximum efficiency (around 70–100 keV), with b_i being the fitted coefficients. The maximal polynomial order N is dependent on the number of calibration points (Canberra, 2002a) and can be set manually. It usually varies between 2 and 4. During the procedure of curve fitting the efficiency uncertainties of the individual points are reduced by the vicinity of neighboring points (Canberra, 2002a).

4.5.3 Peak location and area

Genie 2000 performs peak search based on second difference peak locate algorithm described in Canberra (2002a). The algorithm searches the spectrum for peaks above specified threshold levels and identifies the centroids of found peaks by finding positions of the functions' second difference minima (Genie option "Unidentified Second Difference"). In the following step limits of peak regions are defined, single peaks or multiplets are recognized, and their areas and uncertainties are calculated based on non-linear least square fit.

In the subprogram "Interactive peak fit" the resulting fit can be visually checked for individual peaks also together with fitting residuals and can be manually corrected. The most frequent interventions include inserting not recognized peaks, deleting suspicious lines from multiplets, changing FWHM (from fixed value based on FWHM calibration to a free parameter, Fig. 4.15), re-defining regions of interest (ROIs), re-defining background regions, etc.

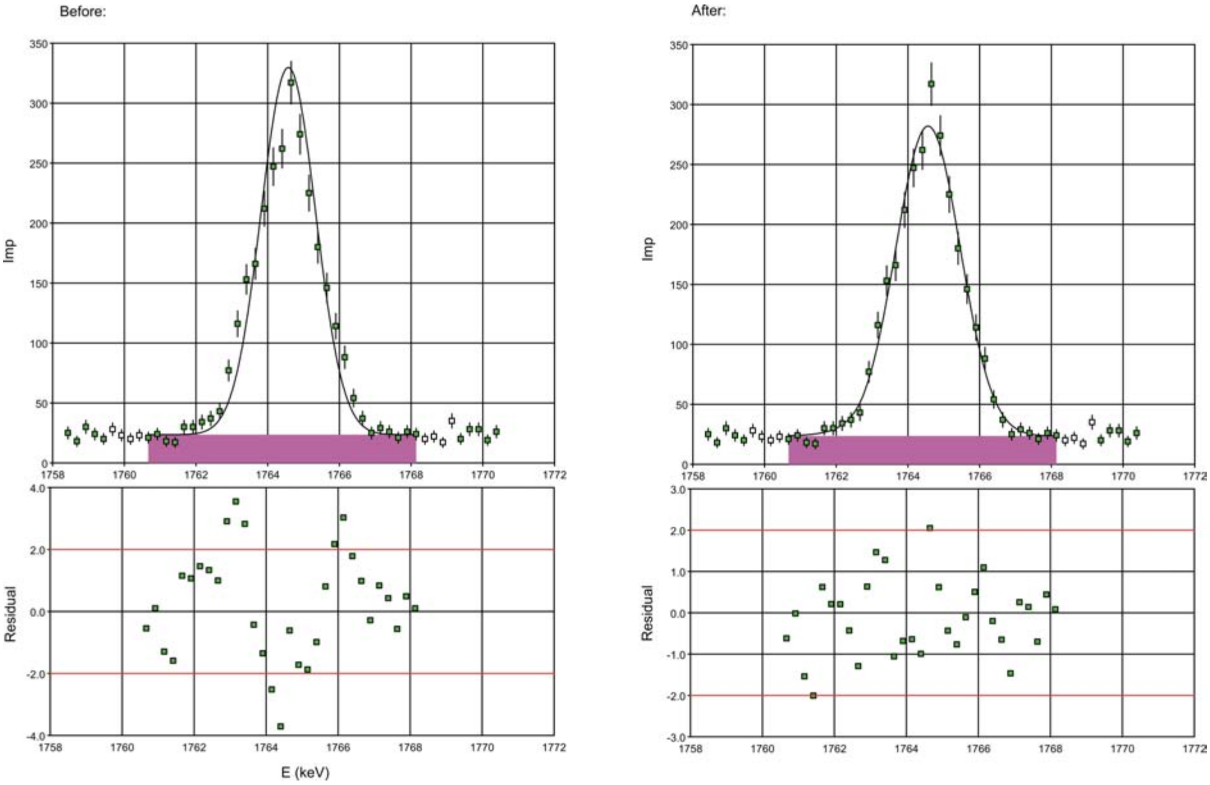

Figure 4.15: *An example of Interactive peak fit use. Due to wrong FWHM calibration (see section 4.5.1) 1764.5 keV peak of* ^{214}*Bi was wrongly fitted (see the systematic pattern in residuals plot in the left). A correction can be done by allowing FWHM to be a free fitted parameter. In this particular case FWHM is corrected from value 1.8 to 2.1. The net peak area uncertainty is reduced from 2.86% to 2.21%.*

If the peak fitting is not satisfactory, making more systematic changes in fitting parameters setting should be considered, such as new FWHM calibration (based on smaller number of data points) or adjusting significance threshold for peak search to lower value (less significant peaks will be found) or to higher value (in order to find only the most significant peaks), followed by repeated peak location and peak area analysis steps.

4.5.4 Background subtraction

Corrections to compensate the effect of background radiation is done by subtraction of net peak areas from a separate background spectrum from matching net peak areas in the actual spectrum (recalculated to the equivalent time). Background spectra are measured approximately once a month. The long-term background spectra study is described in detail in Chapter 5.

4.5.5 Efficiency correction

Here for each of the peaks found in the previous steps efficiency and an associated uncertainty is calculated using the fitted efficiency curve from the efficiency calibration step.

4.5.6 Nuclide identification, activity calculation

Some general nuclide libraries are contained in the Genie 2000 based on National Nuclear Data Center of the Brookhaven National Laboratory NUDAT database, but for special applications like sediment samples custom libraries containing selected radionuclides and lines can be created and applied. In assemblage of natural radionuclides careful attention should be payed to practical setting of half-lives of radionuclides assumed to be in radioactive equilibrium with parent nuclides. This can have consequences for decay corrections (see lower).

An example is ^{214}Pb, with a physical half-life of 26.8 min, but in practical terms its activity is supported by decay of its preceeding longer-lived radionuclides, ^{222}Rn ($T_{1/2}$=3.82 days) and consequently ^{226}Ra ($T_{1/2}$=1600 years), and after approximately 3 weeks of sample sealing they are considered to be in equilibrium. In a similar way, activity of ^{228}Ac with ($T_{1/2}$=6.15 h) is in equilibrium with ^{228}Ra ($T_{1/2}$=5.75 yr), therefore the later half-life is used.

The "Nuclide Identification with Interference Correction" algorithm can be used for identification of nuclides in the spectrum and automatic interference correction and weighted mean calculation based on an identification matrix. Very important in this step is selection of suitable radionuclides and lines in the library, to which the found peaks are compared to using algorithms described in Canberra (2002a). Gamma lines for identification of radioisotopes for sediment chronology and their possible interferences are discussed in a separate Chapter 6.

Activity per mass unit, activity concentration, is calculated from net peak areas as:

$$C = \frac{N_{net}}{M \cdot \epsilon_E \cdot I_\gamma \cdot t_L \cdot K_W \cdot K_C}, \tag{4.22}$$

where M is the sample mass, ϵ_E is the efficiency calculated for given energy, I_γ is probability of emission of the particular gamma energy, t_L is live time[3], and K_W is correction factor for the nuclide decay during the waiting time t_W between sampling and measurement, which in some sediment cores used in this study is up to several years:

$$K_W = e^{-\frac{ln(2) \cdot t_W}{T_{1/2}}}. \tag{4.23}$$

Automatic decay correction must be used carefully in cases of nuclides supported by decay of their parent nuclides. An example for such approach is ^{210}Pb, where only excess ^{210}Pb not supported by decay of its parent nuclide ^{226}Ra should be corrected for waiting time decay. Also ^{241}Am must not simply be decay corrected as described by Eq. 4.23, because in many cases in sediment samples ^{241}Am is generated by a decay of its parent nuclide ^{241}Pu, as shown in the

---

[3] Live time is the total counting time lowered by dead time (a sum of time during which the signals of individual decay events is being processed and no other events can be registered during those very short periods).

Fig. 4.4. In these cases it might be considered determining activities in sample to the date of counting and applying decay corrections subsequently in a spreadsheet software.

Another correction factor K_C is applied for the nuclide decay during counting (measurement real time t_R), which is relevant only for isotopes with half-lives in the same order of magnitude or shorter than counting times:

$$K_C = \frac{T_{1/2}}{ln(2) \cdot t_R} \left(1 - e^{-\frac{ln(2) \cdot t_R}{T_{1/2}}}\right). \tag{4.24}$$

Application of this correction is hardly ever the case for sediment chronology purposes, because the shortest lived applicable radionuclide ^{234}Th has a half-life of 24 days and measurement times do not frequently exceed 5 days.

As mentioned earlier, if activity concentration can be deduced from several (N) energy lines (interference-free) of the same isotope, for example in the case of ^{214}Pb or ^{214}Bi, weighted mean of activities expressed from each of the lines are used for the calculation of weighted activity concentration as

$$C_{Ave} = \frac{\sum_{i=1}^{N} \frac{C_i}{\sigma^2(C_i)}}{\sum_{i=1}^{N} \frac{1}{\sigma^2(C_i)}}, \tag{4.25}$$

where $\sigma(C_i)$ is the activity concentration uncertainty.

Furthermore, if one or more of the multiple isotope lines are interfering with lines from other nuclides, the Genie 2000 algorithm (Canberra, 2002a) enables calculation of the average activity by minimizing the quantity

$$\chi^2 = \sum_i \sum_j w_i \cdot (y_i - BR_{ij} x_j)^2, \tag{4.26}$$

where w_i is the reciprocal of the combination of the area uncertainty and the efficiency uncertainty at the i$^{\text{th}}$ observed peak $\frac{1}{\sigma(N_{net}) \cdot \sigma(\epsilon)}$, y_i is the area of the i$^{\text{th}}$ peak divided by its efficiency $\frac{N_{net}}{\epsilon}$, BR_{ij} is the branching ratio of the j$^{\text{th}}$ nuclide that was matched with the i$^{\text{th}}$ peak and x_j is the unknown activity of the j$^{\text{th}}$ nuclide.

Although some authors prefer to use only a single line for an isotope quantification (G. Kirchner, personal communication), using multiple lines of the same radionuclide (or several radionuclides in equilibrium) for activity determination leads to reduction of counting uncertainty. This is discussed in Chapters 6 and 8 on example of direct ^{226}Ra analysis using multiple lines of ^{234}Th, ^{234m}Pa and ^{226}Ra. Similar approach was used for determination of ^{226}Ra via ^{214}Pb and ^{214}Bi using their multiple lines in a project presented in Chapter 10.

4.5.7 True coincidence-summing corrections

True coincidence summing (TCS), sometime also called cascade summing, is an effect resulting from registering of gamma rays (and sometimes accompanying x-rays) emitted nearly simultaneously from the nucleus, i.e. the time in which the emissions follow is shorter than resolving time of the gamma spectrometry system. When this happens, with certain probability a pulse that represents the sum of the two individual energies is recorded. At the same time it results in loss of the count from the full energy peak. It is mainly a problem of radionuclides with complex decay schemes in close and bulk geometries and well detectors (Bronson, 2003).

The correction for TCS was implemented in Genie 2000 in the laboratory by Chehade (2007). In the sediment samples examined during current study gamma emitters were detected which show this effect, namely ^{208}Tl, ^{228}Ac and ^{214}Bi. For these isotopes corrections were performed. In some cases these corrections reached up to 18%. Other isotopes with pronounced cascade summing effects with high importance in environmental studies, although not detected within this work, are for example ^{134}Cs or ^{60}Co.

4.6 Statistics

4.6.1 Counting statistics

In gamma spectrometry, counting statistics play an important role in true value, uncertainty and detection limits determination. Similarly as in other counting measurements, where the results can only be positive integer values, the random deviations can usually be described by the Poisson distribution. Here the probability that a count n will be observed is:

$$P(n) = \frac{N^n e^{-N}}{n!},\ n = 1, 2, \dots \tag{4.27}$$

with N being the expected count number (average). The standard deviation is

$$\sigma = \sqrt{N}. \tag{4.28}$$

For a small number of events Poisson distribution is asymmetric, but for a large number (>100) it can be approximated by Gaussian (normal) distribution (Debertin & Helmer, 1988). For repeated measurements of the same parameter, the probability of measuring a value x is

$$P(x) = \frac{1}{\sigma\sqrt{2\pi}} e^{-\frac{1}{2}(\frac{x-\mu}{\sigma})^2}, \tag{4.29}$$

given an expected value (or mean) μ around which the individual measurements scatter with a standard deviation σ. Probability that a measured value lies within interval ($\mu - \sigma \leq x \leq \mu + \sigma$) is approximately 0.68. For 2σ and 3σ intervals the probabilities are: $P(\mu - 2\sigma \leq x \leq \mu + 2\sigma) \approx 0.95$ and $P(\mu - 3\sigma \leq x \leq \mu + 3\sigma) \approx 0.997$ (Fig. 4.16).

4.6.2 Uncertainty

For expressing uncertainty for a quantity X which is a function of other independent quantities Z_1, Z_2, $\cdots$ Z_n the function $X = f(Z_1, Z_2, \cdots Z_n)$, the so called “error propagation law” is used. For calculation of products and ratios the combined uncertainty is expressed as:

$$\left(\frac{\sigma(X)}{X}\right)^2 = \left(\frac{\sigma(Z_1)}{Z_1}\right)^2 + \left(\frac{\sigma(Z_2)}{Z_2}\right)^2 + \cdots \left(\frac{\sigma(Z_n)}{Z_n}\right)^2. \tag{4.30}$$

Combined uncertainty of activity concentration from Eq. 4.22 is therefore calculated as

$$\sigma(C) = C \cdot \sqrt{\left(\frac{\sigma(N_{net})}{N_{net}}\right)^2 + \left(\frac{\sigma(M)}{M}\right)^2 + \left(\frac{\sigma(\epsilon_E)}{\epsilon_E}\right)^2 + \left(\frac{\sigma(I_\gamma)}{I_\gamma}\right)^2 + \left(\frac{\sigma(K)}{K}\right)^2}, \tag{4.31}$$

where K is composite decay correction factor ($K_W \cdot K_C$). Within sediment chronology applications correction for decay during counting K_C can be neglected and only the correction factor

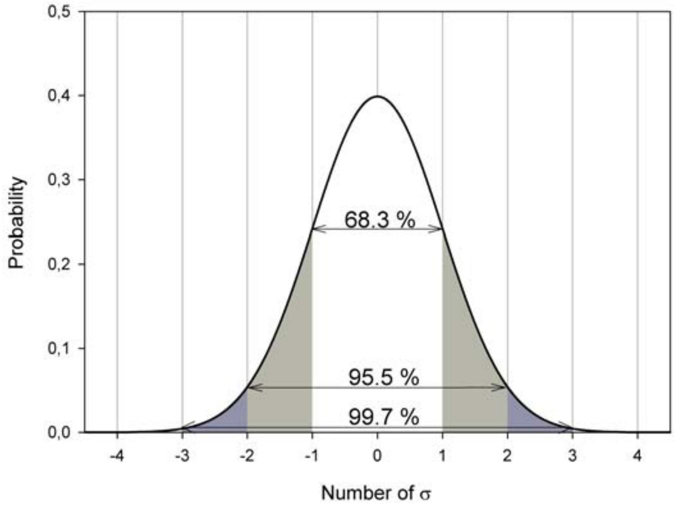

Figure 4.16: *Standard normal (Gaussian) probability density function ($\mu = 0$ and $\sigma = 1$) with 1σ, 2σ and 3σ intervals.*

K_W for decay between sampling and measurement is taken into account (Canberra, 2002a):

$$\sigma(K_W) = \frac{K_W \cdot ln(2) \cdot t_W}{T_{1/2}} \cdot \sigma(T_{1/2}). \tag{4.32}$$

The uncertainty of the weighted average activity concentration from multiple lines (Eq. 4.25) is calculated as

$$\sigma(C_{Ave}) = \sqrt{\frac{1}{\sum_{i=1}^{N} \frac{1}{\sigma^2(C_i)}}}. \tag{4.33}$$

4.6.3 Decision thresholds and detection limits

The limits for qualitative detection and quantitative determination are conceptually and terminologically based on work of Currie (1968). He defined 2 basic levels:

- Critical limit, L_C (also called decision threshold) - the net signal level (instrument response) above which an observed signal may be reliably recognized as “detected” (an “a posteriori” method).
- Detection limit, L_D - the “true” net signal level which may be “a priori” expected to lead to detection.

L_C is used to answer a question: was the detected signal significant?, while L_D: what is the minimum signal that is possible to detect with a given confidence? Therefore, by definition, $L_C < L_D$.

Decision on whether the signal is observed or not is based on hypothesis testing, while two kinds of errors are recognized:

- Error of first kind, α: deciding wrongly that the signal is present when it is not and
- Error of second kind, β: deciding wrongly the signal is not present when it is.

The quantities 1-α and 1-β are confidence levels for not making errors of first and second kind, respectively.

Decision threshold is expressed as

$$L_C = k_\alpha \cdot \sigma(N_{net}), \tag{4.34}$$

where k_α is k-value corresponding to confidence level of normal distribution, for example for k=1.645 there is 5% probability of error of the first kind. $\sigma(N_{net})$ is standard deviation of the observed net signal N_{net} ($N_{net} = N_S - N_0$). When there is no contribution to the signal from the sample ($N_S = 0$), $N_S = N_0$ and Eq. 4.34 can be written as:

$$L_C = k_\alpha \cdot \sqrt{2\sigma(N_0)}. \tag{4.35}$$

Detection limit for equal probabilities of error of first and second type ($\alpha = \beta$ and $k_\alpha = k_\beta = k$) is expressed by the German Nuclear Safety Standards Commission (KTA) norm (KTA, 2007) as

$$L_D = 0.5 \cdot (2 \cdot k)^2 + 2L_C. \tag{4.36}$$

L_C and L_D are expressed in number of counts and can be converted to activity concentration terms (C^* and $C^\#$, respectively) using Eq. 4.22 replacing N_{net} by L_C or L_D, respectively.

Genie 2000 algorithm provides calculation of KTA MDA (minimum detectable activity), which is equivalent to $C^\#$. As a simple approximation, it holds for most of the measurement setups performed within this work, that $C^\# = 2 \cdot C^*$, therefore dividing Genie MDA by factor of 2 enables to express decision threshold at 95% probability.

4.7 Quality control

Quality assurance (QA) measurements have been performed in the gamma spectroscopic laboratory to demonstrate that the equipment used in analysis is operating properly and that the analysis results are correct. QA measurements were performed periodically and were semiautomated using a QA module included in Genie 2000 (S505 Quality Assurance Software).

The QA routines includes the counting of a known radioactive source (^{155}Eu/^{22}Na) in a predetermined geometry for a specific live-time (300 s). After data collection, analysis is made to evaluate whether critical parameters, such as peak position, resolution, and efficiency, are within acceptable limits. The results of test measurements are recorded and plotted against time in the form of control charts with the acceptable ranges marked to show if the measurement value is nearing a limit. The data are further evaluated by statistical testing.

In a similar way, QA modules were used to evaluate individual background spectra for the detectors, which are measured periodically for keeping track of possible contamination.

Chapter 5

Background in gamma spectrometry [1]

5.1 Methods

As a part of the measurement routine in the Laboratory an up-to-date background for each detector is collected approximately once a month. In the individual background spectra, which are usually recorded for 3-4 days, only a limited number of lines is visible, belonging usually to ^{40}K and the strongest lines of gamma emitting progeny of ^{222}Rn. In order to investigate the background of the laboratory's three gamma coaxial HPGe detectors used within this study (whose characteristics are described in Tab. 5.1 in greater detail) the individual spectra were summed up using a method based on the procedure proposed by Bossew (2005) and analyzed by the Genie 2000 software (Pittauerová et al., 2010b; Ulbrich, 2007)[2]. The procedure for summing spectra using Genie 2000 commands is described in Appx. B. In these spectra many additional "exotic" lines, which are not detectable in the individual background spectra, are visible.

The total number of spectra, the time period for which the study was performed, the total summed-up live-time and a mean count rate over all energies of the detected spectra for each of the detectors are listed in the Tab. 5.2.

5.2 Results and discussion

5.2.1 Gamma lines identified in the summed-up spectra

The sources of the common and exotic lines in the background signal were identified in the summed-up spectra and can be divided into following groups:

1. Radon and thoron progeny in the measurement chamber (Tab. A.1 in Appx. A): here gamma-emitting isotopes of ^{214}Pb and ^{214}Bi (^{222}Rn progeny) and ^{212}Pb and ^{208}Tl (^{220}Rn progeny) have been identified.

2. Radionuclides contained in the detector, its accessories and the shielding (Tab. A.2 in Appx. A). Both natural and artificial isotopes have been observed. ^{40}K and members

---

[1] Parts of this section were presented at the 14th expert level meeting on environmental radioactivity surveillance, Freiburg, Germany, March 2009 as D. Pittauerová, S. Ulbrich, B. Hettwig, H.W. Fischer: Long-term background in gamma-spectroscopy.

[2] Data and results presented in this chapter are partially based on work done by Susanne Ulbrich, IUP, University of Bremen (Ulbrich, 2007), who analyzed and evaluated long term background spectra for detectors 5 and 6. Within this work mainly detector 3 was used. The temporary coverage of the background spectra analyses was extended by DP to January 2009 for all 3 detectors and differences between the individual detectors were newly described.

Table 5.1: *Characterization of detectors used for the long background comparison.*

	Det. 3	Det. 5	Det. 6
Description	reverse p-type coaxial Ge detector, Canberra	n-type coaxial Ge detector, Canberra	n-type coaxial Ge detector, Canberra
Size (diameter / length mm)	76 / 60.5	64 / 60	63.5 / 63.5
End- cap	Cu endcap with C epoxy window	Cu endcap with C epoxy window	Cu endcap with C epoxy window
Relative efficiency (%)	51.2	50.8	50.9
FWHM (122 keV / 1332 keV)	0.857 / 1.76	0.931 / 1.87	0.865 / 2.05
Shielding	Pb: 92 mm, Cu: 10 mm, Cd: 1.3 mm, PMMA: 5 mm	Pb: 92 mm, Cu: 10 mm, Cd: 1.3 mm, PMMA: 5 mm	Pb: 100 mm, Cu: 10 mm

Table 5.2: *Summing up data.*

	Det. 3	Det. 5	Det. 6
Number of summed-up spectra	29	43	46
Time period	8/2005-12/2008	8/2004-12/2008	11/2004-12/2008
Total summed-up time (days)	104.5	159.8	171.9
Count rate 20-2040 keV (s^{-1})	1.35	1.28	1.30

of all 3 natural series, namely ^{210}Pb, ^{226}Ra, ^{234}Th and ^{238m}Pa (^{238}U decay chain), ^{228}Ac (^{232}Th decay chain) and gamma lines of ^{235}U, have been identified. Artificial isotopes are represented by ^{137}Cs and ^{60}Co.

3. Short-lived activation products formed by reaction of cosmic radiation induced neutrons with material of the detector itself, its accessories and the shielding (Tab. A.3 in Appx. A). These include isotopes of Ge, Cd, Pb and Cu.

4. Other: annihilation peak 511 keV, x-rays and non-identified lines (Tab. A.4 in Appx. A).

5.2.2 Comparison of summed-up spectra from different detectors

Differential spectra from the 3 detectors (Figs. 5.1–5.3) and the tables of identified lines with numerical values of count rates at individual energies (Tabs. A.2–A.4 in Appx. A) show main differences between the 3 detectors, which are summarized in Tab. 5.3. They reflect detector properties themselves (different efficiencies for different energies), possible differences in the construction material of the detectors and their accessories and mainly differences in construction design of the housing of the detectors. The lowest background contribution to ^{210}Pb peak is at Det. 3. It is therefore the most suitable detector for sediment ^{210}Pb chronology from this point of view.

5.2.3 Time series

The variability of selected peaks in the background spectra is presented in Figs. 5.4 to 5.6. The descriptive statistics of the time series are given in the Tab. 5.4. Here variability is expressed

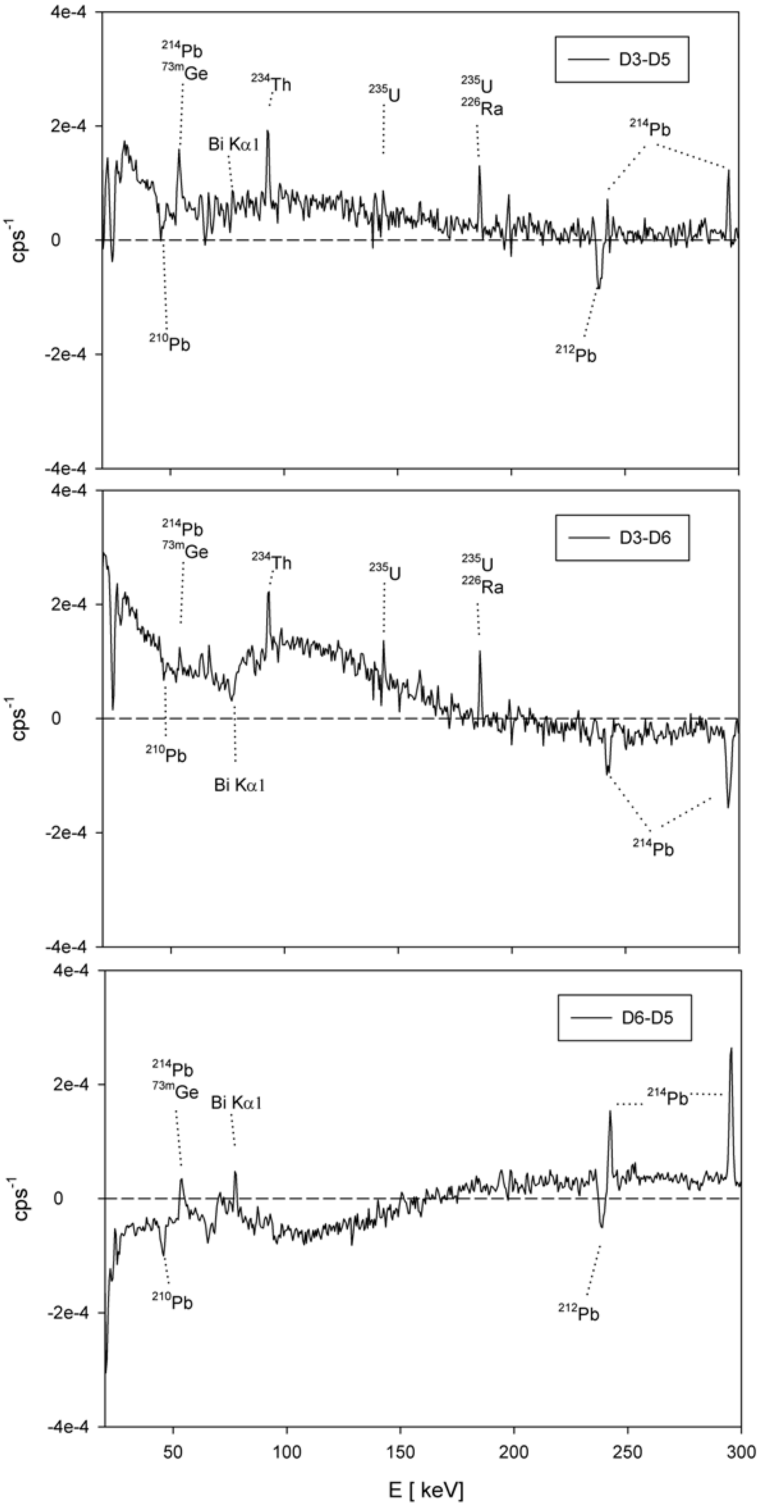

Figure 5.1: *Differential spectra of low energy region (from top to bottom: Det. 3 - Det. 5, Det. 3 - Det. 6, Det. 6 - Det. 5). Differences of the continuum appear as positive or negative deviations from 0 value (marked as a horizontal line), differences between individual gamma-lines appear as positive or negative peaks. Where two isotopes are indicated, it is expected that both of them contribute to the same peak. The same applies for the intermediate and high energy region in the following figures.*

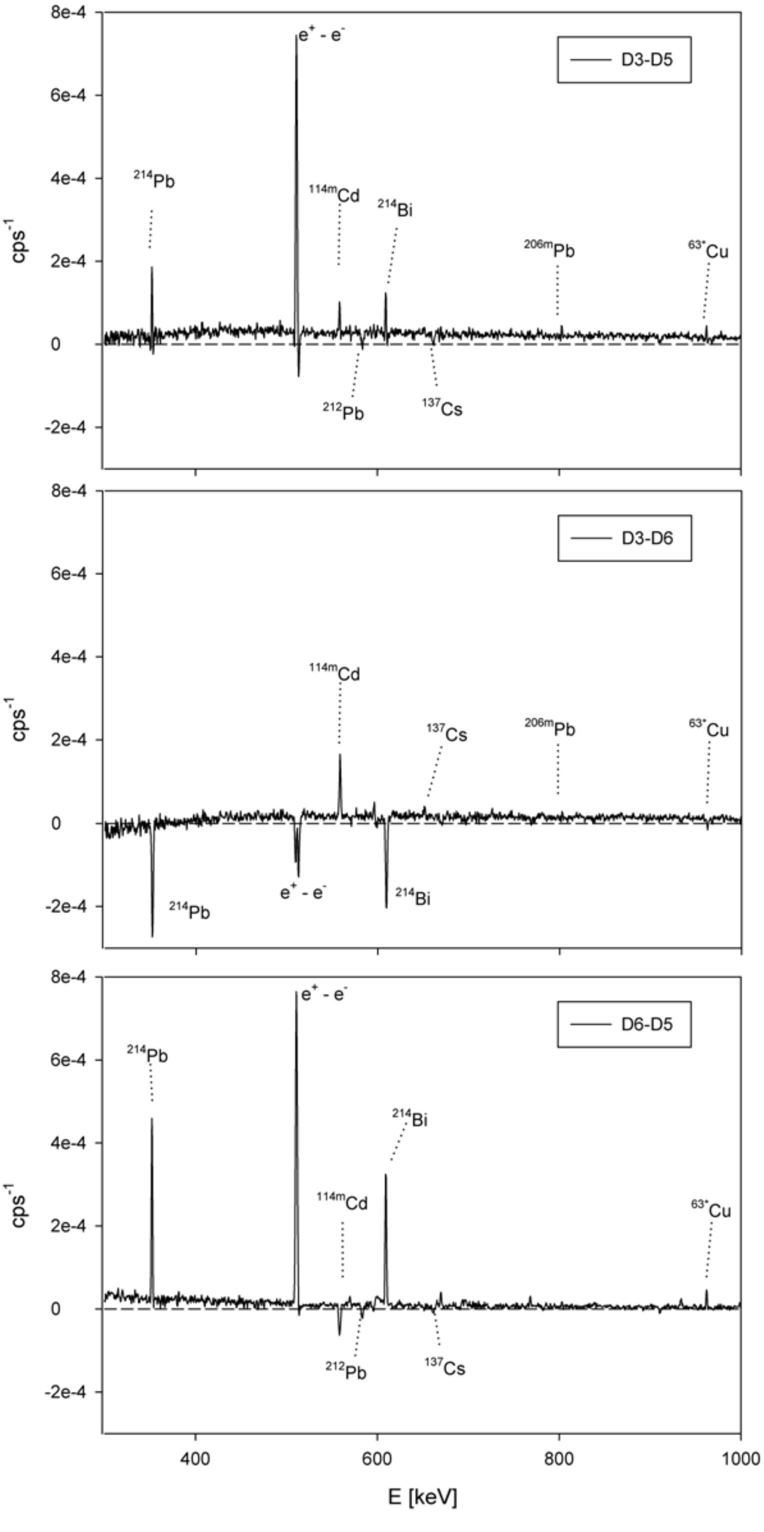

Figure 5.2: *Differential spectra of intermediate energy region (from top to bottom: Det. 3 - Det. 5, Det. 3 - Det. 6, Det. 6 - Det. 5).*

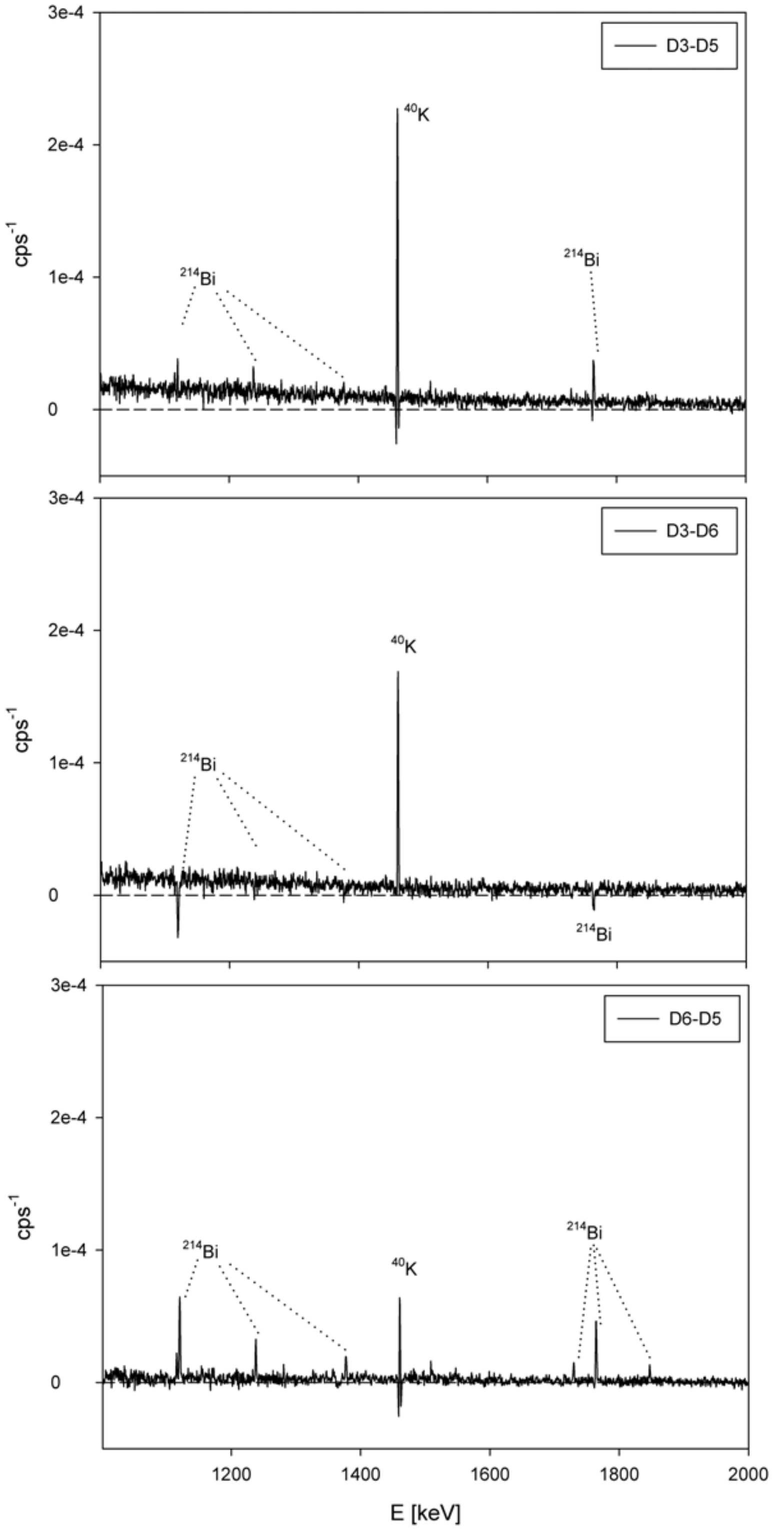

Figure 5.3: *Differential spectra of high energy region (from top to bottom: Det. 3 - Det. 5, Det. 3 - Det. 6, Det. 6 - Det. 5).*

Table 5.3: *Description of the difference of the summed up spectra of 3 detectors with similar characteristics.*

Feature	Difference	Notes
The continuum	20–170 keV: Det. 3 $>$ Det. 5 $>$ Det. 6 170–350 keV: Det. 6 $>$ Det. 3 $\geq$ Det. 5 350–400 keV: Det. 6 $\geq$ Det. 3 $>$ Det. 5 400–1500 keV: Det. 3 $>$ Det. 6 $>$ Det. 5 1500–2000 keV: Det. 3 $>$ Det. 6 $\geq$ Det. 5	Reason: different efficiencies of individual detectors for different energies
Rn daughters (^{214}Pb, ^{214}Bi)	Det. 6 $>>$ Det. 3 $>$ Det. 5	Possible reason: Det. 6 Pb housing has the highest inner volume
^{210}Pb	Det. 5 $>$ Det. 6 $>$ Det. 3	Possible reason: differences in construction material of the detectors (detector holders) or the shieldings.
^{226}Ra, ^{234}Th, ^{238m}Pa, ^{235}U	Det. 3 $>$ Det. 5 $\geq$ Det. 6	
Th series (^{228}Ac)	Det. 5 $>$ Det. 6 $>$ Det. 3	
^{40}K	Det. 3 $>$ Det. 6 $>$ Det. 5	
Artificial isotopes (^{137}Cs, ^{60}Co)	Det. 5 $\geq$ Det. 6 $>$ Det. 3	
x-rays (Pb)	Det. 6 $>$ Det. 3 $>$ Det. 5	Reason: shielding of Det. 6 does not contain Cd and PMMA inner layers
^{114m}Cd	Det. 3 $>$ Det. 5 $>$ Det. 6	Reason: shielding of Det. 6 does not contain Cd inner layer

as the coefficient of variation c_v, defined as

$$c_v = \sigma/\mu, \tag{5.1}$$

where σ is the standard deviation and μ the arithmetical mean.

Table 5.4: *Statistical evaluation of time series (n = number of spectra) of background measurement on individual detectors (for Det. 5 and Det. 6 after January 2006).*

	Detector	n	Minimum $(cps \cdot 10^{-3})$	Maximum $(cps \cdot 10^{-3})$	Arit. mean $(cps \cdot 10^{-3})$	Median $(cps \cdot 10^{-3})$	Std. deviation $(cps \cdot 10^{-3})$	Coef. of variation (%)
^{210}Pb 46.5 keV	Det. 3	29	-0.15	0.75	0.35	0.39	0.21	59
	Det. 5	35	-0.67	1.25	0.53	0.66	0.46	86
	Det. 6	37	-0.10	1.04	0.48	0.45	0.23	48
^{214}Pb 352 keV	Det. 3	29	0.53	2.83	1.24	1.16	0.54	43
	Det. 5	35	0.14	2.10	0.91	0.95	0.40	44
	Det. 6	37	0.24	3.18	1.92	1.82	0.64	33
Annihilation 511 keV	Det. 3	29	19.2	20.9	20.1	20.0	0.5	2.4
	Det. 5	35	15.2	18.8	17.7	17.9	1.0	5.8
	Det. 6	37	18.2	22.7	21.3	21.3	0.8	3.6
^{40}K 1460.8 keV	Det. 3	29	2.33	3.24	2.65	2.64	0.18	6.9
	Det. 5	35	1.71	2.26	1.99	1.96	0.15	7.3
	Det. 6	37	1.22	2.05	2.05	2.07	0.19	9.0
^{137}Cs 662 keV	Det. 3	29	-0.16	0.29	0.05	0.05	0.12	233
	Det. 5	35	-0.12	0.36	0.18	0.18	0.11	63
	Det. 6	37	-0.09	0.37	0.10	0.07	0.12	125
^{214}Bi 1763 keV	Det. 3	29	0.27	0.65	0.42	0.41	0.10	23
	Det. 5	35	0.12	0.55	0.31	0.31	0.09	27
	Det. 6	37	0.12	0.71	0.43	0.42	0.12	28

Variability is high mainly for the Rn progeny. In the Fig. 5.4 it is shown on example of ^{214}Pb (estimated via 352 keV gamma line). In the early part of the time period under consideration a household foil was used to protect the detector endcaps from external contamination, but proved to be inappropriate due to increasing the Rn progeny background caused probably by their electrostatic attachment onto the foil surface. The foil was no longer used from January 2006 on. After this intervention the variability in the Rn progeny background values decreased, as well as the absolute values. For reasons of comparability with newer Det. 3, statistical evaluation (Tab. 5.4) is presented only for values collected after January 2006 (for Det. 5 and Det. 6).

Also ^{210}Pb and ^{137}Cs (Fig. 5.6) show rather high variability. This could be explained by very high experimental uncertainties due to low count rates, often exceeding the actual values. By contrast, count rates of ^{40}K (Fig. 5.5) and annihilation peak 511 keV fluctuate little in time.

5.3 Conclusions

The presented results of the long-term background spectra study of three of the Laboratory's gamma detectors showed that sources of lines in long-term background spectra are radon and thoron (and their daughter products) in the measurement chamber, natural and artificial radionuclides contained in the detector, its accessories and the shielding, short-lived activation products formed by reaction of cosmic radiation induced neutrons with material of the detec-

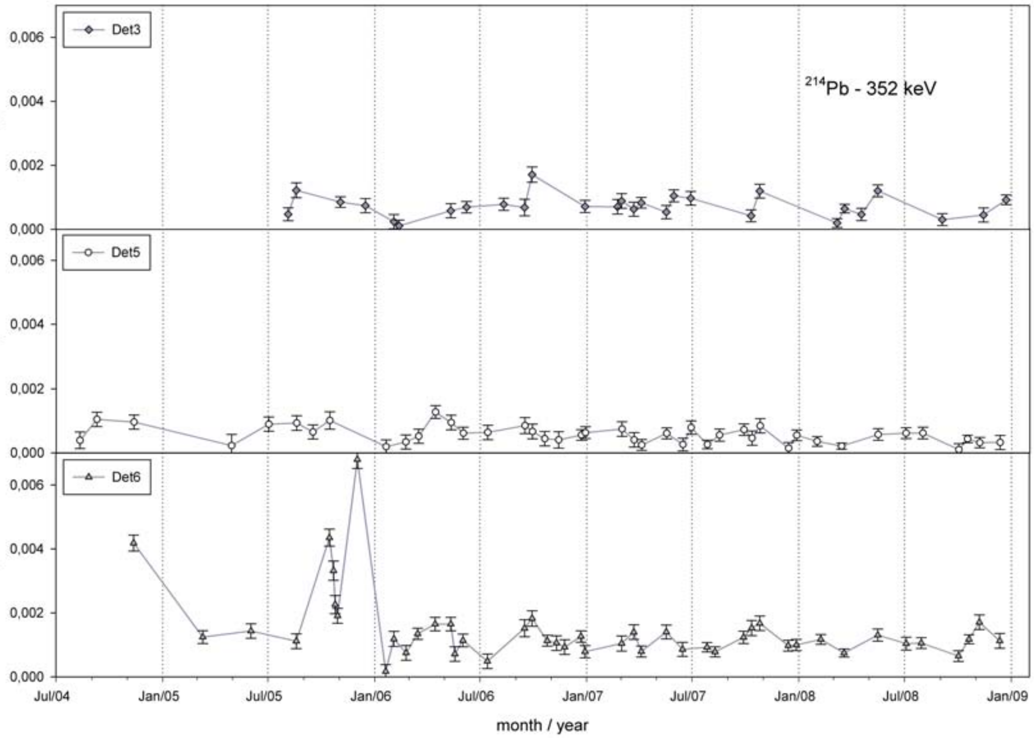

Figure 5.4: *Time series of net count rates observed in* ^{214}Pb *(352 keV) peak.*

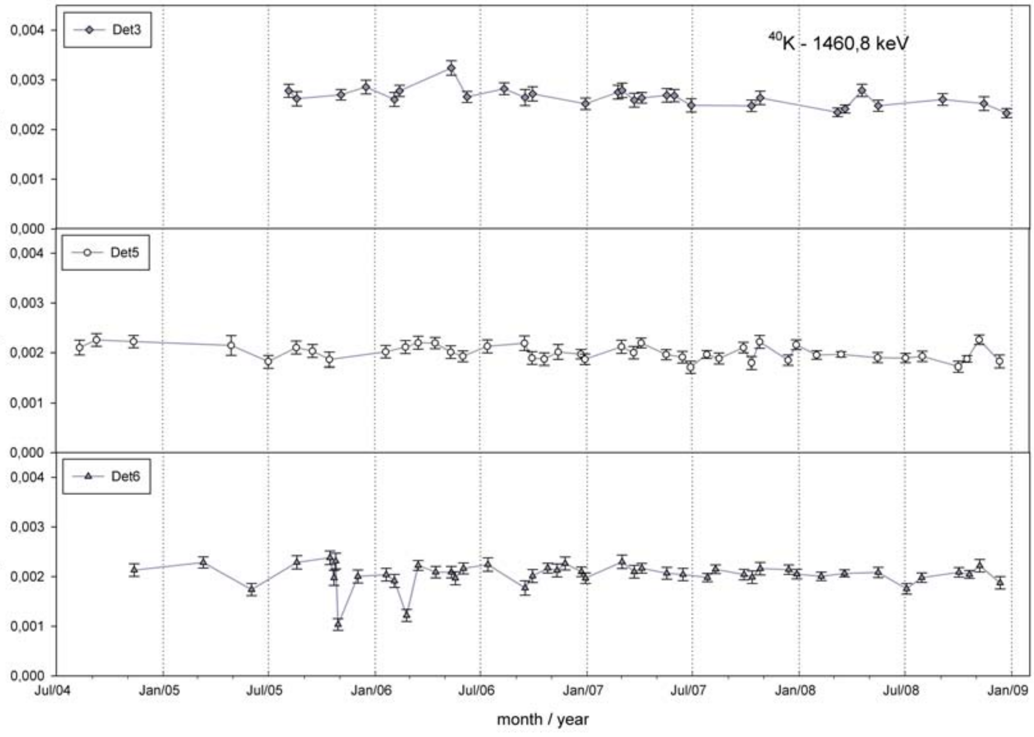

Figure 5.5: *Time series of net count rates observed in* ^{40}K *(1460.8 keV) peak.*

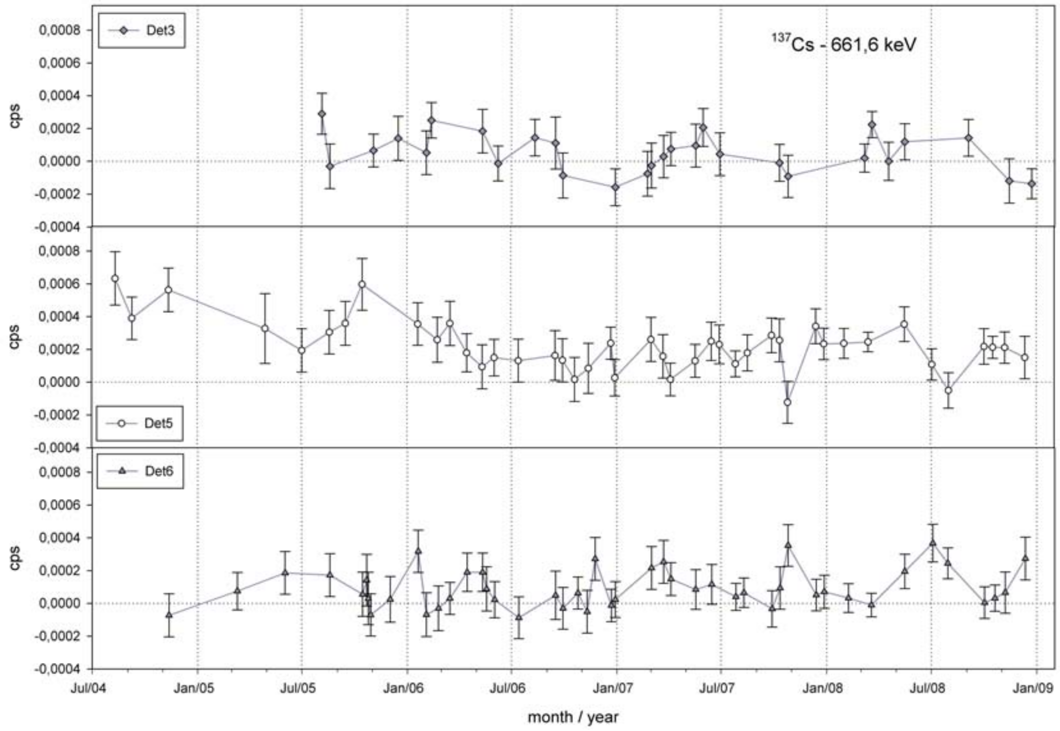

Figure 5.6: *Time series of net count rates observed in ^{137}Cs (661,6 keV) peak.*

tor itself, its accessories and the shielding, annihilation radiation and X-rays. 8 lines remained unidentified. Differences in backgrounds of individual detectors were described and the variability of some prominent lines was investigated.

While currently individual background spectra are used in the Laboratory for background subtraction (Sec. 4.5.4), the use of a long-term background might be an attractive alternative due to reduced uncertainties at individual background peaks over a longer measurement period. This would increase the total number of background lines significantly, because in individual background spectra only several most prominent lines can be identified. Regular new long-term background file creation however is an additional (and relative time consuming task) which would have to be accommodated in the Laboratory's routines.

Chapter 6

Gamma emitters in sediments

Sediments contain gamma emitting radionuclides of different origins. The most prominent are members of ^{238}U and ^{232}Th decay series, as well as another primordial isotope ^{40}K. These isotopes have been present in the Earth's crust since the planet creation and due to their very long half-lives have not decayed completely since. Another natural gamma emitter found in sediments, ^{7}Be, is of cosmogenic origin, produced by cosmic-ray spallation of oxygen and nitrogen.

Additional gamma emitters are of artificial origin, being produced by nuclear fission or activation. In this chapter their detection will be described. In Fig. 6.1 a typical gamma spectrum of a sediment sample is shown.

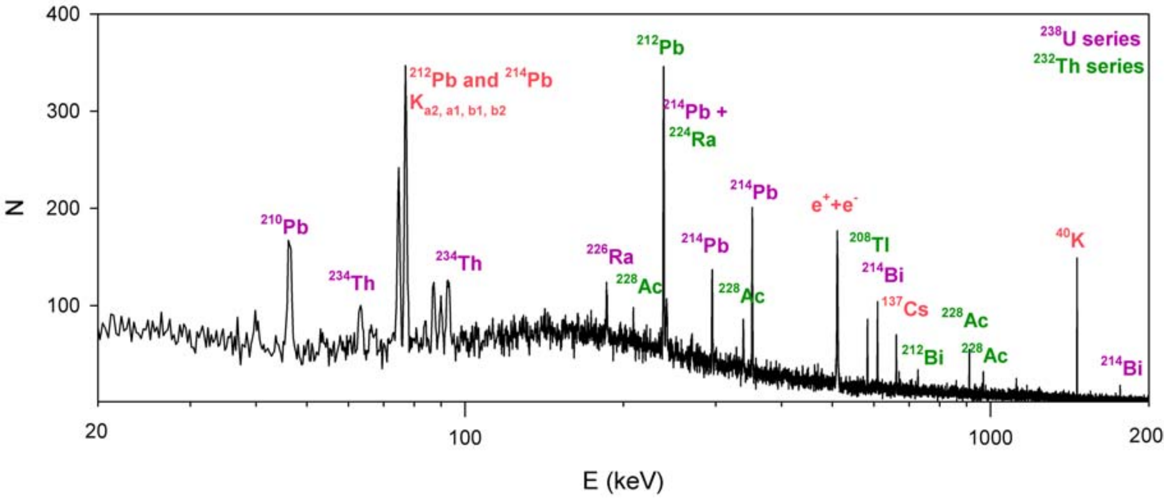

Figure 6.1: *A gamma spectrum (# 3787) of a sediment sample from site HHN3 in the Gulf of Eilat showing the most prominent gamma lines. The sample's mass was 5.7 g and counting life-time 24 hours.*

A list of gamma lines suitable for detection of radionuclides for sediment chronology is presented in Tab. 6.1.

When analyzing spectra of natural radionuclides it is recommended to avoid using peaks with possible interferences (overlaps) or to apply appropriate corrections (Schkade et al., 2000) for them. Also cascades summing corrections (CSC) (Sec. 4.5.7) are of major significance for radionuclides with complex decay schemes.

Table 6.1: *Gamma lines (listed in the order of appearance in this chapter) suitable for detection of radionuclides useful for recent chronologies, data of gamma energies E_γ and emission probabilities I_γ taken from DDEP (Bé et al., 2011) and in case of ^{134}Cs from NNDC (2011). CSC = cascade summing correction needed.*

Nuclide	measured via	E_γ keV	I_γ %	Interferences (E_γ;I_γ) keV; %	Notes
^{210}Pb		46.5	4.25(4)		
^{226}Ra		186.21	3.555(19)	^{235}U (185.7; 57.1)	
	^{214}Pb	242.0	7.268(22)	^{224}Ra (241.0; 4.12)	
		295.2	18.414(36)		
		351.9	35.60(7)	^{211}Bi (351.01; 13.00)	
	^{214}Bi	609.3	45.49(19)		CSC
		1120.3	14.91(3)		CSC
		1764.5	15.31(5)		
^{238}U	^{234}Th	63.3	3.75(8)	^{232}Th(63.8; 0.26)	
		92.4	2.18(19)	^{232}Th $K_{\alpha 1}$ (93.35; 5.6)	
		92.8	2.15(19)		
	^{234m}Pa	766.4	0.323(4)		
		1001.0	0.847(8)		
^{228}Ra	^{228}Ac	209.2	3.97(13)		
		338.3	11.4(4)	^{223}Ra (338.3; 2.85)	
		911.2	26.2(8)		CSC
		969.0	15.9(5)		CSC
		1588.2	3.06(12)		
^{228}Th	^{224}Ra	241.0	4.12(4)	^{214}Pb (242.0; 7.27)	
	^{212}Pb	238.6	43.6(3)		
		300.1	3.18(13)	^{227}Th (300.0; 2.16), ^{231}Pa (300.1; 2.41)	
	^{212}Bi	727.3	6.67(9)		CSC
	^{208}Tl	277.4	6.6(3)		CSC
		583.2	85.0(3)	^{228}Ac (583.4; 0.111)	CSC
		860.6	12.5(1)		CSC
		2614.5	99.79(1)		out of range
^{235}U		143.8	10.94(6)	^{223}Ra (144.3; 3.36)	
		185.7	57.1(3)	^{226}Ra (186.2; 3.555)	
^{40}K		1460.8	10.55(11)		
^{7}Be		477.6	10.44(4)		
^{137}Cs		661.7	85.10(20)		
^{134}Cs		604.7	97.62(11)		CSC
		795.9	85.46(6)	^{228}Ac (794.9; 4.31)	CSC
^{241}Am		26.3	2.31(8)		
		59.5	35.92(17)		

6.1 Uranium-238 series

In the majority of sediment gamma spectra, following members of ^{238}U series can be detected: ^{234}Th, ^{234m}Pa, ^{226}Ra, as well as short lived Rn progeny (^{214}Pb and ^{214}Bi) and ^{210}Pb. These are marked in the decay chain scheme (Fig. 6.2).

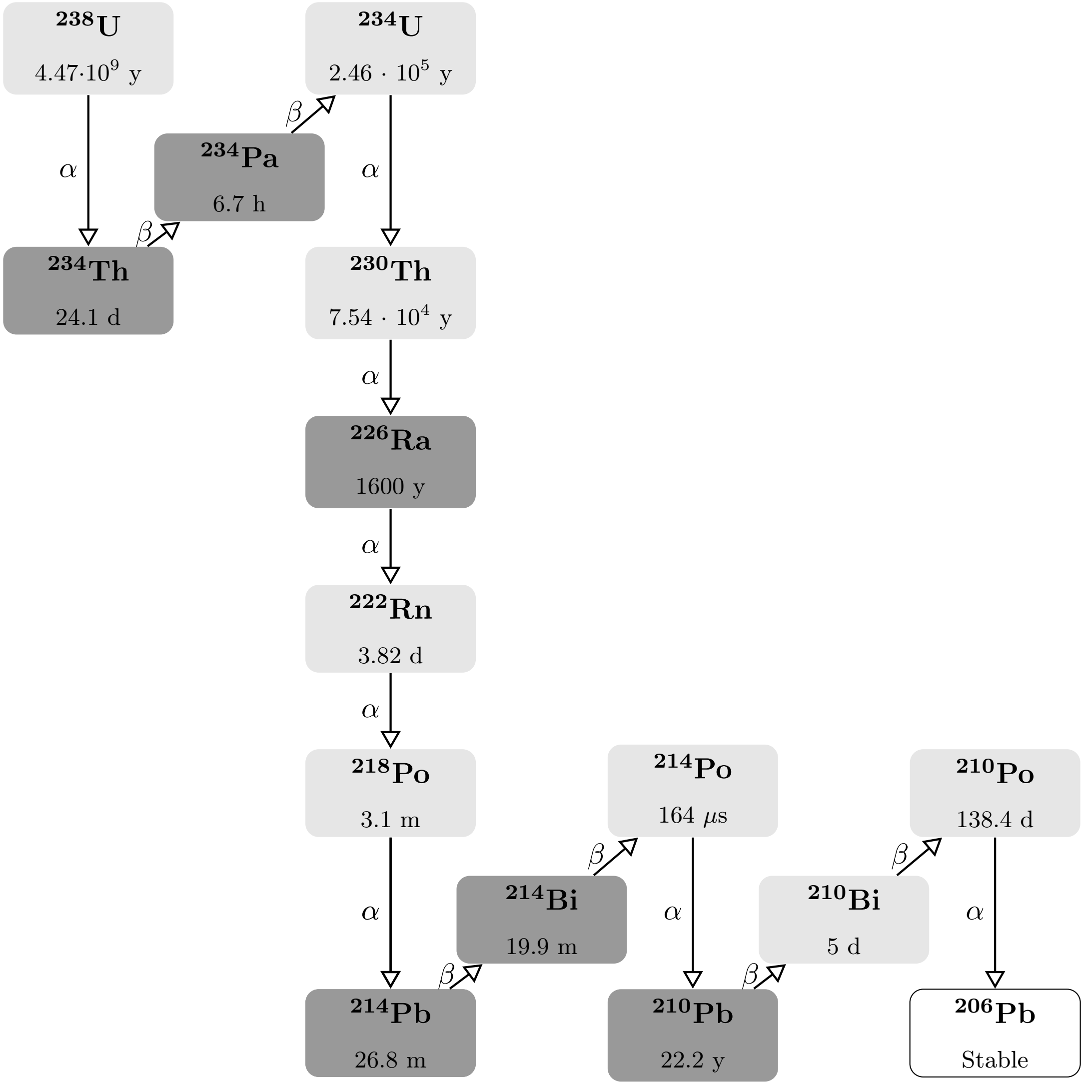

Figure 6.2: *Decay chain of ^{238}U - for simplification, only the major branches (> 99.9% probability) are displayed. In dark grey gamma emitters observed in sediment spectra are highlighted. Decay data were taken from NNDC (2011).*

6.1.1 Lead-210

^{210}Pb is the key gamma emitting radioisotope for recent chronologies. There are multiple possibilities for detecting ^{210}Pb in sediments either directly or by one of its daughter products:

$$\underset{\text{(22 yr)}}{^{210}Pb} \xrightarrow{\beta^-\text{: 16 and 63 keV, }\gamma\text{: 46.5 keV}} \underset{\text{(5 days)}}{^{210}Bi} \xrightarrow{\beta^-\text{: 1.2 MeV}} \underset{\text{(138 days)}}{^{210}Po} \xrightarrow{\alpha\text{: 5.3 MeV}} \underset{\text{(stable)}}{^{208}Pb}$$

Gamma spectrometry can be applied for direct determination of ^{210}Pb via its 46.5 keV line (emission probability $I_\gamma = 4.25\%$), beta counting after chemical separation using daughter product ^{210}Bi or alpha spectrometry of grand-daughter ^{210}Po. A comparison of these three techniques was performed by Moser (1993) and Ebaid & Khater (2006). The main differences are summed up in Tab. 6.2.

Table 6.2: *Comparison of methods for ^{210}Pb analysis in sediments (Ebaid & Khater, 2006)*

	Gamma spectrometry	Beta counting	Alpha spectrometry
Sample size (g)	100	5	1-3
Counting time (s)	60000	60000	60000
Background (cpm)	0.5	0.5	0.005
Counting efficiency (%)	7	40	20
MDA (mBq)	440	7.1	1
Duration of complete analysis	1 day	>10 days	3-6 months*
Emission probability	low	high	high

*3 days, in the case of ^{210}Pb-^{210}Po secular equilibrium existence

Advantages and disadvantages of ^{210}Pb analysis in sediments by the two more common techniques, gamma and alpha spectrometry, for chronological purposes were also evaluated by Zaborska et al. (2007). From the point of view of gamma spectrometry, which is the prevailing technique in the author's Laboratory, they can be summarized as following:

Advantages of gamma spectrometry

- Possibility of a non-destructive sample preparation.
- Relatively uncomplicated sample preparation - in most cases a simple homogenization is sufficient. Alpha spectrometry, on the contrary, requires radiochemical extraction (Zaborska et al., 2007).
- Simultaneous detection of multiple radionuclides within a single spectrum. This is mainly important for supported ^{210}Pb determination via ^{226}Ra and the most common additional tracer ^{137}Cs.
- No need for internal tracer. In alpha spectrometry ^{209}Po it is used for the total efficiency determination. An additional difficulty is the high uncertainty of its half-life value (Collé et al., 2007).
- Efficiency is only dependent on physical parameters.

Disadvantages of gamma spectrometry

- Significantly higher amounts of sample are needed compared to alpha spectrometry.
- High background: low-energy peaks are located at the top of Compton continuum (Sec. 4.4) as opposed to alpha spectrometry with virtually no background to be subtracted.
- In case of general purpose detectors, often also a ^{210}Pb peak is present in background spectra - this is not the case with the specialized low level detector (Det. 3, described in Tab. 5.1) used for sediment chronology in the Laboratory.
- The counting efficiency depends not only on geometry of the sample and energy of emitting gamma rays, but also elemental composition and density of the sample, in which the radiation is attenuated (Chap. 7).

- Acquisition and operating costs of an gamma spectrometry setup are higher than for alpha spectrometry.

6.1.2 Radium-226

For ^{226}Ra which has been used frequently as a proxy of supported ^{210}Pb, analytical options were suggested by Moser (1993). The most simple method, which is sometimes used in combination with alpha spectroscopic determination of ^{210}Pb, is to use the lowest constant activity of a sediment profile (samples with an age older than 100 years). This method assumes a constant activity of ^{226}Ra over the entire sediment profile, which is not always the case. It is also possible to measure Ra by alpha counting after radiochemical separation (Moser, 1993). Another option is detection of ^{226}Ra by ^{222}Rn emanation in a scintillation cocktail, which eliminates the need to perform any further purification, and counting with an ultra low background liquid scintillation system (Sanchez-Cabeza et al., 2010).

Gamma spectrometry using daughter products of ^{222}Rn, namely short lived ^{214}Pb and ^{214}Bi, is a widely used method for ^{226}Ra determination. The prominent gamma lines are listed in Tab. 6.1. Here the main issue is that we have to deal with difficulties related to ^{222}Rn diffusion and recoil emanations from the sample, leading to possible systematic underestimation of ^{226}Ra concentration (Schkade et al., 2007).

In the study of Stoulos et al. (2004) Rn gas leaking from the sample container was resolved by adding active charcoal to the sample. However, this would change properties of the samples, which contradicts one major advantage of gamma spectrometry for sediment chronology being a non-destructive method. A possible solution is using Rn proof steel containers (Stoulos et al., 2004), which leads to a decline in sensitivity of low energy ^{210}Pb gamma radiation detection. A common practice in many gamma spectrometric laboratories is sealing samples using gas-tight foil (often without more detailed specification) and waiting for 3 weeks to allow ingrowth of daughter products.

^{226}Ra can also be directly estimated by its weak gamma line at 186.2 keV ($I_\gamma = 3.6\%$), but interference with the most prominent line of ^{235}U at 185.7 keV ($I_\gamma = 57.1\%$) must be accounted for. The count rate of combined peak at 186 keV consists of contributions of both isotopes:

$$n(186\text{ keV}) = n(^{235}U,\ 185.7\text{ keV}) + n(^{226}Ra,\ 186.2\text{ keV}). \tag{6.1}$$

The contribution of ^{235}U in the 186 keV peak can be determined using another less intensive ^{235}U line at 143.8 keV (Justo et al., 2006), if detectable, as:

$$n(^{235}U,\ 185.7\text{ keV}) = \frac{n(^{235}U,\ 143.8\text{ keV}) \cdot \epsilon_{185.7\text{ keV}} \cdot I_{185.7\text{ keV}}}{\epsilon_{143.8\text{ keV}} \cdot I_{143.8\text{ keV}}}, \tag{6.2}$$

where ϵ_γ stands for FEP efficiencies for individual gamma energies (different for each sample type and geometry) and I_γ for emission probabilities (51.7% for 185.7 keV line and 10.94% for 143.8 keV line, see Tab. 6.1).

Another method for correction of the ^{235}U and ^{226}Ra interference using the 63.3 keV line of ^{234}Th as a proxy for ^{238}U was proposed by Dowdall et al. (2004) (Tab. 6.1). In this case a constant natural activity ratio for ^{238}U/^{235}U=21.7 is assumed.

The methods of gamma spectrometric determination were studied more detailed within this work and are presented in Chapter 8.

6.1.3 Other gamma emitters

Other ^{238}U series radionuclides frequently detectable in sediments are ^{234}Th and ^{234m}Pa (Tab 6.1). Both reach radioactive equilibrium with ^{238}U approximately half a year after sampling, in case they were not in equilibrium originally. Therefore they can be used as ^{238}U proxies. When using the 92.6 keV doublet of ^{234}Th, precautions must be taken due to its potential interference with $K_{\alpha 1}$ line from ^{232}Th (Dowdall et al., 2004), as well as self-absorption of low level gamma radiation in case of all lines. ^{234m}Pa has no interferences, but the emission probability is too low to be sufficient for the quantitative determination in most sediment samples.

6.2 Thorium-232 series

In gamma spectra of sediment samples the following five members of ^{232}Th decay chain can be detected: ^{228}Ac, ^{224}Ra, ^{212}Pb, ^{212}Bi and ^{208}Tl (Fig. 6.3). They are short lived isotopes and can serve as proxies for their parent nuclides ^{228}Ra (^{228}Ac) and ^{228}Th (^{224}Ra, ^{212}Pb, ^{212}Bi and ^{208}Tl).

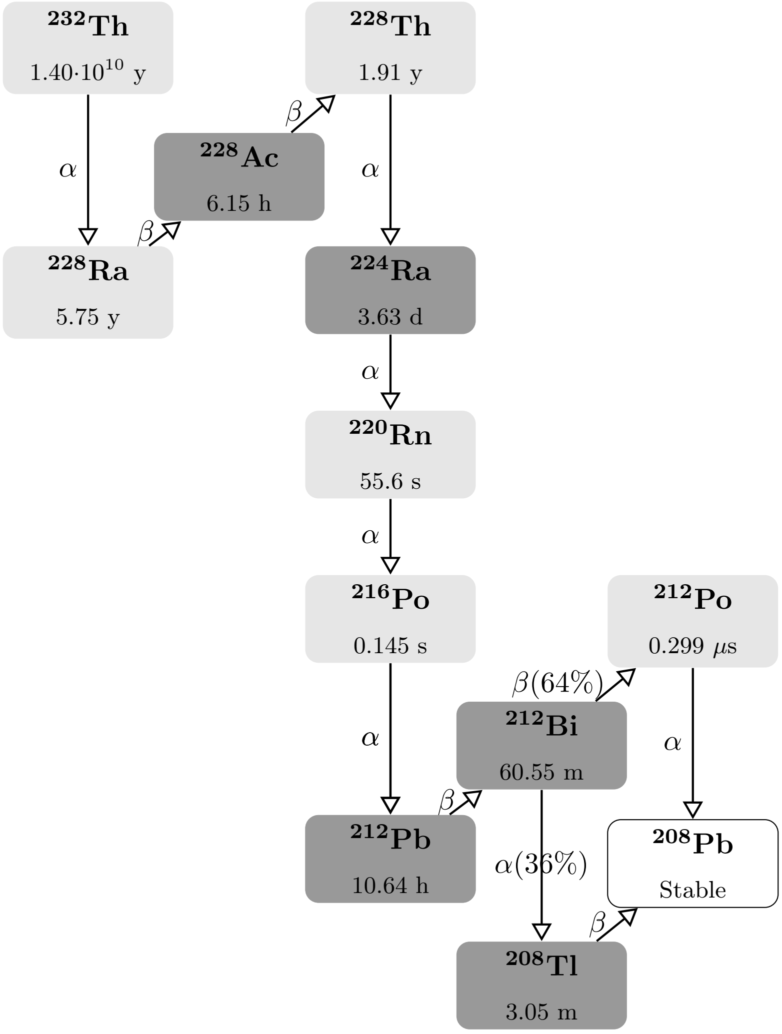

Figure 6.3: *Decay chain of ^{232}Th. In dark grey gamma emitters observed in sediment spectra are highlighted. Decay data were taken from NNDC (2011).*

^{228}Ra can be detected via ^{228}Ac, which with its half-life of 6.7 hours is virtually in radioactive equilibrium with its predecessor (Tab. 6.1). The two most intensive lines at 911.2 and 969.0 keV are suitable after applying CSC.

^{228}Th has multiple short-lived progeny, which in equilibrium can be used for its determination. In practice, the 238.6 keV line of ^{212}Pb and the 583.2 keV line of ^{208}Tl are most suitable. Another option would be 2614.5 keV of ^{208}Tl, but is often out of the range of the traditional gamma spectrometric systems (20-2000 keV). It is more often used by NaI(Tl) detector based systems with limited energy resolution due to its relatively distinct position among the commonly detected environmental isotopes. When using ^{208}Tl lines for ^{228}Th activity determination, the ^{208}Tl activity must be divided by a factor of 0.36, which is the probability of ^{212}Bi decaying by alpha decay to ^{208}Tl.

6.3 Potassium-40

^{40}K is the least abundant of the three naturally occurring potassium isotopes: ^{39}K (93.3%), ^{41}K (6.7%) and ^{40}K (0.0117%). It decays by two distinct modes (β^- decay and electron capture) into the stable isotopes ^{40}Ca and ^{40}Ar. The latter decay is accompanied by gamma emission of 1460.8 keV (decay scheme in Fig. 6.4), which is easily detectable in most environmental media. Knowing ^{40}K activity in a sample, potassium element mass concentration can be calculated applying ^{40}K's specific activity of 31.3 Bq/g K.

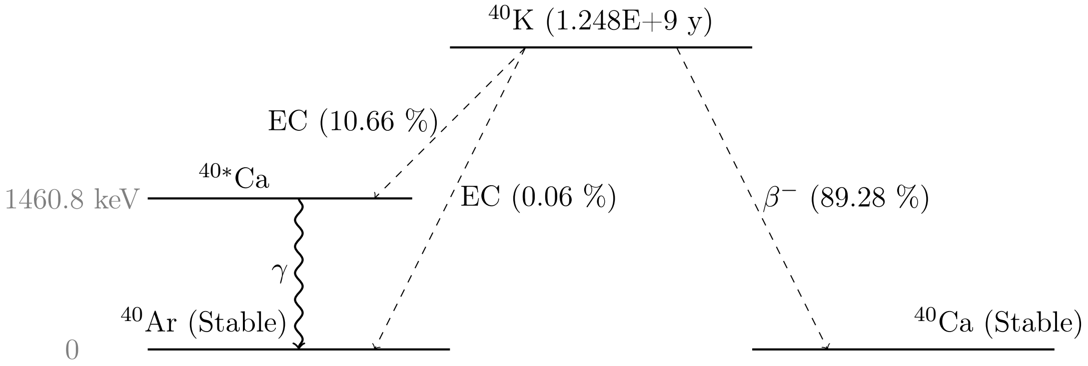

Figure 6.4: *A decay scheme of β^- and EC decay of ^{40}K. Data from: NNDC (2011).*

6.4 Beryllium-7

Cosmogenic ^{7}Be (half-life 53.2 days) can sometimes be observed in fresh sediment samples. For its determination a single gamma line at 477.6 keV (10.44%) is used.

6.5 Artificial isotopes

The most common gamma emitting fission product applied for recent chronologies is ^{137}Cs half-life 30.1 years (Sec. 2.1.3). It is detected by gamma spectrometry via the 661.7 keV gamma line of its daughter nuclide, a metastable nuclear isomer of $^{137\text{m}}$Ba (decay scheme is shown in Fig. 4.6). Quantifying the shorter-lived caesium isotope ^{134}Cs with a half-life of 2.0652(4) yr (NNDC, 2011) in fresh sediments requires applying CSC for both gamma lines: 604.7 and 795.9

keV. The later mentioned can additionally interfere with one of the weaker ^{228}Ac lines (Tab. 6.1).

^{241}Am is another isotope used as an additional chronometer (Sec. 2.1.3). Its detection is possible using its 59.5 keV line (35.9%). Due to relatively low gamma energy similar care must be taken as for ^{210}Pb regarding self-absorption of gamma radiation in the sample itself.

Chapter 7

Efficiency calibration[1]

7.1 Experimental efficiency calibration

The traditional approach for full energy peak (FEP) efficiency determination involves measurement of test sources and calculating efficiencies for given geometry and energy as

$$\epsilon_E = \frac{N_{net}}{t_L \cdot A \cdot I_\gamma}, \tag{7.1}$$

where N_{net} is FEP net count, t_L is counting live time, A is source activity and I_γ probability of emmision of the particular gamma line. Experimental efficiency curves for each detector in the Laboratory had been constructed for "standard geometries". These include for liquid samples Marinelli beakers of several sizes and plastic bottles filled into defined heights (density 1 $g \cdot cm^{-3}$) and for solid samples (soil) pressed pellets, Marinelli beakers (different sizes and density 1.5 and 2.0 $g \cdot cm^{-3}$) and a standard filter geometry. Efficiencies for these geometries had been measured using calibrated solution (or a solid calibration source prepared using calibrated solution mixed with a solid matrix) of gamma emitters mixture over a wide range of energies.

7.2 Density and elemental composition effects

For a single detector, the efficiency does not only vary with geometry, but also with physical and chemical properties of the sample. Variations in sample density and elemental composition play an important role for the efficiency mainly at lower energies (< 100 keV).

As for density correction of samples with density different from that of ”standard geometries” (i.e. water, soil, . . .) it is possible to distribute the sample material in a larger volume of inactive material (for example wax powder proved suitable for this purpose) and preparing pressed pellets of densities close to standards (Kirchner & Ehlers, 1998). This is a good approach mainly for materials with higher activities, when dilution does not play an important role. However, it is a destructive method and does not correct for the effect of chemical composition.

To show the effects of density and composition on detection efficiency the FEP efficiencies were modelled using Monte Carlo (MC) based LabSOCS for a “characterized” detector 3 (see Section 7.4) for some realistic materials that can be encountered in environmental samples. The geometry used for this example (Fig. 7.1) is a plastic cylindrical dish (described as “Large dish”

---

[1] Parts of this chapter were presented in the form of a presentation at the 2^{nd} NKS-B Workshop on Radioanalytical Chemistry, Risø, 2.–6.9.2013 as D. Pittauerová, B. Hettwig and H.W. Fischer: Mathematical efficiency calibration in gamma spectrometry for analysis of natural and fallout radionuclides in sediments.

in Tab. 7.3) with a diameter of 69.2 mm and a height of 22 mm filled with different samples: air, water, paraffin (with modelled efficiency close to water), sand (SiO_2), calcium carbonate ($CaCO_3$) and barite ($BaSO_4$). The presence of a heavier element (Ca, but mainly Ba) has a strong effect especially on lower gamma energy attenuation. Another efficiency plot shows a "real sediment", represented by deep sea sediment of terrigenous origin taken at GeoB site 10065-7 in Lombok basin off Sumba, Indonesia (Chap. 10). The last plot was added to show the effect of a different geometry: the same sediment material filled in a "small dish" with a diameter of 35 mm and a height of 13 mm.

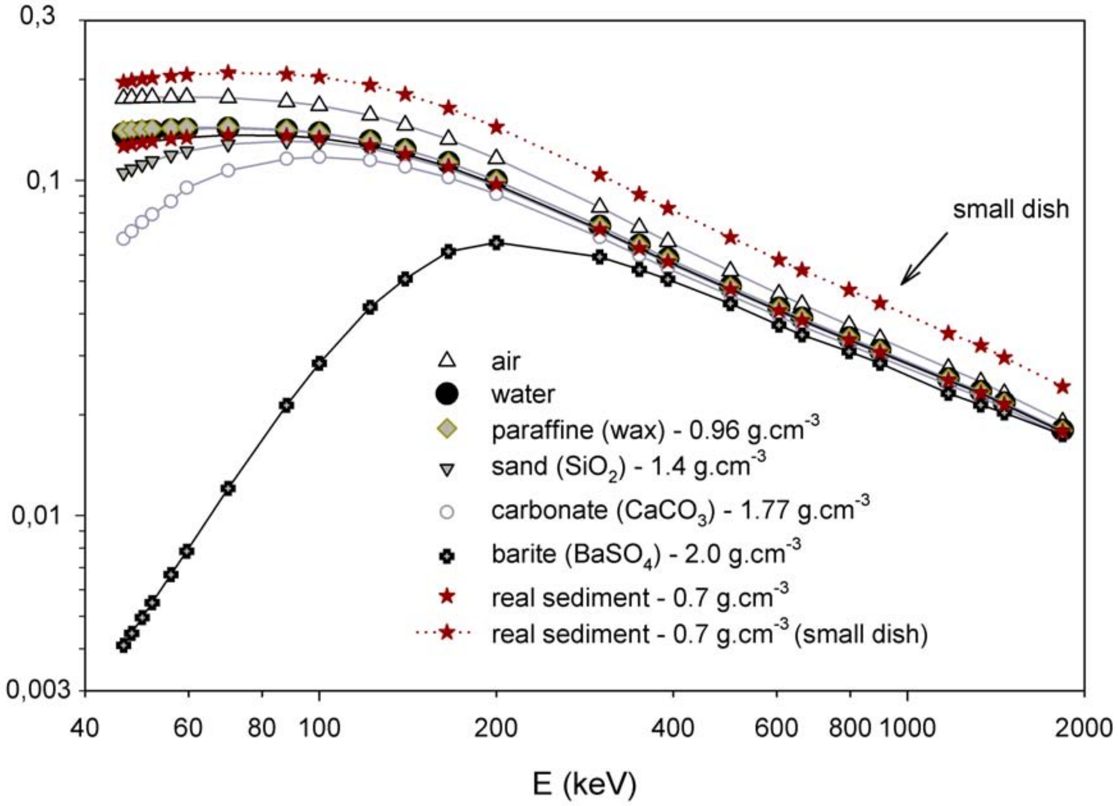

Figure 7.1: *Modelled efficiencies of samples of realistic materials for energies E (log-log scale) for cylindrical "large dishes" filled with materials according to Tab. 7.5 and a "real sediment" (see text). The last plot (the highest efficiency) is for the same "real sediment" in a "small dish" geometry.*

Empirical methods had been proposed on how to deal with self-attenuation of emitted low-energy gamma radiation in voluminous bulk samples. The most frequently used one has the advantage of providing self attenuation correction for samples of unknown density and composition. It involves transmission of the sample in cylindrical geometry using a point source of the energy of the radionuclide in question (Cutshall et al., 1983) and comparing the transmission to a standard sample of water of the same geometry. This approach had been used for quantification of radionuclides like ^{210}Pb (E_γ=46.5 keV, I_γ=4.25%) or ^{241}Am with similarly low gamma energy.

7.3 Mathematical efficiency calibration

Mathematical efficiency calibration includes several possible approaches (Vidmar et al., 2010). One is using general purpose MC codes, other specialized softwares, most of which work as standalone applications and are not parts of gamma spectrometry packages. Some of the specialized software use full MC, while others rely on "efficiency transfer" (transfer of the efficiency of a standard to another sample, which varies from the standard sample in size, density and/or geometry). Both MC and efficiency transfer approaches require precise information about the detector, as well as sample composition and geometry.

The approach combining both experimental measurements and mathematical MC simulations was proposed by other authors (García-Talavera & Peña, 2004; Hurtado et al., 2007). A modification of the method described in Hurtado et al. (2007), combining both experimental measurements and mathematical MC simulations was used in one project within this thesis (Chap. 9). The corrected efficiency is calculated for every energy using

$$\epsilon(x, a) = \epsilon_0(x) \cdot K(a), \tag{7.2}$$

where ϵ_0 is an efficiency calculated using MC simulation of an empty Petri dish for different sample heights x, and K is the self-absorption correction factor, a function of linear attenuation coefficient a. ϵ_0 is fitted using a second order polynomial function of sample height. In this study the ϵ_0 was generated by LabSOCS (Sec. 7.4) for three energies (46.5 keV, 352 keV and 622 keV) for LabSOCS characterized Detector 3 (presented in Fig. 7.2).

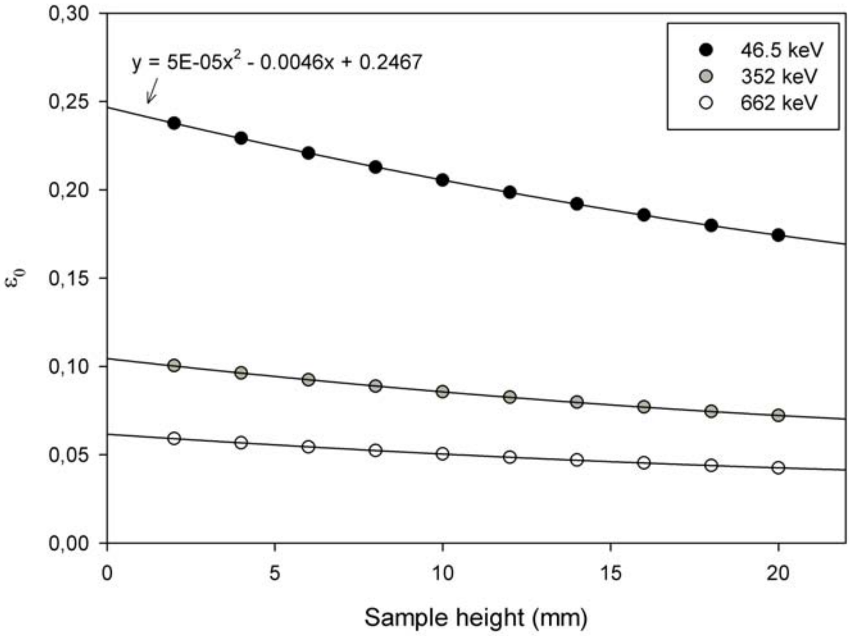

Figure 7.2: *Efficiency ϵ_0 of an empty Petri dish for different sample heights modelled by LabSOCS for Detector 3.*

Corrections were only applied for the lowest energy (46.5 keV) based on a transmission experiment with a ^{210}Pb point source placed on top of the measurement container (for higher less sensitive energies LabSOCS efficiencies were used). The factor K was obtained for each sample individually as

$$K = \frac{1 - e^{a \cdot x}}{a \cdot x}, \tag{7.3}$$

where μ is the linear attenuation coefficient (cm^{-1}) for a given energy and x sample thickness.

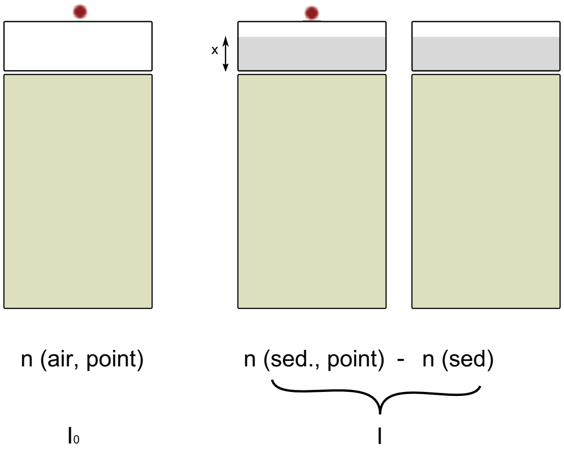

Figure 7.3: *A drawing of the transmission measurement geometries (a modified method after Hurtado et al., 2007). A container filled with a sediment sample into height x is placed on top of a detector and measured with a point source and without it. Net count rates for both measurements in* ^{210}*Pb peak are registered. Also an empty dish is measured with a point source to provide a count rate without sample attenuation.*

Combined term $a \cdot x$ is obtained from a recombination of a negative exponential attenuation relationship from a transmission measurement (Fig. 7.3) performed on each sample:

$$I = I_0 e^{-a \cdot x}, \tag{7.4}$$

where I (attenuated intensity) is a net count rate ($imp \cdot s^{-1}$) in ^{210}Pb FEP in the transmission experiment (with the background effect of the sample subtracted) and I_0 (unattenuated intensity) is a net count rate without a sample (empty dish). Therefore previous knowledge of either thickness or elemental composition and density of the material is not required, provided the material is reasonable homogeneous in the measurement container. This method is suitable for such cases, where it is difficult to estimate these parameters.

7.4 Efficiency calibration with LabSOCS

An innovative method for constructing efficiency curves uses Canberra Genie 2000 module LabSOCS (Laboratory SOurceless Calibration System). For in-situ measurement geometries analogous module ISOCS (In-Situ Object Calibration Software) had been developed. The efficiency curves can be estimated for characterized detectors.

A set of measurements using test sources in very well defined geometries is performed by Canberra in a production facility (Olen, Belgium). The results from the test measurements together with precise data on the detector size are then used for a characterization of the detector with Los Alamos National Laboratory Monte Carlo N-Particle (MCNP) modelling code. This characterization then allows to generate efficiencies for a known sample container, sample and absorber matrix, and a specific source-to-detector geometry (Bronson, 2003) using Genie 2000 Geometry composer.

This is a very promising approach for environmental samples. Material of sediments, for example, originates from different environments and different sources and develops enormous variability of compositions and densities. Also the amount of sample available sometimes varies even within a single core, depending on core section length, water content or previous consumption of part of the sample for different analyses. Using LabSOCS modelled efficiencies, always maximum available amount of sample can be used to achieve the best detection sensitivity.

LabSOCS has been the primary method for efficiency calculation used within this thesis. In order to avoid "blind confidence in factory-calibrated detector" (Bossus et al., 2006; Gilmore, 2008), validation of LabSOCS has been performed within this project (Sec. 7.3) to ensure reliability of the analyses.

The recommended uncertainty in efficiency calculation (Tab. 7.1) is given in the LabSOCS Validation and verification manual (Canberra, 2002b) based on consistency and validation tests for a number of in-situ, laboratory and collimated geometries. A need for an additional error factor might arise in special cases, for example when measuring very small sources in a close distance or at presence of a heavy attenuating absorber between the source and the detector (Canberra, 2002b). LabSOCS uses slightly higher default uncertainties (Tab. 7.1), which were also used for all calculations within this project; that in result increased the experimental uncertainties of all calculated activities toward more conservative values.

Table 7.1: *Recommended uncertainties for LabSOCS efficiencies for laboratory geometries and LabSOCS default values. Source: Canberra (2002b) and Canberra (2002c).*

Recommended uncertainties		LabSOCS default uncertainties	
Energy region keV	Rel. Std. Dev. %	Energy region keV	Rel. Std. Dev. %
50–100	7.1	50–200	10
100–400	5.5	200–500	8
400–7000	4.3	500–1000	6
		1000–2000	4

7.4.1 Detector characterization for LabSOCS

Characterization of a detector for LabSOCS involves three steps described in detail in Canberra (2011). At first a model for the particular detector is developed and validated. The detector model is based on actual physical dimensions of the detector and all internal and surrounding structures (internal contact pin, holder cup, endcap, etc. - Fig. 7.4). In order to determine the FEP efficiency response of the detector the MCNP code is used. Because some of the dimensions and parameters (e.g., dead layers) are not known or not measurable exactly, the model is compared to measurements using traceable sources in 5 different geometries in order to validate the model. The initial detector dimensions are used as a starting point and they are adjusted iteratively until an agreement is reached between measured and modelled efficiencies.

In the next step a large number of efficiency datasets are generated with the validated detector model in response to point-like sources in vacuum at many locations about the detector at 20 energies between 10 and 7000 keV and to a maximum distance of 500 m from the center of the front face of the detector endcap with the highest density of the measurement points being close to the detector.

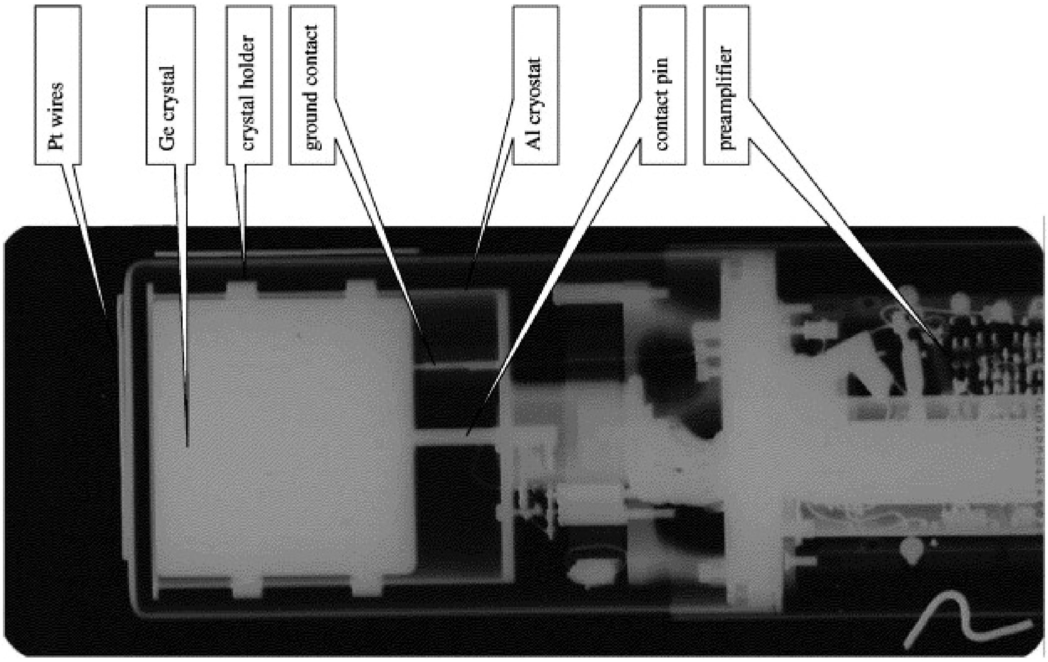

Figure 7.4: *An x-ray image of a HPGe detector with internal and external structures described. From: Dryak & Kovar (2006). Platinum wire of a known length was used to measure dimensions from the radiogram.*

The efficiencies at a large number of nodal points are generated by interpolating between the data for each energy creating a detector calibration grid for a bare detector. Finally, the attenuation due to the external crystal structures are computed point-by-point. The properly attenuated efficiency grids at the 20 energies are then combined to produce the ISOCS detector characterization in a form of the detector characterization file used in LabSOCS calibration software.

The LabSOCS software can then calculate the efficiency for voluminous sources by integrating the response over the volume of a given source. Before finalizing the characterization process in the factory the characterization file is loaded into LabSOCS user-interface software, and efficiencies are generated for 5 five source geometries. Figure 7.5 shows the results of comparison of LabSOCS efficiencies with measured efficiencies for each data set (Canberra, 2011).

7.5 LabSOCS efficiency calibration problems

For all experimental work within this project Detector 3 (see more detailed properties in Tab. 5.1) was used. Initially, only transmission measurements using different absorbers were performed in order to validate the correctness of LabSOCS efficiency calibration (Pittauerová et al., 2009) discussed in Sec. 7.6.3. Later on during the project, some doubts have risen about the correctness of the LabSOCS results based on different activities measured on the same materials in different geometries. Searching for possible causes of these mismatches, another three validation methods (Sec. 7.6) were applied and based on the results it was found that LabSOCS did not produce reliable efficiencies for the characterized detector. The most notable difference was for example systematic overestimation of point sources' activities in close geometries and their

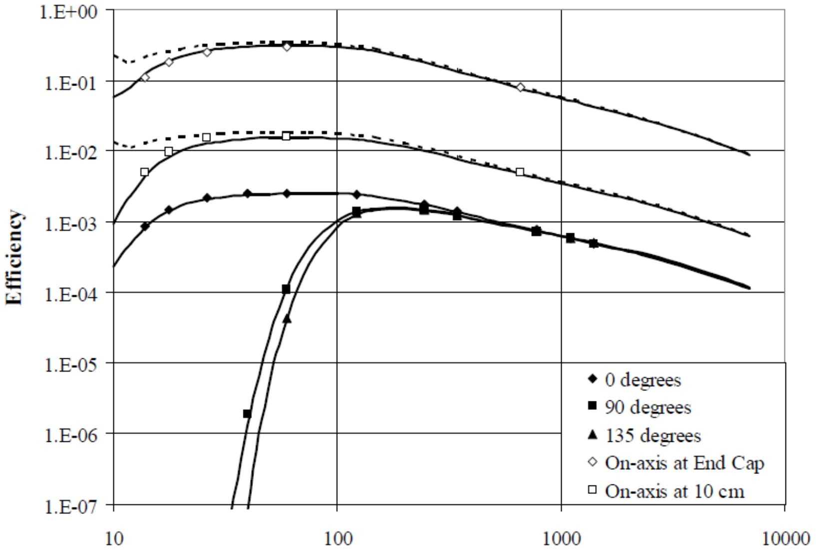

Figure 7.5: *ISOCS efficiencies (solid lines) compared to experimental measurements (points) for validation geometries in Det. 3. The dashed lines are the ISOCS computed efficiencies for the "On-axis at End Cap" and "On-axis at 10 cm" measurement positions, but without the absorbing source mount (a Plexiglas disk). From: Canberra (2011).*

systematic underestimation in more distant geometries (described below).

The detector manufacturer admitted a problem with characterization. A likely explanation for the problem was found only after studying closely the service history of the detector. The detector was commissioned in the Laboratory in 11/2004, but shortly after the beginning of operation the detector was sent for a modification (6–8/2005), since it did not satisfy the Laboratory's needs for low background due to a ^{210}Pb line in the detector background. After the complaint at the manufacturer the standard Al holder had been replaced by a low-background Al holder. There was no detector re-characterization performed after this repair, and although it was not officially admitted by the manufacturer, the position of the detector might have changed slightly within the cryostat, which was enough to be out of specification of the performed characterization.

As a result, the detector was sent for re-characterization in 9/2011 and received back together with a new characterization file in 12/2011. The results of test measurements before and after re-characterization are presented below.

7.6 Validation of LabSOCs efficiency calibration in the Laboratory

A set of experiments was performed in order to validate correctness of the LabSOCS efficiency calibration for detector 3. It included:

1. test measurements of a point source of ^{137}Cs in different distances from the detector[2],
2. test measurements of a voluminous source (^{137}Cs solution) in different distances from the

---

[2] The experiment was designed and performed by DP and Bernd Hettwig (BH), IUP, University of Bremen. The evaluation was done by DP.

detector[3],

3. transmission measurements with ^{210}Pb and ^{137}Cs test points sources and different absorbers (Pittauerová et al., 2009) and
4. test measurement with a soil sample including a consistency test with natural emitters[4].

The first two experiments were used in order to validate mainly the geometrical correctness of the calibration. The third test was designed to check mainly the absorption correction for different energies. The last test combines validation of both previously tested properties.

The measurements were performed before re-characterization and analyses of the spectra were done for efficiencies based on characterization files of old and new characterization. An exception is the first experiment, within which additionally another set of measurements was performed after re-characterization.

7.6.1 Point source test

Materials and methods

A sealed point test source Amersham-Buchler 8421Nds27 with reference activity of 13.2 nCi (488 Bq) ^{137}Cs to 29.09.1975 was used for the experiment. The test source was placed into a sample holder in 9 different defined distances from the top of the detector, with detector to source (D-S) distances ranging from 1.6 mm to 200.6 mm and counted, so that statistical uncertainty of the area of the ^{137}Cs FEP was $< 2\%$.

The obtained spectra were analyzed using Genie 2000 gamma analysis software. Efficiencies were determined using Genie 2000 Geometry Composer (Point source template) with varying D-S distances. Activity of the point source was calculated for each geometry and decay corrected to the test source reference date. New analyses of the same spectra were performed after re-charactization of the detector was performed with a new characterization file.

The test was repeated after detector re-characterization with two other sealed point test sources of ^{137}Cs (Amersham-Buchler 7558AB, 0.678 μCi to 24.04.1972) and ^{210}Pb (Amersham-Buchler 7563Nds36, 0.287 μCi to 24.04.1972). In this experiment D-S distances ranged from 1.5 mm to 198.5 mm and a total of 13 positions was examined (Tab. 7.2).

Results

Measured values of the test source activity determined in different D-S distances are listed in Tab. 7.2 and plotted in relative terms toward the respective test sources' reference activities in the Fig. 7.6. The uncertainties include both counting statistics and efficiency uncertainty. The efficiency uncertainty is reduced by the "dual curve" fit described in Sec. 4.5.2 from 6% and 10% to approximately 3% and 7% at 662 keV and 46 keV, respectively.

In the test with the original detector characterization the calculated activities of the ^{137}Cs point source measured in different D-S positions with mathematical efficiencies using LabSOCS varied considerably depending on the D-S distance showing a systematical decrease with increasing distance. The activities relative to the reference value ranged from 1.057 to 0.928 with a maximum at 10 mm distance. After the re-characterization the newly calculated activities showed a more regular pattern without any systematic overestimation at low energies and they

---

[3] This and the following experiment was designed, performed and evaluated by DP.

[4] The measurement and analysis of the soil sample in large dish and steel dish with efficiency before re-characterization was performed by BH, the other geometries by DP and remaining analysis before and all after re-characterization and the experiment evaluation was done by DP.

Table 7.2: *Activities calculated using LabSOCS efficiencies for ^{137}Cs point source measured in different detector-source (D-S) distances. Left: calculated activities are plotted for the original characterization (before) and the new one (after). Right: the results of a repeated test after the detector re-characterization with a different set of point sources (^{210}Pb and ^{137}Cs) are reported. The reference values for the test sources are listed in the bottom part of the table.*

D-S dist. mm	A (^{137}Cs, before) Bq	Uncert. Bq	A (^{137}Cs, after) Bq	Uncert. Bq	D-S dist. mm	A (^{137}Cs) kBq	Uncert. kBq	A (^{210}Pb) kBq	Uncert. kBq
1.6	504	12	459	12	1.5	24.34	0.76	10.21	0.66
5.0	507	12	467	12	5.0	24.71	0.78	10.35	0.67
10.0	516	14	484	14	10.0	25.51	0.80	10.21	0.68
20.0	482	13	461	13	20.0	25.31	0.80	10.38	0.68
41.6	478	13	464	13	40.0	25.52	0.81	10.86	0.71
80.0	470	11	474	11	60.0	25.18	0.80	10.76	0.70
101.6	460	13	469	13	80.0	26.22	0.83	10.84	0.71
151.6	464	14	475	14	100.0	25.81	0.82	10.61	0.69
200.6	453	11	468	11	120.0	25.87	0.82	10.68	0.70
					140.0	25.30	0.80	10.84	0.71
					160.0	25.71	0.81	10.90	0.71
					180.0	25.20	0.80	10.71	0.70
					198.5	25.73	0.81	10.78	0.70
Reference values (to the issue date)									
	488	24	488	24		25.09	1.25	10.62	0.53

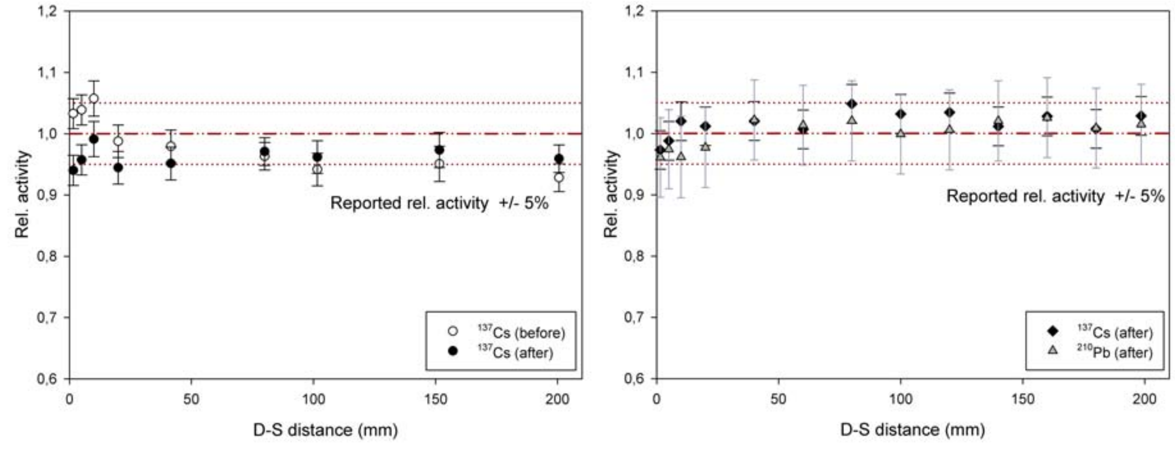

Figure 7.6: *Activities calculated using LabSOCS efficiencies for point source measured in different detector-source distances. Left: For ^{137}Cs point source activities are reported for original characterization (before) and the new one (after). Right: Results of a repeated test with another point sources of ^{137}Cs and ^{210}Pb. Here activities were only calculated for the new characterization.*

varied from 0.959 to 0.992 of the reference value. Also in the repeated test (Tab. 7.2 and Fig. 7.6) the analyzed activities of ^{137}Cs and ^{210}Pb were rather consistent. The activities analyzed ranged from 0.970 to 1.045 for ^{137}Cs and from 0.961 to 1.026 for ^{210}Pb, respectively. The activities of the test sources are reported by the producer with relatively large uncertainties (5%) and all analyzed activities fit well into the 1σ confidence limits of the reference value.

7.6.2 Voluminous source test

Materials and methods

As a test source water solution containing unknown activity of ^{137}Cs was used for the experiment. It was filled in two dishes: a small dish and a large dish (Tab. 7.3).

Table 7.3: *Types, dimensions and sealing methods of measurement containers used for testing and sample measurements.*

Name	Material	Diam. / Height / Wall mm	Sealing method	Remarks
Large dish (Fig. 7.7)	transparent polystyrene	69.2 / 21.8 / 1.3	welding (foil)	bottom of the container flat with a circular dent protruding inside the container (9.0 mm diameter, 1.5 mm max. height)
Small dish	transparent polystyrene	34.7 / 12.6 / 1.0	welding (foil)	completely straight bottom without a dent
Steel dish	steel	101.8 / 31.5 / 0.26	soldering	
Pellet	wax	70.0 / 20.0 / –	welding (foil)	mixing sample material with wax (36:64), pressing to density 1 $g \cdot cm^{-3}$

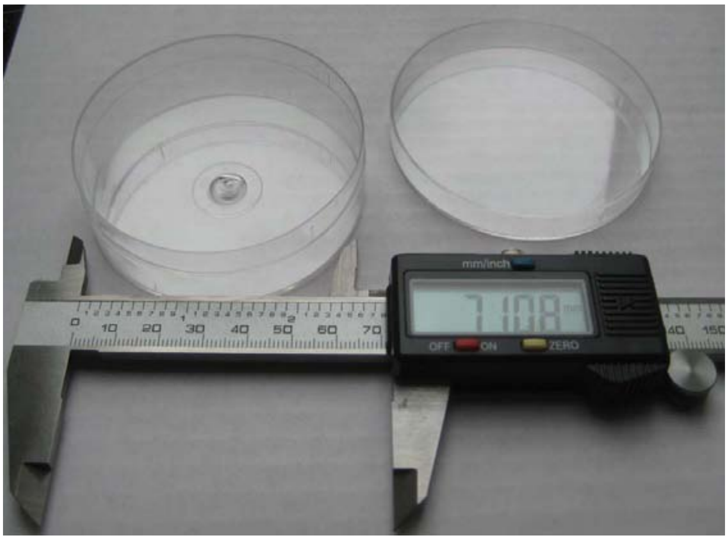

Figure 7.7: *A cylindrical plastic dish used for the experiment described as "large dish".*

The containers were filled with the test solution into height indicated in Tab. 7.4, sealed with an adhesive tape and welded into a thin polyethylene foil to prevent leakage and detector contamination.

The samples were placed centrally either directly on the detector (D-S distance = 0) or in case of the small dish at a defined D-S distance (stepwise up to 123.3 mm - Tab. 7.4) using a sample holder and counted, so that statistical uncertainty of the area of the ^{137}Cs FEP was $< 2\%$.

The spectra were analyzed using Genie 2000 gamma analysis software. Efficiencies were determined using Geometry Composer "Simplified beaker" template and actual measurement container sizes and D-S distances. Activity concentrations of the test solution were calculated for each geometry. After detector re-characterization new analyses of the same spectra were performed using the new characterization file.

Results

Results of the activity concentration of the test solution determined at different geometries before and after detector re-characterization are listed in Tab. 7.4 and plotted in Fig. 7.8. When analyzed using the original characterization the determined activities measured in the same (or comparable) geometry decrease with increasing D-S distance by up to 16%. This is a similar activity decrease with increasing D-S distance to the point source test.

After re-characterization the activities are more consistent. One exception is a measurement in D-S distance of 53.7 mm, which is in both cases higher than the remaining measurements. A possible mistake of D-S distance measurement (or a change of the measurement position due to slipping of the holder before or during of the measurement can not be excluded). The difference between the highest and the lowest measured activity (excluding D-S distance 53.7 mm) is 4% after re-characterization.

Table 7.4: *Activity concentrations (C) calculated using LabSOCS efficiencies for voluminous sources measured in different D-S distances before the re-characterization (before) and after it (after).*

Container	Filling height mm	D-S distance mm	C (before) $kBq \cdot l^{-1}$	Uncert. $kBq \cdot l^{-1}$	C (after) $kBq \cdot l^{-1}$	Uncert. $kBq \cdot l^{-1}$
Small dish	9.5	0.0	53.6	1.3	49.2	1.3
Small dish	9.1	23.1	50.9	1.5	49.3	1.4
Small dish	9.1	53.7	53.7	1.7	52.8	1.6
Small dish	9.1	65.7	48.3	1.5	48.0	1.4
Small dish	9.1	80.7	47.7	1.4	48.1	1.4
Small dish	9.1	123.3	46.1	1.6	47.2	1.5
Large dish	20.2	0.0	48.2	1.2	46.5	1.3

For both old and new characterization, the test solution measured in large dish resulted in lower activities, however after re-characterization the difference is within the 2σ uncertainty to the reference level, calculated as a mean value from all measurements after re-characterization except the outlier at 53.7 mm.

7.6.3 Validation of LabSOCs self absorption correction

Materials and methods

To validate the efficiency calibration generated by LabSOCS, a transmission experiment was performed for different absorbers. As emitters, point test sources of gamma energies of 46.5 keV (^{210}Pb, Amersham-Buchler 7562AB, 49.9 nCi to 24.04.1972) and 662 keV (^{137}Cs, Amersham-Buchler 7557AB, 0.628 μCi to 24.04.1972) were placed on top of the absorbers. Five different materials with various chemical compositions and densities (Tab. 7.5) were used as absorbers, all

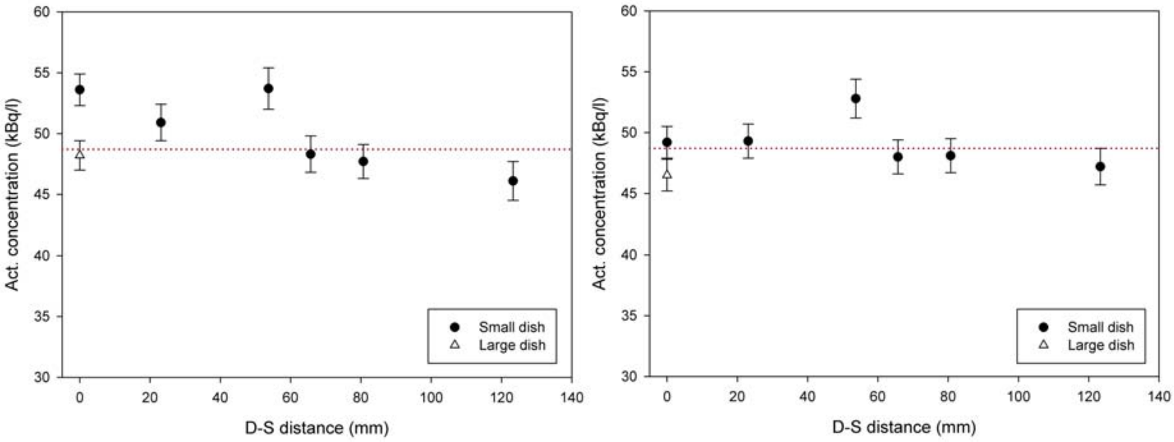

Figure 7.8: Activity concentrations calculated using LabSOCS efficiencies for voluminous sources measured in different D-S distances. They are reported for original characterization (left) and the new one (right). The reference level is an average value of the activity concentration calculated from using efficiencies after re-characterization (excluding the outlier at D-S distance of 53.7 mm).

of them sealed in cylindrical plastic containers (large dishes - Fig. 7.7) filled to 20 mm height. All spectra were counted for times long enough for the uncertainty of count rates in the evaluated peaks dropped below 2%. The efficiencies used for activity calculation were produced using LabSOCS - both for old and new detector characterization. The gamma spectra of absorbers were collected separately and subtracted from spectra of transmission experiments.

Table 7.5: *Activities calculated using LabSOCS efficiencies before and after re-characterization for ^{210}Pb and ^{137}Cs point sources measured on top of different absorbers.*

Material	Bulk density $g \cdot cm^{-3}$	$A(^{210}\text{Pb})$ before Bq	Un-cert. Bq	$A(^{137}\text{Cs})$ before kBq	Un-cert. kBq	$A(^{210}\text{Pb})$ after Bq	Un-cert. Bq	$A(^{137}\text{Cs})$ after kBq	Un-cert. kBq
Air	0.0012	622	49	10.73	0.22	584	44	10.61	0.28
Water	1.00	688	54	10.61	0.23	647	49	10.18	0.23
Wax*	0.96	671	52	10.67	0.23	631	47	10.24	0.23
Sand**	1.40	610	44	10.91	0.25	586	43	10.43	0.23
Carbonate***	1.77	693	58	10.88	0.26	656	53	10.40	0.25
Reference values (to the analysis date)									
		625	31	10.42	0.52	625	31	10.42	0.52

* *Non-certified: a typical constituent of paraffin wax is $CH_3(CH_2)_{29}CH_3$, which comprises of 15% H and 85% C.*
** *Sea sand p. A., produced by AppliChem: composition cristobalite (SiO_2), particle size 0.1–0.3 mm.*
*** *Non-certified: a milled piece of decorative marble ($CaCO_3$) from a stone dealer.*

Results

The calculated activities of point sources were compared to their reported activities (Fig. 7.9). Values relative to the reference using efficiency calibration before re-characterization vary from 1.018 to 1.047 for ^{137}Cs and from 0.976 to 1.109 for ^{210}Pb. After re-characterization the ranges

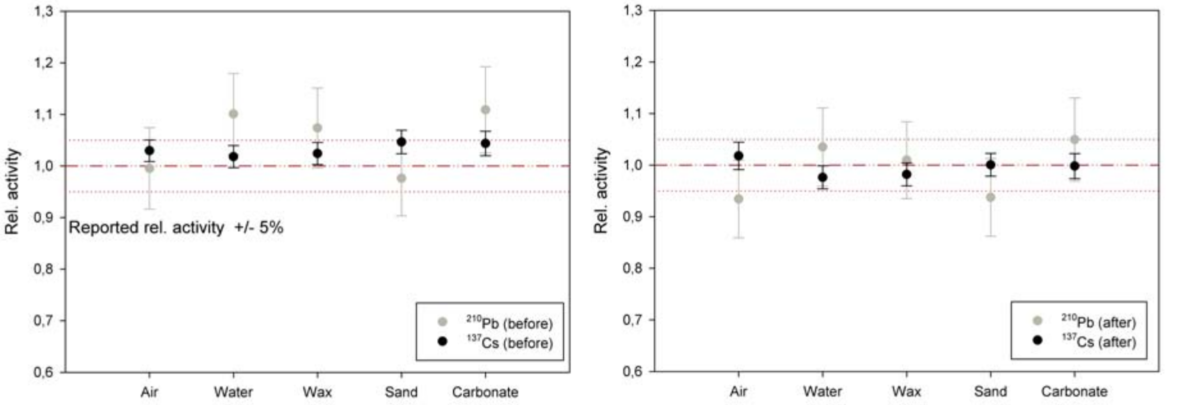

Figure 7.9: *Results of the transmission experiment: relative activities of* ^{210}*Pb and* ^{137}*Cs point test sources estimated by measurement of their activities using absorbers of different chemical compositions and densities. The efficiencies were generated by LabSOCS, left: with old detector characterization and right: after re-characterization.*

improved to 0.977–1.018 for ^{137}Cs and 0.934–1.050 for ^{210}Pb. The experiment showed that activities estimated using LabSOCS generated efficiencies are within the overall uncertainty for all examined absorbers and can be successfully used for purposes of combined ^{210}Pb and ^{137}Cs chronology.

7.6.4 Test measurement with a soil sample and an energy consistency test

Materials and methods

The test sample (RV VII-2006) was a soil used for the 7th Intercomparison of environmental samples organized by the German Federal office for Radiation Protection (BfS) (Schkade et al., 2007). It was taken from an area in the federal state of Thuringia with naturally increased ^{226}Ra levels. This test was performed primarily in order to evaluate the radioactive equilibrium establishing between ^{226}Ra and the daughter products, as discussed in a separate chapter (Chap. 8). The use of the existing spectra for testing the performance of LabSOCS efficiencies at several isotopes for which activities were reported was convenient. Also comparing results of ^{226}Ra activity determination via several daughter lines and evaluating their consistency was possible.

The test material was measured in five different geometries in time series. They included between 3 and 21 repeated measurements for each of the series. The containers are described in Tab. 7.3: a large dish (completely filled with sample), a steel dish (completely filled with sample), a pellet, a small dish I (filled up to 4.9 mm), a small dish II (filled up to 11.1 mm). All samples except of the steel dish, which was soldered, were welded into gas-proof metalized foil[5] bag for purposes of sealing against Rn escape from the sample.

The analyses results of ^{40}K and ^{137}Cs were compared to the reference values of PTB (Physikalisch-Technische Bundesanstalt, the National metrology institute). For a comparison of ^{226}Ra activities determined via different lines, ^{214}Bi and ^{214}Pb, ^{222}Rn daughter products in equilibrium, were used. They included five most prominent energies (Tab. 6.1) over a broad

---

[5] The metallized foil bags are made of aluminium barrier foil A30 T, produced by a company Long life for art. The material is a 3-layer compound foil, consisting of 12 μm polyethylene terephthalate (PETP, PET), 12 μm aluminium 12 and 95 μm low-density polyethylene (LDPE).

energy region from 295.2 keV to 1764.5 keV. The activities of both isotopes at all five energy lines were analyzed in Genie 2000 (including cascade summing corrections) using LabSOCS based efficiencies after detector re-characterization. The cascade summing correction were performed where needed. As the exact composition of soil was not known, a material with composition “DRY DIRT” - an average sediment (Canberra, 2002a) was used. Its elemental composition is defined as: 49.62% O + 27.38% Si + 7.1% Al+ 4.04% Fe + 1.6% Mg + 4.21% Ca + 0.84% Na + 0.36% H + 2.37% K + 0.34% T +2.14% C.

Results

^{40}K and ^{137}Cs

The weighted means of ^{40}K and ^{137}Cs activity concentrations calculated from repeated measurements for each geometry are listed in Tab. 7.6 and plotted in relative terms to the PTB reference values in Fig. 7.10.

Table 7.6: *Activity concentrations of ^{40}K and ^{137}Cs in the reference soil sample RV VII-2006 calculated using LabSOCS efficiencies before detector re-characterization (upper part) and after re-characterization (lower part). The values are calculated as weighted means from the given number of repeated measurements. The PTB reference values with uncertainties (1σ) are presented in the bottom of the table (Schkade et al., 2007).*

	# of measurements	Total live-time days	C(^{40}K) $Bq \cdot kg^{-1}$	Uncert. $Bq \cdot kg^{-1}$	C(^{137}Cs) $Bq \cdot kg^{-1}$	Uncert. $Bq \cdot kg^{-1}$
		Before detector re-characterization				
Large dish	22	15	742	5	28.5	0.2
Steel dish	6	9	826	7	31.2	0.3
Pellet	10	2.9	778	8	28.9	0.3
Small dish I	3	4.4	907	24	34.9	1.0
Small dish II	3	2.2	911	21	34.6	0.8
		After detector re-characterization				
Large dish	22	15	733	5	27.9	0.2
Steel dish	6	9	817	8	31.1	0.3
Pellet	7	12	748	8	28.3	0.3
Small dish I	3	4.4	797	20	30.5	0.8
Small dish II	3	2.2	811	19	30.4	0.6
Reference value			795	12	29.9	0.5

After detector re-characterization the mean results for the small dishes match with the reference values closely (between 1.003–1.020 for both isotopes). Both ^{40}K and ^{137}Cs are overestimated in the steel dish (up to 1.040 relative). For the large dish and the wax pellet both ^{40}K and ^{137}Cs are underestimated (0.922–0.946, relative to the reference value). The values seem to be more effected by geometry effects than absorption of different gamma energies, given values of ^{40}K and ^{137}Cs follow the same pattern (activities relative to the reference values) for all geometries.

The relative value of 0.93 ± 0.02 for ^{40}K in the large dish is in good agreement with a result of another test performed in the Laboratory with potassium chloride (KCl) powder measured in the same container[6]. The expected activity (due to known K content and fraction of ^{40}K in K isotopic composition) is 16.40 $kBq \cdot kg^{-1}$. The analyzed value was 15.42 ± 0.39 $kBq \cdot kg^{-1}$, therefore 0.94 ± 0.02 relative to the reference value.

---

[6] Measurement performed by Bernd Hettwig.

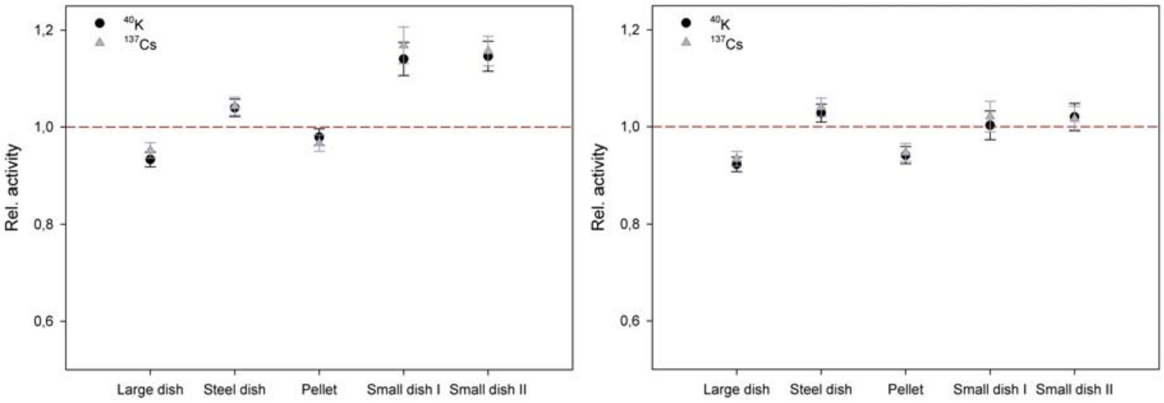

Figure 7.10: *Relative activities (measured activity to reference activity ratios) of ^{40}K and ^{137}Cs measured in different geometries. Left: old characterization, right: new characterization. The values are arithmetic means calculated from repeated measurements.*

^{210}Pb

The above presented results for some of the larger geometries (large dish and pellet) are unsatisfactory. From the point of view of the important sediment chronology gamma emitter ^{210}Pb it is also valuable to estimate whether (and if so to which extent) this activity underestimation is present at lower energies. While the present day activity of ^{210}Pb is not known in the studied intercomparison sample RV VII-2006 (due to presumable ingrowth to equilibrium with ^{226}Ra), its reference value was given to 1.1.2006 (Schkade et al., 2007) as $853 \pm 14\ Bq \cdot kg^{-1}$. This enables to compare experimental efficiencies calculated from the first measurement of the sample at Det. 3 in May 2006 (spectrum #3242) using net count rates of ^{210}Pb, ^{137}Cs and ^{40}K peaks (Eq. 7.1) for a sample in the large dish. The values are listed in Tab. 7.7 together with efficiencies calculated by LabSOCS before and after detector re-characterization.

Table 7.7: *Experimental efficiencies ϵ_{exp} calculated from the sample RV VII-2006 for ^{210}Pb, ^{137}Cs and ^{40}K compared to mathematical efficiencies for the same geometry (large dish) calculated with LabSOCS for Det. 3 before (ϵ_{before}) and after (ϵ_{after}) re-characterization.*

E_γ keV	ϵ_{exp}	uncert.	ϵ_{before}	uncert.	ϵ_{after}	uncert.	$\frac{\epsilon_{before}}{\epsilon_{exp}}$	uncert.	$\frac{\epsilon_{after}}{\epsilon_{exp}}$	uncert.
46.5	0.0829	0.0035	0.0890	0.0089	0.0870	0.0087	1.05	0.11	1.07	0.12
661.7	0.0343	0.0009	0.0369	0.0022	0.0354	0.0021	1.03	0.07	1.07	0.07
1460.8	0.0198	0.0005	0.0208	0.0008	0.0204	0.0008	1.03	0.05	1.05	0.05

While sample RV VII-2006 is not a traceable reference material and therefore its use as a calibration source is not possible, it allows valuable estimation of the efficiency correctness. From Tab. 7.7 it can be seen that for the large dish the efficiency calculated by LabSOCS gives worse results after re-characterization than before, which can also be seen from the comparison of values before and after re-characterization in Fig. 7.10. The factor of the experimental efficiency to the LabSOCS one is however comparable for energies of 46, 662 and 1460 keV.

Energy consistency test

The measured activities of ^{226}Ra are presented in Tab. A.5 (Appx. A). The activities calculated from each of five peaks from each spectrum were normalized by a "mean" activity for the spectrum. That was calculated as a weighed mean of ^{214}Bi and ^{214}Pb activities, which were calculated by Genie 2000 from multiple lines using Eqs. 4.25 and 4.26. The plots of such normalized activities are presented in Fig. 7.11 for each of five measurement geometries and combined into a single diagram in the last plot. The means and standard deviations from the complete dataset are presented in Tab. 7.8.

Table 7.8: *Relative results from normalized activities of ^{226}Ra via 5 different lines for all geometries, showing arithmetic mean μ and standard deviation σ for each of the lines. Number of spectra: 40.*

E_γ	μ	σ
295 keV	0.996	0.011
352 keV	0.998	0.008
609 keV	0.992	0.006
1120 keV	1.010	0.012
1764 keV	1.006	0.010

The ANOVA test (one way analysis of variance, pairwise multiple comparison procedures - Tukey test) was performed on the combined dataset of all measurement geometries in order to compare differences in the mean values among the results derived by individual lines. There were no statistical differences found between 295, 352 and 609 keV lines (at 0.95 probability level). Also no differences were found between 1120 and 1764 keV lines. Results from lines across these two lower and higher energy groups featured differences greater than would be expected by chance. Nevertheless, the difference between the lowest mean for 609 keV (0.992) and the highest for 1120 keV (1.010) does not seem too important compared to the overall uncertainty and the count rate gain from using all lines can counterbalance this disadvantage. The relative uncertainties were halved when analyzed from all lines compared to the single line of 352 keV. Therefore, it seems that using all five lines for ^{226}Ra determination is a reasonable approach.

7.7 Conclusions

While mathematical efficiency calibration with LabSOCS offers an advantage of greater freedom in measurement samples of varying matrices and geometries, it has to be accepted that uncertainties of efficiency calibrations are high, up to 10% for low energies. Any inconsistencies within 7–10% for low energies, or 4–5% for high energies, are usually not considered to be a reason for corrective actions (detector re-characterization, in the worst case) (Canberra, 2011).

The series of tests performed during the LabSOCS validation in the Laboratory for the factory characterized detector 3 showed that the detector needed a new characterization. After it was performed, the efficiency calibration performance improved significantly. The results with the new characterization can be summed up as following:

1. Point test sources measured in difference distances from the detector lead to results relative to the reference value ranging between 0.959 and 1.045 of the reference value for ^{137}Cs and between 0.961 and 1.026 for ^{210}Pb with no obvious systematic activity decrease with increasing distance.

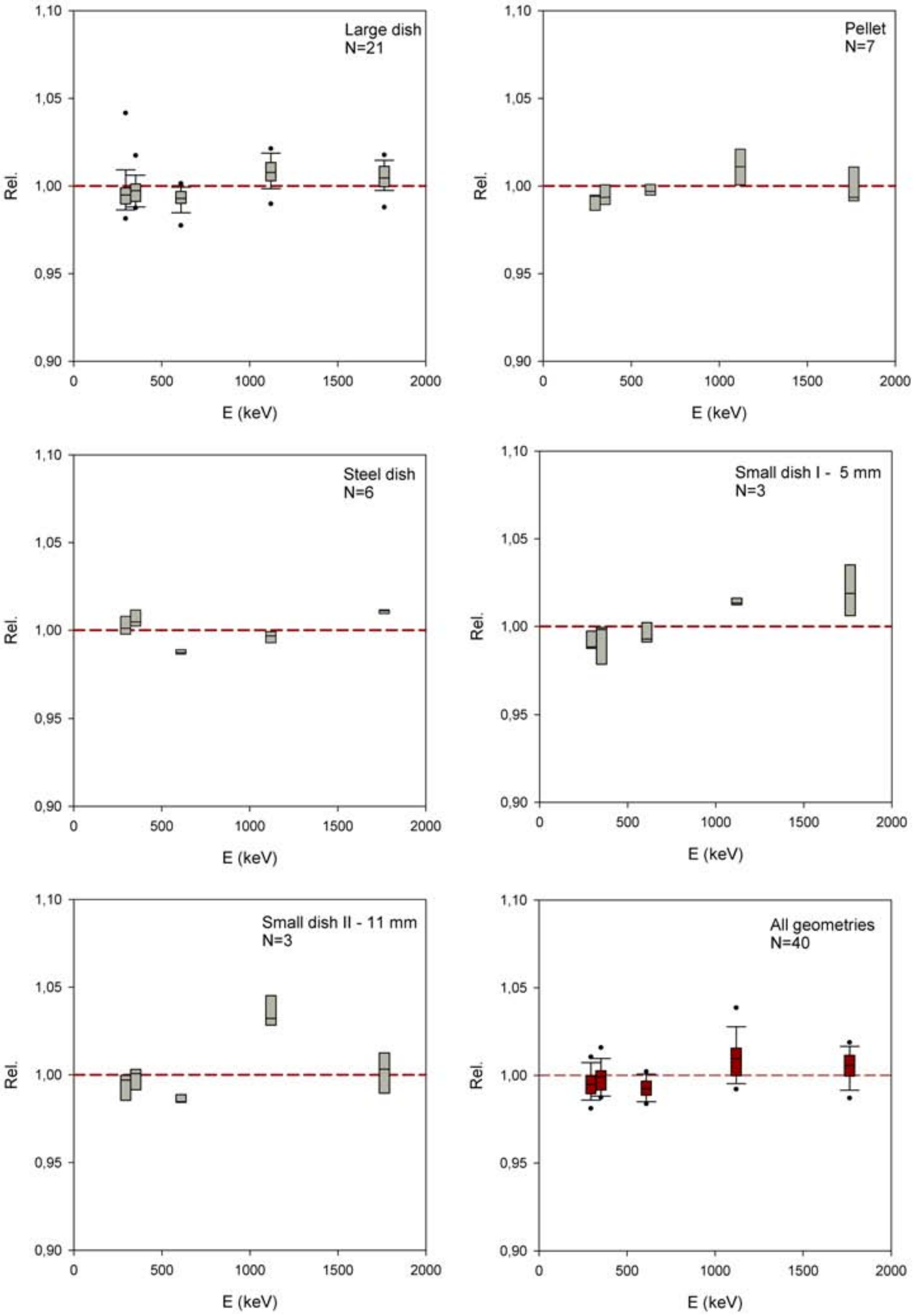

Figure 7.11: *Relative activities calculated via the most intensive gamma lines of ^{222}Rn daughter products related to a weighted mean of ^{214}Pb and ^{214}Bi activities measured repeatedly in different geometries. N stands for number of spectra analyzed for each geometry. In bottom right all data are plotted in a single diagram. The boxes are limited by 25th and 75th percentiles. The line inside the box represents a median. For datasets with 9 and more values also whiskers at 10th and 90th percentiles and dots at 5th and 95th percentiles are depicted.*

2. Non-calibrated ^{137}Cs solution measured in voluminous geometries in different distances from the detector gave values varying by 4% between the highest and the lowest value.

3. Point test sources of ^{137}Cs and ^{210}Pb measured with five different absorbers resulted in an excellent agreement with the reference values for ^{137}Cs (0.977–1.018, relative) and less consistent, nevertheless still acceptable values within overall uncertainties (0.934–1.050) for ^{210}Pb.

4. ^{40}K and ^{137}Cs values in the intercomparison soil sample RV VII-2006 measured in different containers gave results close to the reference values for small dishes and the steel dish. However, the large dish and the wax pellet resulted in underestimation of both ^{40}K and ^{137}Cs by up to 8%. The similarity of the relative results of both radionuclides in all geometries indicates that the problem might be related to geometry more likely than to the absorption correction.

5. Based on the results of a single measurement in the large dish (for which also the ^{210}Pb reference value was known) it appears that ^{210}Pb is underestimated by a comparable factor (7%) as ^{137}Cs (7%) and ^{40}K (5%), suggesting again a comparable factor of underestimation for wide range of energies. For this reason the previously published ^{210}Pb chronologies (relying on LabSOCS calibration) should not be problematic, because excess ^{210}Pb is calculated as a difference between total ^{210}Pb and ^{226}Ra activity concentrations.

6. ^{226}Ra measured via different lines of its daughter products resulted in statistically significant difference between the lower energy lines group (295, 352 and 609 keV) and the higher energy lines (1120 and 1764 keV). However due to the fact the difference is comparably small in context of the overall uncertainty it is a reasonable approach to use averages from multiple ^{226}Ra daughter products lines for determining ^{226}Ra values, instead of a single line (352 keV is frequently used). It might bring particular advantages in case of low activity samples by means of improving the counting statistics and therefore reducing the uncertainty (by more than 50% in the presented case). This approach was used within this thesis for the case study Indonesia (Chap. 10).

Chapter 8

Supported lead in Pb-210 chronology[1]

8.1 Motivation and introduction

As a result of the Laboratory's participation in an intercomparison exercise on gamma emitting radionuclides in soil a possibility of underestimating ^{226}Ra values was suspected. The motivation of this project was to understand if the existing laboratory practice of ^{226}Ra determination via daughter products using plastic sample dishes sealed in presumably gas-proof metallic foil was possibly a weak point. In ^{210}Pb dating determination of ^{226}Ra is one of the key steps for interpreting the profiles, as it is used as a proxy for the supported part of total ^{210}Pb.

In the first and theoretical part of this chapter it is estimated, what effect would such an underestimation of supported ^{210}Pb have on resulting chronologies, using two most widely applied models. From the initial test results it was assumed, that ^{226}Ra underestimation can reach up to 12% (Hettwig, 2010). Another recent study by Scholten et al. (2013) was dealing with a similar topic with the aim to estimate how significant the radon loss from the sample is. They estimated ^{222}Rn loss up to 6% depending on material, measurement container and sealing technique.

The Laboratory adopted a new practical countermeasure in the form of thicker metallized plastic foil bags for sealing samples (described in Sec. 7.6.4). Results of an equilibrium ingrowth experiment was performed using soldered steel containers as well as traditional plastic dishes.

8.2 Effects of supported Pb-210 underestimation on excess Pb-210 sediment depth profiles

In two theoretical models it is illustrated how systematic underestimation of $^{210}\text{Pb}_{\text{sup}}$ can affect the resulting sedimentation rate estimation in $^{210}\text{Pb}_{\text{xs}}$ sediment chronology. The simple example (Profile A - Fig. 8.1) presents a theoretical non-compacted and non-mixed sediment profile with a constant sedimentation rate of 0.25 $cm \cdot yr^{-1}$. The sampling interval is 1 cm and the depth of the profile is 30 cm. $^{210}\text{Pb}_{\text{sup}}$ being constant 25% of the total ^{210}Pb initial activity (top of the profile) is subjected to underestimation by 12%. The value of 25% for ratio between supported lead and total initial ^{210}Pb was selected as a "typical value", although based on our experience, it can vary strongly according to the local environment, often between 5-50%. Underestimation of supported lead in this example leads to a constant shift of $^{210}\text{Pb}_{\text{xs}}$ to higher values.

---

[1] Parts of this chapter were presented in the form of a poster at the International Symposium on Isotopes in Hydrology, Marine Ecosystems, and Climate Change Studies, Monaco, 27.3.–1.4.2011 as D. Pittauerová, B. Hettwig and H.W. Fischer: Supported lead in Pb-210 chronology.

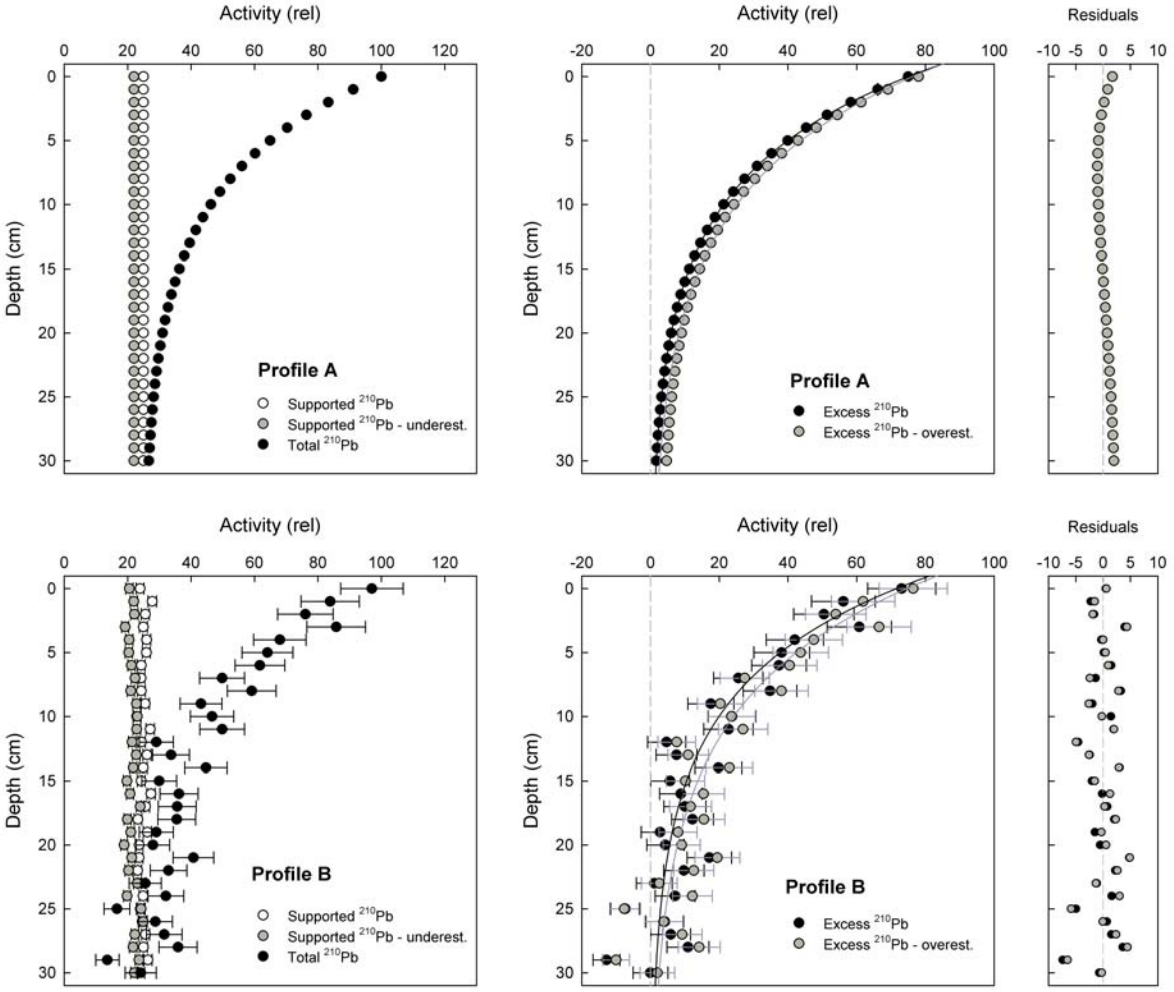

Figure 8.1: *Theoretical* ^{210}Pb *sediment depth profiles described in Sec. 8.2. Top: a simple profile (Profile A) and bottom: a profile with a random scatter (Profile B). For both profiles, in the left figures,* $^{210}Pb_{tot}$ *and both correct and systematically underestimated* $^{210}Pb_{sup}$ *are depicted. In the central figures, the correct and overestimated* $^{210}Pb_{xs}$ *(calculated as* $^{210}Pb_{tot}$*-*$^{210}Pb_{sup}$*), together with simple 2 parameter exponential fits, using a least square algorithm, are plotted. In the right figures, residuals to the fits are shown.*

Another example (Profile B) shows the upper described model modified by adding Gaussian noise to $^{210}\mathrm{Pb}_{\mathrm{tot}}$ and $^{210}\mathrm{Pb}_{\mathrm{sup}}$ data and error bars added (ranging for $^{210}\mathrm{Pb}_{\mathrm{tot}}$ from 10% for the highest activities to 20% for the lowest ones and 5% for $^{210}\mathrm{Pb}_{\mathrm{sup}}$) (Fig. 8.1).

On a real dataset (with scatter caused by counting statistics and other sources) excess ^{210}Pb overestimation can remain unobserved, and could also be attributed to not reaching the "dating horizon" (Sec. 3.2.2). It can possibly be detected by careful examination and finding regular patterns in the residuals plot (after fitting) (Fig. 8.1), but this effect is not obvious in naturally scattered datasets (Fig. 8.1). The described effect will be strongest in environments with higher proportion of supported ^{210}Pb. Systematic error in $^{210}\mathrm{Pb}_{\mathrm{sup}}$ estimation can therefore have consequences for $^{210}\mathrm{Pb}_{\mathrm{xs}}$ derived chronologies leading to systematic underestimation of ages.

8.3 Possible consequences of supported Pb-210 underestimation for chronologies

Two commonly used chronology models were applied to the previously described two theoretical profiles A and B: the Constant Flux - Constant Sedimentation (CF-CS) model (Sec. 3.2.1) and the Constant Rate of Supply (CRS) model (Sec. 3.2.2). In the first case (CF-CS model), $^{210}\mathrm{Pb}_{\mathrm{xs}}$ profiles were fitted by a simple 2 parameter exponential function without an offset using a least square algorithm. Based on resulting parameters, sedimentation rates were calculated. The resulting sedimentation rates are 0.284 ± 0.004 $cm \cdot yr^{-1}$ for Profile A and 0.280 ± 0.026 $cm \cdot yr^{-1}$ for Profile B. In comparison to the initial 0.25 $cm \cdot yr^{-1}$, sedimentation rates were overestimated by over 13%. (When an exponential model with an additional offset parameter is used, the dataset without a scatter results in the correct value of 0.25 $cm \cdot yr^{-1}$, but for Profile B the sedimentation rate is still overestimated, 0.269 ± 0.047 $cm \cdot yr^{-1}$, although within 1σ uncertainty of the 0.25 $cm \cdot yr^{-1}$ value.)

For comparison, $^{210}\mathrm{Pb}_{\mathrm{xs}}$ profiles were used for calculation of ages according to the CRS chronology model, which in case of the non-scattered Profile A led to even more serious age underestimation than for the CF-CS model. Graphical depth/age relationship for both CF-CS and CRS models for profiles A and B are presented in Fig. 8.2.

8.4 Materials and methods

8.4.1 Test samples

The test sample was soil material used for the 7th Intercomparison of environmental samples organized by the German Federal office for Radiation Protection (BfS) (Schkade et al., 2007) (the same material was used for efficiency calibration tests presented in Sec. 7.6.4). The test material was distributed to the participants ground into a fine powder, so that 98.8% of the fraction had a particle size less than 315 μm.

A cylindrical plastic dish with a diameter of 70 mm and a height of 20 mm described in Tab. 7.3 as "Large dish" was filled with the test sample. It was then sealed in the new metallized plastic foil bag, considered to be gas-tight. Another experiment was performed using a steel container with a diameter of 101.8 mm and a height of 31.5 mm ("Steel dish" in Tab. 7.3) into which the test sample was soldered. The reference ^{226}Ra activity determined by PTB is $(1.23 \pm 0,02) \cdot 10^3$ $Bq \cdot kg^{-1}$ (1σ) (Schkade et al., 2007).

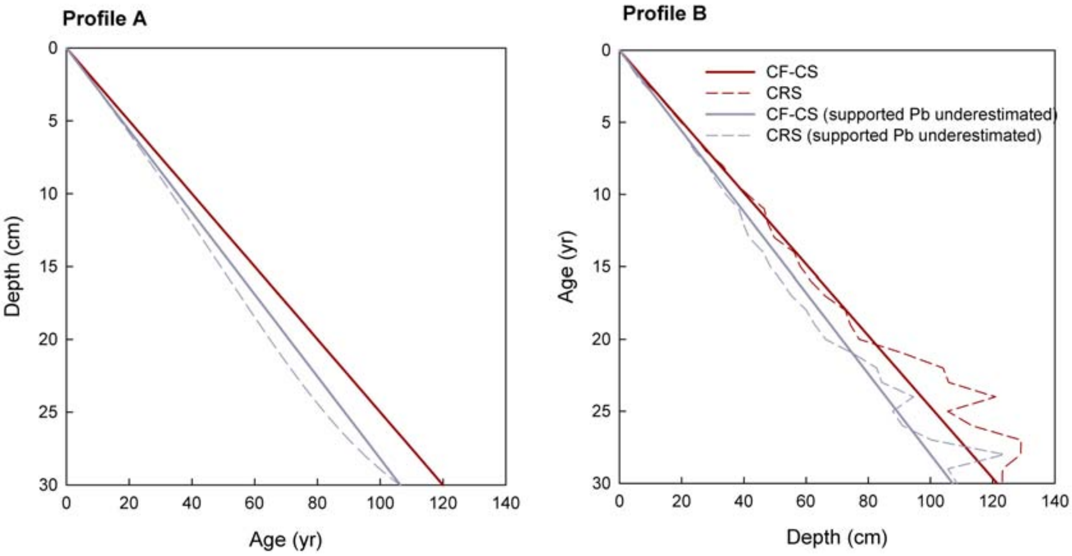

Figure 8.2: *Chronologies derived from the two theoretical profiles: Profile A and scattered Profile B. For both cases chronologies were derived by both CF-CS and CRS models using both correct and overestimated* $^{210}Pb_{xs}$ *profiles.*

8.4.2 Gamma spectrometry and Ra analysis

The samples were measured by low-level low-background gamma spectrometry using a coaxial HPGe detector (Det. 3, see Tab. 5.1). The spectra were analyzed by the Canberra Genie 2000 software. Efficiency calibration was performed using the MC based LabSOCS calibration tool as described in Chapter 7. While the experiment was originally evaluated using the old detector characterization (Hettwig, 2010)[2], a new characterization file was used for all analyses within this chapter, because the new characterization lead to improving the efficiency calibration (as shown in Sec. 7.6.3).

Gamma spectra of the test samples sealed in two previously described containers were recorded repeatedly during approximately 8 weeks (16 ^{222}Rn half-lives) following their sealing in order to observe the process of radioactive equilibrium establishing. The daughter nuclides ^{214}Pb and ^{214}Bi were detected via their 242.0, 295.2 keV, 351.9 keV, 609.3 keV, 1120.3 and 1764.5 keV gamma lines. Their average activities (determined by using Eq. 4.25 for ^{214}Pb and ^{214}Bi and calculating a mean value of the two) were used to quantify the radioactive equilibrium establishing between them (as well as ^{222}Rn) and their parent ^{226}Ra, which is a reasonable approach due to good consistency of the results from individual lines (as it was discussed in Sec. 7.6.4).

^{226}Ra activities were determined also directly using the gamma line 186.2 keV after subtraction of the ^{235}U contribution, for which 3 methods were applied:

1. **Method 1** based on Justo et al. (2006): using the ^{235}U line at 143.8 keV after interference correction from contributing ^{223}Ra, determined by the 154.2, 269.5, 323.9 and 338.3 keV lines, from which the last one is corrected from interference with one of ^{228}Ac lines at 338.3 keV and

---

[2] The experiment was designed by Bernd Hettwig (BH), IUP, University of Bremen together with DP. The measurements and initial analysis were performed by BH and presented at the group seminar (Hettwig, 2010). The analysis after detector re-characterization including the selection of lines for the libraries used for methods 1, 2 and 3 were done by DP.

2. **Method 2** based on Dowdall et al. (2004): using the 63.3 keV and 92.6 keV lines of ^{234}Th and adding the 1001.0 keV line of $^{234\mathrm{m}}$Pa for estimation of ^{238}U with activities derived from the natural ^{238}U/^{235}U activity ratio of 21.7.
3. Finally, a combination of methods 1 and 2 (**Method 3**) was applied, using all 4 mentioned lines for ^{235}U contribution estimation.

In Fig. A.1–A.3 of Appx. A the gamma spectrometry libraries used for all three methods are listed, as well as results of analyses using all three direct methods and the indirect method (Tab. A.6).

8.5 Results and discussion

8.5.1 Comparison of three methods for direct ^{226}Ra determination

The results of gamma analyses of time series measurements are plotted in Fig. 8.3. The results obtained by method 1 and 2 are presented individually using different symbols.

When comparing ^{226}Ra activity concentration means obtained by both direct methods 1 and 2 it was found that results were consistent with no statistically significant difference (two sample t-test (23)=-0.883, p=0.386). It is notable that the typical uncertainty (1σ) of ^{226}Ra activity concentration for $1.2{\cdot}10^4$ s counting time (plastic dish) was 11% when determined using method 1 and it could be reduced to 6% when method 2 was applied. The reason why nearly 42% improvement was achieved is that method 2 is based on detection of a higher number of counts in multiple lines and therefore provides better counting statistics.

Several samples within the later part of the plastic dish measurement series were counted for longer times (between $5.5{\cdot}10^4$ s and $1.0{\cdot}10^5$ s). In these measurements ^{226}Ra activity concentration uncertainties with method 1 were low (6.7%). For the same measurements using method 2 they did not decrease substantially (5.5% uncertainty). The uncertainties can not be reduced by increased measurement times, because they are mainly controlled by the efficiency component rather than by the counting component at this level. Therefore for these samples with high counts the overall improvement between methods 1 and 2 is 17.5% only.

The sample in the steel dish was counted for longer measurement times (mostly over 24 hours) and the ^{226}Ra activity concentration had quite a low uncertainty (6.3%). Method 2 improved the relative uncertainty by 15.6% on average (to 5.4% rel. uncertainty).

The above presented results lead to a conclusion that it is possible to use combined method 3 in order to minimize the uncertainty of direct ^{226}Ra determination. An especially powerful effect can be expected for samples with lower count rate, for which the uncertainty is mainly controlled by counting statistics. In comparison to method 2, method 3 enables further reduction of relative uncertainty by additional 1.5% on average.

8.5.2 Comparison of direct ^{226}Ra to the reference value

Comparing the average ^{226}Ra values analyzed by method 3 from both measurement series to the reference values, systematic underestimation in case of the plastic dish sample (by $5.4 \pm 1.9\%$) and an overestimation in case of the steel dish (by $7.8{\pm}2.9\%$) were revealed (Tab. 8.1). These are likely to be the results of the LabSOCS efficiency calibration and therefore related to problems found within the same measurement series for other two radionuclides as reported in Sec. 7.6.4 (Tab. 7.6 and Fig. 7.10). There activities were similarly underestimated for plastic dishes (by 7.8% and 6.8%) and overestimated for steel dishes (by 2.8% and 4.0%) for ^{40}K and ^{137}Cs, respectively. The source of the systematic error might be either the detector model itself or non-correct characterization of sample and container properties (composition, density, geometry).

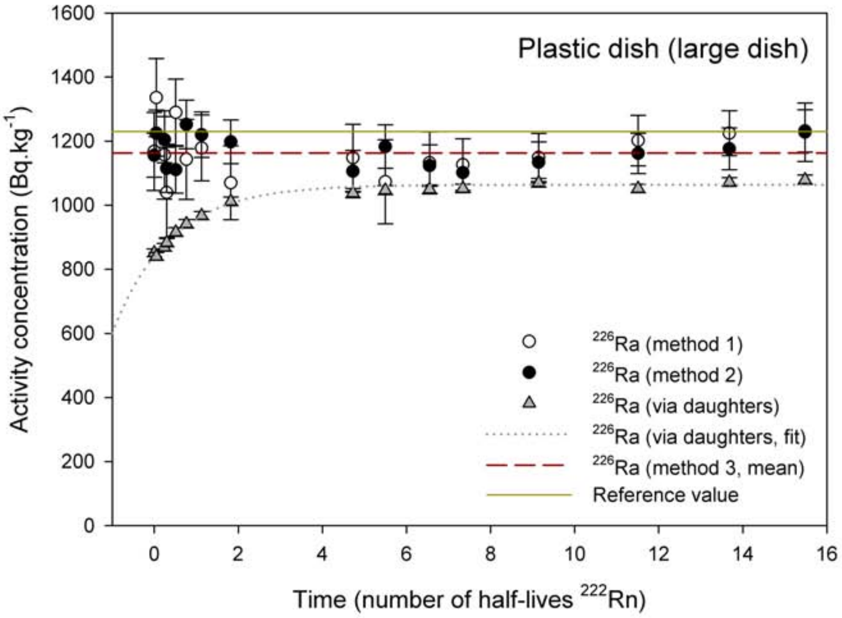

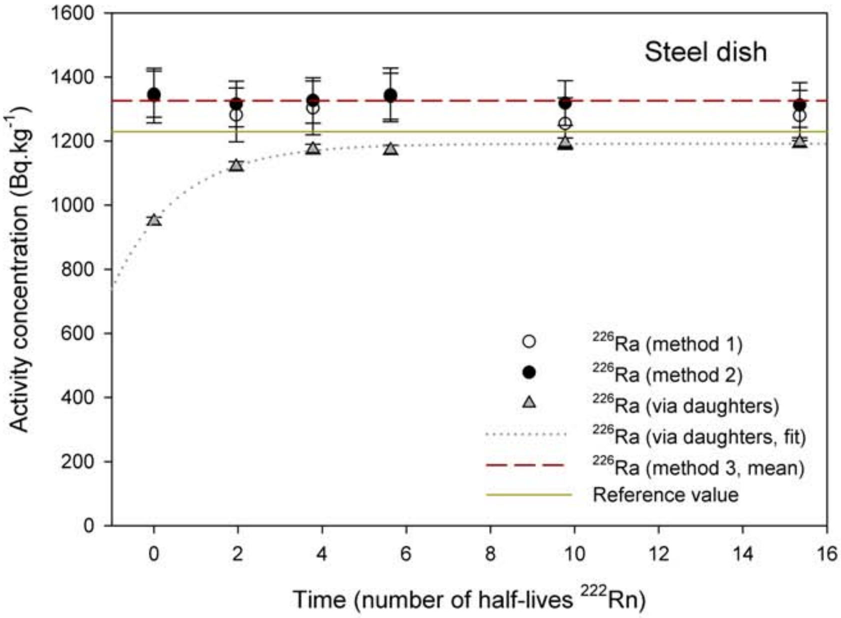

Figure 8.3: *Establishing of radioactive equilibrium in test material RV VII-2006 within the time interval of approximately 8 weeks for (top) a plastic dish (large dish) sealed in metallized plastic foil and (bottom) a soldered steel dish.* ^{226}*Ra was determined by different methods described in Sec. 8.4.2. Results using methods 1 and 2 are depicted by different symbols and an average value from the combined method 3 in dashed red line.* ^{226}*Ra values determined via daughter products are marked by triangles and an exponential fit following the activity ingrowth is depicted in a dotted line. The dashed line indicates the reference value. The error bars for all data are 1 standard deviation (they include counting statistics and calibration of the measuring device).*

Table 8.1: *Activity concentrations (C) of ^{226}Ra in sample RV VII - 2006 determined as a weighed mean of repeated measurements using the direct method 3. For the indirect method using daughter products the equilibrium value from an exponential fit at 10 half-lives is taken. The reference value is taken from the intercomparison report (Schkade et al., 2007).*

	Large dish		Steel dish	
	C $Bq \cdot kg^{-1}$	Uncert. $Bq \cdot kg^{-1}$	C $Bq \cdot kg^{-1}$	Uncert. $Bq \cdot kg^{-1}$
^{226}Ra (direct estimation, average)	1163	14	1326	29
^{226}Ra (via daughters - fit)	1064	4	1192	8
Reference value	1230	20	1230	20
	Rel. %	Uncert. %	Rel. %	Uncert. %
^{226}Ra (direct) / reference value	94.6	1.9	107.8	2.9
^{226}Ra (via daughters) /reference value	86.5	1.4	96.9	1.7
^{226}Ra (via daughters) / ^{226}Ra (direct)	91.5	2.4	89.9	2.9

8.5.3 Indirect ^{226}Ra determination

In comparison to directly determined ^{226}Ra activity concentrations, the progeny radionuclides were building up to the equilibrium activity exponentially, as it was expected (Fig. 8.3). In the steel dish no escape of radon from the sample container is expected, therefore the equilibrium activity should reach the reference value. The activity at 10 Rn half-lives estimated by an exponential function fit (3 parameter exponential ingrowth function with an offset, Sigma Plot) to the data is 96.9 ± 1.7% of the reference value. In case of the plastic dish, the equilibrium activity reaches only 86.5 ± 1.4% of the reference value (Tab. 8.1). However, knowing the problematic results from direct ^{226}Ra determination, this can not simply be interpreted as reaching a near to 100% ^{226}Ra reference value in case of the steel dish and not reaching it in the plastic dish.

As it was mentioned earlier, for steel dish samples overestimation of activity concentrations was found for both ^{40}K and ^{137}Cs, which are determined via a single gamma line each, and for directly estimated ^{226}Ra. While ^{226}Ra is also estimated via a single line, a portion (about 25%) of its count is subtracted as a contribution of ^{235}U. Depending on which method is used exactly, ^{235}U contribution to the peak is determined via mostly low-energy lines (Sec. 8.4.2). It is therefore somewhat confusing that activities determined via daughter products (based on gamma energies from a broad energy range) do not show the same overestimation pattern.

One possible (at this stage rather tentative) explanation could be a process involving redistribution of ^{222}Rn within the sample volume, presumably toward the container walls. This would disrupt the assumed geometric efficiency and lead to lower counts detected if Rn products redistribute further away from the detector. The same would be true for the plastic dishes samples. Mauring & Gäfvert (2013) reached the best results when sealing the samples using Al-lined bag and evacuating it, although sometimes this can lead to deformation of the plastic container. They also found a significant effect of void volume above the sample within the sampling container leading to up to 30% activity underestimation compared to the reference value.

When assumed that the upper mentioned redistribution of Rn within the measurement container is fully responsible for the difference between the direct and the indirect ^{226}Ra determination, it contributes to underestimation of ^{226}Ra by up to 10%. The indirectly determined activity reaches $91.5 \pm 2.4\%$ and $89.9 \pm 2.9\%$ of the activity determined directly for plastic and steel dish, respectively (Tab. 8.1). This is a high value and can be considered to be at the upper limit for most of the sample types due to a very high emanation rate that can be expected for this very fine grained material.

It should be noted that the RV VII-2006 material caused difficulties to many participating laboratories within the intercomparison exercise. The mean value of 66 laboratories for ^{226}Ra was only 88.9% relative to the reference value (Schkade et al., 2007). The reason, according to the report, might be its very high emanation coefficient, due to the high fine particle fraction (65% below 63 μm) which was required for good homogenization of the test material before its distribution to the participants. The high emanation rate was also experimentally determined by one of the participants.

8.5.4 Consequences for supported lead estimation in sediments

The initial motivation of this project included an assumption of ^{222}Rn leak from the plastic dishes causing ^{226}Ra being underestimated when analyzed via daughter products. Had this been proven to be the case, it was planned to apply a correction to supported ^{210}Pb. Such solution would involve a factor deduced from a ratio between indirectly and directly determined ^{226}Ra values. The reason for not using direct ^{226}Ra for sediment samples is its relatively low emission rate. However, for each sediment chronology project assuming constant physical sediment properties with a comparable Rn diffusion rate, all spectra can be summed up in order to improve the counting statistics; there are typically 20–40 samples measured in each sediment profile. The correction factor can be then determined from a single summing spectrum.

This proposed original method could not be tested and applied due to upper mentioned difficulties, related likely to efficiency calibration. As it was discussed above and in Chapter 7, the underestimation of activities for sediment-like material measured in a large plastic dish (the most commonly used dish for sediment chronology projects) seems to be rather similar for low, intermediate and high energies. Therefore, it is likely that $^{210}\mathrm{Pb}_{\mathrm{sup}}$ determination (either by a single line or a range of different energies) is effected by the same systematic error as $^{210}\mathrm{Pb}_{\mathrm{tot}}$ and the resulting $^{210}\mathrm{Pb}_{\mathrm{xs}}$. This should therefore not effect the chronologies based on $^{210}\mathrm{Pb}_{\mathrm{xs}}$ significantly and the same holds for previously published data based on LabSOCS efficiency calibration.

Small dishes (another frequently used geometries for gamma spectrometry of sediments) did not show any problems in the LabSOCS efficiency validation test.

The above discussed additional effect of the relative difference between direct and indirect ^{226}Ra determination is difficult to account for and might in the most pessimistic case contribute to additional underestimation of $^{210}\mathrm{Pb}_{\mathrm{sup}}$ by up to 10%, a value estimated from a difference of the direct and indirect ^{226}Ra determination methods.

8.6 Conclusions

This part of the project was dealing with supported lead analysis using ^{226}Ra from a theoretical and practical point of view. The main conclusions are:

1. A possible ^{226}Ra underestimation would have impact also for supported ^{210}Pb estimation via the ^{226}Ra daughter products. Consequently, systematic underestimation of $^{210}\mathrm{Pb}_{\mathrm{sup}}$ would lead to systematic underestimation in $^{210}\mathrm{Pb}_{\mathrm{xs}}$ derived ages, as it was presented on theoretical examples.

2. Three methods of direct ^{226}Ra determination using different gamma lines for subtraction of the ^{235}U contribution to the combined peak were applied on RV VII-2006 sample and resulted in consistent values. It showed up that using multiple lines leads to significant

count improvements and therefore uncertainty reduction. This is mainly important for samples with lower ^{226}Ra activities (or shorter counting times).

3. The measurement series of the RV VII-2006 sample using the large plastic dish with the new metallized foil and the steel dish for preventing ^{222}Rn leakage from the sample did not give an unambiguous answer regarding the leakage. It however confirmed results from Chapter 7 where LabSOCS efficiency validations were presented. ^{226}Ra when analyzed directly via its 186 keV line shows comparable activity concentration underestimation for the plastic dish and overestimation for the steel dish as ^{40}K and ^{137}Cs.

4. It appears that for the plastic dish (the usual container for sediment measurements) the efficiency underestimation is energy independent. It is therefore assumed that it would have no serious consequences for $^{210}\mathrm{Pb}_{\mathrm{xs}}$ chronologies, because $^{210}\mathrm{Pb}_{\mathrm{xs}}$ is calculated as a difference of $^{210}\mathrm{Pb}_{\mathrm{tot}}$ and $^{210}\mathrm{Pb}_{\mathrm{sup}}$. An additional effect of up to 10% ^{226}Ra underestimation might come into account from a not yet fully understood difference between direct and indirect ^{226}Ra determination.

Chapter 9

Depth aligning of paired core samples based on naturally occurring and artificial radionuclides: A case study from off NW Africa[1]

9.1 Introduction

Within interdisciplinary palaeoclimate and environmental studies, for the youngest part of the sediment profile usually a rather detailed age resolution, as well as detailed resolution of other proxies, is desired. For that reason a gravity core (GC) and an associated set of multicorer cores (MUC) is taken at each studied site during many research cruises. While short MUC cores (usually up to 50 cm length) are considered relatively non-disturbed by the sampling procedure, this is typically not the case for gravity cores (several meters long). In the uppermost part of the gravity cores the water-sediment boundary is often missing. Subsequently, it is important to estimate how much sediment was lost in the upper part of the gravity core during the sampling procedure. In order to address this question, an attempt is made to align matching depths of the associated MUC and GC records.

The need to align associated MUC and GC cores can be described as a special case of cross correlation of cores. Cross correlation is used when it is important to compare records from several cores in a wider region (lake, sedimentary basin), from which only one is dated (master core) based on other available parameters in order to transfer an existing chronology.

Several possible approaches have been described to solve this issue practically, including the alignment of downcore variations in one of several measured parameters. They include for example main and trace element concentrations, water content, spheroidal carbonaceous particle records (Rose et al., 1999), biostratigraphic records (Anderson, 1986), stable isotope ratios, dry weight, bulk organic matter (Thompson et al., 2012), magnetic properties (Loizeau et al., 2003) or radiographic properties in varved sediments (Axelsson, 2001). The approaches using visual

---

[1] Parts of this chapter were presented at international meetings:
International Topical Meeting on Polonium and Radioactive Lead Isotopes, Seville, 26.-28.10.2009: D. Pittauerová, S. Mulitza and H.W. Fischer: Using Pb-210 and Cs-137 record for matching sediment cores.
International Symposium on Isotopes in Hydrology, Marine Ecosystems, and Climate Change Studies, Monaco, 27.3.-1.4.2011: D. Pittauerová, S. Mulitza and H.W. Fischer: Gamma spectrometry for chronology of recent sediments - Tracing human induced climate change in NW Africa.

matching or correlation coefficients, as well as statistical procedures using least-squares cubic splines are described in Clark & Thompson (1979). Another widely used method for automated core correlation is based on a mathematical “sequence-slotting”. This method combines two sequences into a single one based on similarities of the objects while preserving the original ordering of each of the sequences members (Thompson & Clark, 1988).

All these methods are suitable rather for longer sequences and for purposes of our limited MUC lengths they are inappropriately complex. They also rely on a higher variability of studied parameters not necessarily present in the short cores. Scanning methods (multisensor core logging for physical properties or multielement XRF) are performed only on GC halves. The matching sets of data are often missing for MUC cores, which are sliced immediately after retrieval and then analyzed for specialized purposes. Therefore, another analytical method of matching associated gravity and multicores using unsupported (excess) ^{210}Pb (^{210}Pb$_{\mathrm{xs}}$) and ^{137}Cs was developed and tested in two case studies of marine sediment profiles taken off NW Africa.

9.2 Materials and methods

9.2.1 Sampling sites selection

During the cruises with the research vessel METEOR, the shipboard echosounding system PARASOUND was used as a tool for localization of promising coring sites. It provided information about the physical properties of the sea bottom and sediment structures up to a depth of 50 m below sea floor.

In addition, the swath bathymetry system HYDROSWEEP was employed for the general sea bottom morphology survey. The detailed 3D information of the sea floor topography provided by HYDROSWEEP contributed to the interpretation of the 2D PARASOUND cross sections.

Site A, Cape Ghir[2]: Gravity core GeoB 6008-1 (further referred to as GC-A) and multicore GeoB 6008-2 (MUC-A) were recovered from 355 m water depth from the continental slope off Cape Ghir, off the coast of Marocco (Tab. 9.1, Figs. 9.1a, 9.1b). This area, the Agadir canyon, consists of a system of numerous canyons of various sizes, whose morphology is generally very steep. Undisturbed sediment packages were localized at the very upper part of the continental slope by PARASOUND (Neuer & cruise participants, 2000). Later, geochemical analyses of samples from these sediment cores were used to investigate upwelling and environmental histories of this area for the recent past (McGregor et al., 2007).

Site B, Mauretania Canyon: Terrigenous sediments deposited at marine site GeoB 9501 were sampled by gravity core GeoB 9501-5 (further referred to as GC-B) and multicore GeoB 9501-4 (MUC-B) on the northern rim of the Mauretania Canyon in the mud belt in front of the Senegal River mouth, from 323 m (and 330 m, respectively) water depth (Tab. 9.1, Figs. 9.1a, 9.1c). The site was selected based upon previous PARASOUND and HYDROSWEEP survey (Mulitza & cruise participants, 2006). This set of cores was used as a sediment archive for studying the Holocene history of Sahel droughts (Mulitza et al., 2010).

---

[2] The dataset for the first case study at site A was not measured and analyzed as a part of the author’s work. The analyses had been performed in the IUP Laboratory previously. The dataset was taken over by DP from the electronic database PANGEA as a supplement to McGregor et al. (2007) paper (DOI:10.1594/PANGAEA.603182 and DOI:10.1594/PANGAEA.603181).

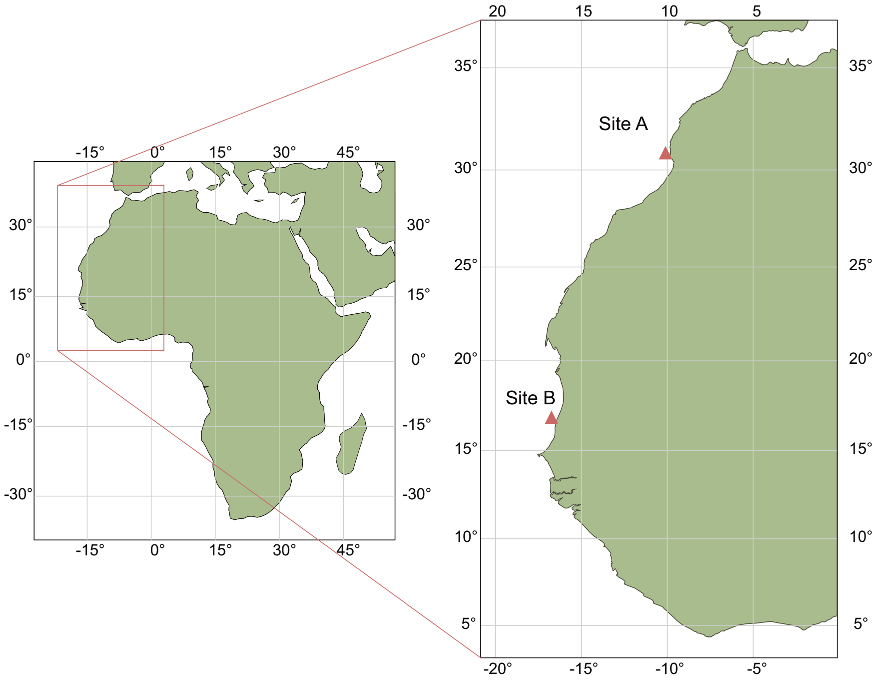

(a) Map of the studied area

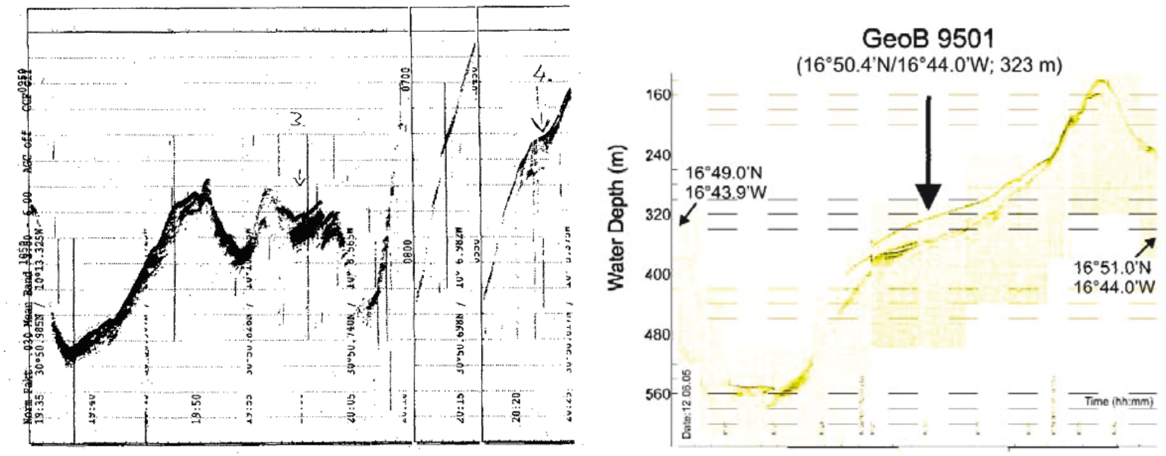

(b) Site A

(c) Site B

Figure 9.1: *(a) Map of the sampling area. (b) Site A: Digital W-E PARASOUND seismogram section towards the Moroccan coast recorded on the northern profile off Cap Ghir. Changes in the water depth range of ParaDigMa are indicated. Number 4 marks the station GeoB 6008 with undisturbed sediment packages (Neuer & cruise participants, 2000). (c) Site B: PARASOUND profile across station GeoB 9501 at the northern rim of the Mauretania canyon. Black and white scale bars at bottom are 1 km wide (Mulitza & cruise participants, 2006).*

Table 9.1: *Summary of sediment cores' sampling and measurement data, remarks to core slicing*

Site	Cruise	Core	Notation	Position, water depth	Sampling date	Remarks
A	METEOR Cruise	MUC GeoB 6008-2	MUC-A	30°50.7′N, 10°05.9′W, 355 m	18.10.1999	Total 32 slices (1 cm thick) measured
	M45/5 1999	GC GeoB 6008-1	GC-A	30°50.7′N, 10°05.9′W, 355 m	18.10.1999	Upper 15 slices (1-2 cm thick) of the top 17 cm long part of the core measured
B	METEOR Cruise	MUC GeoB 9501-4	MUC-B	16°50.38′N, 16°43.96′W, 330 m	12.06.2005	Total 42 slices (1 cm thick) measured
	M65/1 2005	CG GeoB 9501-5	GC-B	16°50.44′N, 16°43.97′W, 323 m	12.06.2005	Every other slice (1 cm thick) of the top 42 cm long section of the core (total 21 slices) measured

9.2.2 Sampling

At both sites[3], a multicorer had been deployed to recover the sediment-water interface, the undisturbed sediment surface and the overlaying water. It was equipped with 8 large and 4 small plastic tubes, each of 60 cm length and 10 and 6 cm in diameter, respectively. A core recovered from one of the larger plastic tubes was used for radiometric analysis. A gravity corer had been deployed to recover longer sediment sequences and only samples from the cores's uppermost parts were studied by gamma spectrometry.

9.2.3 Sample preparation

Site A: Wet sediment material from each 1 cm interval of MUC-A had been placed in an 85 mm diameter by 15 mm high Petri dish, so that the dish was filled completely. Sediment material of the GC-A had been divided into 1-2 cm thick intervals, freeze dried and the upper 15 slices had been placed in the Petri dishes described before.

Site B: Each 1 cm interval of MUC-B and each other 1 cm interval of GC-B (upper 42 cm long part of the core - 21 slices) were placed in the wet form into cylindrical plastic containers with a diameter of 69 mm and a height of 22 mm described as "Large dishes" in Tab. 7.3. The MUC-B samples were filled into different heights in the measurement containers in order to use the maximal amount of material, while the GC-B samples were filled to a uniform height of 10 mm because uniform experimental efficiency calibration was used.

All measurement dishes were sealed in radon proof foil for a minimum of 3 weeks to establish a radioactive equilibrium between ^{226}Ra and ^{222}Rn (and its daughter products). Wet samples were stored at 4°C.

9.2.4 Gamma spectrometry

The samples of both gravity cores and multicores were analyzed using coaxial HPGe detectors (Det. 3 for MUC-B, Det. 5 and 6 for MUC-A, GC-A and GC-B, for specifications see Tab. 5.1) operated under the Canberra Genie 2000 software. Activity concentrations in $Bq \cdot kg^{-1}$ of ^{210}Pb, ^{137}Cs, ^{214}Bi, ^{214}Pb and ^{40}K were determined. Activity concentrations in $Bq \cdot cm^{-3}$ were calculated using measured wet densities (for MUC-A and MUC-B) or dry densities (for GC-A). For GC-B the sediment volume was not estimated reliably, therefore activity concentrations in $Bq \cdot cm^{-3}$ were not known and activity concentrations in $Bq \cdot kg^{-1}$ dry mass were used instead.

^{210}Pb$_{\mathrm{xs}}$ activity concentrations were calculated for each sample as difference between total ^{210}Pb and supported ^{210}Pb. For estimation of supported ^{210}Pb, ^{214}Pb in equilibrium with ^{226}Ra was used. Efficiency calibration for core MUC-B with varying sample sizes was performed using

---

[3] DP was not present to sampling.

a modification of a method proposed by Hurtado et al. (2007), combining both experimental transmission measurements and mathematical Monte Carlo (MC) simulations (Sec. 7.3). For the other cores (MUC-A, GC-A and GC-B) with constant geometries of samples the efficiency obtained experimentally with test sources of a similar geometry was used.

9.2.5 Determination of bulk elemental concentrations

Bulk samples were freeze-dried, powdered and homogenized. The main element concentrations had been determined on 4 g of dry subsamples by energy-dispersive polarization x-ray fluorescence (EDP-XRF) spectroscopy using a Spectro Xepos instrument[4]. The instrument had been operated under Spectro X-Lab Pro software. Quality assurance had been performed by repeated analyses of the certified standard reference material MAG-143. The measured values were within 1% of the accepted value for Si, Al, K, Ca and Fe and within 2% for Ti. The standard deviation of repeated measurements was less than 2%.

9.2.6 Modelled profiles

For testing the proposed aligning procedure, artificial $^{210}Pb_{xs}$ and ^{137}Cs profiles were modelled (Tab. A.7). For the MUC $^{210}Pb_{xs}$ model the initial activity was chosen to be 100 (arbitrary units, a.u.) and with the activities decreasing monotonously towards deeper parts following a simple physical decay law assuming a constant sedimentation rate of 0.25 $cm \cdot y^{-1}$, as well as constant $^{210}Pb_{xs}$ flux. No compaction, mixing or other physical or chemical post-depositional processes were assumed. The sampling interval was set to 1 cm and the depth of the profile to 25 cm. For the GC model the same procedure was applied and the upper 5 cm were cut off. Gaussian noise was added to both MUC and GC profile data to simulate the counting statistics related uncertainty (Fig. 9.2a). The standard deviation ranged from 10% at the top of the profile to about 60% in the bottom part, which are realistic values commonly observed in real activity profiles.

The shape of the modelled ^{137}Cs MUC and GC profiles was derived from an annual ^{137}Cs direct nuclear bomb fallout deposition in the northern hemisphere in 1945–1993 as reported by (UNSCEAR, 2000) with the individual yearly contributions decay-corrected to 1993 (assumed sediment core sampling date). The values (arbitrary units, a.u.) in each 1 cm depth interval represent the relative activity that could be observed when the sediment accumulates with a constant rate (0.25 $cm \cdot y^{-1}$) and no post-depositional disturbance is assumed. Gaussian noise (with standard deviation of 9–12%, depending on activity) was added to the data. Activity values in each profile section under 1% fraction of total fallout deposition were assumed not to be detectable (Fig. 9.2b). This would be the case for activities deposited before 1950 and beyond 1980.

9.2.7 Matching procedure

For both MUC and GC profiles of $^{210}Pb_{xs}$ and ^{137}Cs a numerical matching procedure was performed by a MATLAB code developed for this purpose (Appx. B). Within this procedure, the depth profiles were shifted against each other step-by-step by the smallest sampling interval and the depth region of their overlap (a region where non-zero activities were detected within both profiles) was studied. A value χ, a weighted sum of squared deviations between corresponding pairs of activity concentration values, is determined for each step with a relative offset of both

---

[4] The EDP-XRF analysis had been performed by Matthias Zabel at MARUM, University of Bremen.

cores x:

$$\chi_x = \frac{\sum_{i=1}^{L} w_i (C_{MUC,i} - C_{GC,i})^2}{\sum_{i=1}^{L} w_i} \tag{9.1}$$

where $C_{MUC,i}$ and $C_{GC,i}$ are the i-th data points in the region of overlap of the MUC and GC profiles, respectively. The uncertainty of χ_x is calculated based on error propagation. L is the number of data points within the region of overlap. Only regions with $L \geq 3$ were taken into account. Higher weight w_i was given to values with lower experimental uncertainty, expressed as:

$$w_i = \sigma^2_{C_{MUC,i} - C_{GC,i}} = \sigma^2_{C_{MUC,i}} + \sigma^2_{C_{GC,i}}, \tag{9.2}$$

where $\sigma_{C_{MUC,i} - C_{GC,i}}$ is uncertainty of the i^{th} pair difference and $\sigma_{C_{MUC,i}}$ and $\sigma_{C_{GC,i}}$ the individual experimental uncertainties of activity measurements.

The value of $\chi_x \to 0$ for the best core match and the value of offset x associated to the minimum χ can be used for estimation of the length lost on top of the gravity core during sampling. The procedure was tested on one modelled and the two aforementioned real sets of $^{210}\mathrm{Pb}_{\mathrm{xs}}$ and $^{137}\mathrm{Cs}$ radionuclide profiles.

9.3 Results and discussion

9.3.1 Modelled profiles

When the aligning procedure was applied to the modelled profiles, a minimum value for χ_x was found for the offset $x = 5$ cm for both $^{137}\mathrm{Cs}$ and $^{210}\mathrm{Pb}_{\mathrm{xs}}$ modelled profiles, which agreed exactly with the length of the core being cut off in this model situation (Fig. 9.2c).

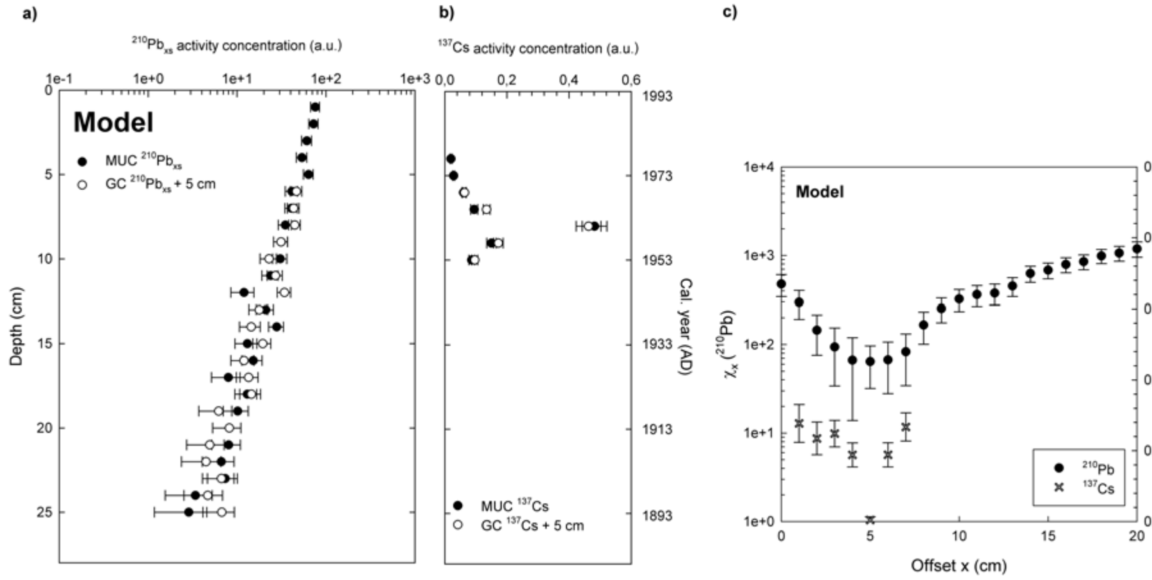

Figure 9.2: *Modelled profiles of a) $^{210}Pb_{xs}$(log-scale) and b) ^{137}Cs (linear scale). c) Calculated χ_x values for MUC and GC offsets for modelled profiles of $^{210}Pb_{xs}$ (log scale) and ^{137}Cs (linear scale). The χ_x error bars are calculated by error propagation.*

9.3.2 Site A

The matching procedure for $^{210}\mathrm{Pb}_{\mathrm{xs}}$ and $^{137}\mathrm{Cs}$ profiles of GC-A and MUC-A cores (Tab. A.8) as described above resulted in wider minima of χ_x at offsets around $x = 9.5$ cm for $^{210}\mathrm{Pb}_{\mathrm{xs}}$ and $x = 12.5$ cm for $^{137}\mathrm{Cs}$ (Fig. 9.3). As opposed to the modelled profile, the offset values are not integer numbers because the slicing of MUC and GC were not carried out at identical intervals. Taking into account both tracers, the material loss in the upper part of the GC-A was estimated to be a value lying in the middle of both upper mentioned values, 11 cm, therefore identical as previously published for this core (McGregor et al., 2007). Although the match between the individual results derived from $^{210}\mathrm{Pb}_{\mathrm{xs}}$ and $^{137}\mathrm{Cs}$ profiles is not completely satisfactory, the 2σ intervals of resulting χ_x at $x = 11$ cm overlap with both respective absolute χ_x minima.

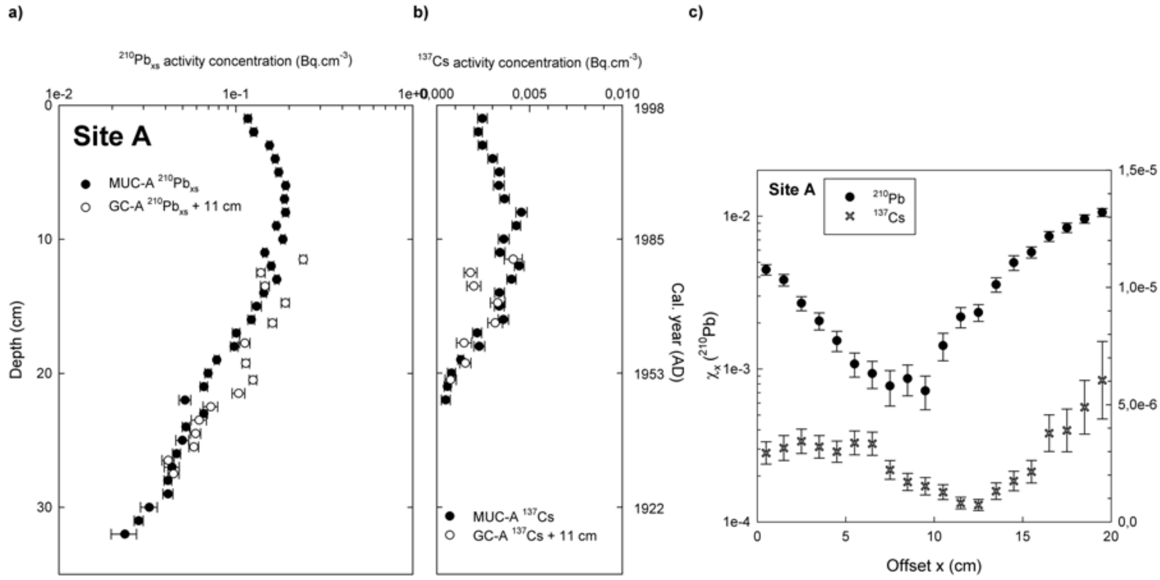

Figure 9.3: *Site A: Depth matching of the multicore and gravity core records. a)* $^{210}Pb_{xs}$ *(log-scale) and b)* ^{137}Cs *(linear scale) profiles.* ^{137}Cs *data points under 22 cm depth for the MUC-A and under 21 cm for the GC-A are under decision threshold. The error bars for all data are 1 standard deviation (they include counting statistics and calibration of the measuring device. c) Calculated* χ_x *values for MUC-A and GC-A offsets x (log scale for* $^{210}Pb_{xs}$*, linear scale for* ^{137}Cs*).*

For MUC-A the constant rate of supply (CRS) (Sec. 3.2.2) $^{210}\mathrm{Pb}$ chronology model had been used (McGregor et al., 2007). Absolute ages had been calculated assuming the top of the core dates back to 1998 AD. The data of $^{137}\mathrm{Cs}$ activity concentration had been compared to the known $^{137}\mathrm{Cs}$ bomb fallout atmospheric input in the northern hemisphere with an absolute maximum in 1963 AD (UNSCEAR, 2000), as a validation of $^{210}\mathrm{Pb}$ chronology. The $^{137}\mathrm{Cs}$ data support the $^{210}\mathrm{Pb}$ chronology, as the maximum of the $^{137}\mathrm{Cs}$ contamination (1964 AD) coincides with the calculated $^{210}\mathrm{Pb}$ age (1963 AD). The MUC-A $^{210}\mathrm{Pb}$ chronology extends to 1913 AD for a depth of 32 cm.

9.3.3 Site B

Depth matching

The depth matching of the gravity core and the multicore was performed using the corresponding $^{210}Pb_{xs}$ and ^{137}Cs profiles (Tab. A.9) by the method described above. Minimum values of χ_x were observed at a broad region of $x = [13.5, 22.5]$ cm for $^{210}Pb_{xs}$ and $x = [20.5, 23.5]$ cm for ^{137}Cs. Since the aligning procedure using $^{210}Pb_{xs}$ and ^{137}Cs records did not lead to completely consistent results (i.e. identical offsets), additional assumptions must be taken into account to make the final offset estimation. As a supporting alignment criterion, the onset of ^{137}Cs in both cores (29.5 cm in MUC-B and 8 cm in GC-B) was used, as the detection thresholds for ^{137}Cs in both sets of samples were comparable. Therefore, approximately 21.5 cm of sediment material was estimated to be lost during gravity coring (Fig. 9.4). The $^{210}Pb_{xs}$ profile appears to be disturbed in the uppermost part of the GC-B (not an unusual finding due to the mechanical force applied during coring), but it shows a good continuity with the MUC-B profile from the composite depth of 43 cm downwards, which enables extension of the chronology.

Verification

The correctness of the matching procedure for site B was additionally verified by inspecting Fe content and (Al+Fe)/(Si+K+Ti) ratio profiles (Fig. 9.5). In this ratio Al and Fe represent the riverborne component of the sediment composition, while Si, K and Ti stand for the aeolian component. The profiles of MUC-B and GC-B showed a good overlap and continuity of both parameters when shifted by 21.5 cm, an offset derived from matching ^{210}Pb and ^{137}Cs profiles. Such chemical or physical parameters that show high variability in the 150 years time scale, like the example from site B in Fig. 9.5, enable parallel core depth alignments. They are not always readily available for each studied station. Therefore, ^{210}Pb and ^{137}Cs profiles provide this opportunity as a by-product of the recent sediment chronology.

MUC sediment chronology

The $^{210}Pb_{xs}$ age model for MUC-B was developed applying the CRS model (Sec. 3.2.2). The absolute chronology extends to 1915 AD in the depth of 42.5 cm (Fig. 9.6).

^{137}Cs activity concentrations were compared to the known ^{137}Cs bomb fallout atmospheric input. According to the ANNEX C of the UNSCEAR (2000) report, the total amount of ^{137}Cs deposited from 1945 to 2000 in a latitudinal band of 10–20°N recalculated to 2007 activities (time of the measurement) is approximately 700 $Bq \cdot m^{-2}$. Comparing the inventory of 141 ± 12 $Bq \cdot m^{-2}$ found in the core GeoB 9501-4 to the UNSCEAR value, only 20% of the expected value was preserved in the sediment record.

The onset of ^{137}Cs in the profile in 1949 AD is in relatively good agreement with atmospheric bomb testing initiation in the early 1950's. Due to rather low ^{137}Cs values the measurement uncertainties are relatively high and do not provide fine resolution. The expected 1963 AD maximum was absent, instead the ^{137}Cs data show a broad maximum in approximately 1959–1982 AD. Contribution from four geographically close French atmospheric tests performed in 1960–61 in Algeria (Menut et al., 2009; Masson et al., 2010; Danesi et al., 2008) can not be expected in the record either due to their very low yield compared to the cumulative global atmospheric test yield. Nevertheless, the shape of the ^{137}Cs profile is compatible with the bomb fallout chronology, possibly followed by a terrestrial (erosion-produced) component.

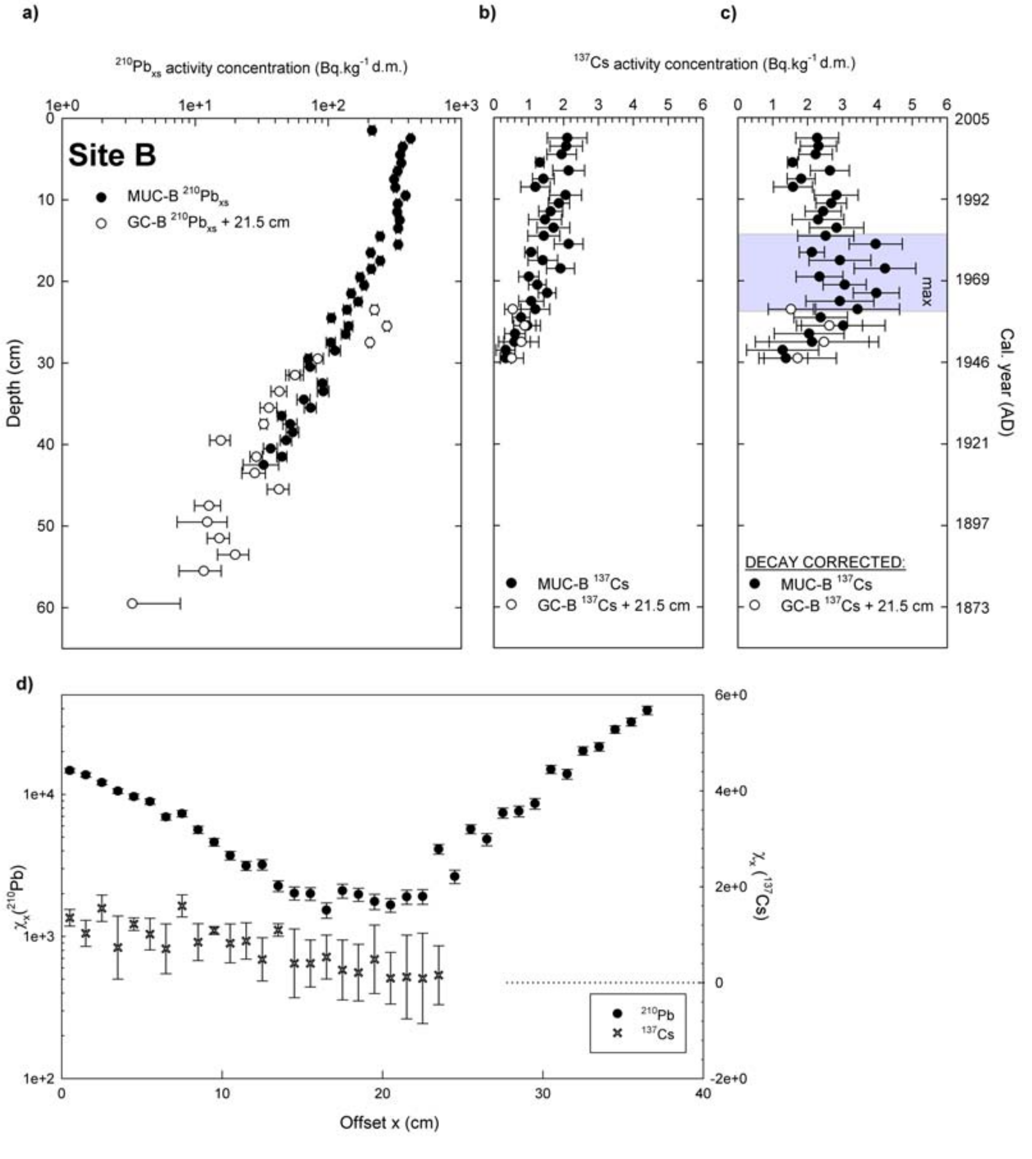

Figure 9.4: *Site B: Depth matching of the multicore and gravity core records. a) $^{210}Pb_{xs}$ (log-scale) and b) ^{137}Cs (linear scale) profiles. In c) ^{137}Cs activity concentrations are decay corrected according to ages derived from the $^{210}Pb_{xs}$ model. A broad fallout maximum is marked. ^{137}Cs data points under 30 cm depth are under decision threshold. The error bars for all data are 1 standard deviation (they include counting statistics and calibration of the measuring device).*
d) Calculated χ_x values for MUC-B and GC-B offsets x (log scale for $^{210}Pb_{xs}$, linear scale for ^{137}Cs).

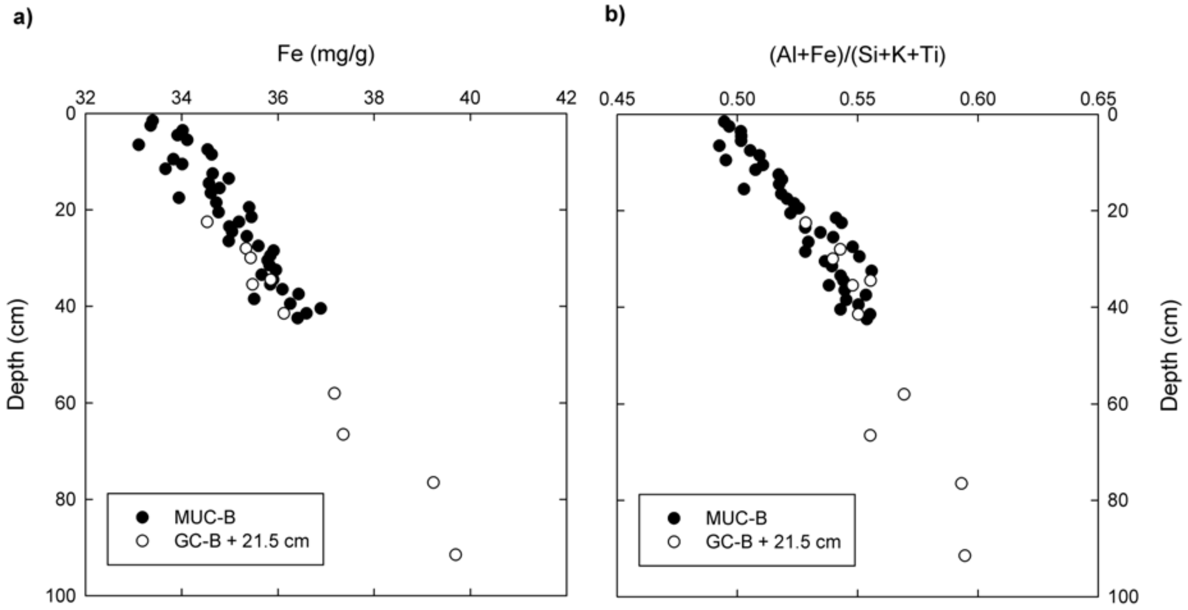

Figure 9.5: *Depth matching of the site B multicore and gravity core records for a) Fe and b) (Al+Fe)/(Si+K+Ti) element profiles.*

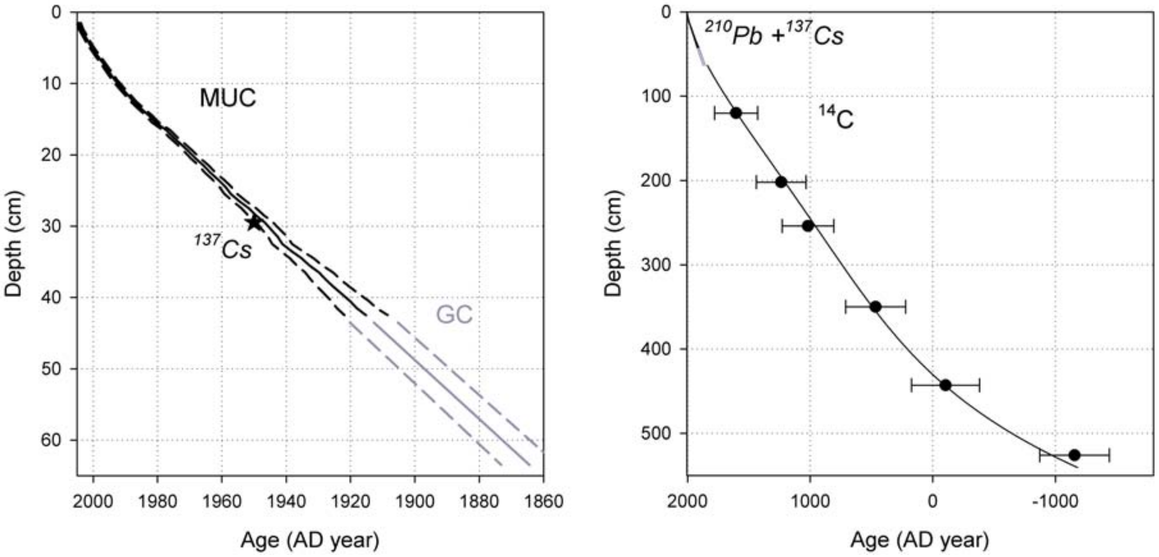

Figure 9.6: *A combined chronology of GC using $^{210}Pb_{xs}$ and ^{14}C. The dashed lines stand for 1 σ confidence limit of $^{210}Pb_{xs}$ ages. ^{137}Cs onset in the depth of 29.5 cm is in good agreement with the $^{210}Pb_{xs}$ chronology. The presented error bars for ^{14}C data represent 2σ uncertainty.*

9.3.4 Reservoir age

The recent chronology also made it possible to quantify local reservoir effects (Sec. 2.1.2) for radiocarbon chronology (Mulitza et al., 2010)[5]. Foraminifera selected from a sample at the bottom of a parallel MUC core (sample KIA35172, the age of the layer was estimated to approximately 1907 AD) had been analyzed by AMS for ^{14}C. The fraction or modern carbon fMC value was determined to be 0.9235 ± 0.0036 and was converted to $\Delta\ ^{14}$C (‰) (a relative value to an international standard) as:

$$\Delta^{14}C = (fMC \cdot e^{\frac{(1950-Y_m)}{\tau}} - 1) \cdot 1000, \tag{9.3}$$

where Y_m is the year of measurement (2008) and τ is the mean life^{14}C (8267 yr). The initial radiocarbon concentration $\Delta\ ^{14}\mathrm{C}_{\mathrm{ini}}$ was determined using:

$$\Delta^{14}C_{ini} = \left((\frac{\Delta^{14}C}{1000} + 1) \cdot e^{\lambda \Delta t} - 1 \right) \cdot 1000, \tag{9.4}$$

where λ is ^{14}C decay constant and Δt the time elapsed between the year of deposition and measurement (101 years). The $\Delta\ ^{14}\mathrm{C}_{\mathrm{ini}}$ can be converted back to fMC_{ini} using a recombination of Eq. 9.3 and the reservoir age ΔR is expressed as:

$$\Delta R = -\tau_L * ln(fMC_{ini}), \tag{9.5}$$

where τ_L is Libby ^{14}C mean life (8033 years). The reservoir age for the early 20th century was estimated as $\Delta R = 541 \pm 31$ yr (Mulitza et al., 2010). It is abut 140 years more than the modern average surface ocean radiocarbon reservoir age of 400 years (Stuiver & Braziunas, 1993).

GC sediment chronology

Following the aligning of MUC-B and GC-B, the age model for the multicore could be extended to the gravity core based on an average sedimentation rate obtained from a combined record of multicore $^{210}\mathrm{Pb}_{\mathrm{xs}}$ data from the depths of 16.5–42.5 cm with the follow-up part of the gravity core (depth 43.5–63.5 cm). This part of the composite profile showed an exponential decrease of activity, which allowed for expressing a mean sedimentation rate based on an exponential fit obtained by the least squares method (CF-CS model - Sec. 3.2.1). The average sedimentation rate was then used for dating the gravity core to the composite depth of 63.5 cm, corresponding to 1864 AD. The combined MUC-B and GC-B chronology based on gamma spectrometry covered the youngest 140 years of the core. Interconnection of the combined $^{210}\mathrm{Pb}_{\mathrm{xs}}$ and ^{137}Cs model with the radiocarbon model of the GC was possible (Fig. 9.6).

In the deeper part of the GC chronology had been built upon AMS ^{14}C measurements on planktonic foraminifera (Tab. A.10 in Appx. A) (Mulitza et al., 2010)[6]. Raw radiocarbon ages had been converted into calendar dates using the CALIB 5.0.2 calibration tool (Stuiver et al., 2005) with the MARINE04 calibration dataset (Hughen et al., 2004) and a reservoir correction of 400 years and an additional constant local reservoir effect of 140 yr presented above.

Two of the analyzed radiocarbon ages had not been included in the final age model. The radiocarbon age at 52 cm falls within the Little Ice Age for which models suggest a considerably

---

[5] The reservoir age had been calculated by Gesine Mollenhauer, MARUM, University of Bremen and AWI, Bremerhaven

[6] The age model for the deeper part of GC had been created by Gesine Mollenhauer, MARUM, University of Bremen and AWI, Bremerhaven

higher reservoir effect for the core location[7] (Franke et al., 2008). Additionally, the age lies at a plateau in the calibration curve, which produces ambiguous results. Another sample at the base of the gravity core at 530 cm had been excluded because potential inclusion of older material from the core catcher.

A forth order polynomial function had been fitted to the pooled remaining calibrated radiocarbon dates and ^{210}Pb dates in order to produce a combined chronology (Mulitza et al., 2010):

$$t = -8.625032 \cdot 10^{-8} \cdot z^4 + 7.714495 \cdot z^3 - 0.0248636 \cdot z^2 - 1.378884 \cdot z + 2.007679 \cdot 10^3, \quad (9.6)$$

where t is age (years AD) and z depth (Fig. 9.6).

Use of the age model for palaeoclimatological interpretations

Further sediment sample parameters had been determined, including bulk geochemistry of Si, Al, Ti, K, Ca and grain size analysis by a team of MARUM. The data had been analyzed and interpreted in Mulitza et al. (2010)[8]. It was found that main constituents of the studied sediment material are aeolian dust (Si rich, with particles up to 200 μm) and fine Senegal river suspension (Al and Fe rich, 95% $<$ 10 μm). The relative proportions of riverine, aeolian and marine contributions were calculated by end-member analysis[9]. Dust and fluvial end-members were constructed using the normalized relative abundances of Si, Al, Ti, K and Ca from modern aeolian and riverborne materials and the marine end-member was constructed theoretically (98% Ca, 2% Si) (Mulitza et al., 2010). The knowledge of sedimentation rates allows calculation of dust fluxes in the past (Fig. 9.7).

The reconstruction of the history of the African dust generation showed, that the onset of commercial agriculture about 200 years ago started to contribute to the overall dust inventory (Fig. 9.7). Corn was introduced to the Sahel in early 18th century. It was gradually replaced by millet and sorghum in the mid 18th century. The steepest dust deposition increase can be observed in the period of commercial peanuts production in Senegal, Nigeria and the Gambia starting with the 1840's. It was suggested, that deforestation and expansion of agricultural use of the land in the Sahel zone contributed extensively to wind erosion in the region (Mulitza et al., 2010).

9.3.5 Limitations

A possible limitation of the presented method for paired core aligning could be neglecting compaction effects, which might eventually vary between different sampling techniques. This issue was not treated within this project. It is not a fully automated technique, but provides a useful tool for making the core aligning process better defined. As it was observed at both case study sites, the results from aligning ^{210}Pb$_{\text{xs}}$ and ^{137}Cs profiles do not necessarily lead to completely consistent results (identical offsets). Even though application of additional knowledge leads to satisfactory estimates.

---

[7] The date had been retrieved from the on-line Reservoirage Database accessible at `http://www.reservoirage.uni-bremen.de` (Franke et al., 2008).

[8] The XRF scanning on GC-B was done by Stefan Mulitza, MARUM. The data were calibrated by David Heslop, MARUM. Inka Meyer and Jan-Berend Stuut, both MARUM, performed grain-size analyses.

[9] The end-member model was calculated by David Heslop, MARUM.

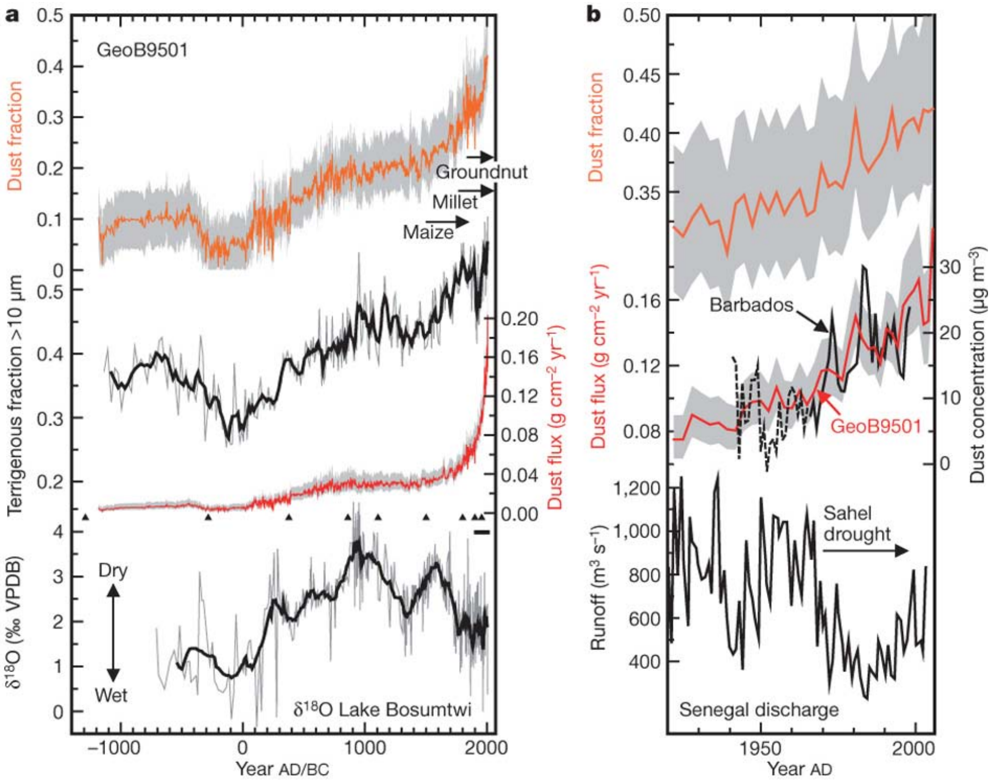

Figure 9.7: a) The mean dust fraction, terrigenous grain-size fraction > 10 μm and dust deposition flux records were compared to literature data on $\delta^{18}O$ authigenic carbonate from lake Bosumtwi (Ghana) (Shanahan et al., 2009), indicating dry and wet periods in the Sahel history. The triangles indicate radiocarbon age control and the horizontal bar the time period dated by $^{210}Pb_{xs}$ and the ^{137}Cs method. b) Recent records of mean dust fraction and dust deposition flux compared to instrumental measurements of airborne African dust concentrations at Barbados from the mid-1960's (Prospero & Lamb, 2003) (the pre-1968 record is estimated from regression with Sahel precipitation) and Senegal river discharge (Isupova & Mikhailov, 2008). Source: Mulitza et al. (2010).

9.4 Conclusions

The $^{210}\mathrm{Pb}_{\mathrm{xs}}$ and $^{137}\mathrm{Cs}$ depth profiles of the corresponding multicores and gravity cores at two studied locations were compared and the best match for the cores was assessed. The method of aligning the cores proved to be suitable specially for situations when there is lack of other information for MUC (elemental composition, physical properties) or these parameters do not show variations within the studied core intervals. Using the radionuclide profiles which usually show variations (as a pre-requisite for the dating method) for aligning the cores is a notable by-product of the radionuclide based chronology. The method was tested on modelled radionuclide profiles and at site B the correctness of core aligning was verified by examining profiles of selected major elements.

As a result, the information about the amount of the sediment missing in the upper part of the gravity cores can be obtained which allows geochemical profiles measured on both types of cores to be aligned and interconnected. At the same time, at site B, it enabled extension of the sediment chronology for another 20 cm down the gravity core and the local radiocarbon reservoir effect to be estimated. This method significantly helps to expand palaeoclimatic proxy data into the Anthropocene, thereby allowing comparing human induced climate change with natural climate variability.

Chapter 10

Artificial radionuclides in deep-sea sediments from Indonesia

10.1 Introduction

A study of natural and artificial radioisotopes in sediments at a site off Sumba Island, Indonesia, has been performed in cooperation with MARUM, University of Bremen, as part of the project "Multi-decadal to centennial-scale development of the Indonesian-Australian summer monsoon over the last 6,000 years" (principal investigator Dr. Stephan Steinke). As the project title suggests, the timescale covered by available sediment cores covers the last 6 millenia and also the youngest time period, presumably containing information of recent climate changes, is of high interest. The dating of the sediment from the last century and also the interconnection of the multi-cores with a gravity core (in a similar way like in Chapter 9) was performed using gamma spectrometry.

Sedimentation rates were estimated by radiocarbon dating on selected cores in the area of the Lombok Basin (GeoB 10065) and the Savu Sea (GeoB 10069) by linear interpolation between radiocarbon dating points (Baumgart et al., 2010). They vary between 0.1–0.2 $\mathrm{cm \cdot yr^{-1}}$.

The aim of the radionuclide study performed on this core was to establish a reliable chronology for multi-cores and for the youngest part of the GC.

10.2 Regional setting

The Indonesian throughflow (ITF) provides a low-latitude connection for warm fresh water to flow from the Pacific to the Indian Ocean. This complex array of passages within the Indonesian archipelago (Fig. 10.1) represents an important pathway for radionuclide transport between both water bodies (Bard et al., 1989; Povinec et al., 2003).

The North Equatorial Current (NEC) is an east-to-west Pacific ocean current corresponding to the southern side of a clockwise subtropical gyre located along 15°N. It is separated from the equator by the west-to-east North Equatorial Countercurrent (NECC). Radionuclide concentrations in the area are influenced by local fallout after nuclear weapon tests carried out at Bikini and Enewetak Atolls, which is a source for radionuclides transported along the NEC. At about 130°E the NEC divides into two branches, of which radionuclides are transported further north by the northern branch - Kuroshio Current (KC) into the western North Pacific margin (e.g., Zheng & Yamada, 2004; Lee et al., 2004), whereas the southern branch, Mindanao Current (MC), is partially diverted towards the Celebes (Sulawesi) Sea and further to the ITF.

The principal straits separating the eastern Indian Ocean from the interior Indonesian Seas (Banda Sea, Flores Sea) are Lombok Strait, Sumba Strait, Ombai Strait, Savu/Dao Straits, and Timor Passage (Hautala et al., 2001; Sprintall et al., 2009). Lombok, Savu and Timor throughflows join to form the northern section of the South Equatorial Current (SEC). Its total volume transport is estimated to 9.5–10 Sv (unit Sverdrup, 1 Sv = $10^6\ m^3 \cdot s^{-1}$, not to be confused with Sievert, a unit of equivalent dose) (Gordon, 2005; Wijffels et al., 2008).

10.3 Artificial radionuclides in the central Indo-Pacific region

The study area is geographically located between the Indian and Pacific oceans. Artificial radioactivity of the Indian ocean is mainly governed by the global nuclear fallout, in the southern part influenced strongly by the SNAP-9A fallout (Sec. 2.1.3).

A minor local effect can be attributed to the Monte Bello Islands British atmospheric nuclear testing series between 1952-56 off NW Australia, with total fission yield estimated to be 0.1 Mt (UNSCEAR, 2000). The largest explosion accounting for practically the entire mentioned yield was preformed in 1965 (MOSAIC-G2 test) on Alpha Island in the Monte Bello archipelago (Child & Hotchkis, 2013). On the other hand, the region of the the western Pacific is strongly affected by local contributions from the American atmospheric tests at the Pacific Proving Grounds (PPG) (Marshall Islands, atolls Bikini and Enewetak). Between 1946-1958 a total estimated fission yield of 57.7 Mt was produced (UNSCEAR, 2000) there, which is an important portion of the estimated total global fission yield of all atmospheric tests of 189 Mt (UNSCEAR, 2000).

Table 10.1 presents an overview of marine radionuclide studies performed in the region of the NW Pacific and adjacent seas, ITF and the Indian ocean. They include tracer studies of artificial radionuclides in sediments and water. The locations of the studies are shown in Fig. 10.2.

Lee et al. (2005) analyzed bottom sediments from 4 sites in the NW Pacific Ocean for ^{137}Cs, ^{90}Sr, ^{241}Am and Pu isotopes. The highest ^{239,240}Pu activities (up to 10 Bq·kg^{-1}) were found in a station located close to Bikini Atoll, a site influenced strongly by local fallout. Nuclear fallout from Marshall Islands tests contributed greatly to the sediment and water column inventory of ^{239,240}Pu and ^{241}Am in the NW Pacific, while ^{137}Cs and ^{90}Sr inventories were comparable to the global fallout. As a result of scavenging, the fraction of ^{241}Am in sediment was found to be much higher than in the water column in the whole study area. The same situation with the ^{239,240}Pu inventory in sediment exceeding that of the water column was observed near the Bikini Atoll, although in the other stations in the NW Pacific most Pu was still present in the water column. The majority of ^{137}Cs and ^{90}Sr inventories also stays in the water column due to their high solubility. These findings about the distribution of Pu between water and sediment are in agreement with Aarkrog (1988), who concluded, that more than 90% of Pu in the open ocean stays in the water column. In coastal waters, though, nearly all Pu is found in the sediment with only a few percent remaining in the water column.

Examinations of grab samples of sediments from 13 sites in the Sea of Japan, Okhotsk Sea and the NW Pacific (Pettersson et al., 1999) showed maximum ^{241}Am values in the range of 0.03–1.85 Bq·kg^{-1} d.m. The activity ratios ^{137}Cs/^{241}Am were reported in the range of 10–50 for samples from Okhotsk Sea, 4 from the Sea of Japan and 2–10 in the NW Pacific. Although these samples were taken in the vicinity of sites of past dumping of radioactive waste, the total inventory of the isotopes in water and sediments, as well as isotopic ratios, can be assigned to global fallout of artificial radionuclides.

Lee et al. (2003) measured Pu and Am isotopes in water and sediments of marginal seas of the NW Pacific. They showed that ^{241}Am/^{239,40}Pu activity ratios are close to the global

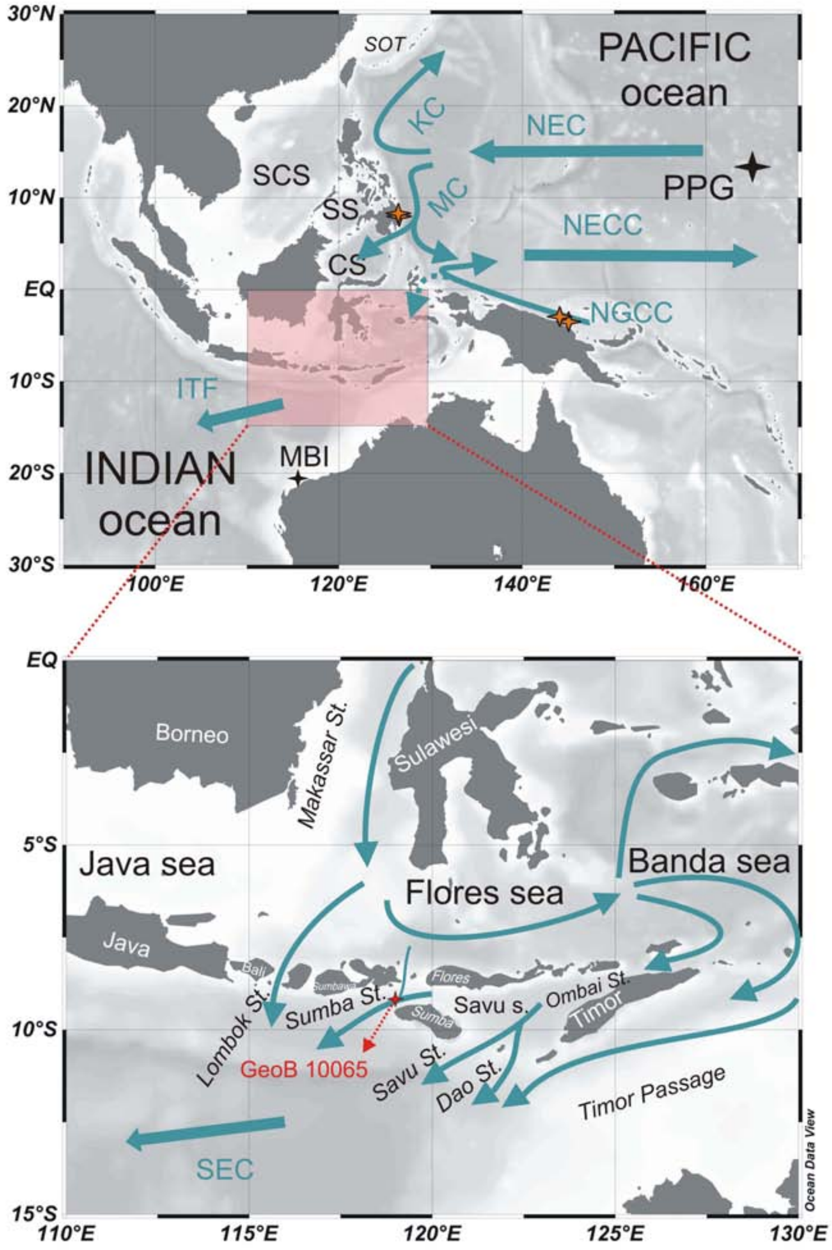

Figure 10.1: *A map of the study area with names of the islands, straits, and seas as well as main currents of the Indonesian throughflow (ITF). Top: PPG = Pacific Proving Ground, MBI = Monte Bello Islands, SOT = South Okinawa Through, SCS = Southern China Sea, SS = Sulu Sea, CS = Celebes Sea, NEC = North Equatorial Current, NECC = North Equatorial Countercurrent, KC = Kuroshio Current, MC = Mindanao Current, NGCC = New Guinea Coastal Current. Bottom: SEC = South Equatorial Current. Modified after Wijffels et al. (2008) and Gordon (2005).*
The studied core GeoB 10065 is marked in the lower map by a red star. Additionally, positions of new GeoB cores East off Mindanao (Philippines), off Sepik River (Papua New Guinea), and Bismarck Sea (Papua New Guinea) for future studies are marked by orange stars in the upper map.

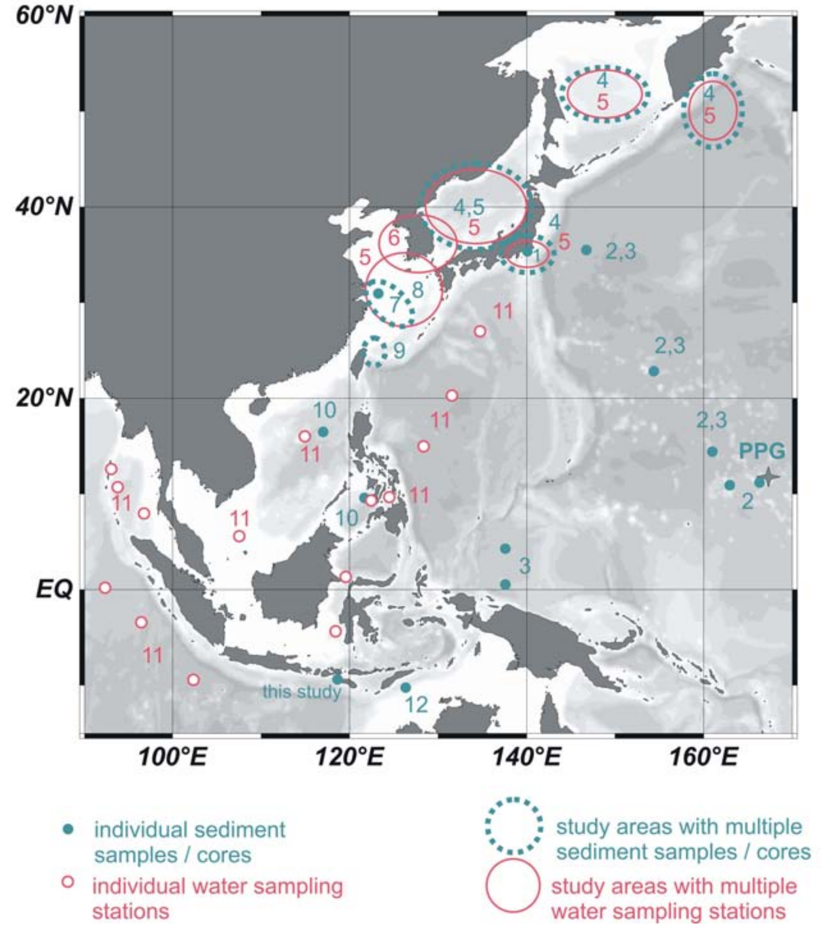

Figure 10.2: *A map of previous artificial radionuclide studies in the Indo-Pacific region. The numbers correspond to studies referred to in Tab. 10.1 (note that studies 13 and 14 had been performed in the Indian ocean and are not included in the map.*

fallout value of 0.37, while sediments are enriched in Am with ratios of 1.0–1.9. This feature was explained by faster scavenging of Am over Pu.

Lee et al. (2004) showed transport of plutonium from the PPG westward from the Marshall Islands by the North Equatorial Current (NEC) followed by northward transport by the Kuroshio current and its deposition to sediments of the Southern Okinawa Trough based on relative positions of ^{239,40}Pu and ^{240}Pu/^{239}Pu ratios subsurface maxima. The transit time from the PPG (5600 km) was estimated to be about 6 years. The plutonium signal related to the PPG was also reported from sediments from the continental shelf of the East China Sea (Pan et al., 2011) and East China Sea and Okinawa Trough (Wang & Yamada, 2005).

Also the study of deep-sea sediment cores from the Sulu and South China Seas (Dong et al., 2010) revealed ^{240}Pu/^{239}Pu ratios higher than global fallout ratios, indicating the source of Pu being the PPG. This agrees with results of the sea water radionuclide study of Kim et al. (2004), who explained increased ^{240}Pu/^{239}Pu ratios in seas around the Korean Peninsula (SW part of Sea of Japan, Yellow Sea and Korea Strait) by transport of Pu from the PPG by prevailing ocean currents.

Yamada et al. (2006) studied artificial radioactivity of surface waters in the NW Pacific, E Indian Ocean and adjacent seas. Based on elevated ^{240}Pu/^{239}Pu atom ratios compared to global fallout values they concluded, that the contribution of plutonium from PPG is 42% in South China Sea and 39% in the area of Sulu and Indonesian Seas (Celebes Sea and Makassar Strait).

Burns et al. (2003) reported relatively high ^{241}Am concentrations in sediment cores and grab samples taken from the Cartier Trough, Timor Sea, in June 2002. The absolute values reached up to 1.3 Bq·kg^{-1} d.m., which is the same order of magnitude as ^{137}Cs at the same site. The original hypothesis was that the origin of this ^{241}Am anomaly can be high fallout from the 1952–56 Monte Bello Island bomb tests (CSIRO Division of Marine Research, 2003), however later non-published plutonium isotopic ratios analyses performed on the same core from 260 m depth (Gregg Brunskill, personal communication) indicate partial PPG origin.

There is other evidence for transport of radionuclides from the Pacific to the Indian Ocean through the ITF based on observation of higher concentrations of ^{3}H, ^{90}Sr and ^{137}Cs in the Indian Ocean region south of the Equator (up to 30°S) explained by the influx of Pacific waters through the Indonesian archipelago and a system of equatorial currents that re-circulates surface water masses in the region (Povinec et al., 2003). The observed levels of transuranic elements in the Indian ocean are higher in areas with lower primary productivity, which is explained by less effective scavenging of particle reactive radionuclides.

10.4 Methods

Samples represented by 4 cores taken at a single station were analyzed. The summaries of sampling data are listed in Tab. 10.2. Three parallel sediment multi-cores GeoB 10065-9 (further only MUC-A, MUC-B and MUC-C) and the upper part of a gravity core GeoB 10065-7 (further only GC) recovered from the eastern Lombok Basin NW off the Indonesian Sumba Island during the RV SONNE SO-184 "PABESIA" expedition in September 2005 (Hebbeln & cruise participants, 2006) were analyzed. The sampling site is located in a region affected by coastal upwelling during the southeast summer monsoon season. Sediments sampled by GC and MUC consist of olive to dark olive nannofossil ooze. The main constituents are the lithogenic portion (73%), formed mainly by clay minerals (Gingele et al., 2001), and $CaCO_3$ (16%) in the surface sediment (Baumgart et al., 2010). A (erosive) turbidite layer occurs in the depth interval of 37 cm to 40 cm in GC.

Table 10.1: *Previous artificial radionuclide studies in the Indo-Pacific region. Ref. # refers to numbers used for localization of study areas in Fig. 10.2.*

Study areas	Radionuclides (water)	Radionuclides (sediment)	References	Ref. #
NW Pacific Ocean (Sagami Bay)		^{137}Cs, ^{239,240}Pu, ^{240}Pu/^{239}Pu	Zheng & Yamada (2004) and references therein	1
NW Pacific Ocean		^{90}Sr, ^{137}Cs, ^{238}Pu, ^{239,240}Pu, ^{241}Am	Lee et al. (2005)	2
NW Pacific Ocean (NW Central and West Caroline basins)		^{90}Sr, ^{14}C, ^{137}Cs, ^{238}Pu, ^{239,240}Pu, ^{241}Am; ^{210}Pb, ^{226}Ra, ^{230}Th, ^{232}Th, ^{238}U	Moon et al. (2003)	3
NW Pacific Ocean Sea of Japan Okhotsk Sea		^{90}Sr, ^{137}Cs, ^{238}Pu, ^{239,240}Pu, ^{241}Am	Pettersson et al. (1999)	4
East China Sea Yellow Sea Sea of Japan Okhotsk Sea NW Pacific Ocean	^{239,240}Pu, ^{241}Am	^{239,240}Pu, ^{241}Am	Lee et al. (2003) and references therein	5
Sea of Japan Yellow Sea Korean Strait	^{239,240}Pu, ^{240}Pu/^{239}Pu		Kim et al. (2004)	6
East China sea		^{137}Cs, ^{239,240}Pu, ^{240}Pu/^{239}Pu	Pan et al. (2011)	7
East China Sea Okinawa Trough		^{239,240}Pu, ^{240}Pu/^{239}Pu; ^{210}Pb	Wang & Yamada (2005)	8
South Okinawa Trough		^{137}Cs, ^{239,240}Pu, ^{240}Pu/^{239}Pu; ^{210}Pb$_{\mathrm{xs}}$	Lee et al. (2004)	9
South China Sea Sulu Sea		^{239,240}Pu, ^{240}Pu/^{239}Pu	Dong et al. (2010)	10
NW Pacific Ocean Sulu and Indonesian Seas East Indian Ocean Bay of Bengal	^{137}Cs, ^{239,240}Pu, ^{240}Pu/^{239}Pu		Yamada et al. (2006) and references therein	11
Timor Sea		^{137}Cs, ^{241}Am; ^{210}Pb$_{\mathrm{xs}}$, ^{228}Th$_{\mathrm{xs}}$, ^{234}Th$_{\mathrm{xs}}$	Burns et al. (2003)	12
Tropical equat. Indian Ocean	^{14}C		Bard et al. (1989)	13
Indian Ocean transect	^{3}H, ^{90}Sr, ^{137}Cs, ^{239,240}Pu, ^{241}Am		Povinec et al. (2003)	14

Table 10.2: *Summary of sediment cores' sampling data*

Sediment core	Notation	Sampling date	Latitude S	Longitude E	Water depth m	Total core length cm
MUC GeoB 10065-9	MUC-A	5.9.2005	9°13.41'	118°53,55'	1284	30
MUC GeoB 10065-9	MUC-B	5.9.2005	9°13.41'	118°53,55'	1284	50
MUC GeoB 10065-9	MUC-C	5.9.2005	9°13.41'	118°53,55'	1284	45
GC GeoB 10065-7	GC	5.9.2005	9°13.42'	118°53.61'	1292	975

10.4.1 Sample preparation

27 sediment samples from MUC-A, always part of the material of 1 cm slices between 3–30 cm depth (the uppermost slices were consumed completely by other analyses), were filled into cylindrical dishes described as "small dishes" in Sec. 7.6.2. The dishes were filled with the samples to heights around 12 mm. The wet masses of each of the samples were between 13–16 g, with a density around 1.25 g·cm^{-3}. The samples contained about 65% of water and the main constituents of the solid fraction were clay minerals and carbonate. The dry masses were estimated after radiometric analysis at MARUM, University of Bremen (Steinke, 2012).

MUC-B sediment samples were measured freeze dried. Material was taken from 1 cm slices between 0–10 cm, 2 cm slices between 10–20 cm and 5 cm slices between 20–50 cm core depth; a total number of 21 samples was measured. Individual sample masses varied between 1–3 g, dry density was 0.6–0.7 g·cm^{-3}. The cylindrical measurement dishes described as "small dishes" in Tab. 7.3 were filled with the samples to heights of 2–5 mm.

In total 8 GC samples were measured freeze dried. Each of the samples covered a 1 cm interval and they were spaced 2 cm between GC depths 0.5 and 15.5 cm. The sample masses varied between 4.5–7.5 g, dry density was 0.3–0.4 g·cm^{-3}. The samples were filled into "large dishes" (Tab. 7.3) to heights between 4.0 and 5.5 mm.

All samples in their respective containers were sealed using a gas tight foil and the measurement was started more than 3 weeks after sealing, in order to ensure, that the radioactive equilibrium between ^{226}Ra, ^{222}Rn and its daughter products had been established. A summary of the measurement data is given in Tab. 10.3.

Table 10.3: *Summary of samples measurement data*

Core	Slices	Sample dry mass mean (min - max) g	Measurement date from-to	Live-time mean (min - max) hours
MUC-A	Total 27 slices, 1 cm thick, depth 3–30 cm	5.46 (4.15–6.79)	1.3.–23.4.2010	32 (21–70)
MUC-B	Total 21 slices, 1, 2 and 5 cm thick, depth 0–50 cm	1.82 (1.05–3.05)	27.9.–17.11.2010	60 (41–114)
GC	Total 8 slices, 1 cm thick, depth 0.5–15.5 cm	6.00 (4.51–7.49)	4.4.-26.4.2011	71 (36–112)

10.4.2 Radiometric measurements and analysis

A coaxial HPGe detector from Canberra Industries described as Det. 3 in Tab. 5.1 was used for gamma spectrometry. The efficiencies were calculated using LabSOCS.

In parallel to the gamma spectrometric analysis for ^{241}Am, radiochemical separation of transuranic elements had been performed on two selected samples, which were analyzed by gamma spectrometry previously, by the Laboratory's technician Regine Braatz. The main objective was to evaluate plutonium isotope levels and ratios, as well as to confirm the results from the gamma analysis of ^{241}Am. The separated samples were analyzed by alpha spectrometry. Alpha spectrometry is an alternative method to gamma spectrometry for ^{241}Am, offering lower detection limits and having the advantage of no correction for self-absorption of radiation in the sample itself, but it is very laborious and is therefore not used as a primary method in the Laboratory.

The separation had been done using Eichrom UTEVA resin (by which Pu^{III} and Am^{III} can be eluted) and TRU resin (for separation of Am from Pu) followed by electroplating. ^{242}Pu and ^{243}Am tracers had been used to determine the chemical yield and overall efficiency. The obtained activities from gamma and alpha spectrometry were compared.

10.4.3 Summing up the spectra

Summing up gamma spectra of individual core samples was performed using Genie 2000 batch commands (Appx. B) in order to achieve improved counting statistics and therefore to better characterize quantities of artificial radionuclides present in the sediment samples. In individual spectra, ^{137}Cs activities of most of the individual samples from the studied area lie under the decision threshold. By summing up spectra of groups of 5 sediment slices for MUC-A (4 sediment slices for GC, respectively), average activities for given sampling intervals can be obtained. Although this approach does not provide fine depth resolution for the radionuclide data, it enables calculating of inventories and radionuclide ratios.

10.4.4 Radionuclide inventories and fluxes

Total inventories of $^{210}\mathrm{Pb}_{\mathrm{xs}}$, ^{241}Am and ^{137}Cs were calculated using Eg. 3.22 from Sec. 3.3.

10.5 Results

All measured activities for MUC-A, MUC-B, MUC-C and GC are reported in Tables A.11, A.12 and A.13, respectively, in Appx. A.

10.5.1 Aligning the cores

The three individual depth profiles were depth aligned using the method described in Chapter 9 based on minimizing the sum of squared residuals. As additional criteria, the characteristic shapes of both MUC-A and MUC-B $^{210}\mathrm{Pb}_{\mathrm{xs}}$ profiles and the onsets of ^{241}Am in all 3 profiles were used. It was estimated, that MUC-A is shifted by 2 cm downwards relative to MUC-B and that there is 20 cm missing on top of the GC relatively to MUC-B. The corrected depths (further on referred to as combined depths) are listed in data Tabs. A.11, A.12 and A.13 in Appx. A and they are used for plotting measured values in Fig. 10.5.

10.5.2 Excess Pb-210

In core MUC-A, the activity concentrations show a steady decrease from 1237 to 532 $\mathrm{Bq{\cdot}kg^{-1}}$ in the upper 5 cm interval. In the 11–15 cm combined depth activities increase back to 1094 $\mathrm{Bq{\cdot}kg^{-1}}$ and in the rest of the profile the activity concentrations fall again with a minimum of 162 $\mathrm{Bq{\cdot}kg^{-1}}$. There are two intervals where the activity concentrations are stagnating (18–23 and 25–32 cm combined depth).

Maximum core MUC-B activity was found in 2–3 cm combined depth (1321 Bq·kg^{-1}). From there down to depth of 11 cm the activities decrease and increase again forming a local maximum at 15 cm depth. The further trend is decreasing down to 31 Bq·kg^{-1} in the deepest sample (45–50 cm).

Activities in core GC decrease monotonously from 659 to 102 Bq·kg^{-1} at 35 cm combined depth.

In general, the initial ^{210}Pb$_{\mathrm{xs}}$ values are very high compared to usual levels, for example those reported within this thesis (in Chapters 9 and 11 from continental slope off NW Africa or gulf of Eilat) or by Burns et al. (2003) from the geographically close Timor Sea. This can be an indication of sediment focusing.

10.5.3 Artificial radionuclides

^{241}Am values above the decision threshold were found in the upper 25 cm combined depth of MUC-A and MUC-B down to 27 cm combined depth in the GC with a broad maximum of approximately 6 Bq·kg^{-1}. Decision thresholds varied depending on the sample mass, measurement geometry and measurement time for each sample, with typical values of 1.2 Bq·kg^{-1} for the MUC-A, 1.5 for the bottom part of MUC-B and 0.7 Bq·kg^{-1} for GC samples.

All ^{137}Cs values were below decision threshold. Typical values of the decision threshold were 1.0–2.0 Bq·kg^{-1} for MUC-A, 1.5–4.5 Bq·kg^{-1} for MUC-B and 0.7–1.0 Bq·kg^{-1} for GC samples.

Two samples from another parallel core MUC-C (10–11 and 24–25 cm combined depth) analyzed using alpha spectrometry showed consistent results with those measured by gamma-spectrometry within 1σ confidence intervals at equivalent depths.

10.5.4 Other gamma emitters

Thorium series radionuclides showed rather low values (close to 15 Bq·kg^{-1} ^{212}Pb) and no ^{228}Th$_{\mathrm{xs}}$ could be evaluated because ^{228}Ac data were below decision threshold for most of the samples. After 4.5 years between sampling and starting of the measurement, only 20% of the unsupported activity would have remained undecayed.

Table 10.4: *GeoB 10065: Descriptive statistics of ^{40}K, ^{226}Ra and ^{228}Th data*

	Arit. mean Bq·kg^{-1}	Std. dev. Bq·kg^{-1}	Min. Bq·kg^{-1}	Max. Bq·kg^{-1}	Median Bq·kg^{-1}	25th percent. Bq·kg^{-1}	75th percent. Bq·kg^{-1}	Coef. of var. %
^{40}K	313	41	238	413	313	293	323	13.1
^{226}Ra	59	7	44	76	57	55	61	11.9
^{228}Th	15.7	2.8	11.0	26.0	15.2	14.1	17.0	17.8

Activity concentrations of ^{40}K, ^{226}Ra and ^{228}Th show a rather high variability (Tab. 10.4, Fig. 10.3). Furthermore, they show a significant positive correlation (Fig. 10.4, Tab. 10.4) at 5% significance level. Spearman rank coefficients and p-values were determined to be 0.474(0.0002), 0.414(0.0016) and 0.438(0.0008) for ^{40}K-^{226}Ra, ^{40}K-^{228}Th and ^{226}Ra-^{228}Th pairs, respectively. As all three radionuclides are likely related to the terrigenous fraction, their variability in the profile can reflect the terrigenous fraction variability in the sediment.

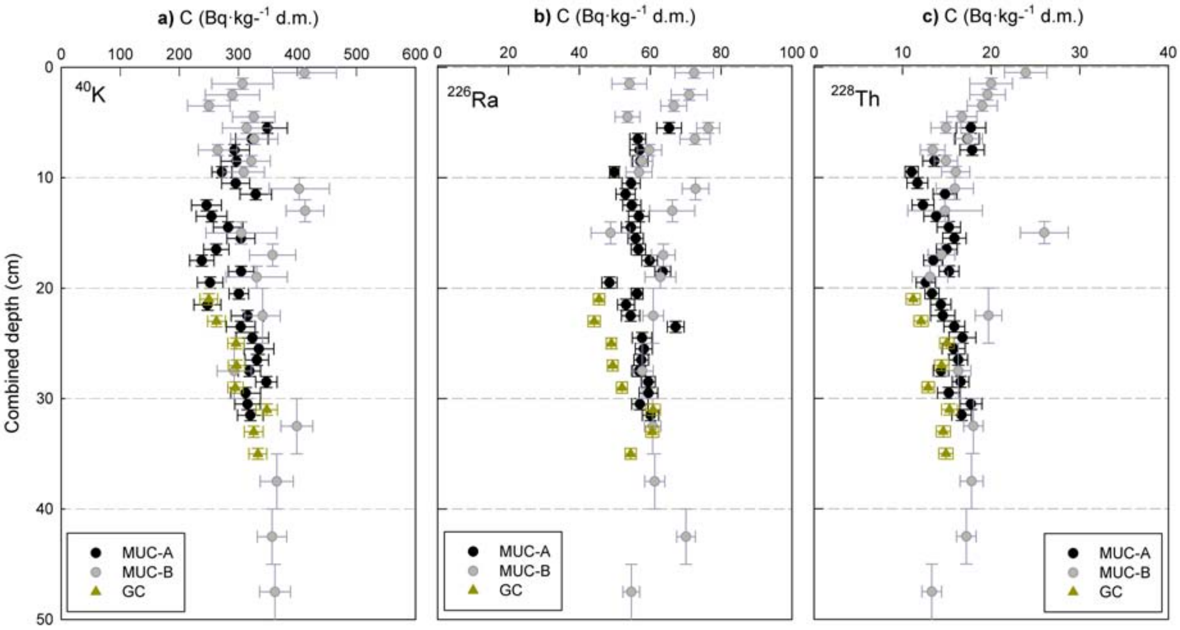

Figure 10.3: *Depth aligned profiles of* ^{40}K, ^{226}Ra *and* ^{228}Th *measured in sediment cores MUC-A, MUC-B and GC. Vertical error bars express uncertainties (1 standard deviation including counting statistics and detector calibration uncertainty), horizontal error bars depth limitation of individual samples.*

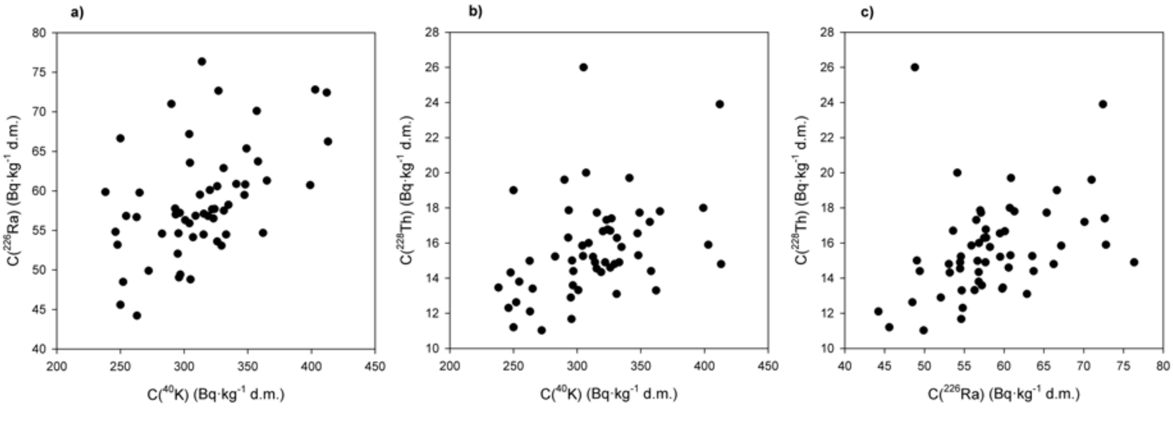

Figure 10.4: *Correlations of* ^{40}K, ^{226}Ra *and* ^{228}Th*.*

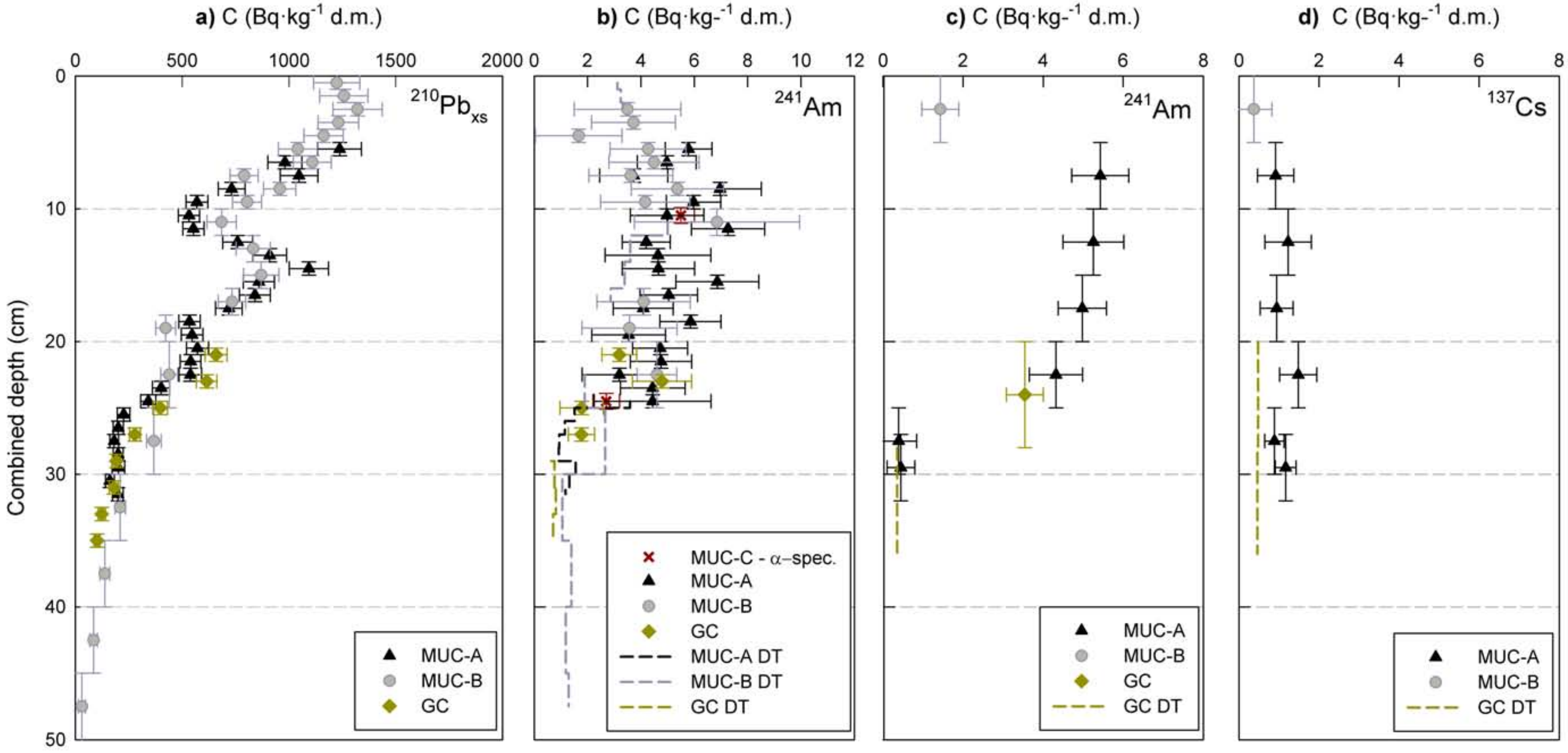

Figure 10.5: *Depth aligned profiles of of $^{210}Pb_{xs}$, ^{241}Am and ^{137}Cs measured in sediment cores MUC-A, MUC-B and GC. Vertical error bars express uncertainties (1 standard deviation including counting statistics and detector calibration uncertainty), horizontal error bars depth limitation of individual samples (a) and (b) or summed up intervals (c) and (d). Values below decision threshold are depicted in dashed lines.*

Table 10.5: *GeoB 10065: Correlations of* ^{40}*K,* ^{226}*Ra and* ^{228}*Th expressed as Spearman rank coefficients and p-values (in brackets).*

	^{40}K	^{226}Ra	^{228}Th
^{40}K	–	0.474 (0.0002)	0.414 (0.0016)
^{226}Ra	–	–	0.438 (0.0008)
^{228}Th	–	–	–

10.5.5 Summed up spectra of artificial radionuclides

Activity concentrations calculated from summed up spectra are listed in Tab. A.14 in Appx. A and plotted in parts c) and d) of Fig. 10.5. The decision thresholds profited from summing the spectra and both artificial radionuclides, ^{241}Am and ^{137}Cs, were detected as deep as 32 cm of combined depth. The maximum ^{241}Am in the interval of 5–10 cm of the combined depth is about 3.5 times higher than the maximum ^{137}Cs in 20–25 cm combined depth.

10.5.6 MUC sediment chronology

The water content did not show any clear decreasing trend with depth. The MUC-A samples, although measured in wet condition, were not stored in a way that their original water content was preserved (Steinke, personal communication). Therefore, corrections for compaction effects were not performed.

The part of the MUC-A ^{210}Pb$_{\text{xs}}$ profile between 14–32 cm combined depth was used for chronology. The uppermost part was omitted from chronology, because it does not show exponential decrease (for purposes of the CF-CS model, described below) and later it was found that the depth of 14 cm is likely to represent recent sediment with another layer of repeated young sequence over the top (see Discussion, Sec. 10.6).

CF-CS model

The CF-CS model (Sec. 3.2.1) was applied to the investigated profile section (Fig. 10.6) and the best fit exponential parameter was used for calculation of the mean sedimentation rate: 0.274 ± 0.021 cm·yr^{-1}, assuming no changes in sedimentation rate and supply of ^{210}Pb$_{\text{xs}}$ in the period covered by the sediment profile. 29.5 cm depth was set as a time marker of the artificial radionuclides' first appearance due to the nuclear testing fallout. It represents the year 1950 ± 5 in the model calculation.

CRS model

The Constant Rate of Supply model (CRS) (Sec. 3.2.2) was applied to the same dataset for comparison to the CF-CS model. This model assumes constant ^{210}Pb$_{\text{xs}}$ flux to the sediment, but the sedimentation rate can vary (Fig. 10.7).

Similarly to the CF-CS model, the AD 1950 (± 2 years) time marker was set to 29.5 cm depth. Because the ^{210}Pb$_{\text{xs}}$ activity in the studied profile did not decrease enough to reach values below the decision threshold (dating horizon), in order to calculate the total inventory an estimation of the activity in the lower part of the profile based on extrapolation of the exponential model was performed down to 100 cm, where the activity reaches values that can not be distinguished from random noise (MacKenzie et al., 2011). The estimated summed up activity under 32 cm combined depth is $1240 \pm 450\ Bq \cdot kg^{-1}$, which accounts for 13% of the total activity in the profile.

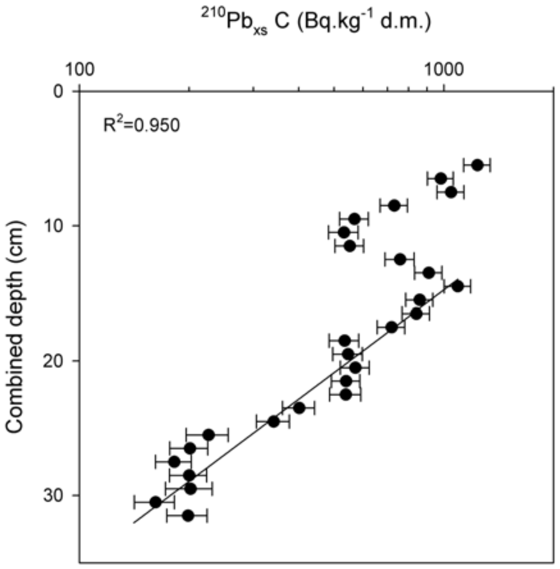

Figure 10.6: *MUC-A: Exponential fit (log-scale) through $^{210}Pb_{xs}$ data performed on 14-32 cm combined depth section.*

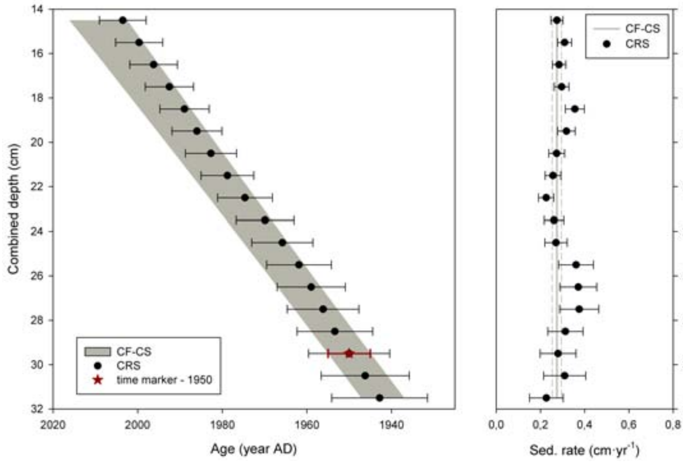

Figure 10.7: *Comparison of chronologies and sedimentation rates derived from the CF-CS model (1 σ interval) and the CRS model.*

Sedimentation rates obtained for individual sections using the CRS model are shown in Fig. 10.7. They oscillate around the value 0.27 cm·yr^{-1} from the previous model (Sec. 10.5.6), to which they are compared. The calendar dates calculated from both models are plotted in Fig. 10.7 and are listed in Tab. A.15 and they show very consistent results. The age of the bottom of the core (31.5 cm) was estimated to be AD 1942 ± 5.

10.5.7 GC chronology

The age of the upper 15 cm of GC GeoB 10065-7 was calculated using the CF-CS model of MUC-A (see above). The gravity core ^{210}Pb chronology of the upper 15 cm extends from AD 1984±6 to AD 1928 ± 5. Furthermore, an attempt was made to extrapolate the simple exponential model to deeper parts of the sediment profile in order to estimate the age above a turbidite layer, which occurs in 36–40 cm core depth. The location of this layer is also clearly visible in the dry bulk density profile (see Fig. A.4 in Appx. A). Assuming a constant sedimentation rate through the entire period, the depth 36 cm (above the turbidite layer) would represent year AD 1845 ± 9.

The chronology of the rest of the GC below the turbidite layer had been constructed[1] based on 39 AMS radiocarbon dates of mixed planktonic foraminifera. They had been analyzed at the National Ocean Sciences Accelerator Mass Spectrometry Facility, Woods Hole, USA and the Keck Carbon Cycle Accelerator Mass Spectrometry Laboratory, University of California, Irvine, USA. All raw radiocarbon dates had been converted to 2σ calendar ages with the CALIB 6.0 software (Stuiver et al., 2005) using the MARINE09 calibration dataset (Reimer et al., 2009) with a reservoir correction of 400 years. An additional 250 years (ΔR) correction had been applied to account for older radiocarbon introduced into the surface water by upwelling and for differences between foraminifera living in surface and thermocline water layers (mixed planktonic foraminifera were mostly used for radiocarbon dating) (Southon et al., 2012).

The AMS-^{14}C ages and calibrated ages are reported in Tab. A.16 in Appx. A. The chronology for the core had been constructed using a second order polynomial fit to the data, so that the age before present (BP) to depth relationship could be translated as:

$$t(z) = 0.0035 \cdot z^2 + 2.5027 \cdot z + 153.36. \tag{10.1}$$

The combined chronology for the GC including both gamma emitters and radiocarbon data is plotted in Fig. 10.8. In this plot the ages were expressed in calendar years (AD) by subtraction of radiocarbon years (BP) from AD 1950, which is for purposes of radiocarbon dating considered as "present".

Above the turbidite layer the chronology based on the CF-CS model (down to 12 cm) followed by its extrapolation to 36 cm is presented. Due to the turbidite, which had likely been an erosive event, a part of the sediment record might be missing. The age model is plotted together with the associated sedimentation rates, which in case of radiocarbon age are based on the polynomial fit. They tend to increase with decreasing depth from 0.11 cm·yr^{-1} at 10 m depth to 0.35 cm·yr^{-1} at 40 cm depth, which might at least partially be caused by compaction. This is also reflected in the dry bulk density depth profile (Fig. A.4 in Appx. A) that shows an increase with depth for at least the upper 200 cm.

---

[1] The work presented in this and the following paragraph was performed by Dr. Stephan Steinke, MARUM, University of Bremen.

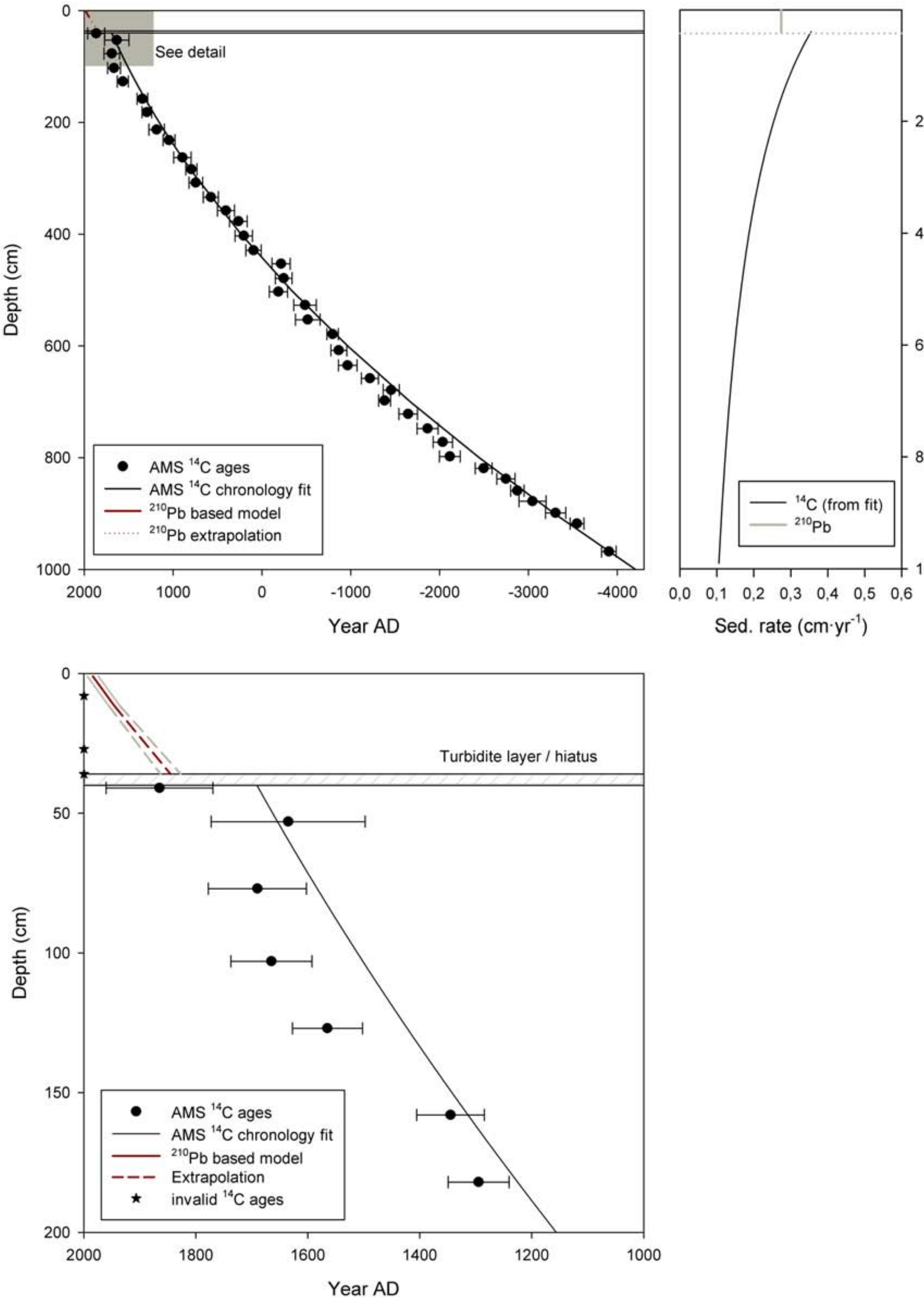

Figure 10.8: *Top left: Combined chronology of GC using* $^{210}Pb_{xs}$ *and* ^{14}C. *Top right: Sedimentation rates. Bottom: Detail of the topmost 200 cm combined chronology. Confidence intervals and error bars represent* 2σ *uncertainty.*

10.5.8 Inventories and fluxes

Radionuclide inventories were calculated from combined profiles of MUC-A and MUC-B. The upper section above 14 cm was omitted (see discussion below). Because dry bulk densities were not known for the studied MUC cores, they were estimated based on values measured in selected depths of the associated GC (Fig. A.4 in Appendix A) for this purpose by linear extrapolation. ^{210}Pb$_{xs}$ inventory was calculated from values between 14 and 30 cm combined depth MUC-A and 30–50 cm combined depth MUC-B as 28,700±1,200 $Bq \cdot m^{-2}$. This is a very high value equivalent to a mean flux of 900 $Bq \cdot m^{-2}yr^{-1}$ compared to a value of 95 $Bq \cdot m^{-2}yr^{-1}$ from Darwin, Australia (Preiss et al., 1996) and can indicate processes of sediment focusing. This is also supported by unusually high sedimentation rates for deep sea sediments.

The inventories of artificial radionuclides were calculated for the same depth intervals based on activities of summed up spectra as 148±13 $Bq \cdot m^{-2}$ ^{241}Am and 55.7±8.5 $Bq \cdot m^{-2}$ ^{137}Cs. A reference value to compare the ^{137}Cs inventory to is about 210 $Bq \cdot m^{-2}$ as a mean value for 0–10° N latitude band, decay corrected to the year 2005 (UNSCEAR, 2000). Here the observed values are lower.

10.6 Discussion

Application of both age models (sections 10.5.6 and 10.5.6) with an additional time marker based on first appearance of artificial radionuclides in the sediment core MUC-A showed consistently that in the combined depth of 14 cm sediment is likely to be very recent, deposited shortly before sampling. The calculated ages correspond to AD 2009±7 and 2004±6 calendar years, respectively, whereas the core was sampled in September 2005. The reason for the existence of additional layers of sediment above 14 cm (Fig. 10.5) can be interpreted as a recent emplacement of the entire sediment sequence on top of the existing sediment. It could be a result of a small scale deformation and/or sliding process triggered by seismic activity that occurs frequently in the earthquake prone region of Indonesia located at the meeting point of several tectonic plates. The mechanism of this event can not be understood without additional physical or textural information from the core, but the monotonous activity decrease within the upper 10 cm would imply a gentle process without mixing of the slided material layer. Earthquake induced deformation of sediments typically appear in layers of thickness varying from centimeters to decimeters as observed for example in lacustrine sediments of the Dead Sea (Wetzler et al., 2010).

An alternative explanation would be dramatic changes in ^{210}Pb$_{xs}$ flux in time. This would make assumptions of both models invalid, but still the information provided by the artificial radionuclides assigns the date of approximately AD 1950 to a combined depth of about 30 cm.

The activity ratio ^{241}Am/^{137}Cs > 1 (value of 2.7 ± 0.5 for the whole profile inventory) is rather untypical for that of global atmospheric nuclear fallout, for which ^{241}Am/^{137}Cs<<1 is reported (Appleby et al., 1991). Also ^{241}Am absolute activities are unusually high. It is epected that ^{241}Am is present in the samples as a decay product of its parent isotope ^{241}Pu, rather than being deposited in-situ. Further investigation of the artificial radionuclides including Pu isotopes in the sediments of this region could explain their meanwhile unclear origin and the processes leading to their accumulation in the ITF sediments.

The ^{240}Pu/^{239}Pu atom ratio can be used for distinguishing global fallout from localized sources, including tests at PPG (Lindahl et al., 2010) or Monte Bello islands (Child & Hotchkis, 2013), ^{238}Pu/^{239,240}Pu ratios can point toward the later contribution from the SNAP-1 event (Hancock et al., 2011).

10.7 Conclusions

Activity concentrations of natural and artificial gamma emitters in four parallel cores from the eastern Lombok Basin, Indonesia, were studied within a paleoclimate study. These are the main results and findings.

1. The multicores were depth-aligned to the associated gravity core based on radionuclide activity profiles.

2. Two models applied to $^{210}\mathrm{Pb}_{\mathrm{xs}}$ data allow constructing a chronology of the MUC-A core supported by the onset of artificial radionuclides, ^{241}Am and ^{137}Cs in the sediment profiles. The age model shows that very recent sediments are likely to be present in the combined depth of 14 cm.

3. High $^{210}\mathrm{Pb}_{\mathrm{xs}}$ inventory can be explained by sediment focusing.

4. A method of spectra summing was successfully used for obtaining results of artificial radionuclide activity concentrations and their ratios and inventories where it was not possible to detect them in individual spectra.

5. Unusually high ^{241}Am absolute concentrations and $^{241}\mathrm{Am}/^{137}\mathrm{Cs}$ activity ratios were revealed.

6. A combined ^{210}Pb and radiocarbon chronology was constructed for the gravity core allowing further palaeoclimatic interpretations (Steinke et al., submitted).

10.7.1 Outlook

The origin of artificial radionuclides in the studied cores are not well understood. Alpha spectrometry and mass spectrometry techniques for plutonium isotopes might help to fingerprint the origins of man-made radionuclides, as the ratios of the major sources are known. $^{239}\mathrm{Pu}/^{240}\mathrm{Pu}$ atom ratio is a suitable parameter for distinguishing between the global fallout from U.S. tests performed at the PPG. British tests at Australian Monte Bello Islands have yet another typical Pu signature. $^{238}\mathrm{Pu}/^{239,240}\mathrm{Pu}$ activity ratios determined by alpha spectrometry can be successfully used for distinguishing global fallout from regional SNAP satellite burnup affected fallout typically increased in the Indian Ocean region. The fingerprint of the artificial radionuclides can be studied on existing core material.

Additionally, during the MARUM (Uni Bremen) R/V SONNE cruise 228 Kaohsiung-Townsville in 5–6/2013 (Mohtadi & cruise participants, 2013) to the ITF entrance area new MUC sediment cores had been taken at 4 sites (Fig. 10.1). Two cores were sampled east off Mindanao (Philippines), where the Mindanao Current enters ITF, from approximately 500 m water depth. Here the effect of PPG radionuclides is expected to be the strongest. Other cores were taken from an area off Sepik River (Papua New Guinea, 590 m water depth) and from Bismarck Sea (Papua New Guinea, 1160 m water depth). At these sites a global fallout signal is expected. Originally the sampling sites were planned also at Seram Trough, where one of the branches of the ITF reaches and mixed signal of PPG fallout and global fallout would be expected, and off Bird's Head Peninsula, W Papua, where S Pacific water enters ITF and global fallout signal expected, but they were excluded from the expedition working plan.

Furthermore, there are existing GeoB MUC cores from ITF from an earlier expedition, namely Savu Sea, available for analysis. Another set of existing samples and data is available from the Timor Sea shelf and slope. 17 kasten cores are archived and available in the Australian

Institute of Marine Science repository. Radiochemical and geochemical data are available for these cores.

The future investigations on the origin of high inventories of Pu and Am nuclides in the pathway of the Indonesian Throughflow, the Savu and Timor Sea might provide a link to the magnitude, speed, and history of the ITF. The study could contribute to understanding of processes leading to long distance transport of these highly particle reactive isotopes and their scavenging to the ITF sediments.

Chapter 11

Radionuclides and recent sedimentation rates in Northern Gulf of Eilat/Aqaba, Red Sea[1]

11.1 Introduction

The Gulf of Eilat (GOE), also Gulf of Aqaba, is the northeastern semi-isolated extension of the Red Sea, connected to the Red Sea by the Straits of Tiran. It is located in a subtropical arid climate with a negligible amount of precipitation ($\sim 30\ mm \cdot yr^{-1}$) and surface runoff and an average evaporation rate of 1.6–1.8 $m \cdot yr^{-1}$ (Ben-Sasson et al., 2009).

11.1.1 Phosphate pollution

Last century's accelerated anthropogenic pollution and input of nutrients, including phosphorus, effect negatively the marine environment of the GOE (Atkinson et al., 2001). The most influential factors of phosphorus pollution in the marine environment in the northern GOE, which influence marine life biodiversity and coral reef health, were identified as (e.g., Atkinson et al., 2001):

1. phosphate ore dust from berths in industrial ports of Eilat (Israel) and Aqaba (Jordan),
2. mariculture and
3. sewage.

Some of these negative factors were gradually eliminated: routine marine discharges of sewage from cities of Eilat and Aqaba were discontinued in the mid 1990's (Atkinson et al., 2001); similarly, fish cage farming introduced to the Israeli part of the GOE in 1995 was abandoned after scientific and political debate in 2004, a process that was accomplished in 2008 (Israeli Ministry of Environmental Protection, 2008).

---

[1] Parts of this chapter were presented in the form of a presentation at the 6th International Symposium on In Situ Nuclear Metrology as a tool for Radioecology (INSINUME), Brussels,Belgium , 11.-15.6.2012 as D. Pittauerová, G. Kirchner, D. Garbe-Schönberg, A. Nishri, B. Herut and H.W. Fischer: Natural and man-made gamma emitters in Gulf of Eilat / Aqaba sediments

Phosphate ore dust pollution

In Aqaba port $1.47 \cdot 10^6$ t phosphate ore was exported in 1974. This number has risen to $5.54 \cdot 10^6$ t in 1987 and a total of $14 \cdot 10^6$ t phosphate was exported between 1980 and 1983 (Abu-Hilal, 1985). Between 1989 and 1993 the phosphate exports ranged from 3.6 to 6.4 $\cdot 10^6$ t annually (World Bank, 1996) and between 1992 and 2010 they varied from 3.2 to $4.5 \cdot 10^6$ t with an average of $3.8 \cdot 10^6$ t (Aqaba Port Corporation, 2011).

During loading and transportation of the phosphate in ports, about 0.05% of the actual weight can be lost in the form of dust (Abu-Hilal, 1985), but other estimates are as high as 0.1–1% (Freemantle et al., 1978). Walker & Ormond (1982) estimated 1-2 tons of phosphate being lost into the sea during loading one ship with an average load of about 20,000 t of phosphate per ship, leading to 0.005–0.01% loss.

Environmental measures were taken also on the Jordanian site (Cleveland Cascades Ltd., 2012; World Bank, 1996) in order to reduce dust generation. As a result, the dust emissions were reduced from estimated 1% of the total load by 80–85% since 1994 with substantial further reductions planned (World Bank, 1996).

The port of Eilat exports $2.5 \cdot 10^5$ t of phosphate ore yearly (Atkinson et al., 2001). A report on the dust monitoring system (Geo-prospect Ltd., 2007) quantifies the amounts to 2.5, 3.6 and $1.7 \cdot 10^5$ t in the years 2004, 2006 and 2007, respectively.

Since May 2002 a loading chute minimizing phosphate dust dispersion into the air during loading has been installed and operated in Eilat port. Using a network of stations to monitor dust and meteorological conditions it was estimated that approximately 0.01% of the load was lost from May to December 2002 (Geo-prospect Ltd., 2003). According to Geo-prospect Ltd. (2007) 2.7 t of phosphate was introduced to the sea in 2007, as compared to 5.7 t in 2006; this implies that the marine environment imission portion was reduced to 0.0016% of total loaded phosphate in both years.

Even though effective environmental actions were taken to reduce the dust pollution in both phosphate exporting ports, it is certain that in the past higher amounts of phosphate dust has been released than at present. The total amount of phosphorus released from both ports was estimated to be $86 \cdot 10^6$ mol P (Atkinson et al., 2001).

11.1.2 Radionuclides in the GOE sediments

Only a limited number of publications deals with radioactivity of the GOE sediments. A study of gamma-emitting radionuclides from sediment cores along a 15 km stretch of the Jordanian coast of the GOE conducted by Ababneh et al. (2010) covered the shallow parts of the coast, down to 35 m water depth. High levels of ^{238}U, ^{226}Ra and ^{235}U were found in the location of the phosphate loading berth, which were by at least a factor of 3 higher than those reported from other locations along the coast in the same study. The increased activities were attributed to phosphate dust generated during shipment. Al-Trabulsy et al. (2011) presented radionuclide spatial distributions in the top layer of bottom sediments along the Saudi coastline and compared them to the worldwide averages, recognizing ^{226}Ra and ^{232}Th concentrations in the studied area being lower, but ^{40}K about double the world average. It was pointed out that the ratio of ^{226}Ra/^{228}Ra tends to decrease southwards with increasing distance from the Jordanian phosphate industry installations.

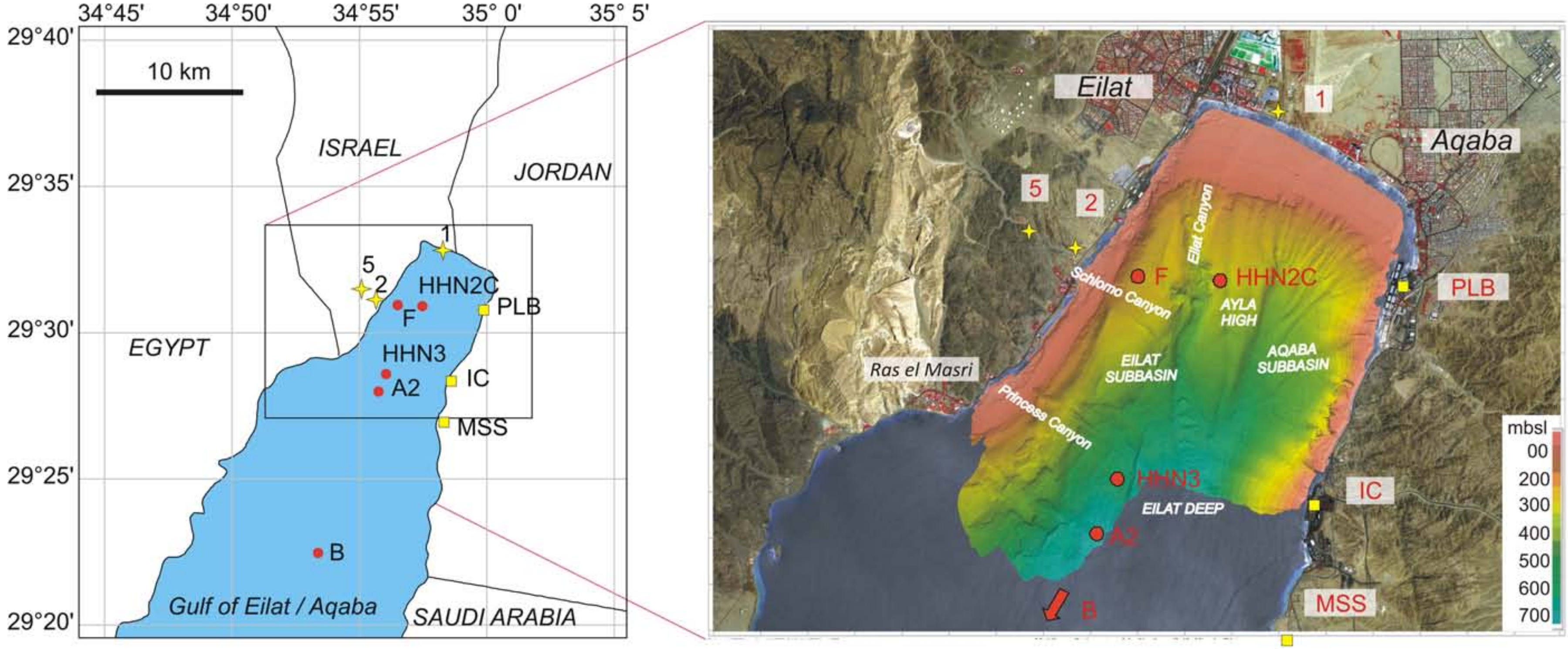

Figure 11.1: *Map of the northern part of the GOE showing the location of sediment cores (red dots), wadi sediments (yellow stars) and aerosol sampling sites (yellow squares). The bathymetry is taken from Sade et al. (2008).*

The main aim of this work, within a larger project dealing with amounts and sources of bioavailable phosphorus in the northern GOE, was to provide mass accumulation rates in deeper parts of the gulf by means of measurement and evaluation of natural and anthropogenic gamma-emitting radionuclide activity concentrations and their inventories in sediments. The findings from this radionuclide study should serve as a basis for further interpretations of sedimentation processes and pollution history based on sediment cores recovered from the northern GOE.

To the author's knowledge, no radionuclide depth profiles from the GOE area were studied or used for estimating recent accumulation rates up to this date. Since the bottom sediments act as a sink for different anthropogenic pollutants, a study of sediment cores can reveal pollution history and its effect on the marine environment.

11.2 Material and methods

11.2.1 Sampling area

Bathymetry of the northernmost part of the GOE (gulf head), where the presented study took place, was described by Tibor et al. (2010) based on a previous multibeam survey (Sade et al., 2008). The gulf is divided here by an elevation - the Ayla high - stretching from about 50 m to 600 m depth, into two subbasins: the Eilat subbasin to the west and the Aqaba subbasin to the east (Fig. 11.1).

The northern shelf is about 1300 m wide in the NE to 1800 m in the NW with active coral reefs extending to 30–50 m water depth. The shelf-slope break occurs at about 70–80 m water depth in the NE part and at 90–100 m in the NW part. The Aqaba subbasin has a short or practically non-existent tectonically based shelf on the eastern side and appears to have a limited sediment supply (Tibor et al., 2010). On the other hand, the Eilat subbasin is supplied with sediments from Arava Valley (a part of the rift valley that Gulf of Eilat is a continuation of). Its western shelf is steeper than the northern one, 400–800 m wide with a shelf-slope break at about 100 m depth. A distinct north-south feature, the 8700 m long underwater Eilat Canyon, dominates the Eilat subbasin. Another two canyons can be observed along its NW side - Schlomo Canyon and Princess Canyon. Both Eilat and Aqaba subbasins join further to the south into a deeper basin - the Eilat deep - which reaches up to 900 m depth.

Prevailing winds from the south maintain oligotrophic conditions in surface waters of the gulf and induce southward bottom currents that might be responsible for the export of fine-grained argillic material towards greater water depths in the south.

Stations F and HHN2C represent shallow water sediments (240 and 316 m), with station F being situated at the western Eilat subbasin slope and HHN2C at the Ayla high. Stations A2 and HHN3 were located in a deeper part of the Eilat subbasin (600–700 m). Another station B was selected further south in the Eilat deep (Fig. 11.1).

11.2.2 Marine sediment sampling

All five short sediment cores analyzed within this study had been taken during three cruises in 2007 and 2008[2]. The sediment cores taken by Perspex tubes had been sliced and centrifuged immediately for determination of pore water content. The sampling details are summarized in Tab. 11.1.

---

[2] The sampling campaigns had been organized and performed by Barak Herut and Ami Nishri from the Israel Oceanographic and Limnological Research, Haifa, Israel.

Table 11.1: *Summary of sampling data.*

Sediment cores	Sampling date	Latitude (N)	Longitude (E)	Water depth (m)	Core length (cm)
F	8.5.2007	29°30.950’	34°56.497’	240	16
HHN2C	26.3.2008	29°30.910’	34°57.467’	316	16
HHN3	26.3.2008	29°28.587’	34°56.042’	602	19
A2	8.5.2007	29°27.992’	34°55.752’	705	22
B	19.3.2008	29°22.657’	34°53.377’	ca. 800	12

Wadi samples	Sampling date	Latitude (N)	Longitude (E)	Description
1	9.9.2009	29°32.731’	34°58.285’	Clay minerals - Arava Valley
2	8.9.2009	29°31.197’	34°55.628’	Shlomo Wadi - near the road
5	9.9.2009	29°31.505’	34°55.052’	Shlomo Wadi - natural route, 1 km from coast line

Dust samples	Sampling date	Latitude (N)	Longitude (E)	Description
IC	25.1.2007–24.5.2007	29°28.297’	34°58.651’	Jordan / Aqaba, Industrial complex
PLB	25.1.2007–24.5.2007	29°30.762’	34°59.905’	Jordan / Aqaba, Phosphate loading berth
MSS	25.1.2007–24.5.2007	29°26.950’	34°58.303’	Jordan / Aqaba, Marine sciences station

Fertilizer/phosphate	Sampling date	Latitude (N)	Longitude (E)	Description
Phosphate	March 2007	29°32.5’	34°57.2’	Natural phosphorite
Mazut	March 2007	29°32.5’	34°57.2’	Coated pulverized and pelletized phosphorite

11.2.3 Sample preparation

After sectioning, samples had been dried to determine water content[3]. Dry bulk density had been calculated from pore water content assuming a solid fraction density of 2.55 $g \cdot cm^{-3}$ and sea water density of 1.04 $g \cdot cm^{-3}$ and constant slice volume (Ami Nishri, 2010). Dry bulk density depth profiles are shown in Fig. 11.3. The values are close to 1 g (d.m.) $\cdot\, cm^{-3}$ (w.m.).

For radiometric analysis dry samples were filled into cylindrical plastic dishes with a diameter of 35 mm and sealed using radon-tight foil. Before measurement they were stored for a minimum of 3 weeks so that radioactive equilibrium between ^{226}Ra and ^{222}Rn (and its daughters) had been established. Information on slicing, sample masses and measurement times are listed in Tab. 11.2.

Table 11.2: *Summary of samples measurement data*

Sediment core	Slices	Sample dry mass (g) mean (min–max)	Meas. time (h) mean (min–max)
F	Total 17 slices, 0.5, 1 or 2 cm thick, depth 0–16 cm	1.01	57 (42–94)
HHN2C	Total 16 slices, 1 cm thick, depth 0–16 cm	9.30 (9.03–10.16)	32 (20–73)
HHN3	Total 19 slices, 0.5, 1 or 2 cm thick, depth 0–19 cm	7.54 (2.03-10.03)	32 (23–70)
A2	Total 21 slices, 0.5, 1 or 2 cm thick, depth 0–22 cm	1.01	65 (47–117)
B	Total 15 slices, 0.5, 1 or 2 cm thick, depth 0–12 cm	7.77 (1.55–10.32)	35 (22–75)

Other samples	Number of samples	Sample dry mass (g) mean (min–max)	Meas.time (h) mean (min–max)
Wadi sediments	3	10.00 (9.97–10.06)	106 (33–194)
Dust	3	0.87 (0.70–1.13)	64 (48–92)
Fertilizer	2	1.01	48–66

---

[3] Sample preparation and water content determination was performed by Barak Herut and Ami Nishri from the Israel Oceanographic and Limnological Research, Haifa, Israel.

11.2.4 Wadi sediment, dust and fertilizer samples

Dry riverbed (wadi) sediment samples had been taken[4] in order to characterize the source material of flush floods after heavy rainfall events, which might contribute to the GOE sediment. Being another constituent of GOE sediment, atmospheric dry aerosol (dust) had been sampled[5] at three stations in Jordan: Industrial complex (IC), Phosphate Loading Berth (PLB) and Marine Sciences Station (MSS) using mash samplers during 4 sampling periods, each of them 1 month long. The sampling took place from 25.1.2007 to 24.5.2007.

Additionally, fertilizer samples had been taken[6] directly from the pier in the port of Eilat. One of the phosphate fertilizer samples is a pulverized natural phosphorite and the other is pulverized and pelletized phosporite coated with bituminous material (so-called "Mazut"). In this form the dust emissions are reduced during manipulation with the phosphate ore.

Wadi sediment, dust and fertilizer samples were prepared for gamma spectrometry by the same procedure as gulf bottom sediments, described in Sec. 11.2.3. Information on the sampling sites is given in Tab. 11.1 and details on the sample masses and counting times in Tab. 11.2.

11.2.5 Gamma spectrometric measurements and analysis

Detector 3 (Tab. 5.1) operated with Genie 2000 software was used for gamma spectrometry. Efficiencies were calculated using LabSOCS.

Following radioisotopes were quantified from the spectra: ^{210}Pb, ^{226}Ra (^{210}Pb$_{\mathrm{sup}}$), ^{137}Cs, ^{40}K, ^{228}Ra and ^{228}Th. The values for ^{210}Pb$_{\mathrm{sup}}$ were derived from the concentrations of ^{226}Ra, measured via the concentration of the strongest line of its daughter product ^{214}Pb at an energy of 352 keV. Excess ^{210}Pb (^{210}Pb$_{\mathrm{xs}}$) was calculated for each sample by subtracting supported ^{210}Pb from total ^{210}Pb measured via its 46 keV gamma line.

Activity concentrations of ^{228}Ra were derived from the daughter ^{228}Ac in equilibrium (weighted mean of activities from decays at 338, 911 and 969 keV) and ^{228}Th via the daughters ^{212}Pb (239 keV) and ^{208}Tl (583 keV).

^{137}Cs was determined via its $^{137\mathrm{m}}$Ba line at 662 keV and ^{40}K via its 1461 keV full energy peak.

Cascade summing corrections were significant for radionuclides with more complicated decay schemes (^{208}Tl and ^{228}Ac) and were performed using LabSOCS and Genie 2000. All data presented in the following are decay corrected to the sampling date.

Sample masses available for radiometric analysis from two of the cores (F and A2) were as low as 1 g each, which resulted in relatively high counting uncertainties even for prolonged measurement times.

All measured data are listed in Tabs. A.17–A.21, Appx. A.

11.2.6 Element composition analysis

The major and trace element analyses had been performed using ICP-MS (Agilent 7500cs) and ICP-OES (Spectro Ciros SOP) following routine procedures as described in Garbe-Schönberg (1993) in the ICP-MS laboratory, Institute of Geosciences, Christian-Albrechts-University Kiel. Content of "total recoverable elements" had been determined after table-top multi-step pressure digestion of 250 mg pulverized and dried sample using hydrofluoric acid, perchloric acid and

---

[4] The sampling campaigns had been organized and performed by Barak Herut and Ami Nishri from the Israel Oceanographic and Limnological Research, Haifa, Israel.

[5] The aerosol sampling had been organized and performed by Mohammed Ali Wedyan, Al Hussein bin Talal University, Jordan.

[6] The sampling campaign had been organized and performed by Barak Herut and Ami Nishri from the Israel Oceanographic and Limnological Research, Haifa, Israel.

aqua regia. Procedural blanks, sample duplicates, and international certified reference material (JLs-1, PACS-3) had been prepared and analyzed along with unknown samples[7]. Typically, the analytical error for the elements reported here was better than 1-3 % RSD (1 σ).

Activities of ^{40}K, ^{238}U and ^{232}Th were calculated from measured concentrations of elements (K, U and Th) by ICP-MS, assuming natural isotopic ratios (Tab.A.22). Mass spectroscopy data are not available for the core HHN3.

11.3 Results and discussion

11.3.1 Accumulation and sedimentation rates using $^{210}\mathrm{Pb_{xs}}$ and $^{137}\mathrm{Cs}$

As the first approach for interpreting $^{210}\mathrm{Pb_{xs}}$ depth profiles (presented in Fig. 11.2A), a simple exponential model assuming constant $^{210}\mathrm{Pb_{xs}}$ flux and constant sedimentation rate, the CF-CS model (Sec. 3.2.1) was applied. The model predicts $^{210}\mathrm{Pb_{xs}}$ profiles in which concentrations plotted against cumulative dry mass decrease exponentially. The model is well applicable also in cases where the temporal fluctuations of the ^{210}Pb flux density into the sediment and/or the sedimentation rate are merely statistical (Kirchner, 2011).

Applying a least square fit to the data (^{210}Pb in excess in upper sections of the profiles showing activity decrease with depth)[8], accumulation rate r ($g \cdot cm^{-2} \cdot yr^{-1}$) and the associated uncertainty can be determined. Even though the mass accumulation rate is constant, the sedimentation rate S ($cm \cdot yr^{-1}$) can vary due to compaction. The mean sedimentation rates were estimated from fitting a negative exponential function to the activity vs depth plots. The fits were again limited to the depth intervals in which $^{210}\mathrm{Pb_{xs}}$ had been detected.

Mixing was not taken into account within this model, as $^{210}\mathrm{Pb_{xs}}$ did not show signs of stagnating activities in the upper part of the cores, a feature often assigned to a mixed surface layer.

Mass accumulation and sedimentation rates and sediment sources

Calculated accumulation rates for the sections with decreasing $^{210}\mathrm{Pb_{xs}}$ activities (with exception of core B, which will be discussed separately) vary between 0.076 ± 0.008 and 0.33 ± 0.16 $g \cdot cm^{-2} yr^{-1}$ (Tab. 11.3). The mean sedimentation rates between 0.077 ± 0.007 and 0.30 ± 0.16 $cm \cdot yr^{-1}$ are higher than those published by Al-Rousan et al. (2004) of 0.042–0.072 $cm \cdot yr^{-1}$ based on ^{14}C accelerator mass spectroscopy dating of three multicores from depths 440–830 m in the northern part of the GOE.

Table 11.3: *Mass accumulation rates (r) and sedimentation rates (S) derived from $^{210}Pb_{xs}$ profiles. Uncertainties in this and all following tables give asymptotic standard deviations.*

Core	Fitted depth interval	r	S
	cm	$g \cdot cm^{-2} yr^{-1}$	$cm \cdot yr^{-1}$
F	0–7	0.33 ± 0.19	0.30 ± 0.16
HHN2C	0–5	0.076 ± 0.008	0.077 ± 0.007
HHN3	0–8	0.16 ± 0.04	0.17 ± 0.04
A2	0–7	0.21 ± 0.16	0.26 ± 0.18

The principal sources of the GOE sediment are dust deposition, material brought to the GOE by floods following heavy rainfall events through wadis (dry river beds), but also earth

---

[7] The sample preparation and ICP-MS had been preformed by Dieter Garbe-Schönberg from Christian-Albrechts-University Kiel, Germany.

[8] For ^{210}Pb the exponential fit parameters were determined by Gerald Kirchner, University of Hamburg, for cores HHN2C, HHN3 and A2.

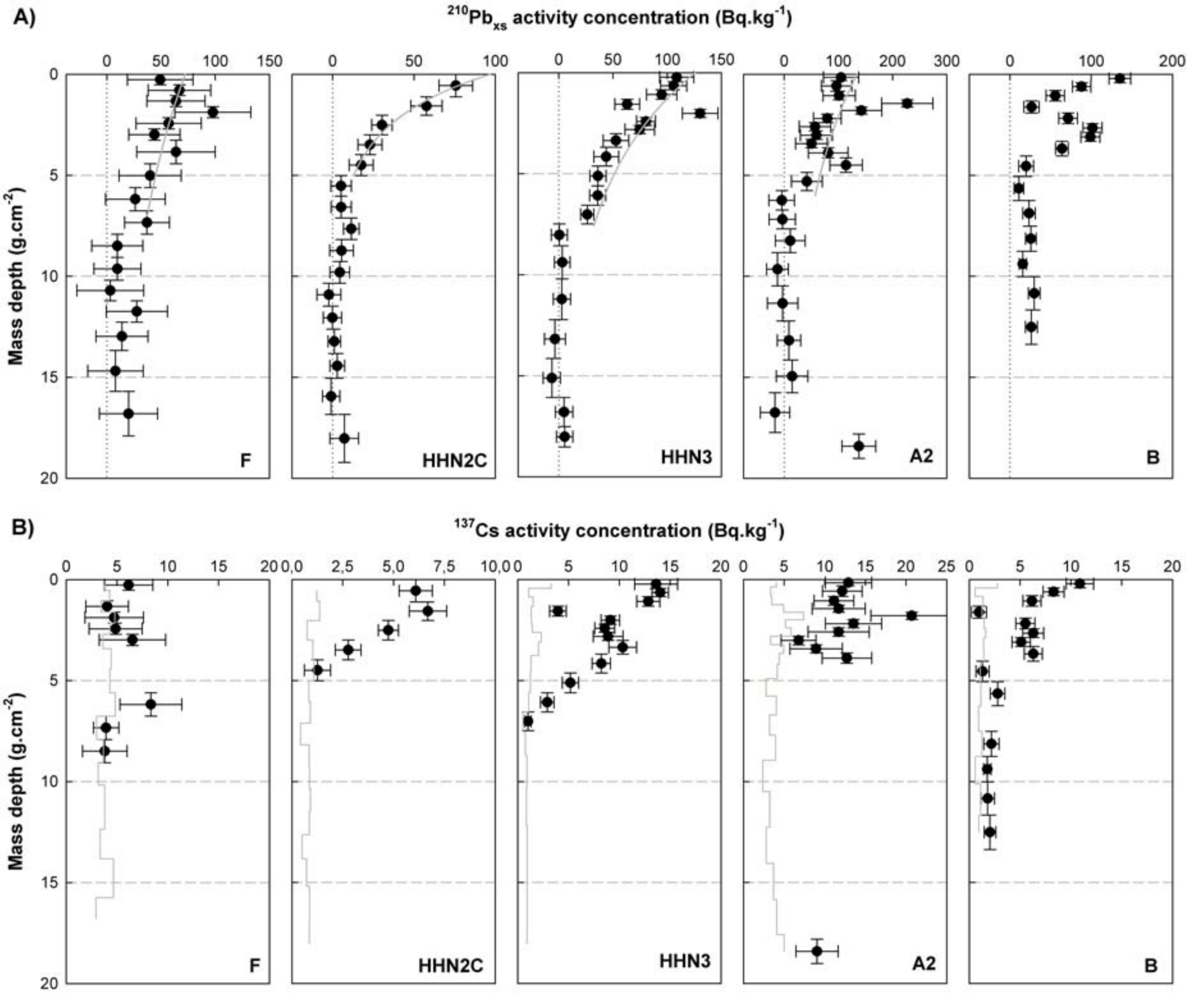

Figure 11.2: *A: Activity concentration profiles of $^{210}Pb_{xs}$. Exponential fits are added.*
B: Activity concentration profiles of ^{137}Cs with decision thresholds.
The horizontal scale is different for each of the cores. Horizontal error bars represent uncertainty of 1σ, vertical error bars show the thickness of the sample slices; this is the case also for all following figures.

quake-induced turbidity currents or resuspension. Additionally an autochtonous carbonate contribution might be expected. Chen et al. (2008) estimated the fluxes of heavy metals in the northern part of the GOE. They calculated an average flux of 342 and 216 $mg \cdot m^{-2}yr^{-1}$ of Al and Fe, respectively. Considering the average Al and Fe concentrations in dust deposition collected in three stations along the Jordanian coast within the wider project - 2% and 1.3% for Al and Fe (Garbe-Schönberg et al., 2010) - and that the bulk density of the marine sediments is approximately 1.55 $g \cdot cm^{-3}$, the expected dust sedimentation is estimated as 0.01 $mm \cdot yr^{-1}$. This value corresponds to less than 1% of the sedimentation rates as presented above. Thus, the atmospheric contribution to the sedimentation in the GOE should be negligible. The normalized trace element pattern of the GOE bed sediments suggest that the major source is riverborne suspended material (Garbe-Schönberg et al., 2010).

^{137}Cs

Anthropogenic ^{137}Cs was detected in all five studied cores. The depth profiles are shown in Fig. 11.2B. For several of the cores the ^{137}Cs activities decrease almost exponentially with increasing depth and a ^{137}Cs peak caused by atmospheric deposition of the weapons fallout maximum in 1963 is not present in any of the cores. The reason might be that the main process leading to depth distribution of radionuclides might not be sedimentation, but mixing or combined effect of mixing and sedimentation. The sedimentation rates from Tab. 11.3 must be therefore considered to be maximum estimates.

Differences between cores

The radionuclide profiles at the deepest site B are difficult to interpret. $^{210}Pb_{xs}$ concentrations are highly scattered within the upper 4 cm of sediment, but become almost constant below this depth with ^{210}Pb still clearly in excess, a feature that could be observed in physically mixed or intensively reworked profiles. At 1.5–2.5 cm also a dry bulk density anomaly occurs (Fig. 11.3) indicating higher compaction; here a fast sedimentation event (e.g. a slump or a turbidite) may have happened. The CF-CS age model is therefore not applicable for this profile. ^{137}Cs was also detected in the entire profile, showing features similar to $^{210}Pb_{xs}$.

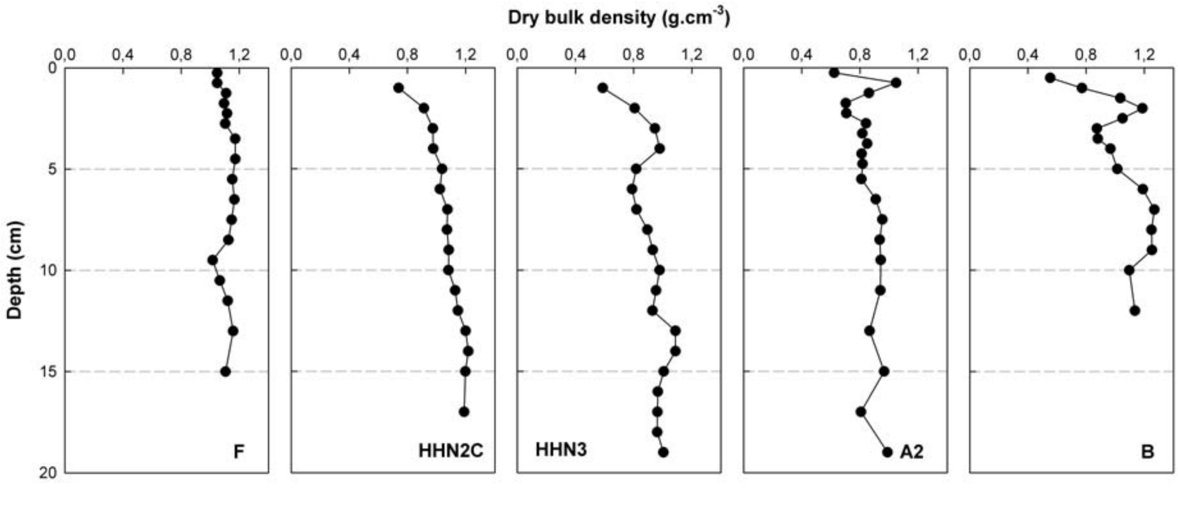

Figure 11.3: A: Depth profiles of dry bulk density in studied cores.

Station F is the most shallow one of all studied sites. The low absolute activity concentrations of all gamma emitting radionuclides compared to other sites may be caused by an autochthonous carbonate dilution. This interpretation is supported by relatively high dry bulk densities of the samples from site F, as aragonite, the principle mineral of coral reefs in the area, has a density of about 2.9 $g \cdot cm^{-3}$ (Enmar et al., 2000) and higher Ca concentrations compared to the other deeper cores.

The ratio of Al_2O_3/CaO varies in different cores. As it can be seen in Fig. 11.4, shallower cores (F and HHN2C) have higher portion of the carbonate constituent which originates mainly from autochthonous sources including algae and products of reef erosion. In deeper cores, on the other hand, the Al_2O_3 portion is higher - it represents allochthonous material originated in riverine (or airborne) sources. Both major components are therefore characterized by an inverse linear relationship, which represents the "dilution" of detritic material by biogenic carbonates.

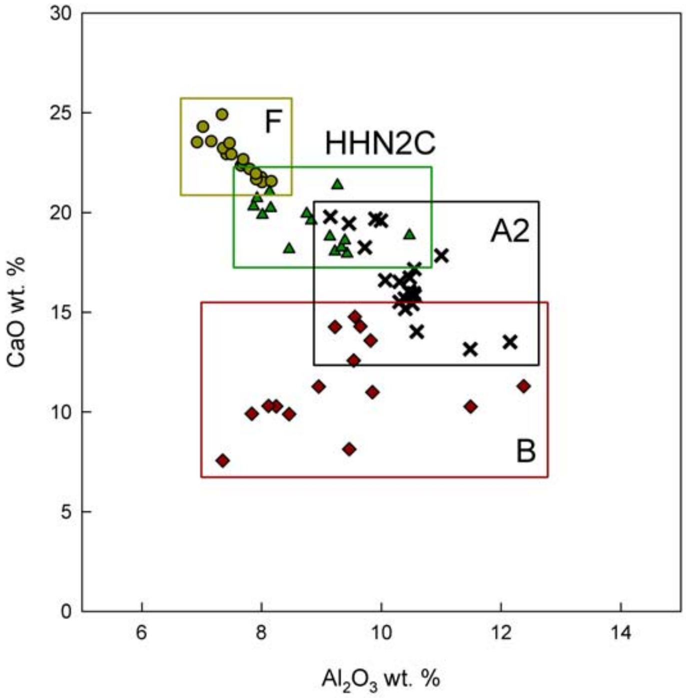

Figure 11.4: *Al_2O_3 vs CaO in cores from the GOE (Source of raw data: Garbe-Schönberg (2010)).*

In core A2, the concentrations of both radiotracers in the deepest sampling interval (20–22 cm) are unexpectedly high. This can most probably be attributed to a mistake during sample handling. The same anomaly occurs for some other main or trace elements and parameters studied on this core (Garbe-Schönberg et al., 2010).

11.3.2 Th series disequilibrium

In most of the sediment profiles strong radioactive disequilibrium between shorter lived members of ^{232}Th series, namely ^{228}Th ($T_{1/2}$=1.9 years) and ^{228}Ra ($T_{1/2}$=5.8 years) was revealed close to the sediment/water boundary (Fig. 11.5A). The measured activity concentrations C were corrected for decay and ingrowth during waiting time t_W elapsed between sample collection and measurement. The activity concentration to the time of sample retrieval $C(0)$ are:

$$C_{Ra-228}(0) = \frac{C_{Ra-228} - C_{Th-232}(0) \cdot (1 - e^{-\lambda_2 t_W})}{e^{-\lambda_2 t_W}} \tag{11.1}$$

and

$$C_{Th-228}(0) = \frac{C_{Th-228} - \frac{\lambda_3}{\lambda_3 - \lambda_2} \cdot a_{Ra-228}(0) \cdot (e^{-\lambda_2 t_W} - e^{-\lambda_3 t_W})}{e^{-\lambda_3 t_W}} \tag{11.2}$$

where λ_2 and λ_3 are decay constants of ^{228}Ra and ^{228}Th, respectively. Decay of ^{232}Th can be considered as negligible in the timescale of interest (maximum 10–20 years). Because ^{232}Th values were not explicitly analyzed within this study by radiometric methods, it is assumed to be constant within each sediment profile. It is estimated as a mean value of ^{228}Ra and ^{228}Th concentrations in the bottom parts of the sediment cores: 30.1 ± 1.6, 35.1 ± 0.4, 41.8 ± 0.5, 46.78 ± 1.5 and 47.3 ± 0.5 $Bq \cdot kg^{-1}$ for cores F, HHN2C, HHN3, A2 and B, respectively. ^{232}Th calculated from Th concentration measured by ICP-MS is included in Fig. 11.5.

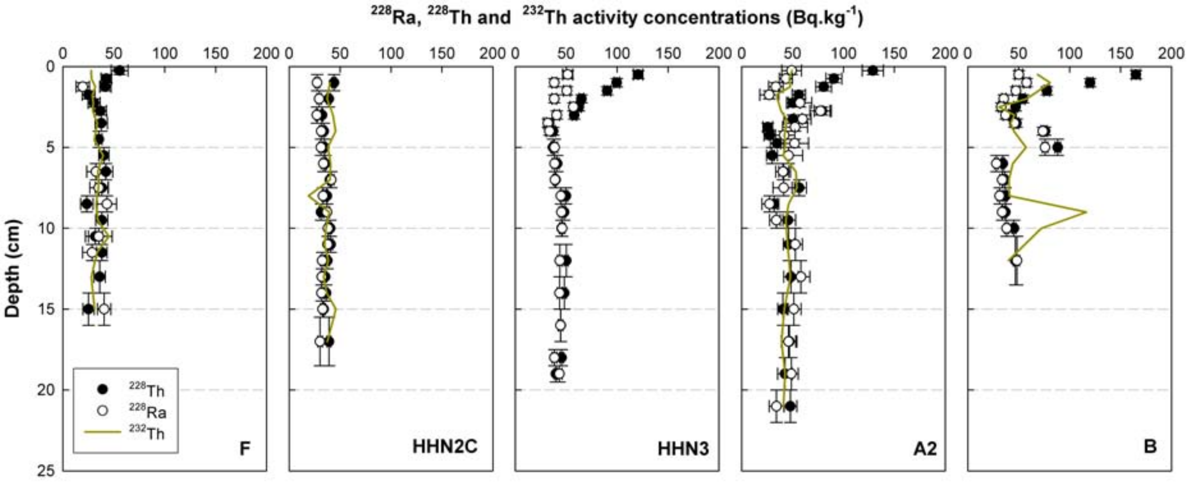

Figure 11.5: Activity concentration profiles of ^{228}Th (full circles) and ^{228}Ra (empty circles) with ^{232}Th calculated from Th concentration (ICP-MS) drawn with full line. In core F ^{228}Ra was under decision threshold in the upper part of the profile.

^{228}Ra has previously been observed to be deficient in the uppermost layers near the sediment/water boundary (Chen & Huh, 1999; Hancock, 2000; Hancock et al., 2000) due to desorption of Ra from bottom sediment to pore water in saline environments. In the GOE cores on the other hand, there is no obvious decrease of ^{228}Ra activity in the top parts. In four cores, however, excess ^{228}Th is present in the upper 3 cm with top layer activities reaching as much as 3 fold the equilibrium activity of ^{228}Th in the same profiles (Fig. 11.5B). In the most shallow core excess ^{228}Th is not evident; the low amount of sample material available did not allow to detect ^{228}Ra in some layers of the upper part of the profile F. However the increased activity of ^{228}Th in the upper centimeters indicates its excess, too.

^{228}Th is produced from ^{228}Ra dissolved in the water column. Being particle reactive, it becomes included into the bottom sediments in excess to ^{228}Ra. The presence of excess ^{228}Th serves as a valuable indicator of a successful recovery of the water/sediment interface during coring, which is an important prerequisite for quantifying processes using ^{210}Pb and ^{137}Cs.

11.3.3 Sediment mixing

Some other features of the radionuclide profiles, mainly quite similar appearance of $^{210}\mathrm{Pb}_{\mathrm{xs}}$ and $^{137}\mathrm{Cs}$ depth profiles, suggested that mixing might be an important process for depth distribution of radionuclides. Therefore diffusive mixing models described in Chapter 3 were applied to $^{210}\mathrm{Pb}_{\mathrm{xs}}$, $^{228}\mathrm{Th}_{\mathrm{xs}}$ and $^{137}\mathrm{Cs}$ data:

- **Model I:** Mixing only, continuous flux of tracers (Eq. 3.18) for $^{210}\mathrm{Pb}_{\mathrm{xs}}$ and $^{228}\mathrm{Th}_{\mathrm{xs}}$
- **Model II:** Mixing only, pulse-like input (Eq. 3.19) for $^{137}\mathrm{Cs}$
- **Model III:** Mixing and sedimentation, pulse-like input (Eq. 3.20) for $^{137}\mathrm{Cs}$.

For $^{210}\mathrm{Pb}_{\mathrm{xs}}$ and $^{228}\mathrm{Th}_{\mathrm{xs}}$ steady state conditions within continuous input were assumed (it is unlikely that it only started short time ago). For the pulse-like input of $^{137}\mathrm{Cs}$ a single spike 44 years ago was assumed representing the maximum atmospheric nuclear testing fallout. This is an approach well established in radionuclide soil diffusion studies (e.g., Bossew & Kirchner, 2004).

The depth profiles with fitted models are plotted in Fig. 11.6. $^{210}\mathrm{Pb}_{\mathrm{xs}}$ depth profiles of cores F and A2 were fitted just for the top part showing exponential decrease (similarly to the sedimentation model above) and additionally along the whole depth. The best fit parameters are listed in Tab. 11.4.

Diffusive mixing coefficients D vary widely between 0.36 ± 0.14 and 1.6 ± 0.8 cm^2yr^{-1} for $^{210}\mathrm{Pb}_{\mathrm{xs}}$, between 0.10 ± 0.04 and 0.50 ± 0.20 cm^2yr^{-1} for $^{137}\mathrm{Cs}$ and 0.64 ± 0.04 and 2.18 ± 0.69 cm^2yr^{-1} for $^{228}\mathrm{Th}_{\mathrm{xs}}$ (when omitting those with uncertainties larger than or very close to the actual values). These are values to be expected in the studied water depths (Soetaert et al., 1996; Henderson et al., 1999).

Table 11.4: *Diffusive mixing coefficients D calculated from fitting models I for* $^{210}Pb_{xs}$ *and* $^{228}Th_{xs}$ *and models II and III for* ^{137}Cs*. In bold results of Model III with significantly better fit than model II are highlighted. In italics values with very high uncertainties are marked.*

Core	D ($^{210}\mathrm{Pb}_{\mathrm{xs}}$) Model I cm^2yr^{-1}	D ($^{228}\mathrm{Th}_{\mathrm{xs}}$) Model I cm^2yr^{-1}	D ($^{137}\mathrm{Cs}$) Model II cm^2yr^{-1}	D ($^{137}\mathrm{Cs}$) Model III cm^2yr^{-1}	S ($^{137}\mathrm{Cs}$) Model III $cm \cdot yr^{-1}$
F (0-7 cm)	*4.0 ± 5.2*	–	*4.3 ± 19.0*	*0.22 ± 0.20*	0.069 ± 0.018
F (0-16 cm)	1.59 ± 0.79	–	–	–	–
HHN2C (0-5 cm)	0.36 ± 0.14	2.18 ± 0.69	0.101 ± 0.041	**0.0331 ± 0.0047**	**0.0263 ± 0.0023**
HHN3 (0-8 cm)	1.50 ± 0.90	1.5 ± 1.2	0.245 ± 0.099	0.21 ± 0.18	0.009 ± 0.036
A2 (0-7 cm)	*2.7 ± 3.5*	*1.9 ± 1.8*	*0.53 ± 0.62*	*0.15 ± 0.16*	0.028 ± 0.019
A2 (0-20 cm)	0.86 ± 0.50	–	–	–	–
B (0-3 cm)	–	0.64 ± 0.04	–	–	–
B (0-12 cm)	–	–	0.50 ± 0.20	–	–

The F-test was performed to decide whether model III (an extension of model II, with an additional advective parameter) provides statistically significant improvement. The results are shown in Tab. 11.5. Model III results in a better fit only for core HHN2. For this core a sedimentation rate of 0.0263 ± 0.0023 $cm \cdot yr^{-1}$ was calculated. This can be compared to 0.077 ± 0.007 $cm \cdot yr^{-1}$ from CF-CS model for the same core and the dust deposition estimation of 0.001 $cm \cdot yr^{-1}$.

From Tab. 11.4 it can be seen that the results of diffusive mixing coefficient vary for each isotope within each core. $^{228}\mathrm{Th}_{\mathrm{xs}}$ tends to provide the highest and $^{137}\mathrm{Cs}$ the lowest D. The reasons for this discrepancy can be various, including effects of non-local mixing, physical or

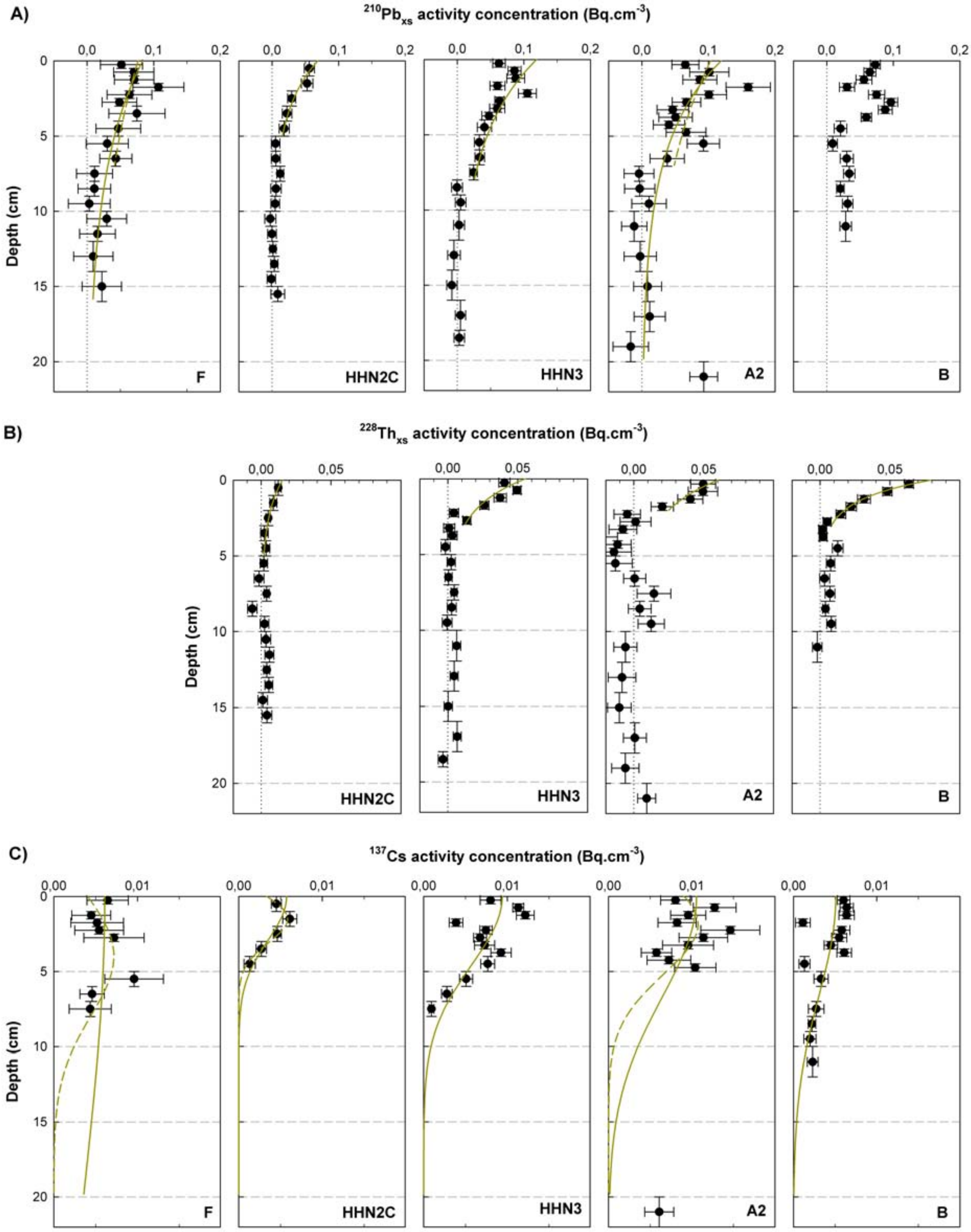

Figure 11.6: *A: Model I fitted to* $^{210}Pb_{xs}$ *depth profile.*
B: Model I fitted to $^{228}Th_{xs}$ *depth profile.*
C: Model II (mixing only, full line) and model III (sedimentation and mixing, dashed line) fitted to ^{137}Cs *depth profile.*

Table 11.5: *Results of F-test for Model II vs Model III.*

Core	RSS_{II}	RSS_{III}	DoF_{II}	DoF_{III}	F	F_{crit}
F	2.233E-5	1.814E-5	6	5	1.2	6.6
HHN2C	3.086E-6	1.793E-7	3	2	**32.4**	18.5
HHN3	5.443E-5	5.413E-5	10	9	0.05	5.12
A2	5.753E-5	5.430E-5	8	7	0.42	5.6

chemical effects leading to different behavior of individual tracers, temporal variations of mixing intensities, or depth variations of mixing intensities.

11.3.4 Radionuclide inventories and fluxes

Total radionuclide inventories in sediment profiles were determined for $^{210}\mathrm{Pb_{xs}}$, $^{228}\mathrm{Th_{xs}}$ and $^{137}\mathrm{Cs}$ using Eq. 3.22 in Sec. 3.3. The mean yearly $^{210}\mathrm{Pb_{xs}}$ flux was calculated using Eq. 3.23.

$^{210}\mathrm{Pb_{xs}}$ inventories

Literature data from geographically close areas summed up in Tab. 11.7 show a very wide span of $^{210}\mathrm{Pb_{xs}}$ inventories of 800–9000 $Bq \cdot m^{-2}$. One remarkable exception is the enormous $^{210}\mathrm{Pb_{xs}}$ inventory in the hypersaline lake Dead Sea, which is caused mainly by in-situ production of $^{210}\mathrm{Pb}$ from dissolved $^{226}\mathrm{Ra}$ (Kirchner et al., 1997).

Calculated radionuclide inventories and $^{210}\mathrm{Pb_{xs}}$ fluxes (Eq. 3.22 and 3.23) for our sediment cores are presented in Tab. 11.6. $^{210}\mathrm{Pb_{xs}}$ inventories are consistent throughout the studied area, between 4150 ± 290 and 6200 ± 1200 $Bq{\cdot}m^{-2}$, with the exception of site HHN2C, which contains approximately half the inventory of the other sites (2220 ± 280 $Bq \cdot m^{-2}$). Naturally, this is reflected by the estimated $^{210}\mathrm{Pb_{xs}}$ fluxes, being 69.3 ± 8.9 $Bq \cdot m^{-2} \cdot yr^{-1}$ at site HHN2C and an average of 160 $Bq \cdot m^{-2} \cdot yr^{-1}$ for the remaining cores. This is in good agreement with a mean $^{210}\mathrm{Pb}$ atmospheric flux over continents in the latitudal band 10°-30° N of 160 $Bq \cdot m^{-2} \cdot yr^{-1}$ compiled globally by Preiss et al. (1996). It is also comparable to $^{210}\mathrm{Pb}$ data from lake Kinneret presented by Stiller & Imboden (1986). They estimated the flux at the sediment-water interface to vary between 100 and 270 $Bq \cdot m^{-2} \cdot yr^{-1}$. The sediment column $^{210}\mathrm{Pb_{xs}}$ inventory based on data from lake Kinneret measured by Kirchner et al. (1997) and Hambright et al. (2004) is 6800 and 5270 $Bq \cdot m^{-2}$, respectively.

Table 11.6: *Inventories ($\mathcal{I}$) and fluxes ($\mathcal{F}$) of $^{210}Pb_{xs}$, ^{137}Cs and $^{228}Th_{xs}$.*

Core	$^{210}\mathrm{Pb_{xs}}$		$^{137}\mathrm{Cs}$	$^{228}\mathrm{Th_{xs}}$
	$\mathcal{I}$ $Bq \cdot m^{-2}$	$\mathcal{F}$ $Bq \cdot m^{-2} yr^{-1}$	$\mathcal{I}$ $Bq \cdot m^{-2}$	$\mathcal{I}$ $Bq \cdot m^{-2}$
F	5400 ± 1100	167 ± 33	>329 ± 59	–
HHN2C	2220 ± 280	69.3 ± 8.9	193 ± 15	323 ± 54
HHN3	4150 ± 290	129.5 ± 9.1	495 ± 26	858 ± 68
A2	6200 ± 1200	195 ± 36	501 ± 65	800 ± 140
B	4740 ± 310	148.0 ± 9.7	>370 ± 25	1086 ± 69

Table 11.7: *Inventories of* $^{210}Pb_{xs}$ *and* ^{137}Cs *in sediment cores published previously from adjacent areas. N is the number of cores analyzed in the individual projects. Inventories are corrected to reference years listed in the table. Values are reported as (Minimum–Maximum) and Median, for N>3. In the lower part of the table compilations of data for* $^{210}Pb_{xs}$ *inventories (based on mean* ^{210}Pb *atmospheric fluxes over continents in selected latitudal bands) and for* ^{137}Cs *(an estimated areal deposition from global nuclear fallout, not including Chernobyl accident fallout) are listed.*

Site	Depth m	N	Ref. year	$^{210}\mathrm{Pb_{xs}}$ inventory $Bq \cdot m^{-2}$	$^{137}\mathrm{Cs}$ inventory $Bq \cdot m^{-2}$	Reference
Gulf of Eilat	240–800	5	2007,8	2220–6200 (4740)	305–415 (360)	Present study
Lake Kinneret	250	1	1995	5270	1320	Hambright et al. (2004)
Lake Kinneret	42	1	1994	6800	2790	Kirchner et al. (1997)
Dead Sea	320	1	1979	338500	1120	Kirchner et al. (1997)
E-Mediterranean	2800–4000	6	2000	1800–3900 (2400)	100–140 (120)	Garcia-Orellana et al. (2009)
E-Mediterranean - Aegean Sea	–	6	–	800–1800 (1200)	–	Uğur (Tanbay) & Yener (2001)
E-Mediterranean	2100–4300	4	2007	1100–9000 (1600)	–	Barsanti et al. (2011)
E-Mediterranean	340–4600	13	2004	1100–6600 (2900)	–	Basso et al. (2004)
E-Mediterranean - Gulf of Patras	50–120	8	2005	–	250–790 (380)	Evangeliou et al. (2009)
E-Mediterranean - NE Aegean Sea	70	6	2005	–	330–920 (370)	Evangeliou et al. (2009)
W-Mediterranean	2500–3600	7	2007	2500–7200 (4200)	70–180 (140)	Barsanti et al. (2011)
W-Mediterranean	2900	3	2000	2200–2700	70–80	Garcia-Orellana et al. (2009)
W-Mediterranean	~ 1000		1995	–	~ 230	Papucci et al. (1996) and references therein
10-30° N latitude band (GOE)	–	–	–	5160	–	Preiss et al. (1996)
30-60° N latitude band (Mediterranean)	–	–	–	3750	–	Preiss et al. (1996)
20-30° N latitude band (GOE)	–	–	2007	–	980	UNSCEAR (2000)
30-40° N latitude band (E-Mediterranean)	–	–	2007	–	1300	UNSCEAR (2000)
GOE	–	–	2007	–	290–410	Estimate, Sec. 11.3.4

^{137}Cs inventories

Previously reported ^{137}Cs inventories from the region reach values of 100–920 $Bq \cdot m^{-2}$ in the Eastern Mediterranean and considerably higher in sediments of the Dead Sea and Lake Kinneret (Tab. 11.7). An estimation of cumulative surface deposition of ^{137}Cs can be obtained from data of UNSCEAR (2000). Here the sum of annual deposition of radionuclides produced in atmospheric nuclear testing in the northern hemisphere (decay corrected to 2007) together with latitudal distribution of deposition can be used for estimating ^{137}Cs deposited in the GOE area to approximately 1000 $Bq \cdot m^{-2}$. This value is a global estimate of the 20–30° N latitudal band and does not take into account the local conditions, for example precipitation. Fallout was found to be directly proportional to precipitation (e.g., Pálsson et al., 2013) and the relationship can be described by a non-linear (power) function (Pálsson et al., 2013). The UNSCEAR value also does not take the fine resolution of the latitudal effect into account.

Data on global fallout (^{90}Sr) in the Middle East are available from the Environmental Measurements Laboratory database (EML, 2011). Although the database does not include data measured in close vicinity of the studied area, it can be used for estimation of fallout in the Gulf of Eilat area. The data compiled from the EML database contained samples from 6 locations in the Middle East collected between 1960–1975: Qamishli and Damascus (Syria), Tehran (Iran), Beirut (Lebanon), Cairo (Egypt) and Dhahran (Saudi Arabia). The locations cover geographical latitudes from 37°N to 26°N. The values were reported monthly, but the datasets are not continuous. In Tab. 11.8 the monthly measured depositions are integrated into yearly sums in order to eliminate seasonal variability. For Tehran, Beirut, Cairo and Dhahran two columns of values are reported in the table, I and II. In the column I depositions are reported for the years when (close to) complete data coverage is available (10-12 months of the year). In the other column II yearly depositions for only partial coverage years (6-9 months) are reported. The data coverage for some stations was poor (< 6 months), therefore the data for those years were omitted.

Table 11.8: *Yearly ^{137}Cs depositions in 6 Middle East locations. Source: EML (2011). Column I: the values are given when (close to) complete data coverage is available (10-12 months of the year). Column II: the values are given when only partial coverage years (6-9 months) are reported. In the last line total inventories estimates (using Eq. 11.4) originating from fallout between 1945–1993 are presented.*

Year	UNSCEAR (2000) $Bq \cdot m^{-2}$	Qamishli $Bq \cdot m^{-2}$	Tehran $Bq \cdot m^{-2}$		Beirut $Bq \cdot m^{-2}$		Damascus $Bq \cdot m^{-2}$	Cairo $Bq \cdot m^{-2}$		Dhahran $Bq \cdot m^{-2}$	
		I	I	II	I	II	I	I	II	I	II
1960	18.9					7.7				14.6	
1961	26.1				60.4					10.2	
1962	109.6			25.5	174.2						
1963	204.4		215.5		267.3				40.6		
1964	131.6	155.2	83.0		210.0		69.9	24.7		54.5	
1965	62.9	91.3	47.5		121.1		43.1		10.1		8.8
1966	27.3	33.1		7.7		14.0	19.6			5.4	
1967	14.4			9.5						8.4	
1968	17.0		21.0		22.1					4.3	
1969	13.1		17.1		15.0					3.5	
1970	18.7		6.1			18.4					
1971	17.7		15.7							5.8	
1972	8.2			6.9						3.7	
1973	3.1			8.3						0.3	
1974	12.1									4.7	
1975	6.0										2.4
Total deposition (1945–1993, decay corr. 2007)	981	1213	941		1454		561	184		412	

The deposition data were originally reported for ^{90}Sr. In order to obtain approximate values for ^{137}Cs, they were multiplied by a factor of 1.5 assuming a constant Cs/Sr ratio (UNSCEAR, 2000). Eventually, all data were decay corrected to the year 2007.

The time dependent source term was derived from the yearly depositions (1960–1975) in the 20–30° N latitudal band reported in UNSCEAR (2000) - Tab. 11.8. The deposition in the Middle East is assumed here to be following this source term multiplied by a scaling factor K:

$$d(t, x) = K(x) \cdot f(t, 20\text{–}30^\circ \text{ N}). \tag{11.3}$$

The estimates of depositions at individual sites were obtained by the least square fits of the source-term function to yearly fallout data (Fig. 11.7). For the fit only data from columns I of Tab. 11.8 were used and the data from columns II are plotted in Fig. 11.7 as additional information only.

The total inventory in the 20–30° N latitudal band (UNSCEAR, 2000) between 1945 and 1993 decay corrected to year 2007 is 981 $Bq \cdot m^{-2}$. The factors $K(x)$ obtained from the least square fit were used for estimation of total deposition in individual monitoring locations (presented in the last line of Tab. 11.8) as

$$\mathcal{I}(x) = K(x) \cdot \mathcal{I}(20\text{–}30^\circ \text{ N}). \tag{11.4}$$

It can be seen in Fig. 11.8 that in more northerly locations (Qamishli, Tehran, Beirut and Damascus) the total calculated inventories reached higher values than those measured in southerly locations (Cairo and Dhahran). Also a direct relationship of the ^{137}Cs deposition to rainfall can be seen in the Fig. 11.8. From these data however it is not possible to decide which of these two parameters has a more significant effect on deposition.

Pálsson et al. (2013) presented a model describing monthly deposition as a function of rainfall and latitude, which can be reduced for purposes of total inventory as:

$$ln(\mathcal{I}) = L + b \cdot ln(rain) + c \cdot latitude + h(network), \tag{11.5}$$

where L is a constant to be determined, $rain$ is yearly precipitation in mm and $latitude$ is expressed in °N. $network$ is categorical variable (for data originating from EML it equals 0). For 20–30° N following variables were found by Pálsson et al. (2013): $b = 0.33 \pm 0.01$ and $c = 0.048 \pm 0.002$ (2σ uncertainty). From these it can be estimated that increase of yearly precipitation from 20 to 900 mm can lead to 3.5 fold increase in fallout deposition, while increase of latitude from 26°N to 27°N could explain 1.7 fold increase of deposition. Fig. 11.8 shows combined effect of both.

Fitting the model (Eq. 11.5) to rainfall and latitude data for the 6 locations vs. estimated total depositions from Tab. 11.8 using a non-linear surface fit (using Origin), a coefficient $L = 28.0 \pm 3.7$ can be determined. It is then used for calculating expected vales for inventory in the GOE using Eq. 11.5 with mean precipitation of 30 $mm \cdot yr^{-1}$ and latitude of 29.9° N. The inventory was estimated to be 360 ± 55 $Bq \cdot m^{-2}$ (2σ uncertainty). A comparison of fallouts in all evaluated Middle East locations together with the GOE is plotted in Fig. 11.9.

An important contribution from the Chernobyl accident fallout is not expected in the studied area based on results from Egypt (Shawky & El-Tahawy, 1999) and southern Jordan (Hamarneh et al., 2003). Schlesinger et al. (1987), on the other hand, report the post-Chernobyl deposition in southern Israel of some 400 $Bq \cdot m^{-2}$, from which 250 $Bq \cdot m^{-2}$ would remain undecayed until 2007. Kirchner et al. (1997) found a small Chernobyl related maximum in the sediment profile of lake Kinneret and they concluded, that most of ^{137}Cs has been brought by erosion from the watershed and by resuspension and focusing from shallower zones and not by

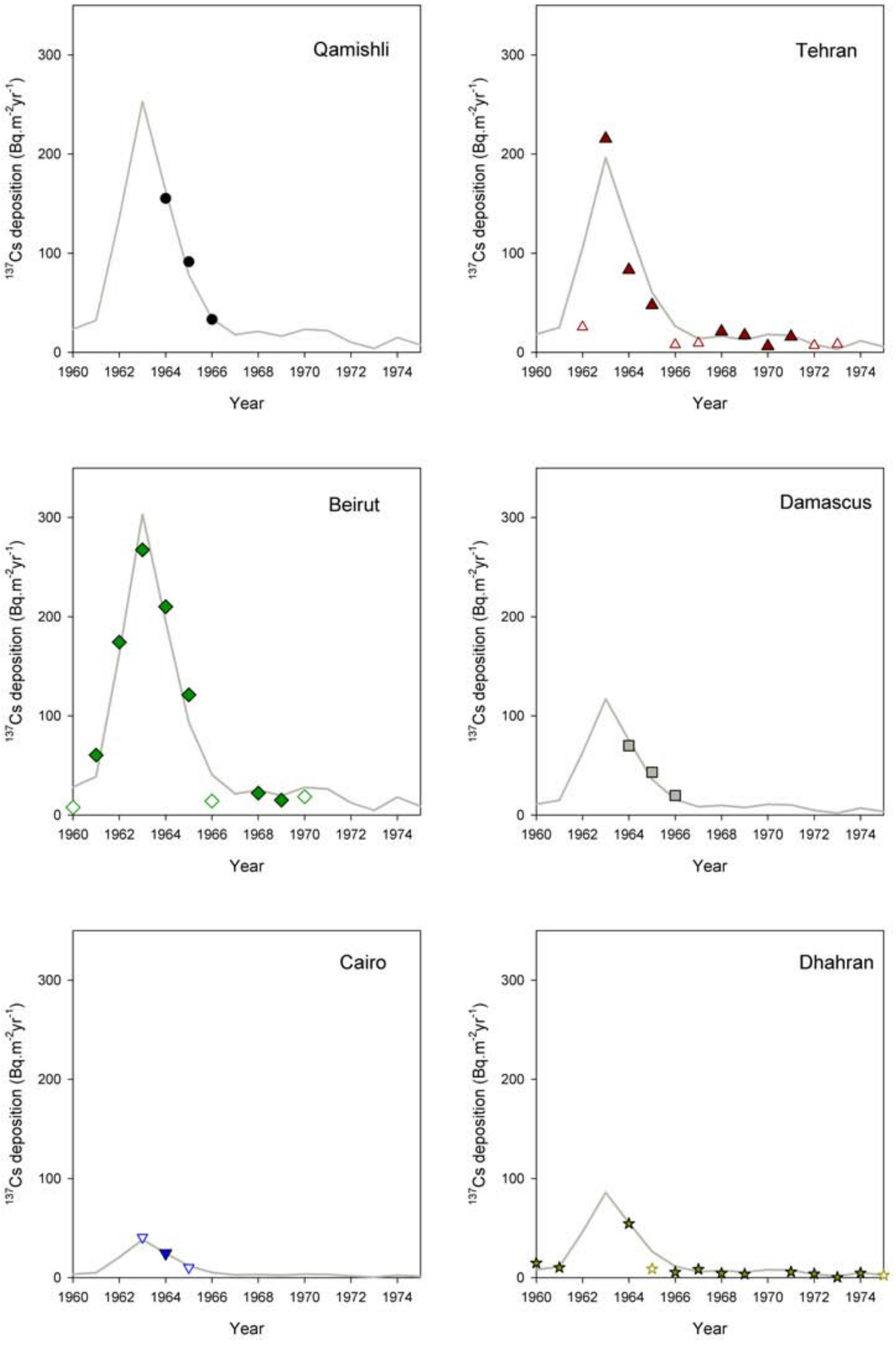

Figure 11.7: *Yearly activities of ^{137}Cs fallout in 6 Middle East sites. The full lines represent the least square fits of the source term (UNSCEAR, 2000) through the yearly activities of (close to) complete data points (full symbols). Empty symbols represent the data points where only partial coverage is available.*

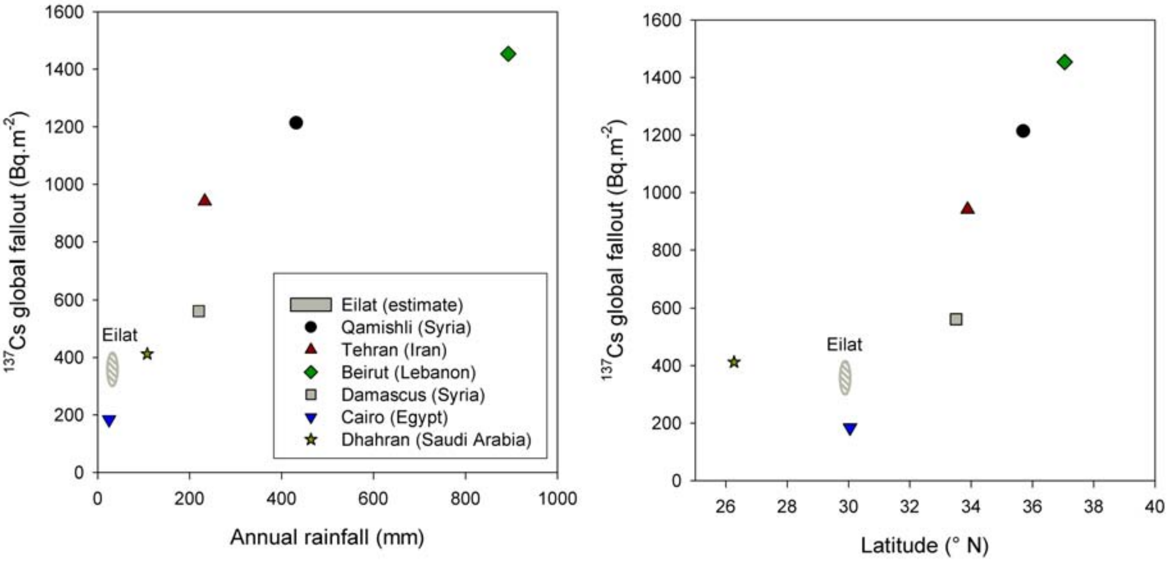

Figure 11.8: *Left:* ^{137}Cs *total fallout at Middle East locations in relation to mean annual precipitation (WMO, 2012) and right: latitude. The total inventory (corrected to year 2007) in the GOE is estimated to lie between 305–415* $Bq \cdot m^{-2}$.

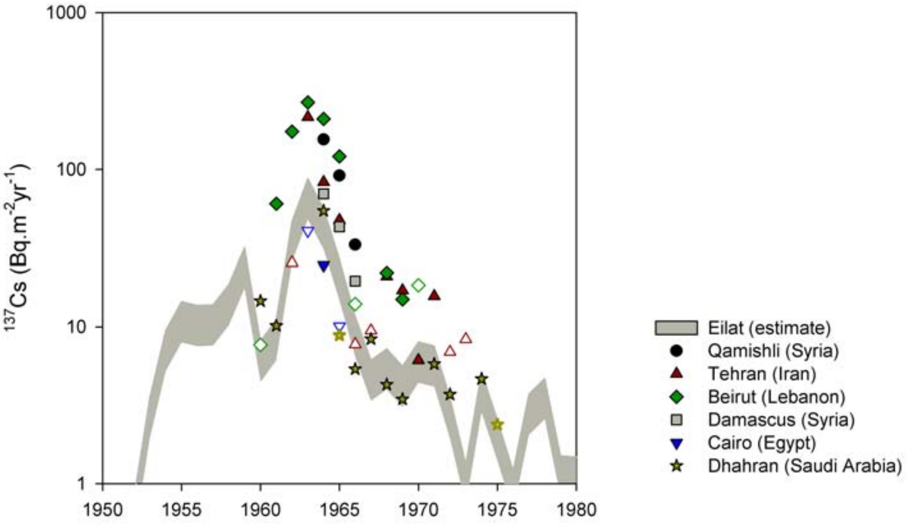

Figure 11.9: *Global fallout* ^{137}Cs *deposition at six locations in the Middle East (log-normal scale). The data points represent yearly integrations of reported monthly depositions. Full symbols stand for years when a (close to) complete dataset is available (10-12 months), open symbols stand for years when only partial coverage is available (6–9 months). The shaded area is a minimum to maximum estimate of the fallout in the GOE.*

direct fallout. ^{137}Cs sediment inventories in lake Kinneret sediments based on Kirchner et al. (1997) and Hambright et al. (2004) are 2780 $Bq \cdot m^{-2}$ and 1320 $Bq \cdot m^{-2}$, respectively.

Inventories of ^{137}Cs found in our cores from GOE vary between 193 ± 15 and 501 ± 65 $Bq \cdot m^{-2}$. They show comparable values in both deep sites HHN3 and A2 - 495 ± 26 and 501 ± 65 $Bq \cdot m^{-2}$, respectively. Site B has a lower inventory (370 ± 25 $Bq \cdot m^{-2}$), but due to the fact that non-zero values of ^{137}Cs were observed throughout the core there is a possibility that the total inventory at this site would have reached greater values if the recovered core had been longer.

Both shallow sites, F and HHN2C, have low ^{137}Cs inventories of 329 ± 59 and 193 ± 15 $Bq \cdot m^{-2}$, respectively. In site F this number is likely to be underestimated, as some of the values were close to decision thresholds and there was probably some unobserved ^{137}Cs inventory present which could not be taken into account due to the activity below our detection capabilities.

All observed inventories are consistent with the above presented estimate of 305–415 $Bq \cdot m^{-2}$ for direct fallout from atmospheric weapons testing.

^{228}Th$_{xs}$ inventories

^{228}Th$_{xs}$ inventories vary between 323 ± 52 and 1086 ± 69 $Bq \cdot m^{-2}$. ^{228}Th$_{xs}$ is rarely used as a tracer and therefore comparison can be only done internally between 4 GOE sites. The inventory is lowest in core HHN2C and highest at site B.

Focusing

The low values of all 3 nuclide inventories at site HHN2C indicate that sedimentation conditions at this site might be influenced by its proximity to an underwater canyon slope, an environment not very suitable for accumulation. On the other hand, deep water sites HHN3, A2 and B with high inventories can be areas of fine particle focusing.

11.3.5 Wadi sediment, dust and fertilizer samples

The activity concentrations of radionuclides analyzed in wadi sediments, dust and fertilizer samples are reported in Tab. 11.9 and compared to the mean activity concentrations measured in individual GOE sediment cores in Tab. A.23 in Appx. A. For the sediment samples the activities are calculated as arithmetic means of two depth intervals: the upper 5 cm and bottom rest of the cores. Generally, 5 cm is the depth from which concentrations of phosphorus, heavy metals (Garbe-Schönberg, 2010) and also ^{226}Ra in studied cores are observed to start rising.

^{40}K

Concentrations of ^{40}K are comparable in wadi sediments (404–691 $Bq \cdot kg^{-1}$) and GOE bottom sediments (375–470 $Bq \cdot kg^{-1}$) (Fig. 11.10). Mean activities for deeper cores are 410–470 $Bq \cdot kg^{-1}$, likely due to higher clay mineral content (Herut & Nishri, 2004), and 373–403 $Bq \cdot kg^{-1}$ for shallow cores, being likely diluted by biogenic carbonates (Fig. 11.4). ^{40}K is low for dust samples and fertilizer (mazut), but high for the phosphate ore. The reason for such difference between fertilizer (mazut) and phosphate ore (factor of 4 reduction, while ^{226}Ra is reduced only by factor of 2) is not known, but can possibly be a result of natural variability of K content (Al-Hwaiti et al., 2010).

Table 11.9: *Activity concentrations of gamma emitting radionuclides measured in samples of wadi sediment, dust and fertilizers.*

Sample	Number	^{40}K $Bq \cdot kg^{-1}$ $\gamma-$spec.	^{137}Cs $Bq \cdot kg^{-1}$ $\gamma-$spec.	^{210}Pb $Bq \cdot kg^{-1}$ $\gamma-$spec.	^{226}Ra $Bq \cdot kg^{-1}$ $\gamma-$spec.	^{228}Ra (^{228}Ac) $Bq \cdot kg^{-1}$ $\gamma-$spec.	^{228}Th (^{212}Pb, ^{208}Tl) $Bq \cdot kg^{-1}$ $\gamma-$spec.	^{40}K $Bq \cdot kg^{-1}$ ICP-MS	^{238}U $Bq \cdot kg^{-1}$ ICP-MS	^{232}Th $Bq \cdot kg^{-1}$ ICP-MS
Wadi sediment	1	512 ± 14	8.2 ± 0.3	65.3 ± 5.0	44.8 ± 0.9	55.4 ± 1.1	62.1 ± 1.6	446	31.9	34.8
Wadi sediment	2	404 ± 21	12.4 ± 1.0	97.0 ± 11.9	48.3 ± 2.1	27.2 ± 2.1	27.8 ± 1.5	216	23.7	14.2
Wadi sediment	5	691 ± 30	1.4 ± 0.3	78.7 ± 9.0	51.3 ± 1.9	57.1 ± 2.2	60.3 ± 3.2	626	41.1	43.2
Dust	Dust IC	172 ± 67	< 5.4	125 ± 32	44.7 ± 8.3	< 21.6	22.6 ± 3.3	135	43.2	18.9
Dust	Dust PLB	221 ± 77	< 5.8	88 ± 27	29.4 ± 7.6	< 22.5	15.2 ± 5.8	168	51.6	18.7
Dust	Dust MSS	164 ± 38	< 2.6	86 ± 18	42.4 ± 4.0	< 10.9	18.0 ± 1.7	147	49.9	19.0
Fertilizer	Phosphate	1202 ± 134	< 4.0	1145 ± 139	1234 ± 89	< 17.1	4.1 ± 2.3	1170	2011	3.0
Fertilizer	Mazut	292 ± 46	< 4.3	620 ± 78	651 ± 47	< 17.2	5.2 ± 1.8	56	2545	3.7

^{40}K measured by gamma spectroscopy is in a good agreement with results obtained by ICP-MS in sediment samples (Tab. A.23). In wadi, dust and fertilizer samples there are up to factor of 2 deviations, though. The reason for this mismatch might be that measurements were performed on a different set of small subsamples, which may not have been ideally representative for the studied material. Aluminum normalization was performed in order to account for grain size effects in ^{40}K content in sediment, wadi and dust samples (Tab. A.24, Fig. 11.10). The normalized values were comparable for sediment samples, and dust, and slightly higher for wadi samples.

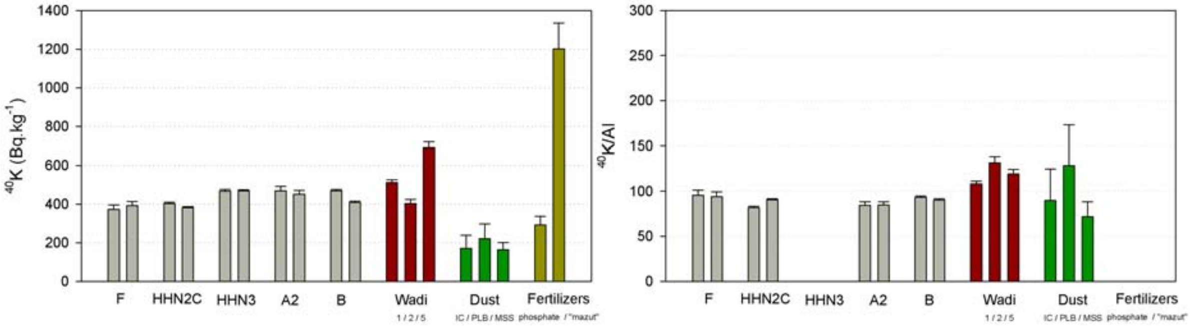

Figure 11.10: *Mean activities of ^{40}K in sediments, wadi sediments and fertilizer samples (left) and those normalized by Al (right) - not applicable for fertilizer samples.*

^{137}Cs

^{137}Cs could only be detected in wadi sediments. There was no nuclear fallout pollution expected to be found in fertilizer samples and ^{137}Cs was also below the decision threshold in dust samples (possibly also due to very low sample amount available, being below 1 g on average).

^{226}Ra, Ra/U activity ratio and ^{210}Pb

High ^{226}Ra activity concentrations were found in samples of fertilizer: 1200 $Bq \cdot kg^{-1}$ for phosphate rock and >600 $Bq{\cdot}kg^{-1}$ for mazut (Fig. 11.11). Similar activity concentrations of uranium series radionuclides in phosphate rocks from Aqaba and Eshidiya, Jordan, were reported by Al-Hwaiti et al. (2010). Activity concentrations of ^{226}Ra are comparable for wadi sediment and dust samples (in the range of 30–50 $Bq \cdot kg^{-1}$). A rather low concentration was found also in the dust sample PLB, collected in the vicinity of the phosphate loading berth, where an increase in ^{226}Ra concentration as a result of phosphate dust pollution was expected. ^{238}U is enriched in both fertilizer samples compared to ^{226}Ra, with ^{238}U/^{226}Ra activity ratios of 1.6 and 3.9, respectively (Tab. A.25). The U/Ra ratio was also reported to vary between 2–10 in samples from Jordanian phosphate rock (Al-Hwaiti et al., 2010).

Excess ^{210}Pb is present mainly in top parts of sediment cores, but also in dust and wadi samples. Radioactive equilibrium between ^{210}Pb and ^{226}Ra was found in samples of fertilizer (Fig. 11.11).

Th series

Thorium series radionuclides were present in low concentrations in fertilizer samples (about 3–5 $Bq \cdot kg^{-1}$), higher (about 20 $Bq \cdot kg^{-1}$) in dust samples and highest (14–62 $Bq \cdot kg^{-1}$) in wadi

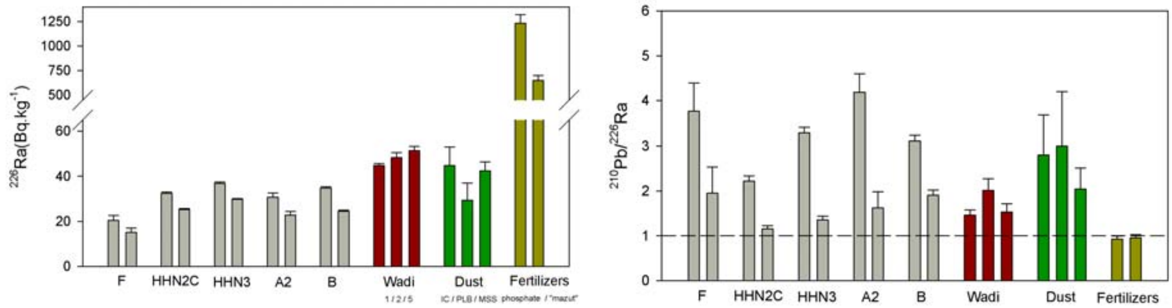

Figure 11.11: *Mean activities of ^{226}Ra in sediments, wadi sediments and fertilizer samples (left). ^{210}Pb/^{226}Ra activity ratios (right).*

sediment samples. GOE sediment samples also showed a wide range of activity means, 30–57 $Bq \cdot kg^{-1}$ ^{232}Th (Tab. A.23).

11.3.6 Radionuclide correlations with other elements

Correlation of selected radionuclides (^{226}Ra, ^{228}Ra and ^{40}K) with elemental composition measured in 4 cores (F, HHN2C, A2 and B) was examined. Due to the fact that most of the datasets were non-normally distributed, the Spearman rank correlation coefficient was used to describe their relationship. In Tab. 11.10 positive and negative correlations that were found to be statistically significant (p-value < 0.01) are listed.

Table 11.10: *Statistically significant (p-value<0.01) correlation of radionuclide data with elemental composition expressed as the Spearman's correlation coefficient r_S.*

Nuclide	Core	Strong positive correlation $r_S > 0.75$	Positive correlation $0.60 < r_S < 0.75$	Negative correlation $r_S < 0$
^{226}Ra	F (N=17)	–	Cd, Mo	–
	HHN2C (N=16)	Pb, Sn, Cd, Mo, Zn, Cu	^{40}K, W, La, Cs, Sb, Y, Ga, Ni, Co, Cr, V, Sc, P, Mn, Fe, Al	Ca, Sr
	A2 (N=20)	–	Zn, Cu, Ni, Co, V, P	Li
	B (N=15)	Pb, Ba, Cs, Cd, Mo, Ga, Zn	^{40}K, W, La, Sb, Sn, Rb, Cu, Ni, Co, Cr, V, Sc, Li, P, K, Na, Al	–
^{228}Ra	F (N=17)	–	–	–
	HHN2C (N=16)	–	U	–
	A2 (N=20)	–	Sb	–
	B (N=15)	Mo, Co, Mn	^{226}Ra, Cs, Ni, Sc	–
^{40}K	F (N=17)	–	W, Ti, K, Mg	–
	HHN2C (N=16)	–	Tl, Cs, Sn, Mo, Rb, Ga, Zn, Co, Cr, Ti, K, Mg, Mn, Fe, Al	–
	A2 (N=20)	–	–	–
	B (N=15)	Tl, Ba, K, Na	Pb, Rb	–

Positive correlations of ^{226}Ra with heavy metals (Pb, Cd, Mo, Zn (Fig. 11.12), Cu, Ni, Co, Cr, ...) were to a certain degree found in all of the studied cores. ^{226}Ra (Fig. 11.11) as well as heavy metals seem to be enriched at the core upper approximately 5 cm as a consequence of industrial pollution during the latest decades. Also in three of the cores ^{226}Ra is positively correlated with phosphorous (Fig. 11.12) and in two cases with ^{40}K, which are elements enriched in phosphate ore. ^{226}Ra is positively correlated with aluminium (Fig. 11.12), likely due to negative correlation with grain size. ^{226}Ra negative correlation was found for calcium (Fig. 11.12) and strontium, elements related to biogenic carbonates. Correlations of selected elements with ^{226}Ra are shown in Fig. 11.12 for each core individually and for the whole dataset. For phosphorus, although positive correlation was not obvious in the whole dataset, it is significant for three individual cores. This is also the case for zinc in Fig. 11.12.

^{228}Ra correlation did not show any consistent picture, except of positive relationship with

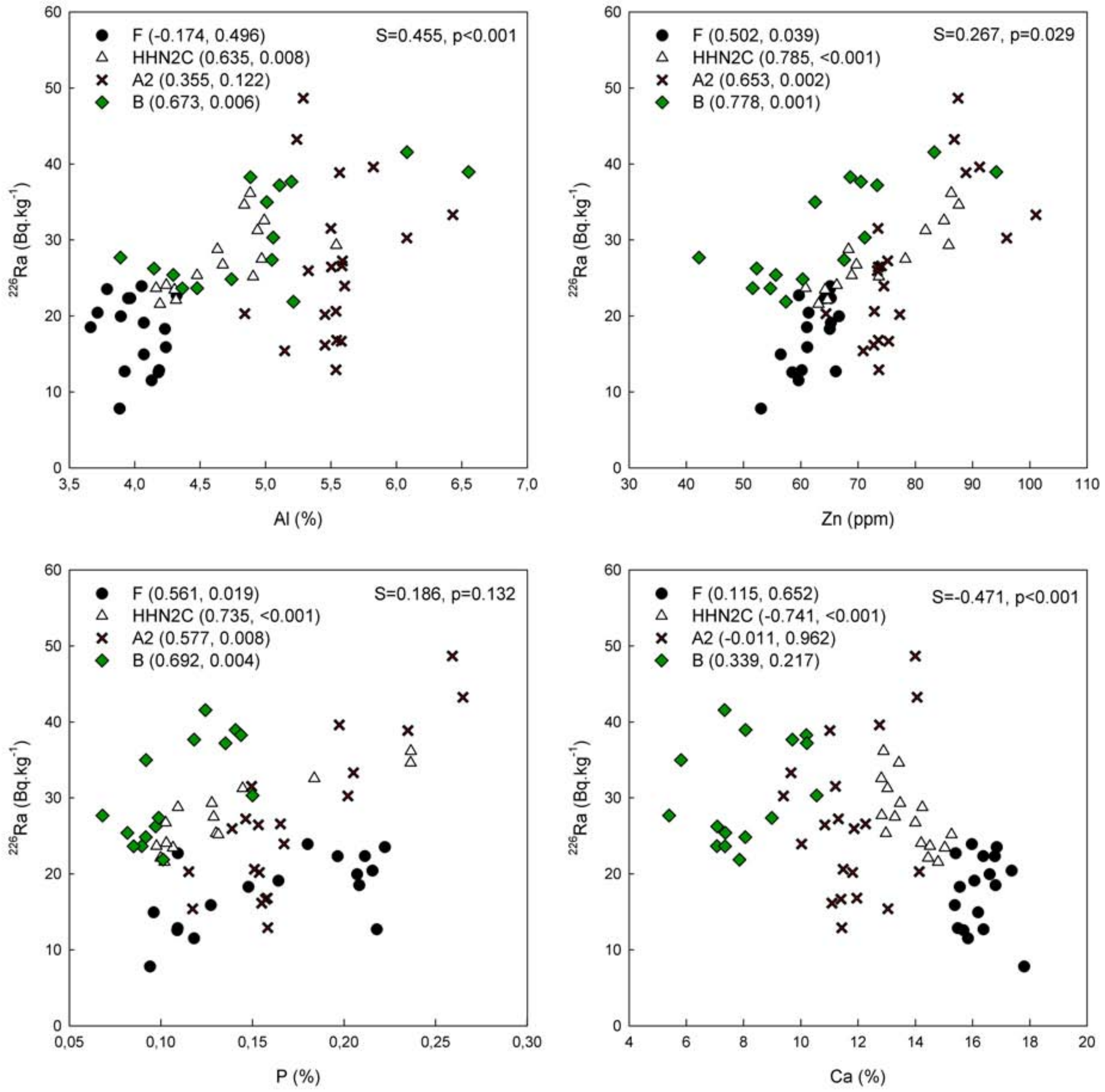

Figure 11.12: *Correlations of* ^{226}*Ra with selected elements. The Spearman correlation coefficient (*r_S*) and P-values are presented in brackets after each core. In right upper corners of each plot the correlation coefficient with associated P-value is given for the entire dataset.*

some heavy metals. ^{40}K is correlated with heavy metals and lithogenic elements. Its positive correlation with potassium is significant, although not perfect. This is likely due to the fact that ^{40}K variations in the cores are minimal and often caused more by counting statistics than real variability.

11.4 Conclusions

The study of the radionuclide depth profiles from the northern Gulf of Eilat provides new information on accumulation rates, mixing rates, sedimentation processes and sources in the studied area. The main conclusions can be summed up as follows:

1. Recent sediment accumulation rates based on $^{210}\mathrm{Pb}_{\mathrm{xs}}$ CF-CS age model range between 0.076–0.33 $g \cdot cm^{-2}yr^{-1}$. In the shallow part (250 m depth) the accumulation rate is increased by an authigenic carbonate contribution, which dilutes the material from terrestrial sources. These rates must be considered as maximum estimates due to likely contribution of mixing.
2. None of the cores showed the common ^{137}Cs peak concentration caused by deposition of the weapons fallout radiocaesium in the 1960's. Instead, ^{137}Cs concentrations are highest in the topmost parts showing in some of them an almost exponential decrease with depth.
3. Similar shapes of $^{210}\mathrm{Pb}_{\mathrm{xs}}$, ^{137}Cs and $^{228}\mathrm{Th}_{\mathrm{xs}}$ profiles are the main argument for mixing being the major contributor to radionuclides' depth distribution in the studied GOE sediments.
4. Mixing rates were quantified by means of diffusive mixing coefficient for $^{210}\mathrm{Pb}_{\mathrm{xs}}$, ^{137}Cs and $^{228}\mathrm{Th}_{\mathrm{xs}}$, which varied between 0.10 ± 0.04 and 2.18 ± 0.69 cm^2yr^{-1}. These are typical values for sediments in given water depths.
5. A contribution of sedimentation to the radionuclides' depth distribution could be quantified for one study site using a combined mixing and sedimentation model. The sedimentation rate was 0.026 ± 0.002 $cm \cdot yr^{-1}$.
6. The contribution of airborne material to the sediment in the studied area is expected to be minor. The most important source of material apart from internal focusing might be periodic floods bringing terrestrial material to the gulf through wadis.
7. Higher inventories of $^{210}\mathrm{Pb}_{\mathrm{xs}}$, ^{137}Cs and $^{228}\mathrm{Th}_{\mathrm{xs}}$ in deeper sites compared to the shallow ones indicate focusing of fine particles in the Eilat deep.
8. ^{226}Ra in sediments is positively correlated mainly with P and heavy metals. Their increased concentrations in the upper parts of the sediment profiles might be results of industrial pollution to the GOE in recent decades.

Chapter 12

Summary and outlook

> The solutions all are simple... after you have arrived at them. But they're simple only when you know already what they are.
>
> ROBERT M. PIRSIG, *Zen and the Art of Motorcycle Maintenance*

12.1 Technical aspects of gamma spectrometry of sediments

Within this work the use of non-destructive gamma spectrometric radionuclide dating with mathematically derived efficiencies was further established in the Laboratory. Emphasis was put on non-destructive analysis, because the samples are often very valuable and further reused for other types of analyses within interdisciplinary projects.

The series of validation experiments testing the correctness of the mathematically derived efficiency calibration revealed the need for detector re-characterization, which was conducted by the manufacturer. LabSOCS derived efficiencies have the disadvantage of greater uncertainties than experimental efficiencies (up to 10% for low energies), but the advantage of greater flexibility in sample geometry and matrix. Most importantly, the samples can be analyzed in a non-destructive manner.

LabSOCS based efficiency calibration is in principle suitable for sediment chronology, but should not be used without care and validation of its performance is highly recommended for each characterized detector, along with the QA routine (based on point test sources). Especially test measurements with voluminous samples of similar matrices to the sediment samples should be considered before using the detector for sediment chronology purposes for the first time, ideally immediately after its characterization. Calibrated sources used for experimental efficiency calibration, but also other reference samples, can be applied for that purpose.

While relatively high uncertainties are not strictly limiting for some tracer applications (for example studying ^{137}Cs depth profiles), it is important to know LabSOCS performance at different energies when data used for models are based on values calculated from multiple nuclides. This can cause propagation of systematic errors within applied models.

^{210}Pb based chronology does not only rely on correct determination of ^{210}Pb, but also its supported part, which is determined based on ^{226}Ra activity in sediments. It was shown within this study that the relative importance of supported lead analytics should not be underestimated, as systematic errors due to ^{226}Ra analysis can affect age estimations.

A new method of aligning parallel sediment cores based on ^{210}Pb and ^{137}Cs profiles was proposed and successfully tested in three case studies within this thesis. The method enables the interconnection of the last century sediment archives to pre-industrial ages, which is an important prerequisite of studies of recent human contribution to climate change and environmental pollution.

For studying inventories and activity ratios of artificial isotopes in sediment cores a method of summing spectra of several successive depth intervals was applied. Like that radionuclides that were below detection capabilities in individual spectra could be successfully quantified.

12.2 Site specific results

Besides the technical improvements presented in the thesis, the case studies highlighted some innovative and interesting results.

The study from the Gulf of Eilat presented for the first time sedimentation rates, major particulate sources indicating an insignificant mass contribution from dust and demonstrated the focusing processes of fine particles toward deeper parts of the studied basin. Th series radionuclides were used as additional tracers. Although the original aim of the radionuclide investigation was providing age models for studied cores, it appeared that the leading process controlling the radionuclide depth distribution is mixing rather than sedimentation.

The radionuclide chronology project in Lombok basin, Indonesia, detected unusual artificial radionuclide ratios. To further explain the sources and processes leading to their inventories and ratios a study of Pu isotopes would contribute significantly. This could not be accomplished within the scope of the presented study and therefore further investigations are recommended.

12.3 Outlook

Apart from the aforementioned plan to extend the data set of artificial isotopes in the Indonesian throughflow sediments for future investigations, there are other suggestions of possible improvements of sediment chronology techniques in the Laboratory.

Validation of LabSOCS efficiency calibration for more complex geometries deserves further investigation. One example of this is an on-going study of radionuclides in sediments from a north German lake. Here individual sample masses and radionuclide activities are low due to high organic content in the sediment. In this study an approach is being applied to combine several successive core slices for measurement within a single spectrum without physically combining the samples. This improvement allows shortening measurement times and reducing detection limits.

Another refinement leading to detection limit and / or measurement time reduction can be achieved by background suppression. It is planned (and initial steps had been taken) to construct an anticoincidence system for one of the Laboratory's detectors in order to suppress the cosmic ray induced background.

Publications connected to this thesis

Steinke, S., Mohtadi, M., Prange, M., Varma, V., Pittauerová, D., and Fischer, H. W. (submitted). Mid- to Late-Holocene Australian-Indonesian summer monsoon variability. *Quaternary Science Reviews.*

Pittauerová, D., Kirchner, G., Garbe-Schönberg, D., Herut, B., Nishri, A. and Fischer, H. W. (in review). Radionuclides and recent sedimentation rates in Northern Gulf of Eilat/Aqaba, Red Sea. *Journal of Marine Systems.*

Pittauerová, D., Mulitza, S., and Fischer, H. W. (2013). Gamma spectrometry for chronology of recent sediments. In *Isotopes in Hydrology, Marine Ecosystems and Climate Change Studies, Proceedings of an International Symposium, Monaco, 27 March–1 April 2011, IAEA*, Vol. 1: 41–48.

Pittauerová, D., Hettwig, B., and Fischer, H. W. (2013). Supported lead in Pb-210 chronology. In *Isotopes in Hydrology, Marine Ecosystems and Climate Change Studies, Proceedings of an International Symposium, Monaco, 27 March–1 April 2011, IAEA*, Vol. 2: 477–484.

Pittauerová, D., Hettwig, B., and Fischer, H. W. (2011). Pb-210 sediment chronology: Focused on supported lead. *Radioprotection*, 46(6):277–282.

Mulitza, S., Heslop, D., Pittauerová, D., Fischer, H., Meyer, I., Stuut, J.-B., Zabel, M., Mollenhauer, G., Collins, J., Kuhnert, H., and Schulz, M. (2010). Increase in African dust flux at the onset of commercial agriculture in the Sahel region. *Nature*, 466(7303):226–228.

Pittauerová, D., Ulbrich, S., Hettwig, B., and Fischer, H. W. (2010). Long-term background in gamma-spectroscopy. In *Schriftenreihe Fachgespräch Überwachung der Umweltradioaktivität. Freiburg, 24.–26.03.2009*: 314–321.

Pittauerová, D., Mulitza, S., Hettwig, B., Chehade, W., Stuut, J.-B., Mollenhauer, G., and Fischer, H. W. (2009). Application of self-absorption correction method in gamma spectroscopy for ^{210}Pb and ^{137}Cs sediment chronology on the continental slope off NW Africa. *Radioprotection*, 44(5):457–461.

Publications not included in this thesis

Fischer, H. W., Ulbrich, S., Pittauerová, D., and Hettwig, B. (2013). Medical and other radioisotopes as tracers in the wastewater-river-sediment. In *Isotopes in Hydrology, Marine Ecosystems and Climate Change Studies, Proceedings of an International Symposium, Monaco, 27 March–1 April 2011, IAEA*, Vol. 2: 403–408.

Zonneveld, K. A., Chen, L., Elshanawany, R., Fischer, H. W., Hoins, M., Ibrahim, M. I., Pittauerová, D., and Versteegh, G. J. (2012). The use of dinoflagellate cysts to separate human-induced from natural variability in the trophic state of the Po River discharge plume over the last two centuries. *Marine Pollution Bulletin*, 64(1): 114–132.

Pittauerová, D., Hettwig, B., and Fischer, H. W. (2011). Fukushima fallout in Northwest German environmental media. *Journal of Environmental Radioactivity*, 102(9): 877–880.

Fischer, H. W., Hettwig, B., and Pittauerová, D. (2011). Traces of Fukushima fallout in the environment of Northwest Germany. *Radioprotection*, 46(6): 181–185.

Pittauerová, D., Kolb, W., Rosenstiel, J., and Fischer, H. (2010). Radioactivity in Trinitite - a review and new measurements. In *Proceedings: Third European IRPA Congress, 14–18 June 2010, Helsinki, Finland*, P16: 2569–2578.

Fischer, H. W., Ulbrich, S., Pittauerová, D., and Hettwig, B. (2009). Medical radioisotopes in the environment - following the pathway from patient to river sediment. *Journal of Environmental Radioactivity*, 100(12): 1079–1085.

Goliáš, V., Vylita, T., Třískala, Z., Procházka, R., and Pittauerová, D. (2009). Short-term radioactive disequilibrium in thermal mineral waters in Karlovy Vary (Carlsbad) spa, Czech Republic. *Radioprotection*, 44(5): 155–158.

Stuut, J.-B. W., Fischer, H. W., Mollenhauer, G., Mulitza, S., Pittauerová, D., Zabel, M., and Schulz, M. (2008). Late holocene interdecadal climate variability in the Sahel: Inferences from a marine dust record offshore Senegal. In *Geophysical Research Abstracts*, Vol. 10.

Appendix A

Measured data

Table A.1: *Long-term background: Radon and thoron progeny in the measurement chamber*

			Det 3			Det 5			Det 6		
Nuclide	Energy keV	I_γ %	Energy keV	Count rate $10^{-3}s^{-1}$	Rel. uncert. % (1σ)	Energy keV	Count rate $10^{-3}s^{-1}$	Rel. uncert. % (1σ)	Energy keV	Count rate $10^{-3}s^{-1}$	Rel. uncert. % (1σ)
^{214}Bi	609.3	46.1	609.2	0.9285	4.2	609.2	0.7718	2.6	609.1	1.9034	1.1
	665.5	1.46	664.8	0.0590	22.3	-	-	-	665.3	0.0564	18.1
	768.4	4.94	768.1	0.1118	12.0	768.6	0.0840	12.8	768.3	0.1657	6.4
	934.1	3.03	934.0	0.0423	37.8	934.1	0.0156	68.1	934.0	0.0873	20.5
	1120.3	15.1	1120.2	0.2402	5.2	1120.2	0.2212	4.6	1120.2	0.4527	2.3
	1155.2	1.63	1155.0	0.0318	47.4	-	-	-	1155.0	0.0422	41.0
	1238.1	5.79	1238.0	0.1422	15.7	1238.0	0.0872	25.7	1238.1	0.1809	0.9
	1281.0	1.43	1280.4	0.0202	80.2	-	-	-	1280.9	0.0420	35.5
	1377.7	4	1377.8	0.0986	22.2	1378.0	0.0764	10.1	1377.6	0.1392	11.3
	1385.3	0.757	-	-	-	1385.3	0.0242	28.8	-	-	-
	1401.5	1.27	1401.0	0.0405	23.5	-	-	-	1401.4	0.0430	16.6
	1408.0	2.95	1408.2	0.0462	20.1	1407.6	0.0481	14.9	1407.8	0.0679	10.9
	1509.2	2.11	1508.7	0.0233	78.1	1508.4	0.0557	13.4	1509.0	0.1045	8.2
	1538.5	0.376	-	-	-	-	-	-	1538.6	0.0322	22.6
	1661.3	1.15	1661.3	0.0460	39.8	1660.6	0.0154	66.2	1661.0	0.0218	25.1
	1729.6	2.92	1729.6	0.0637	20.9	1729.3	0.0502	12.6	1729.7	0.1047	11.5
	1764.5	15.4	1764.6	0.4210	4.6	1764.4	0.3439	5.4	1764.4	0.4807	12.4
	1847.4	2.11	1847.5	0.0484	29.3	1847.0	0.0263	22.7	1847.4	0.0696	19.1
^{214}Pb	53.5*	1.2	53.5	0.3764	13.4	-	-	-	53.4	0.2877	13.1
	242.0	7.43	242.0	0.2290	10.1	242.0	0.2772	8.6	242.0	0.5411	4.7
	295.2	19.3	295.3	0.6464	9.0	295.3	0.6230	8.5	295.2	1.3315	3.3
	351.9	37.6	351.9	1.1721	4.1	351.9	0.8964	2.5	351.9	2.3322	1.7
	786.0	1.07	-	-	-	-	-	-	786.0	0.0760	30.4
^{212}Pb	238.6	43.3	238.7	0.1385	17.0	238.6	0.7236	3.9	238.7	0.2429	9.1
^{208}Tl	583.5	84.5	583.1	0.0844	16.3	583.3	0.2957	5.2	583.3	0.1150	12.2
	1592.5	**	1592.6	0.1007	9.5	1592.5	0.0929	8.3	1592.6	0.0628	10.9

* Interference with ^{73m}Ge (53.5 keV). ** ^{208}Tl double escape peak

Table A.2: *Long-term background: Radionuclides contained in the detector, its accessories and the shielding*

			Det 3			Det 5			Det 6		
Nuclide	Energy keV	I_γ %	Energy keV	Count rate $10^{-3}s^{-1}$	Rel. uncert. % (1σ)	Energy keV	Count rate $10^{-3}s^{-1}$	Rel. uncert. % (1σ)	Energy keV	Count rate $10^{-3}s^{-1}$	Rel. uncert. % (1σ)
Primordial											
^{40}K	1460.8	11	1460.8	2.6333	1.1	1460.7	2.0103	1.1	1460.7	2.0292	1.0
^{238}U series											
^{210}Pb	46.5	4.25	46.4	0.2947	29.5	46.3	0.5852	5.6	46.6	0.4803	12.6
^{226}Ra	186.2*	3.59	185.9	0.3963	16.6	186.0	0.1924	15.5	-	-	-
^{234}Th	63.3	4.8	63.5	0.1685	14.6	-	-	-	-	-	-
	92.4 / 92.8	2.81 / 2.77	92.7	0.3492	35.2	-	-	-	93.0	0.1012	45.8
^{238m}Pa	1001	0.837	1001.2	0.0395	64.1	-	-	-	-	-	-
^{235}U series											
^{235}U	143.8	10.96	143.5	0.0839	35.8	-	-	-	-	-	-
	185.7*	57.2	185.9	0.3963	16.6	186.0	0.1924	15.5	-	-	-
^{232}Th series											
^{228}Ac	338.3	11.27	337.5	0.1330	37.1	-	-	-	-	-	-
	911.2	25.8	911.3	0.0450	53.7	911.2	0.1638	7.0	911.5	0.1043	20.7
	969	15.8	969.6	0.0410	27.3	968.9	0.0928	4.3	968.6	0.0474	18.2
	1588.2	3.22	1588.1	0.0552	15.5	1588.2	0.0396	16.0	1588.2	0.0209	28.1
Artificial											
^{60}Co	1173.2	100	1172.9	0.0535	40.6	1173.1	0.0897	10.3	1172.9	0.1373	13.9
	1332.5	100	1331.9	0.0223	36.8	1332.4	0.0458	16.2	1332.0	0.0428	16.7
^{137}Cs	661.7	85.1	661.7	0.1055	13.2	661.6	0.2559	4.9	661.7	0.1382	7.9

* Interfering lines of ^{226}Ra and ^{235}U

Table A.3: *Long-term background: Short-lived activation products formed by reaction of cosmic radiation induced neutrons with material of the detector itself, its accessories and the shielding*

			Det 3			Det 5			Det 6		
Nuclide	Energy keV	Reaction	Energy keV	Count rate $10^{-3}s^{-1}$	Rel. uncert. % (1σ)	Energy keV	Count rate $10^{-3}s^{-1}$	Rel. uncert. % (1σ)	Energy keV	Count rate $10^{-3}s^{-1}$	Rel. uncert. % (1σ)
Ge											
^{71m}Ge	23.4	^{70}Ge(n,γ)^{71m}Ge,	-	-	-	23.9	0.3615	10.6	24.1	0.6038	5.9
	198.3 *	^{72}Ge(n,2n)^{71m}Ge	198.3	0.5518	6.5	198.1	0.6248	5.3	198.3	0.4549	5.6
^{72*}Ge	691+ **	^{72}Ge(n,n')^{72*}Ge	694.0	1.1978	4.8	694	1.1913	3.7	694	1.4401	3.0
^{73*}Ge	68.7+ **	^{73}Ge(n,n')^{73*}Ge	70.0	0.0898	24.8	-	-	-	-	-	-
^{73m}Ge	53.5 ***	^{72}Ge(n,γ)^{73m}Ge,	53.5	0.3764	13.4	-	-	-	53.4	0.2877	13.1
	66.8 ****	^{74}Ge(n,2n)^{73m}Ge	66.3	0.4531	6.4	66.3	0.4708	7.1	66.3	0.2869	14.9
^{74*}Ge	595.9+ **	^{74}Ge(n,n')^{74*}Ge	594.5	1.7370	5.2	594.5	1.7324	4.0	594.5	1.9599	3.5
^{75m}Ge	139.5	^{74}Ge(n,γ)^{75m}Ge, ^{76}Ge(n,2n)^{75m}Ge	139.8	0.3527	10.1	139.7	0.4574	18.1	139.8	0.3127	19.3
^{77m}Ge	159.5	^{76}Ge(n,γ)^{77m}Ge	159.3	0.2803	27.9	159.2	0.2245	18.7	159.5	0.1315	42.1
Cd											
^{114m}Cd	651	^{113}Cd(n,γ)^{114m}Cd	651.5	0.0945	29.9	-	-	-	-	-	-
	805.7		-	-	-	806	0.0374	28.2	806.2	0.0354	26.9
	558.3		558.4	0.5761	7.1	558.4	0.3292	6.3	-	-	-
Pb											
^{206*}Pb	803.1	^{206}Pb(n,n')^{206*}Pb	803.0	0.1740	16.0	803	0.0982	13.0	803	0.1287	8.8
^{207*}Pb	569.7	^{207}Pb(n,n')^{207*}Pb	569.6	0.0493	27.9	-	-	-	569.7	0.1057	27.3
Cu											
^{63*}Cu	669.6	^{63}Cu(n,n')^{63*}Cu	669.8	0.3110	5.3	669.8	0.3189	4.1	669.8	0.3926	3.4
	962.1		962.1	0.4353	3.5	962.2	0.4559	1.3	962.2	0.5529	2.1
	1327		1326.9	0.1034	9.8	1327	0.1463	6.2	1326.9	0.1544	5.7
	1412.1		1412.2	0.0692	14.6	1412.2	0.0705	10.8	1412.3	0.0786	9.8
	1547		-	-	-	-	-	-	1546.9	0.0626	13.2
^{64*}Cu	278.3	^{63}Cu(n, γ)^{64*}Cu, ^{65}Cu(n,2n)^{64*}Cu	278.3	0.1751	29.5	278.1	0.3123	17.0	278.1	0.2770	16.8
^{65*}Cu	770.8	^{65}Cu(n,n')^{65*}Cu	770.6	0.1154	11.8	770.7	0.1182	10.1	770.8	0.1162	8.5
^{65*}Cu, ^{65}Zn	1115.5	^{65}Cu(n,n')^{65*}Cu, ^{70}Ge(n,2n)^{65}Zn	1115.6	0.1569	7.3	1115.6	0.1515	6.2	1115.5	0.1980	4.4
^{65*}Cu	1481.7	^{65}Cu(n,n')^{65*}Cu	1481.8	0.0456	35.2	1481.6	0.0403	29.0	1482	0.0450	25.3

* Summing peak 174.9+23.4 keV. ** Degraded peaks by Doppler effect (nucleus recoil). *** Interference with ^{214}Pb (53.5 keV). **** Summing peak 13.3+53.5keV

Table A.4: *Long-term background: other lines (annihilation peak, X-rays and non-identified lines)*

		Det 3			Det 5			Det 6		
Line	Energy keV	Energy keV	Count rate $10^{-3}s^{-1}$	Rel. uncert. % (1σ)	Energy keV	Count rate $10^{-3}s^{-1}$	Rel. uncert. % (1σ)	Energy keV	Count rate $10^{-3}s^{-1}$	Rel. uncert. % (1σ)
e+ -e-	511	511.0	20.1171	0.3	511	18.0024	0.3	510.9	21.3373	0.2
X-rays										
Bi $K_{\alpha 1}$*	77.1	77.2	0.2489	10.6	-	-	-	77.1	0.3981	5.5
Bi $K_{\alpha 2}$*	74.8	74.7	0.1843	13.6	-	-	-	74.9	0.2058	9.3
Bi $K_{\alpha 2}$*	89.8	-	-	-	-	-	-	87.0	0.0841	47.9
unidentified										
?	203	203.0	0.2128	14.4	203.1	0.2110	13.5	203	0.1024	18.8
?	725.7	725.7	0.0551	25.2	-	-	-	-	-	-
?	899	899.2	0.0760	34.1	898.8	0.0693	14.3	898.8	0.0925	23.0
?	979	-	-	-	979.7	0.0174	21.9	-	-	-
?	1163	1163.0	0.0895	24.0	1163.5	0.0203	37.0	-	-	-
?	1345	-	-	-	1345.3	0.0368	19.9	-	-	-
?	1514	-	-	-	1514	0.0490	14.8	1514	0.0651	11.9
?	1861.1	1860.6	0.0391	35.7	1861.1	0.0251	23.3	1861.1	0.0381	40.6

* From ^{212}Pb and ^{214}Pb decay

Table A.5: *Measured values of activity concentrations of ^{222}Rn daughters estimated during repeated measurements of test soil material in different geometries for different gamma lines (Sec. 7.6.4). Uncertainties are expressed as 1 standard deviation including counting statistics and detector calibration uncertainty. In the right part of the table, ^{214}Bi and ^{214}Pb were estimated as weighted means of ^{214}Bi and ^{214}Pb lines, respectively, in Genie2000. The $^{226}Ra_{ave}$ value was calculated as a weighted mean of both previous values.*

Spectrum	^{214}Bi						^{214}Pb									
	C (609 keV) $Bq \cdot kg^{-1}$	Uncert. $Bq \cdot kg^{-1}$	C (1120 keV) $Bq \cdot kg^{-1}$	Uncert. $Bq \cdot kg^{-1}$	C (1764 keV) $Bq \cdot kg^{-1}$	Uncert. $Bq \cdot kg^{-1}$	C (295 keV) $Bq \cdot kg^{-1}$	Uncert. $Bq \cdot kg^{-1}$	C (352 keV) $Bq \cdot kg^{-1}$	Uncert. $Bq \cdot kg^{-1}$	^{214}Bi $Bq \cdot kg^{-1}$	Uncert. $Bq \cdot kg^{-1}$	^{214}Pb $Bq \cdot kg^{-1}$	Uncert. $Bq \cdot kg^{-1}$	^{226}Ra$_{ave}$ $Bq \cdot kg^{-1}$	Uncert. $Bq \cdot kg^{-1}$
Large dish																
3242	921	25	939	26	937	25	921	33	931	30	932	15	926	22	930	12
3977	888	24	901	23	896	23	900	32	901	29	895	14	901	22	897	12
3979	847	23	868	23	859	22	849	30	858	28	858	13	854	20	857	11
3982	843	24	870	28	851	26	890	37	851	31	853	15	849	21	852	12
3983	840	24	831	27	840	26	836	31	856	28	837	15	847	21	840	12
3984	870	25	868	29	866	27	868	32	871	29	868	15	870	21	869	12
3985	882	25	883	28	883	27	878	32	889	29	883	16	884	22	883	13
3986	895	25	926	29	926	28	926	34	917	30	914	16	921	23	916	13
3987	934	27	959	30	944	29	939	34	935	31	945	16	937	23	942	13
3989	965	27	986	28	955	27	966	35	967	32	968	16	967	23	968	13
3990	1005	28	1018	29	1025	28	1006	36	1000	33	1016	16	1003	24	1012	13
3995	1034	29	1043	30	1042	29	1040	37	1027	33	1040	17	1033	25	1038	14
3996	1042	29	1055	30	1061	29	1027	37	1040	34	1053	17	1034	25	1047	14
3998	1047	29	1064	30	1050	29	1048	38	1037	34	1053	17	1042	25	1050	14
3999	1045	29	1063	28	1058	27	1041	37	1046	34	1056	16	1044	25	1053	13
30003	1058	29	1075	28	1086	28	1055	38	1070	35	1073	16	1063	25	1070	13
30009	1044	29	1067	28	1057	27	1041	37	1044	34	1056	16	1043	25	1052	13
30013	1068	29	1074	28	1085	28	1067	38	1062	34	1076	16	1064	25	1073	13
30018	1062	29	1092	29	1099	28	1070	38	1066	34	1085	17	1067	26	1080	14
30051	1068	29	1082	27	1088	27	1064	37	1071	35	1080	16	1068	25	1077	13
30065	1073	29	1077	27	1088	27	1077	38	1076	35	1080	16	1076	26	1079	14
Pellet																
30071	885	25	896	25	880	24	880	32	898	29	887	14	889	22	888	12
30076	1037	29	1042	30	1060	30	1037	37	1033	34	1046	17	1035	25	1043	14
30081	1093	31	1104	33	1085	30	1097	40	1085	36	1093	18	1090	27	1092	15
30086	1090	31	1095	31	1106	31	1079	39	1095	36	1097	18	1088	27	1094	15
30092	1101	31	1124	30	1096	29	1098	40	1098	36	1107	17	1098	27	1104	14
30097	1083	30	1100	29	1063	28	1071	38	1066	34	1081	17	1069	26	1077	14
30153	1105	31	1156	35	1115	32	1081	40	1100	36	1123	19	1092	27	1113	16
Steel dish																
30067	938	26	943	24	961	25	959	34	960	31	947	14	960	23	951	12
30070	1110	30	1116	28	1134	29	1124	40	1128	36	1120	17	1126	27	1122	14
30075	1160	32	1176	30	1190	30	1169	41	1177	38	1176	18	1173	28	1175	15
30080	1158	32	1165	29	1179	30	1182	42	1192	39	1168	17	1187	28	1173	15
30091	1181	32	1193	30	1208	30	1193	42	1199	39	1194	18	1196	29	1195	15
30106	1180	32	1194	29	1209	30	1196	42	1199	39	1195	18	1198	29	1196	15
Small dish I																
30288	1072	32	1094	43	1100	46	1067	39	1079	36	1085	23	1073	26	1080	17
30295	1120	33	1144	39	1137	42	1127	40	1128	37	1132	22	1127	27	1130	17
30298	1157	36	1173	50	1195	51	1140	42	1130	38	1170	25	1135	28	1154	19
Small dish II																
30287	1073	31	1116	37	1074	41	1082	39	1086	35	1086	21	1084	26	1085	16
30294	1153	35	1209	47	1186	50	1171	43	1175	39	1176	24	1165	28	1171	18
30299	1172	34	1244	42	1194	45	1173	42	1180	38	1199	23	1177	28	1190	18

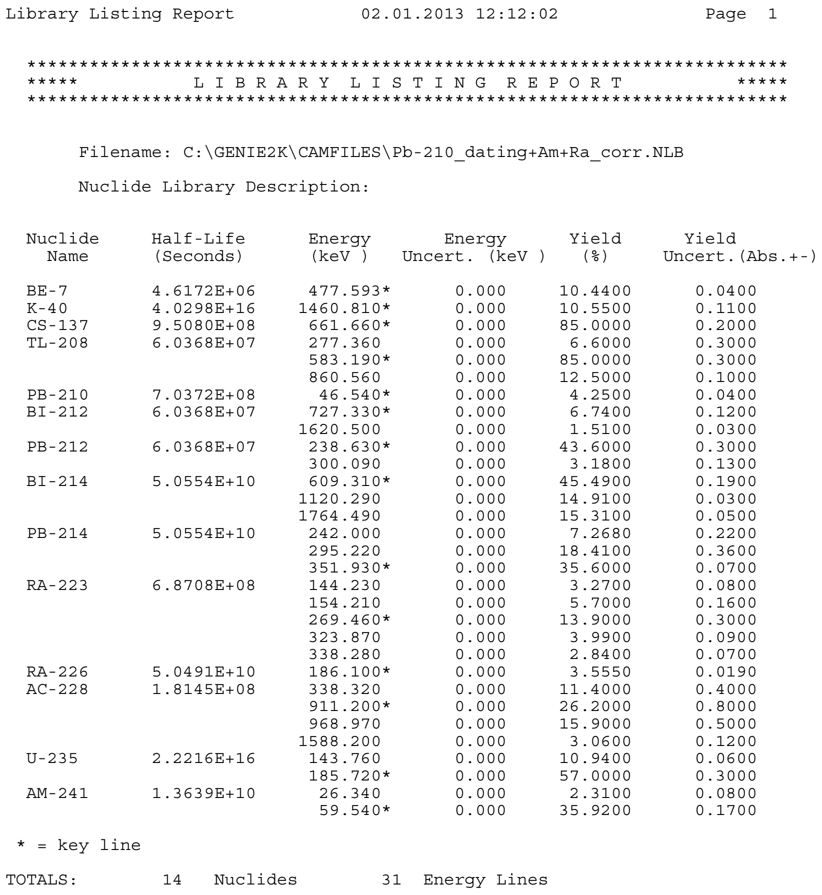

```
Library Listing Report          02.01.2013 12:12:02            Page  1

  *************************************************************************
  *****          L I B R A R Y  L I S T I N G  R E P O R T          *****
  *************************************************************************

       Filename: C:\GENIE2K\CAMFILES\Pb-210_dating+Am+Ra_corr.NLB

       Nuclide Library Description:

  Nuclide     Half-Life      Energy       Energy      Yield      Yield
    Name      (Seconds)      (keV )    Uncert. (keV )   (%)     Uncert.(Abs.+-)

  BE-7        4.6172E+06     477.593*      0.000      10.4400      0.0400
  K-40        4.0298E+16    1460.810*      0.000      10.5500      0.1100
  CS-137      9.5080E+08     661.660*      0.000      85.0000      0.2000
  TL-208      6.0368E+07     277.360       0.000       6.6000      0.3000
                             583.190*      0.000      85.0000      0.3000
                             860.560       0.000      12.5000      0.1000
  PB-210      7.0372E+08      46.540*      0.000       4.2500      0.0400
  BI-212      6.0368E+07     727.330*      0.000       6.7400      0.1200
                            1620.500       0.000       1.5100      0.0300
  PB-212      6.0368E+07     238.630*      0.000      43.6000      0.3000
                             300.090       0.000       3.1800      0.1300
  BI-214      5.0554E+10     609.310*      0.000      45.4900      0.1900
                            1120.290       0.000      14.9100      0.0300
                            1764.490       0.000      15.3100      0.0500
  PB-214      5.0554E+10     242.000       0.000       7.2680      0.2200
                             295.220       0.000      18.4100      0.3600
                             351.930*      0.000      35.6000      0.0700
  RA-223      6.8708E+08     144.230       0.000       3.2700      0.0800
                             154.210       0.000       5.7000      0.1600
                             269.460*      0.000      13.9000      0.3000
                             323.870       0.000       3.9900      0.0900
                             338.280       0.000       2.8400      0.0700
  RA-226      5.0491E+10     186.100*      0.000       3.5550      0.0190
  AC-228      1.8145E+08     338.320       0.000      11.4000      0.4000
                             911.200*      0.000      26.2000      0.8000
                             968.970       0.000      15.9000      0.5000
                            1588.200       0.000       3.0600      0.1200
  U-235       2.2216E+16     143.760       0.000      10.9400      0.0600
                             185.720*      0.000      57.0000      0.3000
  AM-241      1.3639E+10      26.340       0.000       2.3100      0.0800
                              59.540*      0.000      35.9200      0.1700

 * = key line

TOTALS:        14   Nuclides        31  Energy Lines
```

Figure A.1: *A library used for gamma spectrometry of sediment samples - method 1 from section 8.4.2.*

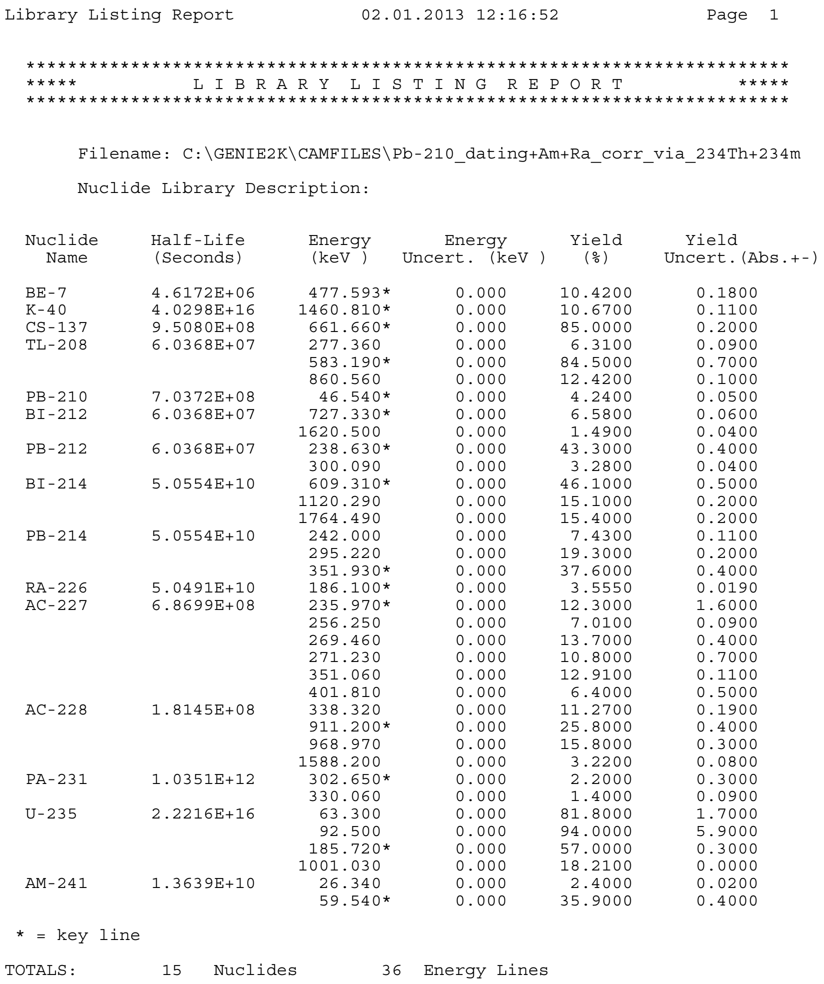

```
Library Listing Report          02.01.2013 12:16:52             Page  1

  ************************************************************************
  *****          L I B R A R Y   L I S T I N G   R E P O R T         *****
  ************************************************************************

       Filename: C:\GENIE2K\CAMFILES\Pb-210_dating+Am+Ra_corr_via_234Th+234m

       Nuclide Library Description:

  Nuclide     Half-Life      Energy       Energy      Yield      Yield
    Name      (Seconds)      (keV )    Uncert. (keV )   (%)     Uncert.(Abs.+-)

  BE-7        4.6172E+06     477.593*      0.000     10.4200      0.1800
  K-40        4.0298E+16    1460.810*      0.000     10.6700      0.1100
  CS-137      9.5080E+08     661.660*      0.000     85.0000      0.2000
  TL-208      6.0368E+07     277.360       0.000      6.3100      0.0900
                             583.190*      0.000     84.5000      0.7000
                             860.560       0.000     12.4200      0.1000
  PB-210      7.0372E+08      46.540*      0.000      4.2400      0.0500
  BI-212      6.0368E+07     727.330*      0.000      6.5800      0.0600
                            1620.500       0.000      1.4900      0.0400
  PB-212      6.0368E+07     238.630*      0.000     43.3000      0.4000
                             300.090       0.000      3.2800      0.0400
  BI-214      5.0554E+10     609.310*      0.000     46.1000      0.5000
                            1120.290       0.000     15.1000      0.2000
                            1764.490       0.000     15.4000      0.2000
  PB-214      5.0554E+10     242.000       0.000      7.4300      0.1100
                             295.220       0.000     19.3000      0.2000
                             351.930*      0.000     37.6000      0.4000
  RA-226      5.0491E+10     186.100*      0.000      3.5550      0.0190
  AC-227      6.8699E+08     235.970*      0.000     12.3000      1.6000
                             256.250       0.000      7.0100      0.0900
                             269.460       0.000     13.7000      0.4000
                             271.230       0.000     10.8000      0.7000
                             351.060       0.000     12.9100      0.1100
                             401.810       0.000      6.4000      0.5000
  AC-228      1.8145E+08     338.320       0.000     11.2700      0.1900
                             911.200*      0.000     25.8000      0.4000
                             968.970       0.000     15.8000      0.3000
                            1588.200       0.000      3.2200      0.0800
  PA-231      1.0351E+12     302.650*      0.000      2.2000      0.3000
                             330.060       0.000      1.4000      0.0900
  U-235       2.2216E+16      63.300       0.000     81.8000      1.7000
                              92.500       0.000     94.0000      5.9000
                             185.720*      0.000     57.0000      0.3000
                            1001.030       0.000     18.2100      0.0000
  AM-241      1.3639E+10      26.340       0.000      2.4000      0.0200
                              59.540*      0.000     35.9000      0.4000

 * = key line

TOTALS:        15   Nuclides        36  Energy Lines
```

Figure A.2: *A library used for gamma spectrometry of sediment samples - method 2 from section 8.4.2.*

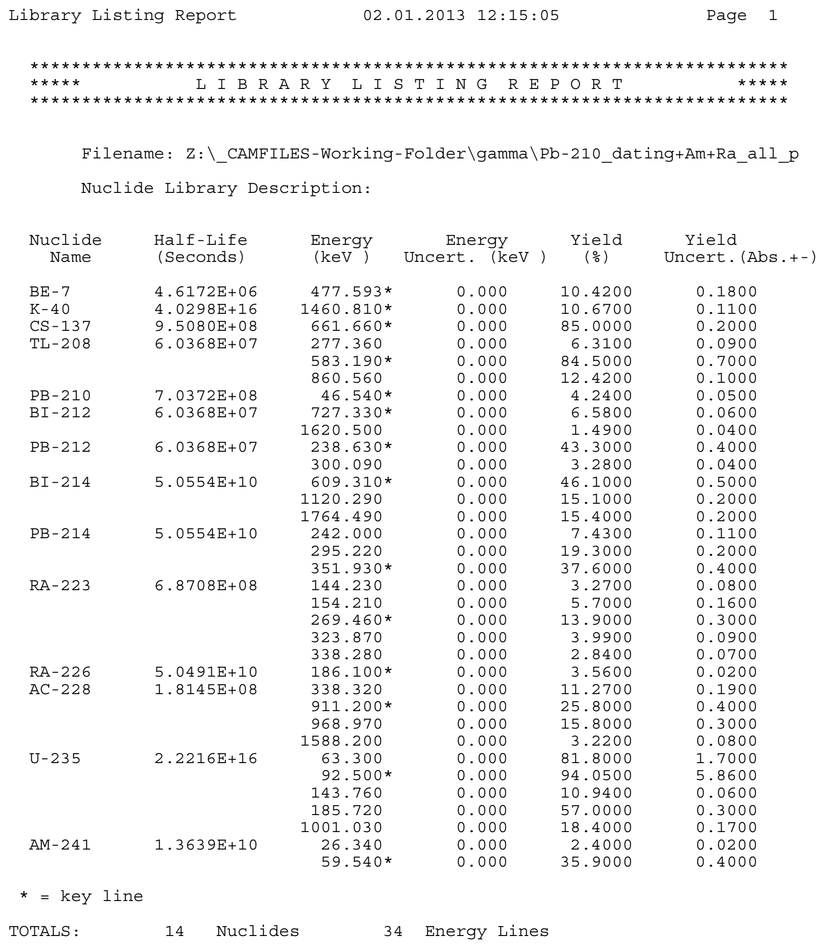

```
Library Listing Report            02.01.2013 12:15:05             Page  1

  ************************************************************************
  *****          L I B R A R Y  L I S T I N G  R E P O R T          *****
  ************************************************************************

       Filename: Z:\_CAMFILES-Working-Folder\gamma\Pb-210_dating+Am+Ra_all_p

       Nuclide Library Description:

  Nuclide     Half-Life      Energy       Energy      Yield      Yield
    Name      (Seconds)      (keV )    Uncert. (keV )  (%)     Uncert.(Abs.+-)

  BE-7        4.6172E+06     477.593*      0.000     10.4200      0.1800
  K-40        4.0298E+16    1460.810*      0.000     10.6700      0.1100
  CS-137      9.5080E+08     661.660*      0.000     85.0000      0.2000
  TL-208      6.0368E+07     277.360       0.000      6.3100      0.0900
                             583.190*      0.000     84.5000      0.7000
                             860.560       0.000     12.4200      0.1000
  PB-210      7.0372E+08      46.540*      0.000      4.2400      0.0500
  BI-212      6.0368E+07     727.330*      0.000      6.5800      0.0600
                            1620.500       0.000      1.4900      0.0400
  PB-212      6.0368E+07     238.630*      0.000     43.3000      0.4000
                             300.090       0.000      3.2800      0.0400
  BI-214      5.0554E+10     609.310*      0.000     46.1000      0.5000
                            1120.290       0.000     15.1000      0.2000
                            1764.490       0.000     15.4000      0.2000
  PB-214      5.0554E+10     242.000       0.000      7.4300      0.1100
                             295.220       0.000     19.3000      0.2000
                             351.930*      0.000     37.6000      0.4000
  RA-223      6.8708E+08     144.230       0.000      3.2700      0.0800
                             154.210       0.000      5.7000      0.1600
                             269.460*      0.000     13.9000      0.3000
                             323.870       0.000      3.9900      0.0900
                             338.280       0.000      2.8400      0.0700
  RA-226      5.0491E+10     186.100*      0.000      3.5600      0.0200
  AC-228      1.8145E+08     338.320       0.000     11.2700      0.1900
                             911.200*      0.000     25.8000      0.4000
                             968.970       0.000     15.8000      0.3000
                            1588.200       0.000      3.2200      0.0800
  U-235       2.2216E+16      63.300       0.000     81.8000      1.7000
                              92.500*      0.000     94.0500      5.8600
                             143.760       0.000     10.9400      0.0600
                             185.720       0.000     57.0000      0.3000
                            1001.030       0.000     18.4000      0.1700
  AM-241      1.3639E+10      26.340       0.000      2.4000      0.0200
                              59.540*      0.000     35.9000      0.4000

 * = key line

TOTALS:        14   Nuclides        34  Energy Lines
```

Figure A.3: *A library used for gamma spectrometry of sediment samples - method 3 from section 8.4.2.*

Table A.6: *Measured values of activity concentrations of ^{226}Ra estimated in time series with test soil material in two geometries using different methods (Sec. 8.5.1). Uncertainties are expressed as 1 standard deviation including counting statistics and detector calibration uncertainty.*

Spectrum	# of half-lives	Life-time s	^{226}Ra (1) $Bq \cdot kg^{-1}$	Uncert. $Bq \cdot kg^{-1}$	^{226}Ra (2) $Bq \cdot kg^{-1}$	Uncert. $Bq \cdot kg^{-1}$	^{226}Ra (3) $Bq \cdot kg^{-1}$	Uncert. $Bq \cdot kg^{-1}$	^{226}Ra (via daughters) $Bq \cdot kg^{-1}$	Uncert. $Bq \cdot kg^{-1}$
Plastic dish (large)										
3982	0.0	13000	1168	122	1156	69	1134	68	852	12
3983	0.1	12000	1336	122	1225	72	1193	70	840	12
3984	0.2	12000	1157	138	1205	72	1186	70	869	12
3985	0.3	12000	1040	141	1115	75	1106	71	883	13
3986	0.5	12000	1290	104	1111	73	1123	69	916	13
3987	0.8	12000	1143	125	1252	76	1217	74	942	13
3989	1.1	24000	1179	103	1220	71	1193	70	968	13
3990	1.8	24000	1070	115	1198	68	1178	67	1012	13
3995	4.7	24000	1148	105	1106	65	1091	62	1038	14
3996	5.5	24000	1073	131	1183	68	1165	66	1047	14
3998	6.6	24000	1133	96	1124	65	1112	64	1050	14
3999	7.3	92948	1127	81	1102	62	1104	61	1053	13
30003	9.1	80469	1149	75	1134	64	1134	63	1070	13
30009	11.5	99849	1202	79	1162	63	1152	62	1052	13
30013	13.7	66807	1225	70	1176	65	1172	63	1073	13
30018	15.5	64950	1228	91	1232	66	1204	65	1080	14
Steel dish										
30067	0.0	64129	1342	85	1347	72	1332	71	951	12
30070	2.0	80790.0	1282	84	1316	71	1315	70	1122	14
30075	3.8	81092.0	1304	84	1327	71	1319	70	1175	15
30080	5.6	78258.0	1344	84	1340	72	1354	71	1173	15
30091	9.8	108697.0	1255	80	1319	70	1305	69	1195	15
30106	15.4	400656.0	1280	78	1313	70	1333	69	1196	15

Table A.7: *Modelled profiles (Chap. 9): Artificial $^{210}Pb_{xs}$ and ^{137}Cs profiles of MUC and GC, arbitrary units (a.u.). For GC the upper 5 cm were cut off.*

Modelled MUC					Modelled GC				
Depth cm	^{210}Pb$_{xs}$ a.u.	Uncert. a.u.	^{137}Cs a.u.	Uncert. a.u.	Depth cm	^{210}Pb$_{xs}$ a.u.	Uncert. a.u.	^{137}Cs a.u.	Uncert. a.u.
1	75.8	8.7							
2	72.6	8.5							
3	60.9	7.8							
4	53.6	7.3	0.0198	0.0033					
5	63.7	8.0	0.0286	0.0030					
6	41.3	6.4	0.0607	0.0059	1	46.7	6.8	0.0576	0.0059
7	40.9	6.4	0.095	0.011	2	43.3	6.6	0.111	0.011
8	34.9	5.9	0.482	0.040	3	44.6	6.7	0.428	0.040
9	31.4	5.6	0.150	0.015	4	31.3	5.6	0.159	0.015
10	30.6	5.5	0.0868	0.0091	5	22.9	4.8	0.0920	0.0091
11	23.9	4.9			6	27.0	5.2		
12	12.0	3.5			7	34.1	5.8		
13	21.0	4.6			8	17.8	4.2		
14	27.9	5.3			9	14.4	3.8		
15	13.1	3.6			10	19.5	4.4		
16	15.2	3.9			11	12.0	3.5		
17	8.0	2.8			12	13.5	3.7		
18	13.1	3.6			13	14.5	3.8		
19	10.2	3.2			14	6.2	2.5		
20	8.2	2.9			15	8.2	2.9		
21	8.0	2.8			16	4.9	2.2		
22	6.6	2.6			17	4.5	2.1		
23	7.4	2.7			18	6.7	2.6		
24	3.4	1.8			19	4.7	2.2		
25	2.9	1.7			20	6.7	2.6		

Table A.8: *Site A (GeoB 6008): Measured values of $^{210}Pb_{xs}$ and ^{137}Cs activity concentrations of in MUC and GC profiles. Uncertainties are expressed as 1 standard deviation including counting statistics and detector calibration uncertainty. Values below decision threshold are left out.*

MUC-A					GC-A				
Depth cm	^{210}Pb$_{xs}$ Bq·cm^{-3}	Uncert. Bq·cm^{-3}	^{137}Cs Bq·cm^{-3}	Uncert. Bq·cm^{-3}	Depth cm	^{210}Pb$_{xs}$ Bq·cm^{-3}	Uncert. Bq·cm^{-3}	^{137}Cs Bq·cm^{-3}	Uncert. Bq·cm^{-3}
1	0.1169	0.0051	0.00246	0.00026	0.5	0.2404	0.0104	0.00412	0.00048
2	0.1262	0.0048	0.00224	0.00021	1.5	0.1385	0.0075	0.00182	0.00034
3	0.1549	0.0051	0.00246	0.00023	2.5	0.1462	0.0082	0.00200	0.00037
4	0.1668	0.0055	0.00301	0.00025	3.5	0.1816	0.0098	0.00303	0.00039
5	0.1746	0.0062	0.00337	0.00026	4.5	0.1758	0.0087	0.00321	0.00039
6	0.1914	0.0060	0.00335	0.00029	5.5	0.1530	0.0077	0.00286	0.00040
7	0.1883	0.0054	0.00365	0.00025	6.5	0.1205	0.0077	0.00175	0.00040
8	0.1910	0.0075	0.00456	0.00030	7.5	0.1132	0.0055	0.00151	0.00030
9	0.1696	0.0047	0.00429	0.00023	8.5	0.1162	0.0060	0.00138	0.00030
10	0.1845	0.0052	0.00361	0.00028	9.5	0.1251	0.0060	0.00075	0.00030
11	0.1458	0.0041	0.00341	0.00026	10.5	0.1037	0.0085		
12	0.1584	0.0055	0.00444	0.00026	11.5	0.0721	0.0068		
13	0.1704	0.0048	0.00403	0.00025	12.5	0.0621	0.0061		
14	0.1439	0.0056	0.00338	0.00026	13.5	0.0592	0.0039		
15	0.1311	0.0083	0.00337	0.00026	14.5	0.0579	0.0037		
16	0.1223	0.0053	0.00359	0.00028	15.5	0.0415	0.0032		
17	0.1006	0.0049	0.00218	0.00024	16.5	0.0445	0.0032		
18	0.0980	0.0048	0.00229	0.00029					
19	0.0780	0.0025	0.00130	0.00015					
20	0.0697	0.0028	0.00079	0.00022					
21	0.0660	0.0032	0.00058	0.00018					
22	0.0516	0.0039	0.00048	0.00024					
23	0.0659	0.0031							
24	0.0523	0.0025							
25	0.0499	0.0042							
26	0.0462	0.0024							
27	0.0436	0.0042							
28	0.0413	0.0021							
29	0.0413	0.0027							
30	0.0324	0.0035							
31	0.0282	0.0016							
32	0.0236	0.0039							

Table A.9: *Site B (GeoB 9501): Measured values of* $^{210}Pb_{xs}$ *and* ^{137}Cs *activity concentrations of in MUC and GC profiles. Uncertainties are expressed as 1 standard deviation including counting statistics and detector calibration uncertainty. Values below decision threshold are left out.*

MUC-B					GC-B				
Depth cm	^{210}Pb$_{xs}$ Bq·kg^{-1}	Uncert. Bq·kg^{-1}	^{137}Cs Bq·kg^{-1}	Uncert. Bq·kg^{-1}	Depth cm	^{210}Pb$_{xs}$ Bq·kg^{-1}	Uncert. Bq·kg^{-1}	^{137}Cs Bq·kg^{-1}	Uncert. Bq·kg^{-1}
1.5	213.8	9.5			2.0	223.1	11.5	0.54	0.23
2.5	417.1	11.7	2.11	0.57	4.0	276.4	11.0	0.89	0.32
3.5	363.9	12.7	2.08	0.47	6.0	205.9	6.2	0.79	0.50
4.5	348.2	12.2	1.95	0.42	8.0	83.5	8.4	0.52	0.33
5.5	354.5	13.0	1.32	0.12	10	56.4	8.5		
6.5	332.8	13.9	2.14	0.46	12	42.9	5.8		
7.5	313.5	11.8	1.42	0.31	14	35.9	5.2		
8.5	320.2	10.1	1.19	0.42	16	32.8	1.9		
9.5	381.9	11.5	2.06	0.46	18	15.6	2.7		
10.5	334.0	10.9	1.87	0.31	20	28.9	3.1		
11.5	330.2	12.8	1.63	0.34	22	28.1	5.6		
12.5	344.9	11.2	1.47	0.47	24	42.7	8.0		
13.5	336.2	13.5	1.71	0.47	26	12.7	2.8		
14.5	245.7	11.5	1.44	0.46	28	12.3	5.0		
15.5	335.7	14.2	2.14	0.41	30	15.2	2.9		
16.5	208.9	8.9	1.07	0.18	32	20.0	5.3		
17.5	246.4	11.3	1.40	0.42	34	11.6	4.1		
18.5	210.9	10.7	1.91	0.40	36	- 0.3	3.2		
19.5	173.6	8.9	1.00	0.29	38	3.4	4.4		
20.5	186.6	7.6	1.25	0.25	40	- 1.9	5.2		
21.5	149.0	7.5	1.53	0.25	42	- 4.6	4.3		
22.5	168.1	10.5	1.07	0.36					
23.5	138.6	8.4	1.19	0.42					
24.5	105.7	5.8	0.78	0.25					
25.5	142.5	10.7	0.96	0.38					
26.5	135.3	9.8	0.61	0.30					
27.5	104.8	8.4	0.59	0.45					
28.5	112.4	11.0	0.34	0.27					
29.5	70.8	3.2	0.34	0.16					
30.5	73.1	7.6							
31.5	56.2	5.6							
32.5	90.5	7.9							
33.5	91.9	9.2							
34.5	65.7	7.5							
35.5	73.8	7.7							
36.5	44.7	3.1							
37.5	51.9	6.3							
38.5	54.2	5.8							
39.5	48.2	4.8							
40.5	37.0	4.4							
41.5	45.0	3.9							
42.5	32.7	9.8							

Table A.10: *GeoB 9501: AMS-^{14}C ages and calibrated ages (MARINE04 calibration curve + additional reservoir age of 140±100 yr). Missing values (–) stand for invalid ages for the calibration curve.*

Lab. code	Sample depth cm	Core GeoB	^{14}C age yr BP	2σ cal. age range yr AD
KIA 35172[a]	45–46	9501-4 (MUC-B)	640 ± 30	–
KIA 32642[b]	4–5	9501-5 (GC-B)	-30 ± 70	–
Poz-31132[c]	52	9501-5 (GC-B)	910 ± 40	1348–1730
KIA 3743	120	9501-5 (GC-B)	1040 ± 30	1289–1640
KIA 3744	202	9501-5 (GC-B)	1440 ± 30	894–1299
KIA 3745	254	9501-5 (GC-B)	1655 ± 30	668–1089
KIA 3746	350	9501-5 (GC-B)	2195 ± 30	82–571
KIA 3747	443	9501-5 (GC-B)	2675 ± 35	(-522)–33
KIA 32641	524–528	9501-5 (GC-B)	3540 ± 45	(-1581)–(-1013)
KIA 3748[d]	530	9501-5 (GC-B)	4130 ± 40	–

[a] Used for estimating local reservoir effect.

[b] Contains bomb radiocarbon.

[c] Not included into the age model because of a larger reservoir age during the Little Ice Age.

[d] Not included into the age model because of disturbance and potential inclusion of older material around the core catcher.

Table A.11: *MUC-A and C (GeoB 10065): Gamma and alpha spectroscopy. Measured values of activity concentrations. Uncertainties are expressed as 1 standard deviation including counting statistics and detector calibration uncertainty. Values below decision threshold are expressed for 5% type I error probability.*

Sample #	Spectrum #	Life-time s	Depth from cm	to cm	average cm	corrected depth cm	Mass g (w.m.)	Mass g (d.m.)	^{40}K Bq·kg^{-1}	Uncert. Bq·kg^{-1}	^{210}Pb Bq·kg^{-1}	Uncert. Bq·kg^{-1}	^{226}Ra Bq·kg^{-1}	Uncert. Bq·kg^{-1}	^{241}Am Bq·kg^{-1}	Uncert. Bq·kg^{-1}	^{137}Cs Bq·kg^{-1}	Uncert. Bq·kg^{-1}	^{210}Pb$_{xs}$ Bq·kg^{-1}	Uncert. Bq·kg^{-1}	^{228}Th Bq·kg^{-1}	Uncert. Bq·kg^{-1}
MUC-A: Gamma spectrometry																						
1	30093	83865	3	4	3.5	5.5	12.718	4.154	349	34	1136	89	65.3	3.5	5.8	0.9	< 2.3		1237	103	17.7	1.7
2	30094	89034	4	5	4.5	6.5	14.995	5.431	323	28	906	69	56.5	2.2	5.0	1.1	< 1.7		982	80	17.3	1.4
3	30084	109902	5	6	5.5	7.5	14.623	4.585	293	26	963	77	57.0	2.7	3.7	1.3	< 1.8		1047	89	17.9	1.4
4	30088	86463	6	7	6.5	8.5	15.371	5.078	297	26	690	54	57.2	2.1	7.0	1.5	< 1.7		732	63	13.6	1.3
5	30120	238546	7	8	7.5	9.5	15.396	5.878	272	17	542	45	49.9	1.3	6.0	1.0	< 0.9		569	51	11.0	0.7
6	30089	85350	8	9	8.5	10.5	15.819	5.529	296	24	515	43	54.6	2.5	5.0	1.4	< 1.7		532	50	11.7	1.2
7	30090	87286	9	10	9.5	11.5	15.482	5.072	329	27	531	43	53.1	2.7	7.3	1.4	< 1.8		553	49	14.8	1.3
8	30095	82966	10	11	10.5	12.5	15.527	5.148	246	25	712	60	54.8	2.6	4.2	0.9	< 1.8		759	70	12.3	1.2
9	30096	88397	11	12	11.5	13.5	15.052	4.637	254	26	844	68	56.8	2.9	4.6	2.0	< 1.9		910	79	13.8	1.4
10	30098	77211	12	13	12.5	14.5	15.126	5.458	283	25	1001	80	54.6	2.7	4.7	1.4	< 2.0		1094	92	15.2	1.3
11	30099	80569	13	14	13.5	15.5	15.247	5.799	304	24	799	63	55.9	2.1	6.9	1.6	< 1.6		859	73	15.9	1.3
12	30103	92008	14	15	14.5	16.5	15.450	6.188	263	21	784	62	56.7	2.0	5.0	1.1	< 1.5		841	72	15.0	1.2
13	30100	84108	15	16	15.5	17.5	16.217	6.787	238	21	682	54	59.9	2.2	4.1	1.1	< 1.5		719	63	13.5	1.1
14	30101	96654	16	17	16.5	18.5	15.752	6.588	305	22	526	43	63.5	2.2	5.9	1.1	< 1.4		535	50	15.3	1.1
15	30104	86552	17	18	17.5	19.5	15.345	6.330	252	22	521	44	48.5	2.2	3.5	1.4	< 1.4		546	51	12.6	1.1
16	30102	252631	18	19	18.5	20.5	15.329	5.813	301	16	551	45	56.3	1.7	4.7	1.0	< 0.9		572	52	13.3	0.8
17	30107	106685	19	20	19.5	21.5	15.398	5.507	248	23	520	42	53.2	2.4	4.8	1.1	< 1.4		540	49	14.3	1.1
18	30105	85893	20	21	20.5	22.5	15.134	4.973	315	27	520	46	54.5	2.6	3.2	1.4	< 1.9		539	53	14.5	1.4
19	30108	95279	21	22	21.5	23.5	15.857	5.894	304	24	414	35	67.2	2.4	4.4	1.2	< 1.5		401	41	15.8	1.2
20	30109	76116	22	23	22.5	24.5	15.415	5.001	324	27	353	31	57.7	2.7	4.4	2.2	< 2.0		342	35	16.8	1.5
21	30111	87458	23	24	23.5	25.5	15.519	5.520	335	25	254	26	58.2	2.4	< 1.5		< 1.7		226	30	15.8	1.3
22	30114	161382	24	25	24.5	26.5	15.459	5.297	331	20	231	21	57.5	2.1	< 1.2		< 1.2		201	24	16.3	1.1
23	30110	241074	25	26	25.5	27.5	15.092	5.208	319	19	214	18	56.8	1.9	< 0.9		< 1.0		182	21	14.3	0.9
24	30115	246375	26	27	26.5	28.5	15.560	5.330	347	18	233	20	59.5	2.0	< 0.9		< 1.0		200	23	16.6	0.9
25	30117	85484	27	28	27.5	29.5	15.496	5.500	312	25	234	25	59.5	2.6	< 1.5		< 1.6		202	29	15.2	1.3
26	30116	96221	28	29	28.5	30.5	15.751	5.856	316	22	197	17	57.1	2.3	< 1.3		< 1.4		162	20	17.7	1.2
27	30118	159763	29	30	29.5	31.5	15.151	4.954	320	22	232	22	60.1	2.3	< 1.2		< 1.3		199	25	16.7	1.1
MUC-C: Alpha spectrometry																						
6	a4154a	410252	8	9	8.5	10.5		1.02	n.a.	n.a.	n.a.	n.a.	n.a.	n.a.	5.5	0.6	n.a.	n.a.	n.a.	n.a.	n.a.	n.a.
20	a3164a	410252	22	23	22.5	24.5		1.11	n.a.	n.a.	n.a.	n.a.	n.a.	n.a.	2.7	0.6	n.a.	n.a.	n.a.	n.a.	n.a.	n.a.

Table A.12: *MUC-B (GeoB 10065): Gamma spectroscopy. Measured values of activity concentrations. Uncertainties are expressed as 1 standard deviation including counting statistics and detector calibration uncertainty. Values below decision threshold are expressed for 5% type I error probability.*

Sample	Spectrum	Life-time	Depth from	to	average	corrected depth	Mass	Mass	^{40}K	Uncert.	^{210}Pb	Uncert.	^{226}Ra	Uncert.	^{241}Am	Uncert.	^{137}Cs	Uncert.	^{210}Pb$_{xs}$	Uncert.	^{228}Th	Uncert.
#	#	s	cm	cm	cm	cm	g (w.m.)	g (d.m.)	Bq·kg^{-1}	Bq·kg^{-1}	Bq·kg^{-1}	Bq·kg^{-1}	Bq·kg^{-1}	Bq·kg^{-1}	Bq·kg^{-1}	Bq·kg^{-1}	Bq·kg^{-1}	Bq·kg^{-1}	Bq·kg^{-1}	Bq·kg^{-1}	Bq·kg^{-1}	Bq·kg^{-1}
1	30218	195935	0	1	0.5	0.5		1.110	412	54	1115	92	72.4	5.4	< 3.1		< 3.9		1224	108	23.9	2.4
2	30217	148062	1	2	1.5	1.5		1.270	307	52	1127	96	54.1	4.9	< 3.2		< 4.0		1257	113	20.0	2.4
3	30219	230712	2	3	2.5	2.5		1.260	290	46	1194	98	71.0	5.1	3.5	2.0	< 3.2		1321	115	19.6	2.0
4	30220	171584	3	4	3.5	3.5		1.883	250	36	1114	81	66.6	3.7	3.7	1.6	< 2.7		1232	95	19.0	1.7
5	30231	177394	4	5	4.5	4.5		1.866	326	36	1044	78	53.6	3.5	1.7	1.6	< 2.9		1163	92	16.7	1.7
6	30221	190801	5	6	5.5	5.5		1.560	314	41	962	77	76.4	3.3	4.3	1.4	< 3.7		1041	91	14.9	1.7
7	30222	274280	6	7	6.5	6.5		1.509	327	40	1016	75	72.7	4.3	4.5	1.7	< 2.6		1109	88	17.4	1.6
8	30223	236345	7	8	7.5	7.5		1.793	265	33	732	56	59.8	3.4	3.6	1.6	< 2.5		790	66	13.4	1.4
9	30224	334847	8	9	8.5	8.5		1.755	322	32	872	64	57.7	3.0	5.4	1.7	< 2.1		957	75	14.9	1.3
10	30225	167883	9	10	9.5	9.5		1.997	309	35	750	58	56.9	3.7	4.2	1.7	< 2.6		804	68	16.0	1.6
11	30232	240521	10	12	11.0	11.0		1.125	403	51	651	58	72.8	3.7	6.9	3.1	< 3.5		685	68	15.9	2.1
12	30233	175209	12	14	13.0	13.0		1.050	413	32	775	68	66.2	6.4	< 3.6		< 4.6		833	80	14.8	4.2
13	30234	168912	14	16	15.0	15.0		1.133	305	60	788	70	48.8	5.5	< 3.4		< 4.1		870	83	26.0	2.7
14	30235	251724	16	18	17.0	17.0		1.573	358	39	690	55	63.7	3.4	4.1	1.8	< 2.5		733	65	14.4	1.5
15	30237	183980	18	20	19.0	19.0		1.294	331	52	424	39	62.9	4.4	3.6	1.8	< 3.4		423	46	13.1	2.0
16	30236	161458	20	25	22.5	22.5		2.562	341	30	435	34	60.9	2.9	4.6	0.7	< 2.2		439	40	19.7	1.5
17	30226	195817	25	30	27.5	27.5		2.397	293	29	373	29	57.8	3.1	< 2.7		< 2.0		368	34	16.3	1.4
18	30227	411871	30	35	32.5	32.5		2.374	399	27	239	20	60.7	2.3	< 1.1		< 1.2		210	24	18.0	1.1
19	30228	175158	35	40	37.5	37.5		2.815	365	28	179	19	61.3	2.9	< 1.4		< 1.9		138	23	17.8	1.3
20	30229	258500	40	45	42.5	42.5		2.847	357	25	143	15	70.1	2.6	< 1.2		< 1.6		85	18	17.2	1.1
21	30230	185792	45	50	47.5	47.5		3.045	362	26	79	14	54.7	2.3	< 1.3		< 1.7		31	17	13.3	1.1

Table A.13: *GC (GeoB 10065): Gamma spectroscopy. Measured values of activity concentrations. Uncertainties are expressed as 1 standard deviation including counting statistics and detector calibration uncertainty. Values below decision threshold are expressed for 5% type I error probability.*

Sample	Spectrum	Life-time	Depth from	to	average	corrected depth	Mass	Mass	^{40}K	Uncert.	^{210}Pb	Uncert.	^{226}Ra	Uncert.	^{241}Am	Uncert.	^{137}Cs	Uncert.	^{210}Pb$_{xs}$	Uncert.	^{228}Th	Uncert.
#	#	s	cm	cm	cm	cm	g (w.m.)	g (d.m.)	Bq·kg^{-1}	Bq·kg^{-1}	Bq·kg^{-1}	Bq·kg^{-1}	Bq·kg^{-1}	Bq·kg^{-1}	Bq·kg^{-1}	Bq·kg^{-1}	Bq·kg^{-1}	Bq·kg^{-1}	Bq·kg^{-1}	Bq·kg^{-1}	Bq·kg^{-1}	Bq·kg^{-1}
1	30263	129847	0.5	1.5	1.0	21.0		7.494	250	15	598	43	45.6	1.6	3.2	0.7	< 0.9		659	51	11.2	0.8
2	30264	169941	2.5	3.5	3.0	23.0		6.291	263	15	560	40	44.2	1.8	4.8	1.1	< 1.0		615	48	12.1	0.8
3	30265	236841	4.5	5.5	5.0	25.0		6.274	296	14	382	29	49.1	1.4	1.8	0.8	< 0.8		397	35	15.0	0.8
4	30266	257938	6.5	7.5	7.0	27.0		6.563	297	14	283	21	49.4	1.5	1.8	0.5	< 0.7		279	25	14.4	0.8
5	30267	261460	8.5	9.5	9.0	29.0		6.777	295	13	213	16	52.1	1.6	< 0.6		< 0.7		192	19	12.9	0.7
6	30268	255887	10.5	11.5	11.0	31.0		4.708	348	18	212	17	60.8	2.1	< 0.9		< 1.0		180	20	15.3	0.9
8	30269	404291	12.5	13.5	13.0	33.0		4.509	326	16	164	14	60.6	1.8	< 0.7		< 0.8		123	17	14.6	0.8
9	30271	336554	14.5	15.5	15.0	35.0		5.422	333	15	140	12	54.5	1.6	< 0.7		< 0.8		102	14	14.9	0.8

Table A.14: *Gamma spectroscopy (GeoB 10065): Values of activity concentrations for summed up core intervals. Uncertainties are expressed as 1 standard deviation including counting statistics and detector calibration uncertainty. Values below decision threshold are expressed for 5% type I error probability.*

Summed up samples	Life-time	Depth from	to	average	corrected depth	Mass[a]	^{241}Am	Uncert.	^{137}Cs	Uncert.
#	s	cm	cm	cm	cm	g (d.m.)	Bq·kg^{-1}	Bq·kg^{-1}	Bq·kg^{-1}	Bq·kg^{-1}
MUC-A										
1–5	607810	3	8	5.5	7.5	14.823	5.4	0.7	0.9	0.5
6–10	421210	8	13	10.5	12.5	15.403	5.3	0.8	1.2	0.6
11–15	439891	13	18	15.5	17.5	15.604	5.0	0.6	0.9	0.4
16–20	616604	18	23	20.5	22.5	15.405	4.3	0.7	1.5	0.5
21–25	821773	23	28	25.5	27.5	15.391	0.4	0.4	0.9	0.2
23–27[b]	828917	25	30	27.5	29.5	15.400	0.4	0.3	1.2	0.3
MUC-B										
1–5	923690	0	5	2.5	2.5	1.462	1.4	0.5	0.4	0.5
GC										
1–4	794567	1	7	4	24	6.570	3.5	0.5	<0.5	
5–9	1258192	9	15	12	32	5.265	<0.4		<0.5	

[a] Measurement time weighted mean of individual sample masses

[b] Overlapping with previous interval

Table A.15: *MUC-A: Chronology. Uncertainties are expressed as 1 standard deviation. Results of an extrapolation of the CF-CS model to deeper layers of sediment profiles are listed below.*

				CF-CS model				CRS model					
Depth cm	Combined depth cm	Activity Bq·kg-1	Uncert. Bq·kg-1	Calendar year AD	Uncert. yr	Sedimentation rate cm·yr-1	Uncert. cm·yr-1	Cumulative activity Bq·kg-1	Uncert. Bq·kg-1	Calendar year AD	Uncert. yr	Sedimentation rate cm·yr-1	Uncert. cm·yr-1
12.5	14.5	1094	92	2009	7	0.274	0.021	9603	496	2004	6	0.274	0.027
13.5	15.5	859	73	2005	7	0.274	0.021	8509	487	2000	6	0.309	0.032
14.5	16.5	841	72	2001	6	0.274	0.021	7650	481	1996	6	0.284	0.030
15.5	17.5	719	63	1997	6	0.274	0.021	6809	476	1992	6	0.296	0.033
16.5	18.5	535	50	1994	6	0.274	0.021	6090	472	1989	6	0.356	0.043
17.5	19.5	546	51	1990	6	0.274	0.021	5556	469	1986	6	0.317	0.040
18.5	20.5	572	52	1986	6	0.274	0.021	5009	466	1983	6	0.273	0.036
19.5	21.5	540	49	1982	6	0.274	0.021	4437	464	1979	6	0.257	0.035
20.5	22.5	539	53	1978	5	0.274	0.021	3898	461	1975	6	0.226	0.035
21.5	23.5	401	41	1974	5	0.274	0.021	3359	458	1970	7	0.261	0.044
22.5	24.5	342	35	1970	5	0.274	0.021	2958	456	1966	7	0.270	0.050
23.5	25.5	226	30	1966	5	0.274	0.021	2616	455	1962	8	0.361	0.079
24.5	26.5	201	24	1962	5	0.274	0.021	2390	454	1959	8	0.371	0.083
25.5	27.5	182	21	1958	5	0.274	0.021	2189	453	1956	8	0.375	0.088
26.5	28.5	200	23	1954	5	0.274	0.021	2007	453	1953	9	0.313	0.080
27.5	29.5	202	29	1950	5	0.274	0.021	1806	452	1950	10	0.279	0.081
28.5	30.5	162	20	1946	5	0.274	0.021	1605	451	1946	10	0.309	0.095
29.5	31.5	199	25	1942	5	0.274	0.021	1443	451	1943	11	0.227	0.076
								1244 [a]	450				
Extrapolation to GC:													
1	21			1984	6	0.274	0.021						
15	35			1928	5	0.274	0.021						
36	56			1845	9	0.274	0.021						

[a] Estimation of cumulative residual activity in interval 32–100 cm (combined depth).

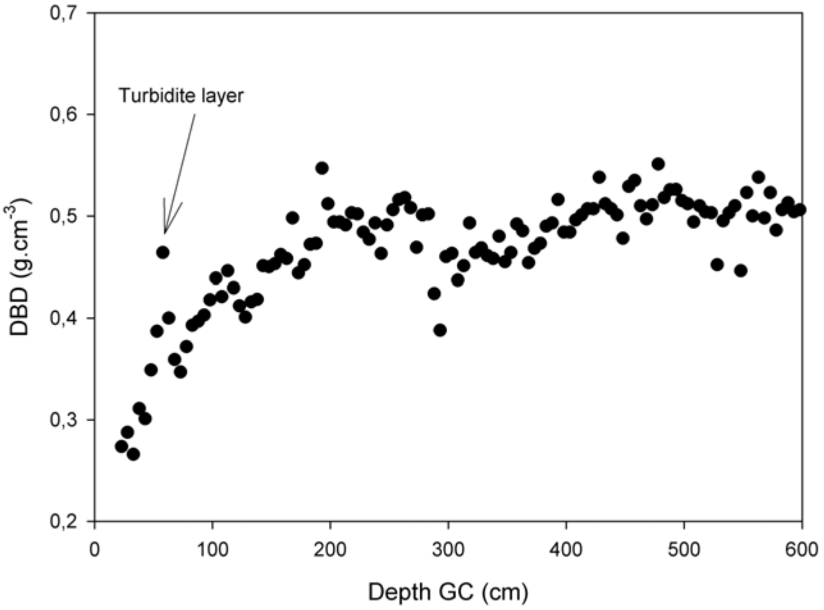

Figure A.4: *GeoB 10065-7: Dry bulk density measured in selected depths of the GC. "Combined depth" (of MUC and GC combined profile, as discussed in Sec. 10.5.1) can be calculated as depth - 20 cm. Data: Steinke (2012)*

Table A.16: *GeoB 10065-7: AMS-^{14}C ages and calibrated ages (MARINE09 calibration curve). Missing values (–) stand for invalid ages for the calibration curve.*

Lab. code	Sample depth (cm)	Foraminifera species	^{14}C age (yr BP)	Cal. age BP	Cal. age range[a] (relative area)
NOSAMS-OS-64679[b]	8	*Mixed planktonic foraminifera*	415 ± 30	–	–
NOSAMS-OS-81188[b]	27	*Mixed planktonic foraminifera*	690 ± 25	–	–
UCIAMS-89139[c]	36	*G. ruber + G. sacculifer*	630 ± 20	–	–
UCIAMS-84721[c]	41	*Mixed planktonic foraminifera*	755 ± 20	140	0-23 (0.061) 48-239 (0.939)
NOSAMS-OS-73005[b]	53	*Mixed planktonic foraminifera*	970 ± 75	370	230-505 (1.0)
NOSAMS-OS-81189[b]	77	*Mixed planktonic foraminifera*	890 ± 30	315	153-156 (0.001) 228-403 (0.999)
NOSAMS-OS-64680[b]	103	*Mixed planktonic foraminifera*	935 ± 30	340	270-415 (1.0)
NOSAMS-OS-81229[b]	127	*Mixed planktonic foraminifera*	1050 ± 25	440	374-499 (1.0)
NOSAMS-OS-72100[b]	158	*Mixed planktonic foraminifera*	1340 ± 30	660	567-580 (0.017) 595-716 (0.983)
NOSAMS-OS-81230[b]	182	*Mixed planktonic foraminifera*	1410 ± 25	710	653-762 (1.0)
NOSAMS-OS-64681[b]	213	*Mixed planktonic foraminifera*	1530 ± 35	820	733-907 (1.0)
NOSAMS-OS-81232[b]	232	*Mixed planktonic foraminifera*	1650 ± 25	960	892-1027 (1.0)
NOSAMS-OS-72101[b]	263	*Mixed planktonic foraminifera*	1800 ± 30	1110	1010-1205 (1.0)
NOSAMS-OS-81231[b]	284	*Mixed planktonic foraminifera*	1900 ± 25	1210	1149-1275 (1.0)
NOSAMS-OS-64750[b]	308	*Mixed planktonic foraminifera*	1960 ± 35	1260	1180-1333 (1.0)
NOSAMS-OS-81233[b]	334	*Mixed planktonic foraminifera*	2140 ± 30	1430	1348-1518 (1.0)
NOSAMS-OS-72102[b]	358	*Mixed planktonic foraminifera*	2280 ± 30	1600	1506-1696 (1.0)
NOSAMS-OS-81234[b]	377	*Mixed planktonic foraminifera*	2400 ± 30	1740	1639-1837 (1.0)
NOSAMS-OS-64751[b]	403	*Mixed planktonic foraminifera*	2460 ± 35	1800	1704-1901 (1.0)
NOSAMS-OS-81235[b]	429	*Mixed planktonic foraminifera*	2550 ± 30	1910	1820-1994 (1.0)
NOSAMS-OS-72103[b]	453	*Mixed planktonic foraminifera*	2800 ± 40	2220	2116-2320 (1.0)
NOSAMS-OS-81327[b]	479	*Mixed planktonic foraminifera*	2840 ± 35	2250	2151-2338 (1.0)
NOSAMS-OS-64752[b]	503	*Mixed planktonic foraminifera*	2760 ± 30	2190	2087-2293 (1.0)
NOSAMS-OS-81328[b]	527	*Mixed planktonic foraminifera*	3020 ± 25	2490	2360-2615 (0.957) 2624-2649 (0.043)
NOSAMS-OS-64767[b]	553	*Mixed planktonic foraminifera*	3030 ± 25	2520	2385-2662 (1.0)
NOSAMS-OS-81329[b]	579	*Mixed planktonic foraminifera*	3280 ± 25	2800	2734-2864 (1.0)
NOSAMS-OS-64768[b]	608	*Mixed planktonic foraminifera*	3350 ± 25	2870	2778-2955 (1.0)
NOSAMS-OS-81330[b]	635	*Mixed planktonic foraminifera*	3430 ± 25	2970	2867-3075 (1.0)
NOSAMS-OS-72104[b]	658	*Mixed planktonic foraminifera*	3600 ± 25	3220	3125-3318 (1.0)
NOSAMS-OS-81331[b]	679	*Mixed planktonic foraminifera*	3820 ± 30	3460	3372-3551 (1.0)
NOSAMS-OS-64769[b]	698	*Mixed planktonic foraminifera*	3750 ± 25	3385	3318-3452 (1.0)
NOSAMS-OS-81332[b]	722	*Mixed planktonic foraminifera*	3970 ± 30	3650	3545-3754 (1.0)
NOSAMS-OS-72105[b]	748	*Mixed planktonic foraminifera*	4150 ± 35	3870	3748-3986 (1.0)
NOSAMS-OS-81333[b]	772	*Mixed planktonic foraminifera*	4280 ± 30	4040	3933-4150 (1.0)
NOSAMS-OS-64770[b]	798	*Mixed planktonic foraminifera*	4340 ± 30	4120	4007-4241 (1.0)
NOSAMS-OS-81334[b]	819	*Mixed planktonic foraminifera*	4610 ± 30	4500	4406-4597 (1.0)
NOSAMS-OS-72106[b]	838	*Mixed planktonic foraminifera*	4810 ± 35	4750	4643-4848 (1.0)
NOSAMS-OS-81335[b]	859	*Mixed planktonic foraminifera*	4900 ± 30	4880	4807-4958 (1.0)
NOSAMS-OS-64771[b]	878	*Mixed planktonic foraminifera*	5020 ± 30	5050	4898-5201 (1.0)
NOSAMS-OS-81336[b]	899	*Mixed planktonic foraminifera*	5190 ± 30	5310	5138-5145 (0.004) 5195-5423 (0.996)
NOSAMS-OS-72107[b]	918	*Mixed planktonic foraminifera*	5450 ± 35	5550	5473-5629 (1.0)
NOSAMS-OS-64772[b]	968	*Mixed planktonic foraminifera*	5770 ± 30	5910	5827-5990 (1.0)

[a] 2 σ enclosing 95.4% of probability distribution

[b] Measured at the National Ocean Sciences Accelerator Mass Spectrometry Facility , Woods Hole, USA

[c] Measured at the Keck Carbon Cycle Accelerator Mass Spectrometry Facility, Earth System Science Department, University of California, Irvine, USA

Table A.17: *GOE Core F: Measured values of activity concentrations. Uncertainties are expressed as 1 standard deviation including counting statistics and detector calibration uncertainty. Values below decision threshold (DT) are expressed for 5% type I error probability.*

Mean depth	Cumulative mass	^{40}K	Uncert.	^{137}Cs	Uncert.	^{137}Cs DT	^{226}Ra via ^{214}Pb	Uncert.	^{210}Pb$_{\text{xs}}$	Uncert.	^{228}Th via ^{212}Pb and ^{208}Tl	Uncert.	^{228}Ra via ^{228}Ac	Uncert.
cm	$g \cdot cm^{-2}$	$Bq \cdot kg^{-1}$	$Bq \cdot kg^{-1}$	$Bq \cdot kg^{-1}$	$Bq \cdot kg^{-1}$	$Bq \cdot kg^{-1}$	$Bq \cdot kg^{-1}$	$Bq \cdot kg^{-1}$	$Bq \cdot kg^{-1}$	$Bq \cdot kg^{-1}$	$Bq \cdot kg^{-1}$	$Bq \cdot kg^{-1}$	$Bq \cdot kg^{-1}$	$Bq \cdot kg^{-1}$
0.25	0.26	321	64	6.1	2.4	3.8	20.9	8.2	49.2	30.2	-	-	55.8	8.3
0.75	0.79	412	69	-	-	4.3	22.2	7.8	67.0	28.8	-	-	42.7	5.2
1.25	1.32	406	61	4.0	2.1	3.4	14.1	7.2	63.8	26.8	19.5	6.5	41.7	5.6
1.75	1.88	326	62	4.7	2.9	4.8	12.2	10.2	97.8	35.0	-	-	25.3	6.3
2.25	2.43	293	59	4.9	2.6	4.3	20.4	6.8	57.1	30.1	-	-	30.7	5.9
2.75	2.98	433	65	6.5	3.3	3.6	19.4	7.0	44.0	23.7	-	-	36.7	6.1
3.50	3.84	328	63	-	-	4.4	19.7	8.6	63.8	36.2	-	-	37.7	6.0
4.50	5.02	465	70	-	-	4.3	4.5	6.9	40.0	28.6	-	-	35.4	3.2
5.50	6.18	330	57	8.3	3.0	4.8	22.6	6.8	26.3	27.5	-	-	40.3	5.1
6.50	7.33	438	70	3.9	1.3	3.0	16.4	4.7	37.0	20.7	32.6	9.2	42.2	6.8
7.50	8.49	445	65	3.8	2.2	3.7	12.6	7.2	9.7	23.6	35.4	8.9	38.3	6.5
8.50	9.63	345	58	-	-	3.2	6.9	6.2	9.7	21.7	43.2	9.4	23.6	6.1
9.50	10.70	383	65	-	-	3.8	22.0	8.3	3.2	30.8	-	-	38.2	6.0
10.50	11.74	503	76	-	-	3.8	10.5	7.3	27.7	28.2	35.3	13.1	31.9	6.8
11.50	12.97	438	64	-	-	3.4	1.6	6.4	13.9	24.0	28.7	9.3	38.3	5.1
13.00	14.68	289	62	-	-	4.7	12.0	7.3	8.0	25.6	-	-	36.2	5.5
15.00	16.80	369	60	-	-	2.9	4.8	6.2	20.0	26.7	40.6	6.6	25.2	5.5

Table A.18: *GOE Core HHN2C: Measured values of activity concentrations. Uncertainties are expressed as 1 standard deviation including counting statistics and detector calibration uncertainty. Values below decision threshold (DT) are expressed for 5% type I error probability.*

Mean depth cm	Cumulative mass $g \cdot cm^{-2}$	^{40}K $Bq \cdot kg^{-1}$	Uncert. $Bq \cdot kg^{-1}$	^{137}Cs $Bq \cdot kg^{-1}$	Uncert. $Bq \cdot kg^{-1}$	^{137}Cs DT $Bq \cdot kg^{-1}$	^{226}Ra via ^{214}Pb $Bq \cdot kg^{-1}$	Uncert. $Bq \cdot kg^{-1}$	^{210}Pb$_{xs}$ $Bq \cdot kg^{-1}$	Uncert. $Bq \cdot kg^{-1}$	^{228}Th via ^{212}Pb and ^{208}Tl $Bq \cdot kg^{-1}$	Uncert. $Bq \cdot kg^{-1}$	^{228}Ra via ^{228}Ac $Bq \cdot kg^{-1}$	Uncert. $Bq \cdot kg^{-1}$
0.5	0.55	413	18	6.10	0.82	1.22	33.1	2.1	75.8	10.3	44.0	1.9	27.5	2.3
1.5	1.56	398	19	6.69	0.92	1.37	33.6	2.4	57.7	9.6	39.0	1.9	29.5	2.1
2.5	2.51	380	13	4.75	0.49	0.75	32.0	1.5	30.3	6.2	32.4	1.1	27.2	1.2
3.5	3.48	389	17	2.77	0.63	1.02	29.9	2.2	22.9	7.4	34.0	1.9	31.6	1.9
4.5	4.49	435	19	1.26	0.65	1.08	26.8	1.9	17.6	7.4	34.6	1.6	31.2	1.9
5.5	5.52	374	32	-	-	0.83	25.6	1.9	5.2	6.2	35.5	1.5	33.7	2.1
6.5	6.57	436	19	-	-	0.91	31.5	2.3	5.3	6.2	40.0	1.9	41.4	2.6
7.5	7.64	381	13	-	-	0.42	26.7	1.6	11.4	4.8	37.0	1.1	33.4	1.3
8.5	8.72	383	18	-	-	0.85	26.0	1.9	5.5	7.2	31.3	1.9	37.2	2.5
9.5	9.80	384	17	-	-	0.87	28.9	1.9	4.3	6.1	40.4	1.7	38.2	2.3
10.5	10.91	411	19	-	-	0.91	28.6	1.9	-2.3	7.3	40.8	1.9	37.7	2.3
11.5	12.05	341	16	-	-	0.86	23.5	1.8	-0.1	5.6	37.6	2.0	32.4	1.9
12.5	13.22	368	13	-	-	0.50	24.4	1.4	1.0	3.9	35.4	1.2	32.1	1.4
13.5	14.43	381	17	-	-	0.72	22.6	1.6	2.8	4.5	36.3	1.6	31.8	1.7
14.5	15.94	364	17	-	-	0.87	22.2	1.7	-0.9	5.3	33.9	1.7	32.9	2.3
15.5	18.02	378	18	-	-	0.86	20.9	1.8	7.2	8.8	33.8	1.9	30.3	2.3

Table A.19: *GOE Core HHN3: Measured values of activity concentrations. Uncertainties are expressed as 1 standard deviation including counting statistics and detector calibration uncertainty. Values below decision threshold (DT) are expressed for 5% type I error probability.*

Mean depth cm	Cumulative mass $g \cdot cm^{-2}$	^{40}K $Bq \cdot kg^{-1}$	Uncert. $Bq \cdot kg^{-1}$	^{137}Cs $Bq \cdot kg^{-1}$	Uncert. $Bq \cdot kg^{-1}$	^{137}Cs DT $Bq \cdot kg^{-1}$	^{226}Ra via ^{214}Pb $Bq \cdot kg^{-1}$	Uncert. $Bq \cdot kg^{-1}$	^{210}Pb$_{xs}$ $Bq \cdot kg^{-1}$	Uncert. $Bq \cdot kg^{-1}$	^{228}Th via ^{212}Pb and ^{208}Tl $Bq \cdot kg^{-1}$	Uncert. $Bq \cdot kg^{-1}$	^{228}Ra via ^{228}Ac $Bq \cdot kg^{-1}$	Uncert. $Bq \cdot kg^{-1}$
0.25	0.22	472	32	13.62	2.12	3.29	45.6	4.0	106.5	16.1	120.6	4.7	51.5	4.9
0.75	0.64	499	20	14.03	0.81	1.07	42.4	2.5	106.6	12.2	99.7	2.9	38.3	2.2
1.25	1.08	560	25	12.85	1.13	1.52	48.1	2.9	92.8	14.1	90.3	3.3	50.7	3.3
1.75	1.56	457	19	3.96	0.83	1.31	38.6	2.5	61.7	11.6	65.0	2.3	38.3	2.3
2.25	2.01	442	21	9.12	0.91	1.36	42.4	2.7	128.8	16.6	62.4	2.5	57.1	3.2
2.75	2.41	455	20	8.56	0.98	1.44	35.1	2.5	80.4	9.0	57.9	2.3	40.7	2.8
3.25	2.81	406	28	8.89	1.46	2.31	28.2	3.4	73.1	13.8	33.2	2.8	32.0	4.0
3.75	3.36	447	23	10.34	1.36	2.06	29.2	2.5	53.3	12.0	37.2	2.1	33.5	3.2
4.50	4.16	476	21	8.23	0.90	1.30	29.1	2.2	43.8	11.5	37.0	2.0	38.7	2.8
5.50	5.11	459	19	5.19	0.81	1.25	32.2	2.2	33.7	7.7	41.1	1.9	38.7	2.3
6.50	6.08	437	18	2.91	0.67	1.07	28.4	1.9	35.3	7.5	39.6	1.7	39.0	2.1
7.50	7.02	467	15	1.01	0.31	0.51	32.5	1.6	26.2	6.2	49.7	1.8	44.8	1.5
8.50	8.03	472	18	-	-	0.76	31.8	2.0	-0.4	7.5	47.9	1.8	45.3	2.3
9.50	9.39	482	20	-	-	0.90	26.4	1.9	4.7	7.3	45.5	1.6	45.9	2.7
11.00	11.21	489	19	-	-	0.84	29.3	2.0	2.6	8.1	50.0	2.0	43.7	2.2
13.00	13.18	466	20	-	-	0.91	32.7	2.1	-5.2	9.8	48.2	1.9	43.5	2.3
15.00	15.11	493	21	-	-	0.93	31.0	2.0	-8.4	8.1	44.7	2.0	44.4	2.4
17.00	16.80	467	20	-	-	0.93	28.7	1.9	5.0	8.1	45.5	1.9	38.4	2.3
18.50	18.02	458	20	-	-	0.91	32.5	2.2	2.9	7.7	39.9	1.8	43.3	2.7

__Table A.20:__ GOE Core A2: Measured values of activity concentrations. Uncertainties are expressed as 1 standard deviation including counting statistics and detector calibration uncertainty. Values below decision threshold (DT) are expressed for 5% type I error probability.

Mean depth	Cumulative mass	^{40}K	Uncert.	^{137}Cs	Uncert.	^{137}Cs	^{226}Ra	Uncert.	^{210}Pb$_{xs}$	Uncert.	^{228}Th	Uncert.	^{228}Ra	Uncert.
						DT	via ^{214}Pb				via ^{212}Pb and ^{208}Tl		via ^{228}Ac	
cm	$g \cdot cm^{-2}$	$Bq \cdot kg^{-1}$	$Bq \cdot kg^{-1}$	$Bq \cdot kg^{-1}$	$Bq \cdot kg^{-1}$	$Bq \cdot kg^{-1}$	$Bq \cdot kg^{-1}$	$Bq \cdot kg^{-1}$	$Bq \cdot kg^{-1}$	$Bq \cdot kg^{-1}$	$Bq \cdot kg^{-1}$	$Bq \cdot kg^{-1}$	$Bq \cdot kg^{-1}$	$Bq \cdot kg^{-1}$
0.25	0.16	449	62	12.8	2.8	4.1	31.9	7.4	104.9	32.5	128.9	10.4	49.2	9.7
0.75	0.57	480	63	12.0	2.4	3.4	24.4	6.5	96.6	28.1	90.6	7.7	43.5	6.5
1.25	1.05	521	68	11.0	2.4	3.5	40.6	8.0	101.2	29.8	80.7	7.7	33.7	7.1
1.75	1.44	449	72	11.6	3.2	5.0	41.3	8.3	227.1	47.3	56.1	6.5	27.2	9.3
2.25	1.79	414	67	20.5	5.0	7.4	51.3	9.0	142.5	37.6	50.8	6.6	57.4	11.6
2.75	2.18	502	68	13.4	3.4	5.2	32.1	7.3	79.6	25.5	79.1	7.7	77.5	10.6
3.25	2.60	423	70	11.6	3.7	5.9	15.9	8.2	56.9	29.1	50.4	8.9	59.9	8.3
3.75	3.01	487	70	6.7	2.1	3.3	16.7	7.2	59.5	29.6	25.7	4.8	52.6	12.3
4.25	3.43	516	74	8.8	3.2	4.9	7.9	6.9	50.3	29.0	27.6	5.7	41.9	10.4
4.75	3.89	462	69	12.6	3.0	4.4	23.4	7.3	81.1	36.5	34.8	6.6	52.1	13.7
5.50	4.50	373	62	-	-	4.2	18.2	7.0	114.2	30.0	29.8	5.3	46.1	13.9
6.50	5.31	450	61	-	-	2.8	21.3	9.0	41.8	28.5	41.4	5.0	40.7	7.2
7.50	6.24	464	68	-	-	4.0	22.9	7.9	-4.5	23.6	56.6	7.0	41.4	10.5
8.50	7.18	450	63	-	-	3.2	24.9	7.0	-3.5	24.3	32.0	4.5	27.4	7.4
9.50	8.24	512	73	-	-	3.9	12.8	7.3	11.3	27.5	47.3	7.5	34.1	6.6
11.00	9.65	428	57	-	-	2.4	28.5	6.4	-12.2	20.1	46.4	5.4	52.7	7.0
13.00	11.34	468	54	-	-	3.2	22.4	6.8	-2.9	28.1	48.5	7.2	58.2	8.9
15.00	13.17	445	60	-	-	2.8	32.7	7.5	8.9	21.7	40.7	5.1	51.3	7.1
17.00	14.95	437	66	-	-	3.7	13.3	6.9	14.6	29.0	47.0	7.2	46.1	7.2
19.00	16.74	484	71	-	-	4.1	21.0	5.4	-16.9	27.0	42.6	7.2	48.8	6.8
21.00	18.41	444	62	9.05	2.60	1.3	33.1	7.4	137.8	31.2	47.9	6.3	34.3	7.2

Table A.21: *GOE Core B: Measured values of activity concentrations. Uncertainties are expressed as 1 standard deviation including counting statistics and detector calibration uncertainty. Values below decision threshold (DT) are expressed for 5% type I error probability.*

Mean depth cm	Cumulative mass $g \cdot cm^{-2}$	^{40}K $Bq \cdot kg^{-1}$	Uncert. $Bq \cdot kg^{-1}$	^{137}Cs $Bq \cdot kg^{-1}$	Uncert. $Bq \cdot kg^{-1}$	^{137}Cs DT $Bq \cdot kg^{-1}$	^{226}Ra via ^{214}Pb $Bq \cdot kg^{-1}$	Uncert. $Bq \cdot kg^{-1}$	^{210}Pb$_{xs}$ $Bq \cdot kg^{-1}$	Uncert. $Bq \cdot kg^{-1}$	^{228}Th via ^{212}Pb and ^{208}Tl $Bq \cdot kg^{-1}$	Uncert. $Bq \cdot kg^{-1}$	^{228}Ra via ^{228}Ac $Bq \cdot kg^{-1}$	Uncert. $Bq \cdot kg^{-1}$
0.25	0.2	515	30	10.9	1.4	2.8	41.7	3.8	131.9	13.6	165.1	4.1	50.1	3.9
0.75	0.6	519	22	8.3	1.0	0.6	45.3	2.9	84.0	11.5	120.2	2.9	57.8	3.2
1.25	1.1	555	26	6.2	0.9	1.4	36.8	2.9	54.0	11.5	77.7	2.9	47.3	3.4
1.75	1.6	431	20	1.0	0.7	1.3	28.7	2.3	25.6	9.5	54.2	2.2	35.4	2.2
2.25	2.2	435	20	5.5	0.9	1.4	26.4	2.0	71.4	11.7	47.0	2.1	32.9	2.6
2.75	2.7	419	20	6.3	1.0	1.6	29.7	2.2	110.2	11.8	42.9	2.0	37.2	2.6
3.25	3.1	441	20	5.1	0.9	1.4	29.5	2.2	99.9	11.8	47.9	2.2	45.8	2.4
3.75	3.7	455	16	6.3	0.9	1.4	39.6	2.1	61.6	8.0	76.0	2.2	73.8	1.9
4.50	4.5	455	19	1.3	0.6	1.1	37.2	2.5	20.4	9.4	88.4	2.8	75.9	2.6
5.50	5.6	379	16	2.8	0.7	1.2	25.4	1.9	7.5	6.1	34.5	1.6	28.1	2.0
6.50	6.9	435	18			0.9	23.5	1.6	23.7	7.8	36.4	1.7	33.8	2.3
7.50	8.1	408	18	2.2	0.7	1.2	22.4	1.9	27.1	6.8	37.0	1.7	31.4	2.2
8.50	9.4	402	13	1.8	0.4	0.6	24.9	1.4	16.4	4.6	37.0	1.2	33.8	1.1
9.50	10.8	415	18	1.8	0.7	1.1	26.0	1.9	28.7	7.2	45.5	1.9	38.2	2.2
11.0	12.5	420	18	2.0	0.6	0.9	28.7	2.2	25.0	7.6	46.6	1.8	48.4	2.3

Table A.22: *GOE: Activity concentrations of radionuclides calculated from measured concentrations of U and Th based on natural radionuclide ratios.*

Core F			Core HHN2C			Core A2			Core B		
Depth	^{238}U	^{232}Th	Depth	^{238}U	^{232}Th	Depth	^{238}U	^{232}Th	Depth	^{238}U	^{232}Th
cm	$Bq \cdot kg^{-1}$	$Bq \cdot kg^{-1}$	cm	$Bq \cdot kg^{-1}$	$Bq \cdot kg^{-1}$	cm	$Bq \cdot kg^{-1}$	$Bq \cdot kg^{-1}$	cm	$Bq \cdot kg^{-1}$	$Bq \cdot kg^{-1}$
0.25	37.7	27.8	1.00	42.6	40.0	0.25	44.8	49.6	0.5	54.9	68.7
0.75	38.1	28.1	2.00	42.1	37.3	0.75	43.7	46.8	1.0	54.3	80.8
1.25	39.4	31.8	3.00	42.4	43.1	1.25	44.5	47.8	1.5	46.9	69.6
1.75	37.5	29.0	4.00	45.3	45.7	1.75	42.0	34.1	2.0	31.1	57.7
2.25	38.3	29.8	5.00	42.4	38.0	2.25	41.0	36.4	2.5	33.4	30.4
2.75	39.8	29.2	6.00	46.1	40.8	2.75	39.7	38.8	3.0	42.8	45.9
3.50	43.2	34.0	7.00	47.3	40.1	3.25	39.9	44.1	3.5	44.7	42.2
4.50	43.6	31.0	8.00	29.5	19.0	3.75	39.9	43.6	4.0	41.5	45.3
5.50	45.1	39.5	9.00	48.2	39.4	4.25	39.0	42.1	5.0	44.9	57.1
6.50	42.5	34.4	10.00	46.6	36.2	4.75	40.5	43.0	6.0	35.2	44.1
7.50	40.1	35.0	11.00	46.5	34.8	5.50	38.8	41.1	7.0	33.9	40.5
8.50	37.6	32.6	12.00	49.8	38.5	6.50	44.4	53.3	8.0	35.4	41.0
9.50	37.7	34.2	13.00	47.0	33.8	7.50	46.1	54.3	9.0	46.0	116.6
10.50	40.5	45.2	14.00	45.5	36.8	8.50	40.1	46.2	10.0	58.3	72.3
11.50	39.2	33.6	15.00	45.1	45.8	9.50	41.8	43.4	12.0	41.4	39.9
13.00	38.4	27.9	17.00	43.5	37.5	11.00	42.9	45.2			
15.00	39.4	31.1				13.00	45.5	47.9			
						15.00	43.1	42.0			
						17.00	44.7	39.2			
						19.00	43.5	42.7			
						21.00	46.7	41.0			

Table A.23: *Activity concentrations of gamma emitting radionuclides measured in samples of wadi sediment, dust and fertilizers. In the bottom part of the table for sediment cores mean activities in upper 5 cm sections and mean activities in remaining bottom sections of individual cores are calculated. In order to calculate arithmetic mean of ^{137}Cs in sections of sediment cores 0 values were taken where activity was below decision threshold.*

Sample	Number	^{40}K	^{137}Cs	^{210}Pb	^{226}Ra	^{228}Ra (^{228}Ac)	^{228}Th (^{212}Pb, ^{208}Tl)	^{40}K	^{238}U	^{232}Th
		$Bq \cdot kg^{-1}$	$Bq \cdot kg^{-1}$	$Bq \cdot kg^{-1}$	$Bq \cdot kg^{-1}$	$Bq \cdot kg^{-1}$	$Bq \cdot kg^{-1}$	$Bq \cdot kg^{-1}$	$Bq \cdot kg^{-1}$	$Bq \cdot kg^{-1}$
		γ−spec.	γ−spec.	γ−spec.	γ−spec.	γ−spec.	γ−spec.	ICP-MS	ICP-MS	ICP-MS
Wadi sediment	1	512 ± 14	8.2 ± 0.3	65.3 ± 5.0	44.8 ± 0.9	55.4 ± 1.1	62.1 ± 1.6	446	31.9	34.8
Wadi sediment	2	404 ± 21	12.4 ± 1.0	97.0 ± 11.9	48.3 ± 2.1	27.2 ± 2.1	27.8 ± 1.5	216	23.7	14.2
Wadi sediment	5	691 ± 30	1.4 ± 0.3	78.7 ± 9.0	51.3 ± 1.9	57.1 ± 2.2	60.3 ± 3.2	626	41.1	43.2
Dust	Dust IC	172 ± 67	< 5.4	125 ± 32	44.7 ± 8.3	< 21.6	22.6 ± 3.3	135	43.2	18.9
Dust	Dust PLB	221 ± 77	< 5.8	88 ± 27	29.4 ± 7.6	< 22.5	15.2 ± 5.8	168	51.6	18.7
Dust	Dust MSS	164 ± 38	< 2.6	86 ± 18	42.4 ± 4.0	< 10.9	18.0 ± 1.7	147	49.9	19.0
Fertilizer	Phosphate	1202 ± 134	< 4.0	1145 ± 139	1234 ± 89	< 17.1	4.1 ± 2.3	1170	2011	3.0
Fertilizer	Mazut	292 ± 46	< 4.3	620 ± 78	651 ± 47	< 17.2	5.2 ± 1.8	56	2545	3.7
Sediment core (top 5 cm)	F	373 ± 23	3.3 ± 0.7	76.9 ± 10.1	20.4 ± 2.1	38.3 ± 2.1	–	363	38.8	29.5
Sediment core (bottom)	F	393 ± 21	1.8 ± 0.4	29.4 ± 8.1	15.1 ± 1.9	34.9 ± 2.0	36.0 ± 2.6	384	39.2	33.6
Sediment core (top 5 cm)	HHN2C	403 ± 8	4.3 ± 0.3	71.9 ± 3.6	32.4 ± 0.6	29.4 ± 0.9	36.8 ± 0.8	420	42.6	40.1
Sediment core (bottom)	HHN2C	382 ± 6	0.0 ± 0.0	29.1 ± 1.8	25.3 ± 0.4	34.6 ± 0.6	36.6 ± 0.5	400	45.3	37.2
Sediment core (top 5 cm)	HHN3	468 ± 8	10.0 ± 0.4	120.6 ± 4.2	36.8 ± 0.7	42.3 ± 1.1	67.0 ± 1.0	–	–	–
Sediment core (bottom)	HHN3	469 ± 6	0.9 ± 0.1	40.2 ± 2.4	29.7 ± 0.4	42.7 ± 0.7	45.2 ± 0.6	–	–	–
Sediment core (top 5 cm)	A2	470 ± 22	12.1 ± 1.0	128.5 ± 10.0	30.7 ± 1.8	49.5 ± 3.2	62.5 ± 2.3	448	40.8	43.3
Sediment core (bottom)	A2	451 ± 20	0.0 ± 0.0	36.9 ± 7.8	22.8 ± 1.6	44.7 ± 2.7	43.2 ± 2.0	457	43.5	42.7
Sediment core (top 5 cm)	B	469 ± 7	5.5 ± 2.1	108.3 ± 3.6	34.8 ± 0.6	50.7 ± 0.9	79.9 ± 0.9	454	43.7	51.8
Sediment core (bottom)	B	410 ± 7	1.8 ± 0.8	46.5 ± 2.6	24.5 ± 0.5	35.6 ± 0.8	39.5 ± 0.7	439	43.7	56.7

Table A.24: *GOE: Al normalized activity concentrations of gamma emitting radionuclides measured in samples of wadi sediment and dust. In the bottom part of the table for sediment cores mean activities in upper 5 cm sections and mean activities in remaining bottom sections of individual cores are calculated. In order to calculate arithmetic mean of ^{137}Cs in sections of sediment cores 0 values were taken where activity was below detection limit.*

Sample	Number	Al %	^{40}K / Al $Bq \cdot kg^{-1}/\%$	^{137}Cs / Al $Bq \cdot kg^{-1}/\%$	^{226}Ra / Al $Bq \cdot kg^{-1}/\%$	^{228}Ra / Al $Bq \cdot kg^{-1}/\%$
Wadi sediment	1	4,73	108	1,74	9,5	11,7
Wadi sediment	2	3,07	132	4,04	15,7	8,9
Wadi sediment	5	5,8	119	0,23	8,9	9,8
Dust	IC	1,92	90		23,3	
Dust	PLB	1,72	128		17,1	
Dust	MSS	2,29	72		18,5	
Sediment core (top 5 cm)	F	3,91	95	0,84	5,2	9,8
Sediment core (bottom)	F	4,18	94	0,43	3,6	8,4
Sediment core (top 5 cm)	HHN2C	4,94	82	0,87	6,6	6,0
Sediment core (bottom)	HHN2C	4,22	90	0,00	6,0	8,2
Sediment core (top 5 cm)	A2	5,57	84	2,17	5,5	8,9
Sediment core (bottom)	A2	5,33	85	0,00	4,3	8,4
Sediment core (top 5 cm)	B	5,03	93	1,09	6,9	10,1
Sediment core (bottom)	B	4,55	90	0,39	5,4	7,8

Table A.25: *Activity ratios of gamma emitting radionuclides measured in samples of wadi sediment, dust and fertilizers. In the bottom part of the table for sediment cores mean activities in upper 5 cm sections and mean activities in remaining bottom sections of individual cores are calculated.*

Sample	Number	^{228}Ra / ^{226}Ra	^{232}Th / ^{238}U	^{238}U / ^{226}Ra	^{232}Th / ^{228}Ra
Wadi sediment	1	1.24 ± 0.03	1.09	0.71	0.63
Wadi sediment	2	0.56 ± 0.05	0.60	0.49	0.52
Wadi sediment	5	1.11 ± 0.06	1.05	0.80	0.76
Dust	Dust IC	< 0.48	0.44	0.97	> 0.88
Dust	Dust PLB	< 0.76	0.36	1.76	> 0.83
Dust	Dust MSS	< 0.26	0.38	1.18	> 1.74
Fertilizer	Phosphate	< 0.03 (0.008)*	0.001	1.63	> 0.17
Fertilizer	Mazut	< 0.01 (0.003)*	0.001	3.91	> 0.21
Sediment core (top 5 cm)	F	1.88 ± 0.22	0.76	1.90	0.77
Sediment core (bottom)	F	2.33 ± 0.32	0.86	2.60	0.96
Sediment core (top 5 cm)	HHN2C	0.91 ± 0.03	0.94	1.31	1.36
Sediment core (bottom)	HHN2C	1.37 ± 0.03	0.82	1.79	1.07
Sediment core (top 5 cm)	HHN3	1.15 ± 0.04	–	–	–
Sediment core (bottom)	HHN3	1.44 ± 0.03	–	–	–
Sediment core (top 5 cm)	A2	1.61 ± 0.14	1.06	1.33	0.87
Sediment core (bottom)	A2	1.96 ± 0.18	0.98	1.91	0.96
Sediment core (top 5 cm)	B	1.46 ± 0.04	1.18	1.26	1.02
Sediment core (bottom)	B	1.46 ± 0.04	1.30	1.79	1.59

* In the brackets a ratio of ^{228}Th / ^{226}Ra of 1 is used, assuming radioactive equilibrium between ^{228}Ra and ^{228}Th, which is reasonable for ore samples.

Appendix B

Others

Summing spectra using Genie 2000 commands

(used in Chapters 5 and 10)

Step 1: Normalization

Spectra with different energy calibrations must be normalized first.
Under Windows open command prompt and normalize spectra using following set of commands:

```
DOS> normal c:\genie2k\camfiles\...\Spectrum1.cnf /cal=c:\Genie2k\
    camfiles\...\Spectrum2.cnf /out=c:\genie2k\camfiles\...\Spectrum3.
    cnf.
```

This will convert Spectrum1.cnf with energy calibration of Spectr2.cnf into Spectrum3.cnf. Once all spectra have the same energy calibration, they can be summed up.

Step 2: Adding spectra

Before approaching this step, open each spectrum and note down: Life-time, Real-time, and for control purposes also a count in a certain sellected channel (at 511 keV, for example). Calculate summs of live-times, real-times and counts in the sellected channel.
With a command:

```
DOS> strip c:\genie2k\camfiles\...\Spectrum3.cnf  c:\genie2k\camfiles
    \...\Spectrum2.cnf /factor=-1
```

the Spectrum2.cnf will be added to Spectrum3.cnf.
This step is to be repeated for each added spectrum separately.

Step 3: Live- and real-time correction

Finally, the live-and real-time values must be correcte in the resulting spectrum. For this the summs from step 2 will be used and at this point is it also recommended to check the summ of counts of the selected channel, if the summing process was correct.
With a command:

```
DOS> pars c:\genie2k\camfiles\...\Spectrum3.cnf /elive=yyyy /ereal=
    xxxx
```

the values form live- and real-times are reset.

Semiautomated process

When summing of many spectra is required, it is possible to use "sumspec" (a batch-file script used in the Laboratory, written by Bernd Hettwig). Using a command:

```
sumspec [Folder that includes the spectra to be summed up and where
    the summ-spectrum will be stored] [first spectrum without .cnf] [
    second spectrum without .cnf] [Name of the summ-spectrum] [Summ
    livetime] [Summe real-time]
```

Matlab code

(Used in Chap. 9)

```
%%*********************************************************
%%*********************************************************
%%Matching sediment cores procedure using least square estimation
%%Version 2.10.2013
%%Daniela Pittauerova
%%imput files: core1.txt [depth, activity, uncertainty],
%%core2.txt [depth, activity, uncertainty], 1 cm distances
%%*********************************************************
%%*********************************************************
clear all;
clc;
%%reading data
%load core1.txt
core1 = xlsread('core1.xls')
len1=length(core1);

%load core2.txt
core2 = xlsread('core2.xls')
len2=length(core2);

site = input('Enter site name: ', 's');

vysledek=[0 0 0 0 0];

%%Cycle 1
for offset=1:len2
 %% emptying values
 i=1;
    while i<(len1+len2);
        block1(i,:)=[0 0 0];
        i=i+1;
    end;

    i=1;
    while i<(len1+len2);
        block2(i,:)=[0 0 0];
        i=i+1;
  end;
  %% end of emptying values

  %% filling blocks
    for j=1:len1
        block1(j+step-1,1)=core1(j,1);
        block1(j+step-1,2)=core1(j,2);
        block1(j+step-1,3)=core1(j,3);
    end

    for j=1:len2
        block2(j+len1-1,1)=core2(j,1);
        block2(j+len1-1,2)=core2(j,2);
        block2(j+len1-1,3)=core2(j,3);
    end
    %% end of filling blocks

    %% rel_offset search
    ok=0;
    n=0;
    while ok~=1
        n=n+1;
        if (block1(n,1)~=0) & (block2(n,1)~=0)
            rel_offset=block1(n,1)-block2(n,1);
            ok=1;
        end
    end
    %% rel_offset found

    %% calculation of sum of squares
    chi=0;
```

```
    error_sq=0;
    sum_error_sq=0;
    wei=0;
    sumwei=0;
    overlap=0;
    for poradi=1:(len1+len2-1)
        if (block1(poradi,2)~=0) & (block2(poradi,2)~=0)
            wei=(block1(poradi,3)^2+block2(poradi,3)^2);
            sumwei=sumwei+wei;
            overlap=overlap+1;
            chi=chi+wei*((block1(poradi,2)-block2(poradi,2))^2);
                error_sq=wei*((block1(poradi,2)-block2(poradi,2))^2)*2*sqrt(
                    block1(poradi,3)^2+block2(poradi,3)^2)/(block1(poradi,2)-
                    block2(poradi,2));
            sum_error_sq=sum_error_sq+error_sq^2;
        end
    end
    if (sumwei~=0)
    chi=chi/sumwei;
    error_sq=sqrt(sum_error_sq)/sumwei;
    end

    vysledek(step,:)=[step, rel_offset, chi, error_sq, overlap];
    %% end of calculation of sum of squares
end
 %% end of cycle 1

 %%Cycle 2
 for step=len2:len2+len1-1
   %% emptying values
   i=1;
    while i<(len1+len2);
        block1(i,:)=[0 0 0];
        i=i+1;
    end;

    i=1;
    while i<(len1+len2);
        block2(i,:)=[0 0 0];
        i=i+1;
    end;
  %% end of emptying values

  for j=1:len1
        block1(j+len2-1,1)=core1(j,1);
        block1(j+len2-1,2)=core1(j,2);
        block1(j+len2-1,3)=core1(j,3);
    end

    for j=1:len2
        block2(j+step-len2,1)=core2(j,1);
        block2(j+step-len2,2)=core2(j,2);
        block2(j+step-len2,3)=core2(j,3);
    end

     %% absolute shift search
    ok=0;
    n=0;
    while ok~=1
        n=n+1;
        if (block1(n,1)~=0) & (block2(n,1)~=0)
            rel_offset=block1(n,1)-block2(n,1);
            ok=1;
        end
    end
    %% abs shift found

    %% calculation of sum of squares
    chi=0;
    error_sq=0;
    sum_error_sq=0;
    wei=0;
    sumwei=0;
    overlap=0;
```

```
    for poradi=1:(len1+len2-1)
        if (block1(poradi,2)~=0) & (block2(poradi,2)~=0)
           wei=(block1(poradi,3)^2+block2(poradi,3)^2);
            sumwei=sumwei+wei;
            overlap=overlap+1;
            chi=chi+wei*((block1(poradi,2)-block2(poradi,2))^2);
                error_sq=wei*((block1(poradi,2)-block2(poradi,2))^2)*2*sqrt(
                    block1(poradi,3)^2+block2(poradi,3)^2)/(block1(poradi,2)-
                    block2(poradi,2));
            sum_error_sq=sum_error_sq+error_sq^2;
        end
    end
    if (sumwei~=0)
    chi=chi/sumwei;
    error_sq=sqrt(sum_error_sq)/sumwei;
    end
    vysledek(step,:)=[step, rel_offset, chi, error_sq, overlap];
    %% end of calculation of sum of squares
 end
 %%end Cycle 2

%%reporting values
format ('short')
vysledek
B = sortrows(vysledek,3)
scatter (vysledek(:,2),vysledek(:,3))
headers = {'step', 'rel_offset', 'chi', 'error', 'overlap'};
xlswrite('output.xls', [headers], site, 'A1');
xlswrite('output.xls', B, site, 'A2');
```

Bibliography

Aarkrog, A. (1988). Worldwide data on fluxes of ^{239,240}Pu and ^{238}Pu to the oceans. In *Inventories of Selected Radionuclides in the Oceans* IAEA TECDOC Series No. 481 (pp. 103–137). Vienna, Austria.

Ababneh, Z. Q., Al-Omari, H., Rasheed, M., Al-Najjar, T., & Ababneh, A. M. (2010). Assessment of gamma-emitting radionuclides in sediment cores from the Gulf of Aqaba, Red Sea. *Radiation Protection Dosimetry*, *141*, 289–298.

Abril, J. (2004). Constraints on the use of ^{137}Cs as a time-marker to support CRS and SIT chronologies. *Environmental Pollution*, *129*, 31–37.

Abu-Hilal, A. H. (1985). Phosphate pollution in the Jordan Gulf of Aqaba. *Marine Pollution Bulletin*, *16*, 281–285.

Al-Hwaiti, M., Zielinski, R., Budahn, J., Ranville, J., & Ross, P. (2010). Distribution and mode of occurrences of radionuclides in phosphogypsum from the Aqaba and Eshidiya fertilizer plants, Jordan. *Chinese Journal of Geochemistry*, *25*, 178–178.

Al-Rousan, S., Pätzold, J., Al-Moghrabi, S., & Wefer, G. (2004). Invasion of anthropogenic CO$_2$ recorded in planktonic foraminifera from the northern Gulf of Aqaba. *International Journal of Earth Sciences*, *93*, 1066–1076.

Al-Trabulsy, H., Khater, A., & Habbani, F. (2011). Radioactivity levels and radiological hazard indices at the saudi coastline of the gulf of aqaba. *Radiation Physics and Chemistry*, *80*, 343–348.

Álvarez-Iglesias, P., Quintana, B., Rubio, B., & Pérez-Arlucea, M. (2007). Sedimentation rates and trace metal input history in intertidal sediments from San Simón Bay (Ría de Vigo, NW Spain) derived from ^{210}Pb and ^{137}Cs chronology. *Journal of Environmental Radioactivity*, *98*, 229–250.

Ami Nishri (2010). Unpublished raw data (water content and dry bulk densities in sediment cores from Gulf of Eilat). Oceanographic and Limnological Research, Haifa, Israel.

Anderson, N. (1986). Diatom biostratigraphy and comparative core correlation within a small lake basin. *Hydrobiologia*, *143*.

Appleby, P. G. (1998). *Dating recent sediments by ^{210}Pb: Problems and solutions*. Proc. 2nd NKS/EKO-1 Seminar, Helsinki, 2-4 April 1997, STUK, Helsinki.

Appleby, P. G. (2001). Chronostratigraphic techniques in recent sediments. In W. M. Last, & J. P. Smol (Eds.), *Tracking Environmental Change Using Lake Sediments* (pp. 171–203). Springer Netherlands volume 1 of *Developments in Paleoenvironmental Research*.

Appleby, P. G. (2008). Three decades of dating recent sediments by fallout radionuclides: a review. *Holocene*, *18*, 83–93.

Appleby, P. G., & Oldfield, F. (1978). The calculation of lead-210 dates assuming a constant rate of supply of unsupported ^{210}Pb to the sediment. *CATENA*, *5*, 1–8.

Appleby, P. G., & Oldfield, F. (1992). Applications of Pb-210 to sedimentation studies. In M. Ivanovich, & R. S. Harmon (Eds.), *Uranium series disequilibrium: applications to environmental problems* (pp. 731–778). Clarendon Pr. (2^{nd} ed.).

Appleby, P. G., Richardson, N., & Nolan, P. J. (1991). ^{241}Am dating of lake sediments. *Hydrobiologia*, *214*, 35–42.

Aqaba Port Corporation (2011). Statistics. `http://www.aqabaports.com.jo/En/` accessed in 12/2011.

Aston, S. R., & Stanners, D. A. (1981). Americium in intertidal sediments from the coastal environs of Windscale. *Marine Pollution Bulletin*, *12*, 149–153.

Atkinson, M. J., Birk, Y., & Rosenthal, H. (2001). *Evaluation of Pollution in the Gulf of Eilat*. Report For the Ministries of Infrastructure, Environment and Agriculture.

Axelsson, V. (2001). Monitoring sedimentation by radiographic core-to-core correlation. *Geo-Marine Letters*, *21*, 236–244.

Bailly du Bois, P., Laguionie, P., Boust, D., Korsakissok, I., Didier, D., & Fiévet, B. (2012). Estimation of marine source-term following Fukushima Dai-ichi accident. *Journal of Environmental Radioactivity*, *114*, 2–9.

Bard, E., Arnold, M., Toggweiler, J., Maurice, P., & Duplessy, J. (1989). Bomb ^{14}C in the Indian Ocean measured by accelerator mass spectrometry; oceanographic implications. *Radiocarbon*, *31*.

Barsanti, M., Delbono, I., Schirone, A., Langone, L., Miserocchi, S., Salvi, S., & Delfanti, R. (2011). Sediment reworking rates in deep sediments of the Mediterranean Sea. *Science of The Total Environment*, *409*, 2959 – 2970.

Baskaran, M. (2011). Po-210 and Pb-210 as atmospheric tracers and global atmospheric Pb-210 fallout: a review. *Journal of Environmental Radioactivity*, *102*, 500–513.

Baskaran, M., & Santschi, P. H. (2002). Particulate and dissolved ^{210}Pb activities in the shelf and slope regions of the Gulf of Mexico waters. *Continental Shelf Research*, *22*, 1493–1510.

Baskaran, M., & Swarzenski, P. (2007). Seasonal variations on the residence times and partitioning of short-lived radionuclides (^{234}Th, ^{7}Be and ^{210}Pb) and depositional fluxes of ^{7}Be and ^{210}Pb in Tampa Bay, Florida. *Marine Chemistry*, *104*, 27–42.

Basso, D., Thomson, J., & Corselli, C. (2004). Indications of low macrobenthic activity in the deep sediments of the eastern Mediterranean Sea. *Scientia Marina*, *68*, 53–62.

Bateman, H. (1910). The solution of a system of differential equations occurring in the theory of radioactive transformations. *Proceedings of Cambridge Philosophical Society*, *16*, 423–427.

Baumgart, A., Jennerjahn, T., Mohtadi, M., & Hebbeln, D. (2010). Distribution and burial of organic carbon in sediments from the Indian Ocean upwelling region off Java and Sumatra, Indonesia. *Deep Sea Research Part I: Oceanographic Research Papers*, *57*, 458–467.

Bé, M., Chisté, V., Dulieu, C., Browne, E., Chechev, V., Kuzmenko, N., Helmer, R., Nichols, A., Schönfeld, E., Dersch, R., Baglin, C., Kondev, F., MacMahon, D., Lee, K., Luca, A., Galán, M., Pearce, A., Huang, X., Mougeot, X., Arinc, A., & Wang, B. (2011). *Table of radionuclides, Monographie BIPM-5, 2004, 2006, 2008, 2010 and 2011 in 6 volumes.*. Bureau International des Poids et Mesures.

Ben-Sasson, M., Brenner, S., & Paldor, N. (2009). Estimating air-sea heat fluxes in semienclosed basins: The case of the Gulf of Elat (Aqaba). *Journal of Physical Oceanography*, *39*, 185–202.

Berger, M., Hubbell, J., Seltzer, S., Chang, J., Coursey, J., Sukumar, R., & Zucker, D. (2009). XCOM: Photon cross section database (version 1.4). `http://physics.nist.gov/xcom`, National Institute of Standards and Technology, Gaithersburg, MD. Accessed in November 2010.

Binford, M. W. (1990). Calculation and uncertainty analysis of ^{210}Pb dates for PIRLA project lake sediment cores. *Journal of Paleolimnology*, *3*, 253–267.

Björck, S., & Wohlfarth, B. (2002). ^{14}C chronostratigraphic techniques in paleolimnology. In W. M. Last, & J. P. Smol (Eds.), *Tracking Environmental Change Using Lake Sediments* (pp. 205–245). Springer Netherlands volume 1 of *Developments in Paleoenvironmental Research*.

Boer, W., van den Bergh, G., de Haas, H., de Stigter, H., Gieles, R., & van Weering, T. (2006). Validation of accumulation rates in Teluk Banten (Indonesia) from commonly applied ^{210}Pb models, using the 1883 Krakatau tephra as time marker. *Marine Geology*, *227*, 263–277.

Bossew, P. (2005). A very long-term HPGe-background gamma spectrum. *Applied Radiation and Isotopes*, *62*, 635–644.

Bossew, P., & Kirchner, G. (2004). Modelling the vertical distribution of radionuclides in soil. Part 1: the convection dispersion equation revisited. *Journal of Environmental Radioactivity*, *73*, 127–150.

Bossus, D., Swagten, J., & Kleinjans, P. A. (2006). Experience with a factory-calibrated hpge detector. *Nuclear Instruments and Methods in Physics Research Section A: Accelerators, Spectrometers, Detectors and Associated Equipment*, *564*, 650–654.

Brenner, M., Schelske, C. L., & Kenney, W. F. (2004). Inputs of dissolved and particulate ^{226}Ra to lakes and implications for ^{210}Pb dating recent sediments. *Journal of Paleolimnology*, *32*, 53–66.

Broecker, W. (2011). Radiocarbon. In H. Holland, & K. Turekian (Eds.), *Radioactive Geochronometry* Treatise on geochemistry (pp. 251–268). Elsevier, UK.

Bronson, F. L. (2003). Validation of the accuracy of the LabSOCS software for mathematical efficiency calibration of Ge detectors for typical laboratory samples. *Journal of Radioanalytical and Nuclear Chemistry*, *255*, 137–141.

Burns, K. A., Brunskill, G. J., Zagorskis, I., & Hoj, L. (2003). *Pilot study of hydrocarbon fluxes around Halimeda mounds on the Sahul Shelf and in the Timor Sea*. Report Australian Institute of Marine Science.

Canberra (2002a). *Genie-2000 Spectroscopy System Customization Tools*. Software manual Canberra Industries, Inc., Meriden, CT, USA.

Canberra (2002b). *Model S573/S574/ISOCS/LabSOCS Validation and Verification Manual*. Report V 4.0 9231205E Canberra Industries, Inc., Meriden, CT, USA.

Canberra (2002c). *Model S574 LabSOCS Calibration Software User's Manual*. Report V 4.1 9231580D Canberra Industries, Inc., Meriden, CT, USA.

Canberra (2011). *ISOCS/LabSOCS Detector Characterization Report*. Report Canberra Industries, Inc., Meriden, CT, USA.

Carroll, J., & Lerche, I. (2003). *Sedimentary Processes:Quantification Using Radionuclides* volume 5 of *Radioactivity in the Environment*. Elsevier.

Carroll, J. L., Lerche, I., Abraham, J. D., & Cisar, D. J. (1995). Model-determined sediment ages from ^{210}Pb profiles in un-mixed sediments. *Nuclear Geophysics*, *9*, 553–565.

Carroll, J. L., Lerche, I., Abraham, J. D., & Cisar, D. J. (1999). Sediment ages and flux variations from depth profiles of ^{210}Pb: lake and marine examples. *Applied Radiation and Isotopes*, *50*, 793–804.

Chai, Y., & Urban, N. (2004). Po-210 and Pb-210 distributions and residence times in the nearshore region of Lake Superior. *Journal of Geophysical Research - Oceans*, *109*.

Chanton, J. P., Martens, C. S., & Kipphut, G. W. (1983). Lead-210 sediment geochronology in a changing coastal environment. *Geochimica et Cosmochimica Acta*, *47*, 1791–1804.

Chao, J., Niu, H., Chiu, C., & Lin, C. (2007). A potential dating technique using ^{228}Th/^{228}Ra ratio for tracing the chronosequence of elemental concentrations in plants. *Applied Radiation and Isotopes*, *65*, 641–648.

Chehade, W. (2007). *True Coincidence Summing Correction in Gamma Spectroscopy*. Master thesis University of Bremen, Germany.

Chen, H. Y., & Huh, C. A. (1999). ^{232}Th-^{228}Ra-^{228}Th disequilibrium in east China sea sediments. *Journal of Environmental Radioactivity*, *42*, 93–100.

Chen, Y., Paytan, A., Chase, Z., Measures, C., Beck, A. J., Sañudo-Wilhelmy, S. A., & Post, A. F. (2008). Sources and fluxes of atmospheric trace elements to the Gulf of Aqaba, Red Sea. *Journal of Geophysical Research*, *113*.

Chih-An, H., Zahnle, D. L., Small, L. F., & Noshkin, V. E. (1987). Budgets and behaviors of uranium and thorium series isotopes in Santa Monica Basin sediments. *Geochimica et Cosmochimica Acta*, *51*, 1743–1754.

Child, D., & Hotchkis, M. (2013). Plutonium and uranium contamination in soils from former nuclear weapon test sites in Australia. *Nuclear Instruments and Methods in Physics Research Section B: Beam Interactions with Materials and Atoms*, *294*, 642–646.

Chino, M., Nakayama, H., Nagai, H., Terada, H., Katata, G., & Yamazawa, H. (2011). Preliminary estimation of release amounts of I-131 and Cs-137 accidentally discharged from the Fukushima Daiichi nuclear power plant into the atmosphere. *Journal of Nuclear Science and Technology*, *48*, 1129–1134.

Clark, R. M., & Thompson, R. (1979). A new statistical approach to the alignment of time series. *Geophysical Journal of the Royal Astronomical Society*, *58*, 593–607.

Cleveland Cascades Ltd. (2012). Case studies: Port of Aqaba. Phosphate loading. `http://clevelandcascades.co.uk/case_studies.php` accessed in 09/2012.

CNSC (2009). *Investigation of the Environmental Fate of Tritium in the Atmosphere*. Technical Report INFO-0792 Canadian Nuclear Safety Commission Ottawa.

Cochran, J. (1985). Particle mixing rates in sediments of the eastern equatorial Pacific: Evidence from ^{210}Pb, ^{239,40}Pu and ^{137}Cs distributions at MANOP sites. *Geochimica et Cosmochimica Acta*, *49*, 1195–1210.

Collé, R., Laureano-Perez, L., & Outola, I. (2007). A note on the half-life of ^{209}Po. *Applied Radiation and Isotopes*, *65*, 728–730.

CSIRO Division of Marine Research (2003). *FRV Southern Surveyor. Voyage Plan and Voyage Summary SS 06/2003*. Expedition report. CSIRO Division of Marine Research.

Currie, L. A. (1968). Limits for qualitative detection and quantitative determination. Application to radiochemistry. *Analytical Chemistry*, *40*, 586–593.

Cutshall, N. H., Larsen, I. L., & Olsen, C. R. (1983). Direct analysis of ^{210}Pb in sediment samples: Self-absorption corrections. *Nuclear Instruments and Methods in Physics Research*, *206*, 309–312.

Danesi, P., Moreno, J., Makarewicz, M., & Louvat, D. (2008). Residual radionuclide concentrations and estimated radiation doses at the former French nuclear weapons test sites in Algeria. *Applied Radiation and Isotopes*, *66*, 1671–1674.

Debertin, K., & Helmer, R. G. (1988). *Gamma and X-ray Spectrometry with Semiconductor Detectors*. Elsevier Science Ltd.

DeMaster, D. J., & Cochran, J. K. (1982). Particle mixing rates in deep-sea sediments determined from excess ^{210}Pb and ^{32}Si profiles. *Earth and Planetary Science Letters*, *61*, 257–271.

Dibb, J. E., & Rice, D. L. (1989). Temporal and spatial distribution of beryllium-7 in the sediments of Chesapeake Bay. *Estuarine, Coastal and Shelf Science*, *28*, 395–406.

Dickin, A. P. (2005). *Radiogenic Isotope Geology*. (2^{nd} ed.). Cambridge University Press.

Dong, W., Zheng, J., Guo, Q., Yamada, M., & Pan, S. (2010). Characterization of plutonium in deep-sea sediments of the Sulu and South China Seas. *Journal of Environmental Radioactivity*, *101*, 622–629.

Dowdall, M., Selnaes, O. G., Gwynn, J. P., & Davids, C. (2004). Simultaneous determination of ^{226}Ra and ^{238}U in soil and environmental materials by gamma-spectrometry in the absence of radium progeny equilibrium. *Journal of Radioanalytical and Nuclear Chemistry*, *261*, 513–521.

Dryak, P., & Kovar, P. (2006). Experimental and mc determination of HPGe detector efficiency in the 40–2754 keV energy range for measuring point source geometry with the source-to-detector distance of 25 cm. *Applied Radiation and Isotopes*, *64*, 1346–1349.

Dukat, D. A., & Kuehl, S. A. (1995). Non-steady-state ^{210}Pb flux and the use of ^{228}Ra/^{226}Ra as a geochronometer on the Amazon continental shelf. *Marine Geology*, *125*, 329–350.

Ebaid, Y. Y., & Khater, A. E. M. (2006). Determination of ^{210}Pb in environmental samples. *Journal of Radioanalytical and Nuclear Chemistry*, *270*, 609–619.

El-Daoushy, F. (1988). A summary on the lead-210 cycle in the nature and related applications in Scandinavia. *Environment International*, *14*, 305–319.

EML (2011). Environmental measurements laboratory Global fallout deposition program. On-line database `http://www.nbl.doe.gov/htm/EML_Legacy_Website/databases.htm`. Accessed 1/2011.

Enkelmann, E., Jonckheere, R., & Ratschbacher, L. (2005). The effects of radiation damage accumulation and annealing on fission-track dating of titanite. *Nuclear Instruments and Methods in Physics Research Section B: Beam Interactions with Materials and Atoms*, *227*, 567–576.

Enmar, R., Stein, M., Bar-Matthews, M., Sass, E., Katz, A., & Lazar, B. (2000). Diagenesis in live corals from the Gulf of Aqaba. i. the effect on paleo-oceanography tracers. *Geochimica et Cosmochimica Acta*, *64*, 3123–3132.

Enters, D., Kirchner, G., & Zolitschka, B. (2006). Establishing a chronology for lacustrine sediments using a multiple dating approach–a case study from the Frickenhauser See, central Germany. *Quaternary Geochronology*, *1*, 249–260.

Evangeliou, N., Florou, H., Bokoros, P., & Scoullos, M. (2009). Temporal and spatial distribution of ^{137}Cs in Eastern Mediterranean Sea. horizontal and vertical dispersion in two regions. *Journal of Environmental Radioactivity*, *100*, 626 – 636.

Fairclough, A., Plater, A. J., & Appleby, P. (2006). Determination of Holocene sedimentation rates from a carbonate lake using excess ^{226}Ra profiles. *Earth and Planetary Science Letters*, *243*, 115–127.

Faure, G., & Mensing, T. M. (2004). *Isotopes: Principles and Applications*. (3^{rd} ed.). Wiley.

Fifield, L. K., & Morgenstern, U. (2009). Silicon-32 as a tool for dating the recent past. *Quaternary Geochronology*, *4*, 400–405.

Fischer, H. W., Ulbrich, S., Pittauerová, D., & Hettwig, B. (2009). Medical radioisotopes in the environment - following the pathway from patient to river sediment. *Journal of Environmental Radioactivity*, *100*, 1079–1085.

Franke, J., Paul, A., & Schulz, M. (2008). Modeling variations of marine reservoir ages during the last 45 000 years. *Climate of the Past*, *4*, 125–136.

Freemantle, M., Hulings, N., Mulqi, M., & Watton, E. (1978). Calcium and phosphate in the Jordan Gulf of Aqaba. *Marine Pollution Bulletin*, *9*, 79–80.

Gale, S. (2009). Event chronostratigraphy: A high-resolution tool for dating the recent past. *Quaternary Geochronology*, *4*, 391–399. Dating the Recent Past.

Gale, S., Haworth, R., & Pisanu, P. (1995). The ^{210}Pb chronology of late holocene deposition in an Eastern Australian Lake basin. *Quaternary Science Reviews*, *14*, 395–408.

Garbe-Schönberg, D. (1993). Simultaneous determination of 37 trace elements in 28 international rock standards by ICP-MS. *Geostandards Newsletter*, *17*, 81–93.

Garbe-Schönberg, D. (2010). Unpublished raw data (elemental compositions of sediment cores from Gulf of Eilat). University of Kiel.

Garbe-Schönberg, D., Fischer, H. W., Pittauerová, D., Herut, B., & Nishri, A. (2010). *Anthropogenic entry of particulate phosphorus in the Gulf of Eilat - Sources and possible consequences (In German and English)*. Final Report Project 03F0445A, German Ministry of Science and Technology.

Garcia-Orellana, J., Pates, J., Masqué, P., Bruach, J., & Sanchez-Cabeza, J. (2009). Distribution of artificial radionuclides in deep sediments of the Mediterranean Sea. *Science of The Total Environment*, *407*, 887 – 898.

García-Talavera, M., & Peña, V. (2004). A hybrid method to compute accurate efficiencies for volume samples in γ-ray spectrometry. *Applied Radiation and Isotopes*, *60*, 227–232.

Geo-prospect Ltd. (2003). *Monitoring report for 2003 phosphorite and potassium salt loading at Eilat Port*. Geo-prospect Ltd. (In Hebrew).

Geo-prospect Ltd. (2007). *Monitoring report for 2007 phosphorite and potassium salt loading at Eilat Port*. Geo-prospect Ltd. (In Hebrew).

Gögen, K., & Wagner, G. A. (2000). Alpha-recoil track dating of quaternary volcanics. *Chemical Geology*, *166*, 127–137.

Gilmore, G. (2008). *Practical Gamma-Ray Spectroscopy*. (2^{nd} ed.). Wiley-Blackwell.

Gilmore, G. (2009). Does our software tell us the truth (or should we burn the Black Box)? In P. Nunez, S. Klemola, S. P. Nielsen, S. E. Pálsson, & C. Israelson (Eds.), *GammaSem Proceedings. A Nordic seminar for users of gamma spectrometry, Oslo 15-16 September 2009* NKS-212. Roskilde, Denmark: NKS (Nordic Nuclear Safety Research).

Gingele, F. X., Deckker, P. D., & Hillenbrand, C.-D. (2001). Clay mineral distribution in surface sediments between Indonesia and NW Australia – source and transport by ocean currents. *Marine Geology*, *179*, 135–146.

Goldberg, E. (1963). Geochronology with ^{210}Pb. In *Proceedings of a symposium on Radioative dating*. IAEA.

Goldberg, E. D., & Koide, M. (1962). Geochronological studies of deep sea sediments by the ionium/thorium method. *Geochimica et Cosmochimica Acta*, *26*, 417–450.

Goliáš, V. (2010). Unpublished raw data (Gamma spectrum of Trinitite). Charles University in Prague.

Gordon, A. (2005). Oceanography of the Indonesian seas and their throughflow. *Oceanography*, *18*, 14–27.

Grasty, R. L., Smith, C. W., Franklin, J. M., & Jonasson, I. R. (1988). Radioactive orphans in barite-rich chimneys, Axial caldera, Juan de Fuca ridge. *Canadian Mineralogist*, *26*, 627–636.

Gray, J., Jones, S. R., & Smith, A. D. (1995). Discharges to the environment from the Sellafield site, 1951-1992. *Journal of Radiological Protection*, *15*, 99–131.

Grayson, R. P., & Plater, A. J. (2007). An excess ^{226}Ra chronology for deep-sea sediments from Saanich Inlet, British Columbia. *Chemical Geology*, *244*, 646–663.

Hamarneh, I. A., Wreikat, A., & Toukan, K. (2003). Radioactivity concentrations of ^{40}K, ^{134}Cs, ^{137}Cs, ^{90}Sr, ^{241}Am, ^{238}Pu and $^{239+240}$Pu radionuclides in Jordanian soil samples. *Journal of Environmental Radioactivity*, *67*, 53–67.

Hambright, K. D., Eckert, W., Leavitt, P. R., & Schelske, C. L. (2004). Effects of historical lake level and land use on sediment and phosphorus accumulation rates in Lake Kinneret. *Environmental Science and Technology*, *38*, 6460–6467.

Hancock, G., Edgington, D. N., Robbins, J. A., Smith, J. S., Brunskill, G., & Pfitzner, J. (2002). Workshop on radiological techniques in sedimentation studies: methods and applications. In J.-M. Fernandez, & R. Fichez (Eds.), *Environmental Changes and Radioactive Tracers: 6th South Pacific Environmental Radioactivity Association Conference, 19-23 June 2000, Noumea IRD Centre, New Caledonia*.

Hancock, G., Webster, I., Ford, P., & Moore, W. (2000). Using Ra isotopes to examine transport processes controlling benthic fluxes into a shallow estuarine lagoon. *Geochimica et Cosmochimica Acta*, *64*, 3685–3699.

Hancock, G. J. (2000). Identifying resuspended sediment in an estuary using ^{228}Th/^{232}Th activity ratio: the fate of lagoon sediment in the Bega River estuary, Australia. *Marine and Freshwater Research*, *51*, 659–667.

Hancock, G. J., & Hunter, J. R. (1999). Use of excess ^{210}Pb and ^{228}Th to estimate rates of sediment accumulation and bioturbation in Port Phillip Bay, Australia. *Marine and Freshwater Research*, *50*, 533–545.

Hancock, G. J., Leslie, C., Everett, S. E., Tims, S. G., Brunskill, G. J., & Haese, R. (2011). Plutonium as a chronomarker in Australian and New Zealand sediments: a comparison with ^{137}Cs. *Journal of Environmental Radioactivity*, *102*, 919–929.

Hautala, S. L., Sprintall, J., Potemra, J. T., Chong, J. C., Pandoe, W., Bray, N., & Ilahude, A. G. (2001). Velocity structure and transport of the Indonesian Throughflow in the major straits restricting flow into the Indian Ocean. *Journal of Geophysical Research*, *106*, 19527–19546.

Hebbeln, D., & cruise participants (2006). *Report and preliminary results of RV SONNE Cruise SO-184, PABESIA, Durban (South Africa) – Cilacap (Indonesia) – Darwin (Australia), July 08th – September 13th, 2005*. Expedition report 246 Fachbereich Geowissenschaften, Universität Bremen.

Henderson, G. M., Lindsay, F. N., & Slowey, N. C. (1999). Variation in bioturbation with water depth on marine slopes: a study on the Little Bahamas Bank. *Marine Geology*, *160*, 105–18.

Hennig, G. J., & Grün, R. (1983). ESR dating in quaternary geology. *Quaternary Science Reviews*, *2*, 157–238.

Herut, B., & Nishri, A. (2004). Reconnaissance study on sedimentary phosphorus in the northern Gulf of Eilat. In Y. Cohen, & M. Ottolenghi (Eds.), *Gulf of Eilat Monitoring and Research Program - IET: Recommendations*. Interuniversity Institute for Marine Sciences in Eilat (IUI) and Israel Oceanographic and Limnological Research (IOLR). IET Project No. 11.

Hettwig, B. (2010). Problems in determining the true value for ^{226}Ra. Presented within the series of Seminar on Radioactivity and radiation protection, IUP, University of Bremen on 21.6.2010.

Hua, Q. (2009). Radiocarbon: A chronological tool for the recent past. *Quaternary Geochronology*, *4*, 378–390.

Hughen, K. A., Baillie, M. G. L., Bard, E., Bayliss, A., Beck, J. W., Bertrand, C. J. H., Blackwell, P. G., Buck, C. E., Burr, G. S., Cutler, K. B., Damon, P. E., Edwards, R. L., Fairbanks, R. G., Friedrich, M., Guilderson, T. P., Kromer, B., McCormac, F. G., Manning, S. W., Bronk Ramsey, C., Reimer, P. J., Reimer, R. W., Remmele, S., Southon, J. R., Stuiver, M., Talamo, S., Taylor, F. W., van der Plicht, J., & Weyhenmeyer, C. E. (2004). Marine04 marine radiocarbon age calibration, 26–0 ka BP. *Radiocarbon*, *46*, 1059–1086.

Hughen, K. A., Overpeck, J. T., Lehman, S. J., Kashgarian, M., Southon, J., Peterson, L. C., Alley, R., & Sigman, D. M. (1998). Deglacial changes in ocean circulation from an extended radiocarbon calibration. *Nature*, *391*, 65–68.

Hurtado, S., Villa, M., Manjón, G., & García-Tenorio, R. (2007). A self-sufficient and general method for self-absorption correction in gamma-ray spectrometry using GEANT4. *Nuclear Instruments and Methods in Physics Research Section A: Accelerators, Spectrometers, Detectors and Associated Equipment*, *580*, 234–237.

Israeli Ministry of Environmental Protection (2008). Landmarks in the fish cage controversy. `http://www.sviva.gov.il` accessed in 10/2011.

Isupova, M., & Mikhailov, V. (2008). Hydrological and morphological processes in senegal river mouth area. *Water Resources*, *35*, 30–42.

Jha, A. (2012). *Quantification of short-term erosion rates using the cosmogenic radionuclide* ^{7}Be. Dissertation thesis University of Bremen.

Justo, J., Evangelista, H., & Paschoa, A. S. (2006). Direct determination of ^{226}Ra in NORM/TENORM matrices by gamma-spectrometry. *Journal of Radioanalytical and Nuclear Chemistry*, *269*, 733–737.

Kandlbinder, R., Geißler, V., Schupfner, R., Wolfbeis, O., & Zinka, B. (2009). Analysing of ^{228}Th, ^{232}Th, ^{228}Ra in human bone tissues for the purpose of determining the post mortal interval. *Journal of Radioanalytical and Nuclear Chemistry*, *280*, 113–119.

Kempe, S., & Nies, H. (1987). Chernobyl nuclide record from a North-sea sediment trap. *Nature*, *329*, 828–831.

Kim, C. K., Kim, C. S., Chang, B. U., Choi, S. W., Chung, C. S., Hong, G. H., Hirose, K., & Igarashi, Y. (2004). Plutonium isotopes in seas around the Korean Peninsula. *The Science of The Total Environment*, *318*, 197–209.

Kirchner, G. (2011). ^{210}Pb as a tool for establishing sediment chronologies: examples of potentials and limitations of conventional dating models. *Journal of Environmental Radioactivity*, *102*, 490–494.

Kirchner, G., Bossew, P., & Cort, M. D. (2012). Radioactivity from Fukushima Dai-ichi in air over Europe; part 2: what can it tell us about the accident? *Journal of Environmental Radioactivity*, *114*, 35–40.

Kirchner, G., & Ehlers, H. (1998). Sediment geochronology in changing coastal environments: Potentials and limitations of the ^{137}Cs and ^{210}Pb methods. *Journal of Coastal Research*, *14*, 483–492.

Kirchner, G., Stiller, M., Nishri, A., & Koren, N. (1997). A simultaneous measurement of ^{137}Cs, ^{210}Pb and ^{226}Ra in sediments of the Dead Sea and Lake Kinneret by gamma spectrometry. *Terra Nostra - Schriften der Alfred Wegener Stiftung*, . In: The Dead Sea Rift as a Unique Global Site. Proc. 13th GIF Meeting, Dead Sea, February, 23-27, 1997.

Koide, M., Bertine, K. K., Chow, T. J., & Goldberg, E. D. (1985). The ^{240}Pu/^{239}Pu ratio, a potential geochronometer. *Earth and Planetary Science Letters*, *72*, 1–8.

Koide, M., Bruland, K., & Goldberg, E. (1976). ^{226}Ra chronology of a coastal marine sediment. *Earth and Planetary Science Letters*, *31*, 31–36.

Koide, M., Bruland, K. W., & Goldberg, E. D. (1973). Th-228/Th-232 and Pb-210 geochronologies in marine and lake sediments. *Geochimica et Cosmochimica Acta*, *37*, 1171–1187.

Koide, M., Michel, R., Goldberg, E. D., Herron, M. M., & Langway, C. C. (1979). Depositional history of artificial radionuclides in the Ross Ice Shelf, Antarctica. *Earth and Planetary Science Letters*, *44*, 205–223.

Koide, M., Soutar, A., & Goldberg, E. D. (1972). Marine geochronology with ^{210}Pb. *Earth and Planetary Science Letters*, *14*, 442–446.

Krieger, H. (2007). *Grundlagen der Strahlungsphysik und des Strahlenschutzes (in German).* (2nd ed.). B. G. Teubner Verlag.

Krishnaswamy, S., Lal, D., Martin, J., & Meybeck, M. (1971). Geochronology of lake sediments. *Earth and Planetary Science Letters*, *11*, 407–414.

KTA (2007). *Überwachung der Ableitung radioaktiver Stoffe mit Wasser*. KTA 1504.

Ku, T. L. (1976). The uranium-series methods of age determination. *Annual Review of Earth and Planetary Sciences*, *4*, 347–379.

Laguionie, P., Du Bois, P. B., Boust, D., Fievet, B., Garreau, P., Connan, O., Charmasson, S., Arnaud, M., Duffa, C., & Champion, D. (2012). Consequences of radioactive releases into the sea resulting from the accident at the Fukushima Dai-ichi nuclear power plant - Evolution of expert investigation according to the data available. *Radioprotection*, *47*, 423–447.

Lal, D., Goldberg, E. D., & Koide, M. (1960). Cosmic-ray-produced silicon-32 in nature. *Science*, *131*, 332–337.

Lamoureux, S. (2002). Varve chronology techniques. In W. M. Last, & J. P. Smol (Eds.), *Tracking Environmental Change Using Lake Sediments* (pp. 247–260). Springer Netherlands volume 1 of *Developments in Paleoenvironmental Research*.

Lanphere, M. (2001). Radiometric dating. In R. A. Meyers (Ed.), *Encyclopedia of Physical Science and Technology* (pp. 721–730). New York: Academic Press.

Lee, S.-H., Gastaud, J., Povinec, P. P., Hong, G.-H., Kim, S.-H., Chung, C.-S., Lee, K.-W., & Pettersson, H. B. (2003). Distribution of plutonium and americium in the marginal seas of the northwest Pacific ocean. *Deep Sea Research Part II: Topical Studies in Oceanography*, *50*, 2727–2750.

Lee, S.-H., Povinec, P. P., Wyse, E., Pham, M. K., Hong, G.-H., Chung, C.-S., Kim, S.-H., & Lee, H.-J. (2005). Distribution and inventories of ^{90}Sr, ^{137}Cs, ^{241}Am and Pu isotopes in sediments of the Northwest Pacific Ocean. *Marine Geology*, *216*, 249–263.

Lee, S.-Y., Huh, C.-A., Su, C.-C., & You, C.-F. (2004). Sedimentation in the Southern Okinawa Trough: enhanced particle scavenging and teleconnection between the Equatorial Pacific and western Pacific margins. *Deep Sea Research Part I: Oceanographic Research Papers*, *51*, 1769–1780.

Legeleux, F., Reyss, J.-L., & Schmidt, S. (1994). Particle mixing rates in sediments of the northeast tropical Atlantic: Evidence from ^{210}Pb$_{xs}$, ^{137}Cs, ^{228}Th$_{xs}$ and ^{234}Th$_{xs}$ downcore distributions. *Earth and Planetary Science Letters*, *128*, 545–562.

Lehto, J., & Hou, X. (2010). *Chemistry and Analysis of Radionuclides: Laboratory Techniques and Methodology.* (1st ed.). Wiley-VCH Verlag.

Leslie, C., & Hancock, G. (2008). Estimating the date corresponding to the horizon of the first detection of ^{137}Cs and $^{239+240}$Pu in sediment cores. *Journal of Environmental Radioactivity*, *99*, 483–490.

Lian, O. B., & Roberts, R. G. (2006). Dating the quaternary: progress in luminescence dating of sediments. *Quaternary Science Reviews*, *25*, 2449–2468.

Libby, W. F., Anderson, E. C., & Arnold, J. R. (1949). Age determination by radiocarbon content: World-wide assay of natural radiocarbon. *Science*, *109*, 227–228.

Lindahl, P., Lee, S.-H., Worsfold, P., & Keith-Roach, M. (2010). Plutonium isotopes as tracers for ocean processes: A review. *Marine Environmental Research*, *69*, 73–84.

Loizeau, J.-L., Rozé, S., Peytremann, C., Monna, F., & Dominik, J. (2003). Mapping sediment accumulation rate by using volume magnetic susceptibility core correlation in a contaminated bay (Lake Geneva, Switzerland). *Eclogae Geologicae Helvetiae*, *96*, S73–S79.

Loosli, H. (1983). A dating method with ^{39}Ar. *Earth and Planetary Science Letters*, *63*, 51–62.

Lowe, D. J. (2011). Tephrochronology and its application: A review. *Quaternary Geochronology*, *6*, 107–153.

Luykx, F., & Fraser, G. (1986). Tritium releases from nuclear power plants and nuclear fuel reprocessing plants. *Radiation Protection Dosimetry*, *16*, 31–36.

MacKenzie, A., Hardie, S., Farmer, J., Eades, L., & Pulford, I. (2011). Analytical and sampling constraints in ^{210}Pb dating. *Science of The Total Environment*, *409*, 1298–1304.

Manz, L. A. (2002). In-situ cosmogenic nuclides: Their role in studying the age and evolution of landscapes, or what “as old as the hills” really means. *NDGS Newsletter*, *29*, 1–5.

Masson, O., Baeza, A., Bieringer, J., Brudecki, K., Bucci, S., Cappai, M., Carvalho, F., Connan, O., Cosma, C., Dalheimer, A., Didier, D., Depuydt, G., De Geer, L., De Vismes, A., Gini, L., Groppi, F., Gudnason, K., Gurriaran, R., Hainz, D., Halldórsson, ., Hammond, D., Hanley, O., Holeý, K., Homoki, Z., Ioannidou, A., Isajenko, K., Jankovic, M., Katzlberger, C., Kettunen, M., Kierepko, R., Kontro, R., Kwakman, P., Lecomte, M., Leon Vintro, L., Leppänen, A.-P., Lind, B., Lujaniene, G., Mc Ginnity, P., Mahon, C. M., Malá, H., Manenti, S., Manolopoulou, M., Mattila, A., Mauring, A., Mietelski, J., Møller, B., Nielsen, S., Nikolic, J., Overwater, R., Pálsson, S. E., Papastefanou, C., Penev, I., Pham, M., Povinec, P., Ramebäck, H., Reis, M., Ringer, W., Rodriguez, A., Rulík, P., Saey, P., Samsonov, V., Schlosser, C., Sgorbati, G., Silobritiene, B. V., Söderström, C., Sogni, R., Solier, L., Sonck, M., Steinhauser, G., Steinkopff, T., Steinmann, P., Stoulos, S., Sýkora, I., Todorovic, D., Tooloutalaie, N., Tositti, L., Tschiersch, J., Ugron, A., Vagena, E., Vargas, A., Wershofen, H., & Zhukova, O. (2011). Tracking of airborne radionuclides from the damaged Fukushima Dai-Ichi nuclear reactors by European networks. *Environmental Science and Technology*, *45*, 7670–7677.

Masson, O., Piga, D., Gurriaran, R., & D'Amico, D. (2010). Impact of an exceptional Saharan dust outbreak in France: PM10 and artificial radionuclides concentrations in air and in dust deposit. *Atmospheric Environment*, *44*, 2478–2486.

Mauring, A., & Gäfvert, T. (2013). Radon tightness of different sample sealing methods for gamma spectrometric measurements of ^{226}Ra. *Applied Radiation and Isotopes*, *81*, 92–95.

McGregor, H. V., Dima, M., Fischer, H. W., & Mulitza, S. (2007). Rapid 20th-century increase in coastal upwelling off northwest Africa. *Science*, *315*, 637–639.

Menut, L., Masson, O., & Bessagnet, B. (2009). Contribution of Saharan dust on radionuclide aerosol activity levels in Europe? The 21-22 February 2004 case study. *Journal of Geophysical Research*, *114*, D16202.

MEXT (2013). Readings of sea Area Monitoring at offshore of Miyagi, Fukushima, and Ibaraki Prefecture (Sr) (marine soil)(Sampling Date: Oct 25-Nov 3, 2012).

Mohtadi, M., & cruise participants (2013). *Cruise Report EISPAC-WESTWIND-SIODP, RV SONNE Cruise SO-228. Kaohsiung (04.05.2013) – Townsville (23.06.2013)*. Expedition report Fachbereich Geowissenschaften, Universität Bremen.

Moon, D.-S., Hong, G.-H., Kim, Y. I., Baskaran, M., Chung, C. S., Kim, S. H., Lee, H.-J., Lee, S.-H., & Povinec, P. P. (2003). Accumulation of anthropogenic and natural radionuclides in bottom sediments of the Northwest Pacific Ocean. *Deep Sea Research Part II: Topical Studies in Oceanography*, *50*, 2649–2673.

Morgenstern, U., & Taylor, C. B. (2009). Ultra low-level tritium measurement using electrolytic enrichment and LSC. *Isotopes in Environmental and Health Studies*, *45*, 96–117.

Moser, R. (1993). A comparison of methods for the determination of the dating-nuclides ^{210}Pb and ^{226}Ra. *Journal of Radioanalytical and Nuclear Chemistry*, *173*, 283–292.

Mulitza, S., & cruise participants (2006). *Report and preliminary results of Meteor Cruise M 65/1, Dakar - Dakar, 11.06.- 1.07.2005*. Expedition report 252 Fachbereich Geowissenschaften, Universität Bremen.

Mulitza, S., Heslop, D., Pittauerová, D., Fischer, H. W., Meyer, I., Stuut, J.-B., Zabel, M., Mollenhauer, G., Collins, J. A., Kuhnert, H., & Schulz, M. (2010). Increase in African dust flux at the onset of commercial agriculture in the Sahel region. *Nature*, *466*, 226–228.

NEA (2002). *CHERNOBYL Assessment of Radiological and Health Impacts*. Report 2002 Update of Chernobyl: Ten Years On. OECD Nuclear Energy Agency Paris.

Neuer, S., & cruise participants (2000). *Report and preliminary results of Meteor Cruise M 45/5, Bremen - Las Palmas, October 1 - November 3, 1999*. Expedition report 166 Fachbereich Geowissenschaften, Universität Bremen.

Nijampurkar, V., Rao, D., Oldfield, F., & Renberg, I. (1998). The half-life of ^{32}Si: a new estimate based on varved lake sediments. *Earth and Planetary Science Letters*, *163*, 191–196.

NNDC (2011). Information extracted from the chart of nuclides database, `http://www.nndc.bnl.gov/chart/`, accessed 1/2011-6/2012. National Nuclear Data Center, Brookhaven National Laboratory.

Nozaki, Y., Tsubota, H., Kasemsupaya, V., Yashima, M., & Naoko, I. (1991). Residence times of surface water and particle-reactive ^{210}Pb and ^{210}Po in the East China and Yellow seas. *Geochimica et Cosmochimica Acta*, *55*, 1265–1272.

Nucleonica (2011). Gamma Spectrum Generator, Nucleonica Wiki. `http://www.nucleonica.com/wiki/index.php/Help:Gamma_Spectrum_Generator`, Nucleonica GmbH, Karlsruhe, Germany. Accessed in November 2012.

O'Reilly, J., León Vintró, L., Mitchell, P., Donohue, I., Leira, M., Hobbs, W., & Irvine, K. (2011). ^{210}Pb-dating of a lake sediment core from Lough Carra (Co. Mayo, western Ireland): use of paleolimnological data for chronology validation below the ^{210}Pb dating horizon. *Journal of Environmental Radioactivity*, *102*, 495–499.

Paatero, J., Veleva, B., Holm, E., Buyukay, M., Virkkula, A., Holmén, K., & Hatakka, J. (2009). Airborne lead-210 - spatial and temporal variations. Presented at the International Topical Conference on Polonium and Radioactive Lead Isotopes, Seville.

Pálsson, S., Howard, B., Bergan, T., Paatero, J., Isaksson, M., & Nielsen, S. (2013). A simple model to estimate deposition based on a statistical reassessment of global fallout data. *Journal of Environmental Radioactivity*, *121*, 75–86.

Pan, S., Tims, S., Liu, X., & Fifield, L. (2011). ^{137}Cs, $^{239+240}$Pu concentrations and the ^{240}Pu/^{239}Pu atom ratio in a sediment core from the sub-aqueous delta of Yangtze River estuary. *Journal of Environmental Radioactivity*, *102*, 930–936.

Papastefanou, C., & Ioannidou, A. (2004). Beryllium-7 and solar activity. *Applied Radiation and Isotopes*, *61*, 1493–1495.

Papucci, C., Charmasson, S., Delfanti, R., Gasco, C., Mitchell, P., & Sachez-Cabeza, J. (1996). Time evolution and levels of man-made radioactivity in the Mediterranean Sea. In P. Guéguéniat, P. Germain, & H. Métivier (Eds.), *Radionuclides in the oceans: inputs and inventories* (pp. 177 – 197). Paris: Les editions de physique,.

Pearce, A. (2008). *Recommended Nuclear Decay Data*. NPL REPORT IR 6 National Physical Laboratory Hampton Road, Teddington, UK.

Pettersson, H. B. L., Amano, H., Berezhnov, V. I., Chaykovskaya, E., Chumichev, V. B., Chung, C. S., Gastaud, J., Hirose, K., Hong, G. H., Kim, C. K., Kim, S. H., Lee, S. H., Morimoto, T., Nikitin, A., Oda, K., Povinec, P. P., Suzuki, E., Tkalin, A., Togawa, O., Veletova, N. K., Volkov, Y., & Yoshida, K. (1999). Anthropogenic radionuclides in sediments in the NW Pacific Ocean and its marginal seas: results of the 1994-1995 Japanese-Korean-Russian expeditions. *The Science of The Total Environment*, *237–238*, 213–224.

Pietsch, T. J. (2009). Optically stimulated luminescence dating of young (<500 years old) sediments: Testing estimates of burial dose. *Quaternary Geochronology*, *4*, 406–422.

Piliposian, G., & Appleby, P. (2003). A simple model of the origin and transport of ^{222}Rn and ^{210}Pb in the atmosphere. *Continuum Mechanics and Thermodynamics*, *15*, 503–518.

Pittauerová, D., Hettwig, B., & Fischer, H. W. (2011). Fukushima fallout in Northwest German environmental media. *Journal of Environmental Radioactivity*, *102*, 877–880.

Pittauerová, D., Kolb, W. M., Rosenstiel, J. C., & Fischer, H. W. (2010a). Radioactivity in Trinitite – a review and new measurements. In *Proceedings of the Third European IRPA Congress*. International Radiation Protection Association Helsinki, Finland: IRPA.

Pittauerová, D., Mulitza, S., Hettwig, B., Chehade, W., Stuut, J.-B., Mollenhauer, G., & Fischer, H. W. (2009). Application of self-absorption correction method in gamma spectroscopy for ^{210}Pb and ^{137}Cs sediment chronology on the continental slope off NW Africa. *Radioprotection*, *44*, 457–461.

Pittauerová, D., Ulbrich, S., Hettwig, B., & Fischer, H. W. (2010b). Long-term background in gamma-spectroscopy. In *14. Fachgespräch zur Überwachung der Umweltradioaktivität*. Bundesministerium für Umwelt, Naturschutz und Reaktorsicherheit, Germany Freiburg, Germany: BMU.

Povinec, P. P., Delfanti, R., Gastaud, J., Rosa, J. L., Morgenstern, U., Oregioni, B., Pham, M. K., Salvi, S., & Top, Z. (2003). Anthropogenic radionuclides in Indian Ocean surface waters – the indian ocean transect 1998. *Deep Sea Research Part II: Topical Studies in Oceanography*, *50*, 2751–2760.

Preiss, N., Mélières, M.-A., & Pourchet, M. (1996). A compilation of data on lead 210 concentration in surface air and fluxes at the air-surface and water-sediment interfaces. *Journal of Geophysical Research*, *101*, 28847–28862.

Prescott, J., & Robertson, G. (1997). Sediment dating by luminescence: a review. *Radiation Measurements*, *27*, 893–922.

Pressyanov, D. S. (2002). Short solution of the radioactive decay chain equations. *American Journal of Physics*, *70*, 444–445.

Prospero, J. M., & Lamb, P. J. (2003). African droughts and dust transport to the caribbean: Climate change implications. *Science*, *302*, 1024–1027.

Reimer, P. J., , Baillie, M. G. L., Bard, E., Bayliss, A., Beck, J. W., Blackwell, P. G., Bronk Ramsey, C., Buck, C. E., Burr, G. S., Edwards, R. L., Friedrich, M., Grootes, P. M., Guilderson, T. P., Hajdas, I., Heaton, T. J., Hogg, A. G., Hughen, K. A., Kaiser, K. F., Kromer, B., McCormac, F. G., Manning, S. W., Reimer, R. W., Richards, D. A., Southon, J. R., Talamo, S., Turney, C. S. M., van der Plicht, J., & Weyhenmeyer, C. E. (2009). IntCal09 and Marine09 radiocarbon age calibration curves, 0-50,000 years cal. BP. *Radiocarbon*, *51*.

Reyes, A. O., Moore, W. S., & Stakes, D. S. (1995). ^{228}Th/^{228}Ra ages of a barite-rich chimney from the Endeavour Segment of the Juan de Fuca Ridge. *Earth and Planetary Science Letters*, *131*, 99–113.

Rink, W. (1997). Electron spin resonance (ESR) dating and ESR applications in quaternary science and archaeometry. *Radiation Measurements*, *27*, 975–1025.

Robbins, J. A. (1978). Geochemical and geophysical applications of radioactive lead. In J. O. Nriagu (Ed.), *Biogeochemistry of Lead in the Environment* (pp. 285–393). Elsevier Scientific, Amsterdam.

Robbins, J. A., Edgington, D. N., & Kemp, A. L. W. (1978). Comparative ^{210}Pb, ^{137}Cs, and pollen geochronologies of sediments from lakes Ontario and Erie. *Quaternary Research*, *10*, 256–278.

Rose, N., Harlock, S., & Appleby, P. (1999). Within-basin profile variability and cross-correlation of lake sediment cores using the spheroidal carbonaceous particle record. *Journal of Paleolimnology*, *21*.

Rostan, J., Juget, J., & Brun, A. (1997). Sedimentation rates measurements in former channels of the upper Rhône river using Chernobyl ^{137}Cs and ^{134}Cs as tracers. *Science of The Total Environment*, *193*, 251–262.

Saarinen, T., & Petterson, G. (2002). Image analysis techniques. In W. M. Last, & J. P. Smol (Eds.), *Tracking Environmental Change Using Lake Sediments* (pp. 23–39). Springer Netherlands volume 2 of *Developments in Paleoenvironmental Research*.

Sade, A. R., Hall, J. K., Tibor, G., Niemi, T. M., Ben-Avraham, Z., Al-Zoubi, A. A., Hartman, G., Akawwi, E., Abueladas, A.-R., & Amit, G. (2008). The multinational bathymetric survey: Northern Gulf of Aqaba/Eilat poster. *Israel Journal of Earth Sciences*, *57*, 139–144.

Saito, T. (2007). Estimation of growth rate of hokutolite from Tamagawa hot-spring, Akita, Japan. *Journal of Radioanalytical and Nuclear Chemistry*, *272*, 443–446.

Sanchez-Cabeza, J., & Ruiz-Fernández, A. (2012). ^{210}Pb sediment radiochronology: An integrated formulation and classification of dating models. *Geochimica et Cosmochimica Acta*, *82*, 183–200.

Sanchez-Cabeza, J.-A., Kwong, L. L. W., & Betti, M. (2010). Method to determine ^{226}Ra in small sediment samples by ultralow background liquid scintillation. *Analytical Chemistry*, *82*, 6847–6853.

Schkade, U.-K., Arnold, D., Döring, J., Hartmann, M., & Wershofen, H. (2007). *Gammaspectromectric determination of specific activity of natural radionuclides in environmental samples. 7th Intercomparison "Soil 2006"*. Evaluation report. BfS-SCHR-41/07 German Federal Office for Radiation Protection Berlin, Germany. (In German).

Schkade, U.-K., Naumann, M., & Wiechen, A. (2000). Gamaspektrometrische Bestimmung ausgewählter natürlicher Radionuklide. In *Messanleitungen für die Überwachung radioaktiver Stoffe in der Umwelt und externer Strahlung* γ-SPEKT-NATRAD-01. Bundesministerium für Umwelt, Naturschutz und Reaktorsicherheit. (In German).

Schlesinger, T., Izak-Biran, T., Even, O., Dukhan, R., Shamai, Y., Koch, J., Tal, A., & Israeli, M. (1987). *Monitoring data related to the Chernobyl accident as measured in Israel during May - July 1986 and the assessment of the radiation doses to the population*. Soreq Nuclear Research Center. IA-1430.

Schmidt, S., & Cochran, J. K. (2010). Radium and radium-daughter nuclides in carbonates: a brief overview of strategies for determining chronologies. *Journal of Environmental Radioactivity*, *101*, 530–537. Radium and Radon Isotopes as Environmental Tracers.

Scholten, J. C., Osvath, I., & Pham, M. K. (2013). ^{226}Ra measurements through gamma spectrometric counting of radon progenies: How significant is the loss of radon? *Marine Chemistry*, *156*, 146–152.

Seelmann-Eggebert, W., Flegenheimer, J., Pfennig, G., & Schroeder, H. (1962). *Die mathematische Behandlung der Zerfalls- und Bildungsgesetze der Radioaktivität mit grafisch gelösten Beispielen*. Lecture notes KFK 117 Institut fur Radiochemie, Kernforschungszentrum Karlsruhe Germany. In German.

Shanahan, T. M., Overpeck, J. T., Anchukaitis, K. J., Beck, J. W., Cole, J. E., Dettman, D. L., Peck, J. A., Scholz, C. A., & King, J. W. (2009). Atlantic forcing of persistent drought in west africa. *Science*, *324*, 377–380.

Shawky, S., & El-Tahawy, M. (1999). Distribution pattern of ^{90}Sr and ^{137}Cs in the Nile delta and the adjacent regions after Chernobyl accident. *Applied Radiation and Isotopes*, *50*, 435–443.

Sültenfuß, J., Roether, W., & Rhein, M. (2009). The bremen mass spectrometric facility for the measurement of helium isotopes, neon, and tritium in water. *Isotopes in Environmental and Health Studies*, *45*, 83–95.

Smith, J. N. (2001). Why should we believe ^{210}Pb sediment geochronologies? *Journal of Environmental Radioactivity*, *55*, 121–123.

Soetaert, K., Herman, P. M., Middelburg, J. J., Heip, C., de Stigter, H. S., van Weering, T. C., Epping, E., & Helder, W. (1996). Modeling ^{210}Pb-derived mixing activity in ocean margin sediments: Diffusive versus nonlocal mixing. *Journal of Marine Research*, *54*, 1207–1227.

Southon, J., Mohtadi, M., & De Pol-Holz, R. (2012). Planktic foram dates from the Indonesian Arc: marine reservoir age corrections and a volcanic eruption that wasn't. 21th International Radiocarbon Conference, Paris, France.

Sprintall, J., Wijffels, S. E., Molcard, R., & Jaya, I. (2009). Direct estimates of the Indonesian Throughflow entering the Indian Ocean: 2004–2006. *Journal of Geophysical Research*, *114*, 19.

Steinke, S. (2012). Unpublished raw data (dry masses, dry bulk densities at station GeoB 10065). MARUM, University of Bremen.

Steinke, S., Mohtadi, M., Prange, M., Varma, V., Pittauerová, D., & Fischer, H. W. (submitted). Mid- to Late-Holocene Australian-Indonesian summer monsoon variability. *Quaternary Science Reviews*, .

Stiller, M., & Imboden, D. M. (1986). ^{210}Pb in Lake Kinneret water and sediments: Residence times and fluxes. In P. G. Sly (Ed.), *Sediment and water interactions* (pp. 501–511). Springer-Verlag, New York.

Stoulos, S., Manolopoulou, M., & Papastefanou, C. (2004). Measurement of radon emanation factor from granular samples: effects of additives in cement. *Applied Radiation and Isotopes*, *60*, 49–54.

Stuiver, M., & Braziunas, T. (1993). Modeling atmospheric ^{14}C influences and ^{14}C ages of marine samples to 10,000 BC. *Radiocarbon*, *35*, 137–189.

Stuiver, M., Reimer, P. J., , & Reimer, R. W. (2005). CALIB 5.0. WWW program and documentation. `http://calib.qub.ac.uk/calib` accessed in 9/2012.

Stuiver, M., Reimer, P. J., Bard, E., Beck, J. W., Burr, G. S., Hughen, K. A., Kromer, B., McCormac, G., van der Plicht, J., & Spurk, M. (1998). INTCAL98 radiocarbon age calibration, 24,000-0 cal BP. *Radiocarbon*, *40*, 1041–1084.

Tans, P. P., De Jong, A. F. M., & Mook, W. G. (1979). Natural atmospheric ^{14}C variation and the Suess effect. *Nature*, *280*, 826–828.

Thompson, R., & Clark, R. (1988). Sequence slotting for stratigraphic correlation between cores: theory and practice. In R. Davis (Ed.), *Paleolimnology and the Reconstruction of Ancient Environments* (pp. 229–240). Springer Netherlands.

Thompson, R., Clark, R. M., & Boulton, G. S. (2012). Core correlation. In H. J. B. Birks, A. F. Lotter, S. Juggins, & J. P. Smol (Eds.), *Tracking Environmental Change Using Lake Sediments* (pp. 415–430). Springer Netherlands volume 5 of *Developments in Paleoenvironmental Research*.

Thompson, W. (2007). U-series dating. In S. A. Elias (Ed.), *Encyclopedia of Quaternary Science* (pp. 3099–3104). Oxford: Elsevier.

Thomsen, M. S., Heinemeier, J., Hornshøj, P., Nielsen, H. L., & Rud, N. (1991). Half-life of ^{32}Si measured via accelerator mass spectrometry. *Nuclear Physics A*, *534*, 327–338.

Thunell, R. C., Tappa, E., & Anderson, D. M. (1995). Sediment fluxes and varve formation in Santa Barbara Basin, offshore California. *Geology*, *23*, 1083–1086.

Tibor, G., Niemi, T., Ben-Avraham, Z., Al-Zoubi, A., Sade, R., Hall, J., Hartman, G., Akawi, E., Abueladas, A., & Al-Ruzouq, R. (2010). Active tectonic morphology and submarine deformation of the northern Gulf of Eilat/Aqaba from analyses of multibeam data. *Geo-Marine Letters*, *30*, 561–573.

Turekian, K. K., Cochran, J. K., & Nozaki, Y. (1979). Growth rate of a clam from the Galapagos Rise hot spring field using natural radionuclide ratios. *Nature*, *280*, 385–387.

Ulbrich, S. (2007). *Investigation of long-term background in gamma-spectroscopy*. Student research project University of Bremen, Germany, (in German).

UNSCEAR (2000). *Report to the General Assembly,with scientific annexes. Sources and effects of ionizing radiation*. Volume 1: Sources. Annex C. United Nations Scientific Committee on the Effects of Atomic Radiation New York.

Uğur (Tanbay), A., & Yener, G. (2001). Accumulation rates and sediment deposition in the Gökova Bay in Aegean Sea Turkish Coast. *Applied Radiation and Isotopes*, *55*, 581 – 588.

Vidmar, T., Çelik, N., Díaz, N. C., Dlabac, A., Ewa, I., Carrazana González, J., Hult, M., Jovanović, S., Lépy, M.-C., Mihaljević, N., Sima, O., Tzika, F., Jurado Vargas, M., Vasilopoulou, T., & Vidmar, G. (2010). Testing efficiency transfer codes for equivalence. *Applied Radiation and Isotopes*, *68*, 355–359.

Voltaggio, M., Andretta, D., & Taddeucci, A. (1987). Dating of newly formed minerals in geothermal fields through ^{232}Th series short lived isotopes: Check on mineral of known age and implications to fluid-rock interactions. *Geothermics*, *16*, 255–261.

Wagner, G. A. (1998). *Age determination of young rocks and artifacts: Physical and chemical clocks in Quaternery geology and archaeology*. (1st ed.). Springer, Berlin.

Walker, D., & Ormond, R. (1982). Coral death from sewage and phosphate pollution at Aqaba, Red Sea. *Marine Pollution Bulletin*, *13*, 21–25.

Walker, M. (2005). *Quaternary Dating Methods*. (1st ed.). Wiley, Chichester.

Wan, G., Santschi, P., Sturm, M., Farrenkothen, K., Lueck, A., Werth, E., & Schuler, C. (1987). Natural (^{210}Pb, ^{7}Be) and fallout (^{137}Cs, ^{239,240}Pu, ^{90}Sr) radionuclides as geochemical tracers of sedimentation in Greifensee, Switzerland. *Chemical Geology*, *63*, 181–196.

Wang, Z.-l., & Yamada, M. (2005). Plutonium activities and ^{240}Pu/^{239}Pu atom ratios in sediment cores from the east China sea and Okinawa Trough: Sources and inventories. *Earth and Planetary Science Letters*, *233*, 441–453.

Warneke, T. (2002). *High-precision isotope ratio measurements of uranium and plutonium in the environment*. Dissertation thesis University of Southampton.

Wetzler, N., Marco, S., & Heifetz, E. (2010). Quantitative analysis of seismogenic shear-induced turbulence in lake sediments. *Geology*, *38*, 303–306.

Wieland, E., Santschi, P. H., & Beer, J. (1991). A multitracer study of radionuclides in lake Zurich, Switzerland. 2. Residence times, removal processes and sediment focusing. *Journal of Geophysical Research - Oceans*, *96*, 17067–17080.

Wijffels, S. E., Meyers, G., & Godfrey, J. S. (2008). A 20-yr average of the Indonesian throughflow: Regional currents and the interbasin exchange. *Journal of Physical Oceanography*, *38*, 1965–1978.

Wilson, C. G., Matisoff, G., & Whiting, P. J. (2003). Short-term erosion rates from a ^{7}Be inventory balance. *Earth Surface Processes and Landforms*, *27*, 967–977.

WMO (2012). World meteorological organization. `http://www.wmo.int` accessed in 8/2012.

World Bank (1996). The Hashemite Kingdom of Jordan Gulf of Aqaba environmental action plan. Retrieved from `http://www.thegef.org` website in 10/2012.

Yamada, M., Zheng, J., & Wang, Z.-L. (2006). ^{137}Cs, $^{239+240}$Pu and ^{240}Pu / ^{239}Pu atom ratios in the surface waters of the western North Pacific Ocean, eastern Indian Ocean and their adjacent seas. *Science of The Total Environment*, *366*, 242–252.

Yoshimori, M., Hirayama, H., Mori, S., Sasaki, K., & Sakurai, H. (2003). Be–7 nuclei produced by galactic cosmic rays and solar energetic particles in the Earth's atmosphere. *Advances in Space Research*, *32*, 2691–2696.

Zaborska, A., Carroll, J., Papucci, C., & Pempkowiak, J. (2007). Intercomparison of alpha and gamma spectrometry techniques used in ^{210}Pb geochronology. *Journal of Environmental Radioactivity*, *93*, 38–50.

Zheng, J., Aono, T., Uchida, S., Zhang, J., & Honda, M. C. (2012a). Distribution of Pu isotopes in marine sediments in the Pacific 30 km off Fukushima after the Fukushima Daiichi nuclear power plant accident. *Geochemical Journal*, *46*, 361–369.

Zheng, J., Tagami, K., Watanabe, Y., Uchida, S., Aono, T., Ishii, N., Yoshida, S., Kubota, Y., Fuma, S., & Ihara, S. (2012b). Isotopic evidence of plutonium release into the environment from the Fukushima DNPP accident. *Scientific Reports*, *2*.

Zheng, J., & Yamada, M. (2004). Sediment core record of global fallout and Bikini close-in fallout Pu in Sagami Bay, Western Northwest Pacific margin. *Environmental Science and Technology*, *38*, 3498–3504.

Zhu, J., & Olsen, C. R. (2009). Beryllium-7 atmospheric deposition and sediment inventories in the Neponset river estuary, Massachusetts, USA. *Journal of Environmental Radioactivity*, *100*, 192–197.

Zielinski, R. A., Otton, J. K., & Budahn, J. R. (2001). Use of radium isotopes to determine the age and origin of radioactive barite at oil-field production sites. *Environmental Pollution*, *113*, 299–309.